

Modeling and Simulation of Flash Evaporation of Cryogenic Liquid Jets

Von der Fakultät Energie-, Verfahrens- und Biotechnik der Universität
Stuttgart zur Erlangung der Würde eines Doktors der
Ingenieurwissenschaften (Dr.-Ing.) genehmigte Abhandlung

Vorgelegt von

Jan Wilhelm Gärtner

aus Frankfurt am Main

Hauptberichter: Prof. Dr. Andreas Kronenburg

Mitberichter: Prof. Dr. Michael Oschwald,
Prof. Dr. Stefan Riedelbauch

Tag der mündlichen Prüfung: 8. Mai 2024

Institut für Technische Verbrennung
der Universität Stuttgart
2024

Erklärung

Hiermit versichere ich,

1. dass ich meine Arbeit selbständig verfasst habe,
2. dass ich keine anderen als die angegebenen Quellen benutzt und alle wörtlich oder sinngemäß aus anderen Werken übernommenen Aussagen als solche gekennzeichnet habe,
3. dass die eingereichte Arbeit weder vollständig noch in wesentlichen Teilen Gegenstand eines anderen Prüfungsverfahrens gewesen ist,
4. dass ich die Arbeit noch nicht vollständig veröffentlicht habe und,
5. dass das elektronische Exemplar mit den anderen Exemplaren übereinstimmt.

Stuttgart, im Januar 2024

Jan Wilhelm Gärtner

Acknowledgments

The present work was conducted during my time as a research assistant at the Institute for Combustion Technology (Institut für Technische Verbrennung, ITV) at the University of Stuttgart.

I want to express my deepest gratitude to my supervisor, Prof. Dr. Andreas Kronenburg, for giving me the opportunity to work on this exciting research topic and for his continued support. I am particularly grateful for the numerous constructive comments and discussions. Further, I thank him for giving me the freedom to explore new areas and aspects while keeping the goal of the thesis in mind. This work would not have been possible without it, and I greatly appreciate the time and effort spent. It was a pleasure working together.

Furthermore, I would like to thank Dr. Andreas Rees and Prof. Dr. rer. nat. Michael Oswald for conscientiously conducting the experimental study at DLR Lampoldshausen, which served as the validation cases for the numerical work. I am also grateful for the countless fruitful discussions about flashing sprays and for helping me understand and interpret the experimental data sets.

I also thank Dr. Marvin Sontheimer, Maximilian Karsch, and Karl-Heinz Theil for their support in building and maintaining ITV's IT infrastructure. I would also like to thank all my colleagues at ITV for sharing this journey with me. Another thanks goes to Ricarda Schubert for taking care of the administrative matters, which allowed me to focus on my research project.

Last but not least, I want to thank my family for the continued support throughout this journey.

Finally, I am grateful for the financial support by the Deutsche Forschungsgemeinschaft (DFG, German Research Foundation) within the project SFB-TRR 75, project number 84 292 822.

Further, I appreciate having had the opportunity to run simulations on the high-performance computer systems of the Scientific Computing Center (SCC) in Karlsruhe and the High-Performance Computing Center Stuttgart (HLRS) funded by the Ministry of Science, Research and the Arts Baden-Württemberg and by the German Federal Ministry of Education and Research.

Abstract

In recent years, advancements in orbital maneuvering systems and upper-stage rocket propulsion technologies, exemplified by the cryogenic Ariane 6 Vinci engine, have been directed towards the substitution of conventional toxic and hypergolic propellants by environmentally benign and operationally safer alternatives, such as hydrogen, methane or kerosene. However, the injection of the typically cryogenic liquids into the near vacuum conditions of space prior to ignition causes a depressurization below saturation conditions, leading to rapid bubble nucleation, growth, and subsequent spray breakup, called flash evaporation. Understanding the spray breakup and mixing of the flashing cryogenic liquids is imperative for ensuring the success of engine ignition, particularly when employing advanced ignition techniques such as laser ignition. However, the extreme environmental conditions render experimental investigations extremely challenging and allow only limited optical access. Therefore, numerical tools can provide additional information to gain a complete picture of the flashing process. In this work, a novel compressible, one-fluid, two-phase computational fluid dynamic solver is developed for flashing cryogenic liquids in OpenFOAM. Emphasis is placed on the comprehensive representation of the entire flashing phenomenon, from the nearly incompressible liquid state to the highly compressible vapor-droplet mixture following spray breakup. After validating the solver's capability to capture the transonic effects in 2D and 3D faithfully, it is applied to three different cryogenic liquid nitrogen cases, experimentally investigated at the German Aerospace Center (DLR) Lampoldshausen. This investigation revealed a pronounced recirculation zone in the 2D simulations where motionless or even slightly upstream floating regions have been observed in the shadowgraph images, providing an explanation for the observed phenomenon. However, further 3D investigation with highly resolved large eddy simulations could not reproduce the recirculation zone, yet regions of comparable low axial velocity have been identified at the same location. Therefore, the simpler 2D simulations can predict the overall characteristics of mass flow rate and spray angle yet overpredict the recirculation downstream of the shock front due to missing 3D effects. Further, the dynamics of larger droplets, which do not adhere to the no-slip assumption of the one-fluid model, are studied with the 3D LES by including a cloud of one-way coupled particles. This investigation revealed an excellent agreement with measured particle velocities, indicating that the dynamics of the larger droplets are governed by their inertia and the vapor velocity field captured by the one-fluid model. Finally, a novel model for the development of the surface density of flashing flows called the flashing liquid atomization model (FLAM) is presented. With this model, the lost information of surface density and the mean droplet diameter can be recovered. A comparison of the droplet size measurements of the cryogenic liquid nitrogen cases showed that the model can predict the droplet size on the central axis and capture the trend of decreasing droplet size with increasing superheat ratio. Thus, this work introduces, for the first time, a solver designed for simulating flashing cryogenic flows, including surface density modeling to capture droplet sizes.

Kurzfassung

Die Entwicklung moderner Oberstufentriebwerke und Manövriersysteme, wie das Vinci Triebwerk der Ariane 6, hat unter anderem zum Ziel die hypergolischen Standardtreibstoffe durch umweltfreundlichere und einfacher zu handhabende Treibstoffkombinationen wie Wasserstoff-Sauerstoff oder Methan-Sauerstoff zu ersetzen. Die Einspritzung dieser typischerweise kryogenen Medien in die Brennkammer bei niedrigem Druck, der in hohen Atmosphärenschichten oder im Weltraum vorliegt, führt jedoch zu einem Druckabfall unterhalb der Sättigungsgrenze, was zu Nukleation von Blasen, deren Wachstum und einem fast sofortigen Aufbruch des Strahls führt. Dieser Prozess wird als Flashverdampfung bezeichnet. Für das erfolgreiche Zünden des Triebwerks ist es unerlässlich die Prozesse beim Strahlaufbruch und das darauffolgende Mischen der Treibstoffströme zu verstehen, im Besonderen, wenn neue Zündtechnologien wie Laserzündung zum Einsatz kommen. Die herausfordernden experimentellen Bedingungen von kryogenen Flüssigkeiten im Vakuum erlauben jedoch nur einen eingeschränkten optischen Zugang und Messung der Strömung. Die numerische Strömungssimulation kann deshalb hier helfen weitere, detaillierte Kenntnisse der Strömung und des Flashing für ein vollumfängliches Verständnis zu gewinnen. In der vorliegenden Arbeit wird ein neuer kompressibler Zwei-Phasen, Ein-Fluid Löser für die Simulation von flashverdampfenden kryogenen Flüssigkeiten für die open-source Plattform OpenFOAM entwickelt und zur Simulation von flashverdampfenden, kryogenen Stickstoff verwendet. Hierbei liegt der Schwerpunkt auf der umfassenden Darstellung des gesamten Flashing-Phänomens, vom nahezu inkompressiblen flüssigen Zustand bis zum hochkompressiblen Dampf-Tropfen-Gemisch nach dem Strahlaufbruch. Nach der Validierung des Löser transsonische Effekte aufgrund von Flashing in 2D und 3D realitätsgetreu zu erfassen, wird dieser auf drei verschiedene Fälle von flashverdampfenden kryogenem Flüssigstickstoff, die am Deutschen Zentrum für Luft- und Raumfahrt (DLR) Lampoldshausen experimentell untersucht wurden, angewendet. Die numerische Untersuchung ergab für die 2D Simulationen eine ausgeprägte Rezirkulationszone, die die experimentell beobachteten Bereiche negativer axiale Geschwindigkeiten sowie stationäre oder sogar leicht stromaufwärts bewegene Strukturen in den Schattenaufnahmen erklären kann. Weitere 3D-Untersuchungen mit hochaufgelösten Large-Eddy-Simulationen konnten die Rezirkulationszone nicht reproduzieren, jedoch wurden an derselben Stelle Regionen mit vergleichbar niedriger axialer Geschwindigkeit identifiziert. Daher können die vereinfachten 2D-Simulationen zwar die Gesamtcharakteristiken wie den Massenstroms sowie den Strahlwinkels vorhersagen, führen aber zu einer Überschätzung der Rezirkulation aufgrund fehlender 3D-Effekte. Darüber hinaus wird die Dynamik größerer Tropfen, welche der Strömung nicht perfekt folgen und somit der no-slip Annahme des Löser widersprechen, mit einseitig gekoppelten passiven Partikeln untersucht. Diese Untersuchung ergab eine ausgezeichnete Übereinstimmung mit den gemessenen Partikelgeschwindigkeiten, was darauf hindeutet, dass die Dynamik der größeren Tröpfchen hauptsächlich durch ihre Trägheit und das Geschwindigkeitsfeldes des Gases bestimmt wird. Des Weiteren wird in dieser Arbeit ein neues Modell für die Entwicklung der Oberflächendichte von flashverdampfenden Strömungen vorgestellt, das sogenannte Flashing Liquid Atomization Model (FLAM). Mit diesem Modell können die verlorenen Informationen über die Oberflächendichte und den mittleren Tröpfchendurchmesser wiederhergestellt werden. Ein

Vergleich mit gemessenen Tröpfchengrößen eines flashverdampfenden, kryogenen Stickstofffalls zeigte, dass das Modell die Tröpfchengröße auf der Mittelachse vorhersagen und den Trend der abnehmenden Tröpfchengröße mit zunehmendem Überhitzungsverhältnis erfassen kann.

List of Publications

Parts of this thesis have been presented at conferences and published in the archival literature. The contents included in the present work have been modified with respect to the originally published texts and have been considerably extended to ensure the completeness, coherence and consistency of the present manuscript.

Journal Publications

- (1) J. W. Gärtner, A. Kronenburg, A. Rees, J. Sender, M. Oswald, and G. Lamanna. "Numerical and Experimental Analysis of Flashing Cryogenic Nitrogen". *International Journal of Multiphase Flow*, 130, 2020, doi: 10.1016/j.ijmultiphaseflow.2020.103360.
 - Author's contribution: programming (100 %), data generation (50 %), scientific originality (30 %).
- (2) J. W. Gärtner, A. Kronenburg, and T. Martin. "Efficient WENO Library for OpenFOAM". *Software X*, 12, 2020, doi: 10.1016/j.softx.2020.100611.
 - Author's contribution: programming (75 %), data generation (100 %), scientific originality (40 %).
- (3) J. W. Gärtner, F. Ye, A. Kronenburg, and O. T. Stein. "Numerical Investigation of Spray Collapse in GDI with OpenFOAM". *Fluids*, 6, 3, 2021, doi: 10.3390/fluids6030104.
 - Author's contribution: programming (90 %), data generation (75 %), scientific originality (40 %).
- (4) J. W. Gärtner, A. Kronenburg, A. Rees, and M. Oswald. "Investigating 3-D Effects on Flashing Cryogenic Jets with Highly Resolved LES". *Flow, Turbulence and Combustion*, 2023, doi: 10.1007/s10494-023-00485-4.
 - Author's contribution: programming (100 %), data generation (75 %), scientific originality (40 %).
- (5) J. W. Gärtner, A. Kronenburg. "A Novel ELSA Model for Flash Evaporation". *International Journal of Multiphase Flow*, 2024, doi: <https://doi.org/10.1016/j.ijmultiphaseflow.2024.104784>.
 - Author's contribution: programming (100 %), data generation (100 %), scientific originality (50 %).

Conference Publications

- (1) J. W. Gärtner, A. Rees, A. Kronenburg, J. Sender, M. Oswald, and D. Loureiro. "Large Eddy Simulation of Flashing Cryogenic Liquid with a Compressible Volume of Fluid Solver". *29th Conference on Liquid Atomization and Spray Systems*, Paris, France, 2019.
 - Author's contribution: Programming (100%), data generation (70%), scientific originality (40%).

Contents

Contents	xi
List of Figures	xv
List of Tables	xvii
Nomenclature	xix
1 Introduction	1
1.1 Motivation	1
1.2 State of the Art	3
1.3 Objectives	5
1.4 Thesis Outline	6
2 Fundamentals of Flashing Sprays	7
2.1 Physical and Thermodynamic Processes of Flash Evaporation	7
2.2 Nucleation of Vapor Bubbles	8
2.2.1 Homogeneous nucleation	9
2.2.2 Heterogeneous nucleation	11
2.3 Bubble Growth	12
2.4 Breakup of Flashing Sprays	13
2.4.1 Primary spray breakup	14
2.4.2 Secondary spray breakup	16
2.5 Droplet Evaporation	17
2.6 Transonic Behavior of Flashing Sprays	19
3 Modeling and Simulation of Two-Phase Flows	21
3.1 Governing Equations	22
3.1.1 Equation of state	24
3.1.2 One-fluid model	24
3.1.3 Interface tracking techniques	25
3.2 Turbulence Modeling	26
3.2.1 RANS/LES turbulence models	28
3.2.2 Turbulence modeling of two-phase flows	31
3.3 Surface Density Modeling for Flashing Sprays	32
3.3.1 Principal model design of the source terms	33
3.3.2 Source terms for flashing sprays in the dense region	34
3.3.3 Estimating the final bubble merging radius	37

3.3.4	Droplet evaporation in the dilute spray regime	40
3.4	Phase Change Models	40
3.4.1	Hertz-Knudsen model	41
3.4.2	Adachi model	42
3.4.3	Homogeneous relaxation model	42
4	Solving the Equation System in OpenFOAM	45
4.1	OpenFOAM	45
4.2	Solution Methods for Sub- and Transonic Flows	46
4.2.1	Pressure-velocity solution algorithm	46
4.3	Implementation of the Governing Equations	47
4.3.1	Volume fraction transport	47
4.3.2	Coupling momentum and mass conservation - pressure equation	50
4.3.3	Energy equation	53
4.3.4	Surface density transport equation	55
4.4	Thermophysical Properties and Equation of State	56
5	Simulation of Cryogenic Flashing Nitrogen	57
	Paper 1: Numerical and Experimental Analysis of Flashing Cryogenic Nitrogen	69
	Paper 2: Numerical Investigation of Spray Collapse in GDI with OpenFOAM	85
	Paper 3: Investigating 3-D Effects on Flashing Cryogenic Jets with Highly Resolved LES	105
	Paper 4: A Novel ELSA Model for Flash Evaporation	125
6	Conclusions and Outlook	141
6.1	Summary and Conclusions	141
6.2	Outlook	144
A	Derivation of the Homogeneous Nucleation for Superheated Liquid and Sub- cooled Vapor	147
B	Derivation of the mixture velocity	149
B.1	Velocity of Center of Mass	149
B.2	Velocity of Center of Volume	150
C	Speed of Sound and Compressibility	153
C.1	Difference to weighted average	154
C.2	Compressibility and Phase Change	155
D	Sub- and Transonic Treatment of the Pressure Equation in OpenFOAM	157
D.1	Pressure Equation	157
D.1.1	H-operator of OpenFOAM	158
D.2	Subsonic Solution	158
D.3	Transonic Solution	159
E	Real Gas Treatment in the Energy Equation	161
F	Compressible Two-Phase Solver	163
F.1	Solver Outline	163

F.1.1	Solving the the volume fraction transport in OpenFOAM	163
F.1.2	Continuity equation to determine the mass error	165
F.1.3	Surface density transport equation	166
F.1.4	Momentum predictor step	166
F.1.5	Energy conservation	167
F.1.6	Pressure equation	167
F.1.7	Update velocities	169
F.2	Tabulated Properties	171
F.2.1	Interpolate intermediate values	171
F.2.2	Edge cases	173
F.2.3	Accuracy of interpolated values	174
G	Data Storage	175
G.1	Paper 1	176
G.2	Paper 2	176
G.3	Paper 3	177
G.4	Paper 4	177
	Bibliography	179

List of Figures

1.1	Examples of flash boiling sprays (a) gasoline direct injection with iso-octane [72], (b) flashing acetone spray [73].	2
2.1	Sketch of a p-v diagram with an iso-thermal line.	9
2.2	Minimum work required to form a vapor bubble of radius R	10
2.3	Sketch of the inertia and thermal limited bubble growth conditions in the bubble and superheated liquid.	14
2.4	Flashing cryogenic nitrogen shadowgraph images, representing the four different flashing regimes according to Cleary et al. [27] and Rees et al. [113].	15
2.5	Flashing spray breakup through bubble coalescence, depicting the nucleation, bubble growth and spray breakup within a droplet. Inspired by Rees [111].	15
2.6	Temporal evolution of a bubble growth and shattering of the jet in the transitional flashing regime, captured by Alghamdi et al. [7]. Image taken from Alghamdi et al. [7] with permission of Elsevier.	16
2.7	Sketch of a flash evaporating droplet.	18
2.8	Simplified sketch of the shock structure for transonic flashing sprays, (left) for very highly superheated sprays according to Vieira et al. [138] and (right) superheated sprays with spray breakup [73].	20
3.1	Sketch of the real liquid-vapor interface (a), representation of the volume of fluid field (b), and the interface reconstruction with PLIC (c).	26
3.2	Indicator function and comparison of dense spray turbulent source term modeling for surface density transport. The qualitative spray bubble/droplet morphology for each region of the liquid volume fraction is sketched above, blue is liquid and white represents vapor. The radius of the bubbles when they merge and the spray breakup occurs is marked with R_f	33
3.3	(a) Nucleation rate predicted by CNT for cryogenic nitrogen for $p = 15\,000$ Pa. (b) Normalized homogeneous nucleation rate predicted by CNT.	38
4.1	Flow chart of the PIMPLE algorithm for a compressible flow. Based on the standard <code>rhoPimpleFoam</code> solver of OpenFOAM.	48
5.1	Velocity contour plot of the nitrogen spray compared to the shadowgraph images. The velocity direction is visualized in the simulation with white arrows, and the recirculation zone is marked with a yellow box.	60
5.2	Logarithmic pressure contour for the case of Propane-B for different time steps: (a) 0.020 ms, (b) 0.035ms, (c) 0.040 ms and (d) 0.150 ms. The formed pressure cells are marked in (c) with Roman numerals I and II.	62

5.3	(a) Mean velocity of the LES compared to the experimentally measured droplet velocities marked as circles with a scaled velocity vector in black. The white arrows represent the flow direction of the LES solution. The red marked region denotes experimental measurement points with only a few valid measurements, resulting in a low statistical relevance. (b) Axial velocity of the one-fluid solution (LES), the experimental data (Exp) and sampled particles (Sim), as well as conditioned velocities for droplets larger than 10 μm	64
5.4	(a) Mean Sauter diameter, D_{32} , with the model parameters $R_f^* = 140$, $We_{ev}^{eq} = 0.66$. Subfigure (b) shows a comparison of the new FLAM model to the standard ELSA model (green line) and the ELSA model for flashing sprays proposed by Lyras et al. [86] (orange line).	66
B.1	Example of the velocity of center mass \vec{u}_m , the individual velocities \vec{u}_q, \vec{u}_p , the velocity drift $\vec{u}_{dr,q}$ and the relative velocity \vec{u}_{pq} , [29]	150
B.2	Example of the velocity of center volume \vec{u} , the individual velocities \vec{v}_q, \vec{v}_p , the velocity drift $\vec{v}_{dr,q}$ and the relative velocity \vec{v}_{pq} [29]	151
C.1	Compressibility and speed of sound calculated with Eq. (4.21) for water and air compared to experimental data of Karplus [64].	155
D.1	Sketch of the superscript notation for the time values in OpenFOAM. The superscript k donates the already computed value of the previous time step, p^* is the currently stored value in the field, and $k+1$ is the to compute value of the next time step. Typically values marked with $k+1$ are computed implicitly, whereas k and $*$ denoted values are already known and computed explicitly.	159
F.1	Flow chart of the PIMPLE algorithm for the <code>compressiblePhaseChangeFoam</code> solver. The PISO part of the algorithm is marked with a light gray box.	170
F.2	Bicubic interpolation for points inside the table. Black dots mark table vertices and the cross is the point that is looked up.	172
F.3	Handling of interpolation for a point outside the table.	173
F.4	Handling of interpolation for a point outside the table if the table is only partially filled.	173
F.5	Normalized error calculating the liquid density (a) and liquid enthalpy (b) of the tabulated properties compared to the exact CoolProp value.	174
F.6	Normalized error in calculating the vapor density (a) and vapor enthalpy (b) of the tabulated properties to the exact value calculated by CoolProp.	174

List of Tables

5.1	Boundary values for the cryogenic nitrogen jet.	59
-----	---	----

Nomenclature

Latin Letters

A_I	Interfacial area	m^2
a_p	Matrix coefficients	—
c_p	Specific heat capacity at constant pressure	$\text{J}/(\text{kg K})$
C_S	Modeling constant	—
D	Diameter	m
D_{32}	Sauter mean diameter	m
\mathcal{D}_l	Liquid thermal diffusivity	m^2/s
\mathcal{D}_v	Diffusion coefficient of the vapor	m^2/s
e	Specific energy	J/kg
G	Gibbs free energy	J
g	Gravity	m/s^2
h	Specific enthalpy	J/kg
J	Nucleation rate per unit volume	$1/\text{m}^3$
Ja	Jacob number	—
k_b	Boltzmann constant	J/K
K_c	Model constant	—
k_t	Turbulent kinetic energy	m^2/s^2
\mathcal{L}	Length scale	m
L	Latent heat of evaporation	J/kg
\dot{m}	Evaporation rate	kg/s
M	Molar mass	mol/kg
m	Mass	kg

Ma	Mach number	-
m_d	Mass of one droplet	kg
m_{mol}	Mass of a single molecule	kg
n^*	Normalized surface normal vector	-
N_A	Avogadro number	1/mol
n_b	Bubble number density	1/m ³
p	Pressure	Pa
Pr	Prandtl number	-
\dot{Q}, q	Heat flux	W/m ²
\dot{R}	Bubble growth rate	m/s
R	Radius of a droplet or bubble	m
R_u	Universal gas constant	J K/mol
R_c	Critical radius of a vapor bubble nuclei	m
R_f	Bubble merging radius	m
R_p	Superheat ratio	-
S_{ij}	Strain rate	1/s
Sc	Schmidt number	-
S_h	Energy source term	J/(m ³ s)
S_m	Momentum exchange term	kg/(m ² s ²)
T	Temperature	K
t	Time	s
u	Velocity	m/s
u_Γ	Compression velocity	m/s
u_c	Characteristic velocity	m/s
V	Volume	m ³
v	Specific volume	m ³ /kg
We	Weber number	-

Greek Letters

α	Volume fraction	-
α_{sh}	Heat transfer coefficient	W/(m ² K)
α_d	Volume fraction of dissolved gas	-
χ	Mass fraction	-
Δt	Time interval	s
η	Void fraction	-
Γ_t	Turbulent diffusivity	m ² /s
κ	Thermal conductivity	W/(m K)
δ_{ij}	Kronecker delta	-
μ	Viscosity	kg/(m s)
μ_t	Turbulent viscosity	kg/(m s)
ν	Kinematic viscosity	m ² /s
ν_t	Turbulent kinematic viscosity	m ² /s
Φ	A general variable, e.g., velocity or pressure	
Ψ	Free function, e.g., a blending function	
ψ	Compressibility	s ² /m ²
ρ	Density	kg/m ³
Σ	Surface density	1/m
σ	Surface tension	N/m
$\boldsymbol{\tau}$	Viscous stress tensor	kg/(m s ²)
τ	Relaxation time	s
Θ	Relaxation time for the HRM model	s

Operators

$\widetilde{(\cdot)}$	Favre averaged property
$\frac{D(\cdot)}{Dt}$	Material derivative
$\overline{(\cdot)}$	Reynolds averaged property
∇	Nabla operator
\times	Multiplication

$H(u)$ Discretized momentum equation except the pressure gradient.
See Appendix D.1.1

Subscripts

b Denoting bubble properties, e.g., R_b as the bubble radius
corr Corrected property
 f Cell face value
v Vapor or gaseous properties
 ∞ Far-field value
inj Injection conditions
 k,i,j Indices
 l Liquid properties
sat Saturation conditions
SG Saturated gas
sgs Sub-grid scales
SL Saturated liquid
s Surface

Superscripts

' Sub-filter fluctuation
" Sub-filter fluctuation related to density-weighted average
* Currently stored value of a variable
 k Old-time value of a variable
 $k + 1$ Value of the next time step
eq Equilibrium conditions

Acronyms

CIP Constrained interpolation profile
CNT Classical nucleation theory

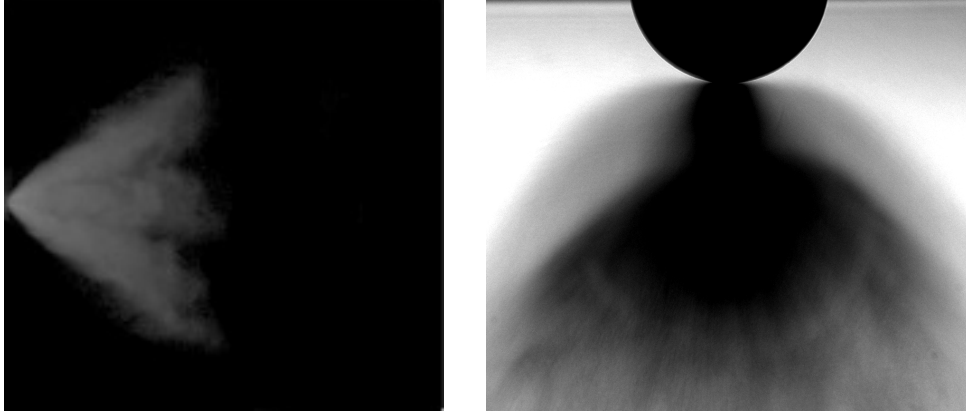
ELSA Eulerian lagrangian spray atomization
FLAM Flashing liquid atomization model
ILES Implicit large eddy simulation
LES Large eddy simulation
MAC Marker-and-cell
MULES Multi-dimensional limiter for explicit solution
PIMPLE Combination of SIMPLE and PISO
PISO Pressure implicit with splitting of operators
PLIC Piecewise linear interface construction
RANS Reynolds averaged Navier-Stokes
SIMPLE Semi-implicit method for pressure linked equations
SST Shear stress transport
WALE Wall adapting local eddy-viscosity
WENO Weighted essentially non-oscillatory

Chapter 1

Introduction

1.1 Motivation

When a high-pressure liquid is injected into a low-pressure atmosphere, respective to its own saturation pressure, bubble nucleation, growth, and subsequent spray breakup occur. Due to the rapid evaporation of the spray, this process is referred to as flash evaporation or flash boiling. Flashing sprays can offer distinct advantages over conventional atomizers, such as small droplet diameters, homogeneous droplet size distribution, and a reduced penetration length [124]. Hence, flashing sprays are applied to various technical problems and industries, ranging from improving efficiency in internal combustion engines [58], to desalination [94, 47], medical products [143], consumer products such as deodorants [125], to rocket engines [52], see Figure 1.1. Despite being used in various contexts, flashing sprays still elude a comprehensive understanding and further research is required. In the last decade, the flashing behavior of cryogenic liquids within rocket engines has gained increased interest due to two parallel developments. The first is the classification of hydrazine, the standard mono-propellant for orbital thrusters, as a candidate of "substances of very high concern" in the REACH (Regulation, Evaluation, Authorization and Restriction of Chemicals) regulations of the European Union in 2006 [131]. Therefore, suitable, more environmentally friendly alternatives, such as the combustion of cryogenic oxygen and hydrogen or methane, must be developed for upper-stage rocket engines and orbital thrusters [112]. In addition to replacing hydrazine, modern mission designs require novel lightweight ignition technologies that allow for multiple restarts and reuse with 100% ignition reliability [89, 20]. Laser ignition, as opposed to conventional pyrotechnical or electrical torch igniters, presents several distinct advantages, including high temporal and spatial precision, minimal ignition delay times, and the ability to decouple engine transients from



(a) Flashing iso-octane spray in a GDI engine.

(b) Flashing acetone spray with visible shock front.

Figure 1.1: Examples of flash boiling sprays (a) gasoline direct injection with iso-octane [72], (b) flashing acetone spray [73].

the ignition system. Over the past decade, numerous experimental studies have been conducted to investigate laser ignition for rocket engines, ranging from sub-scale combustion chambers to full-scale expander cycles [89, 130, 20, 19]. Although successful ignition has been demonstrated, a complete understanding of the underlying processes remains elusive, particularly under flashing injection conditions. Therefore, comprehending the spray dynamics of flashing cryogenic sprays before ignition is imperative for the development of reliable upper-stage rocket engines employing laser ignition. Nonetheless, the significant disparities in time and length scales associated with nucleation, bubble growth, spray breakup, and the macroscopic injector, coupled with the high optical density of flashing sprays and the extreme conditions during cryogenic injection, pose significant challenges for experimental investigations, particularly near the injector exit. In this regard, computational fluid dynamics (CFD) can provide crucial information about spray behavior that is not easily attainable through experiments alone. Further, the advancements in computational capabilities and resources available make it now feasible to run full-scale investigations, from cost-efficient two-dimensional Reynolds averaged to transient three-dimensional simulations, resolving larger turbulent structures. Therefore, this work aims to develop the necessary numerical tools and models to simulate cryogenic flashing sprays and to give further insight into the spray dynamics.

1.2 State of the Art

Flashing is a complex multiscale process encompassing vapor bubble nucleation at the nanometer scale, spray breakup and droplets in the micrometer range, and the macroscopic scale of the injector. This wide separation of time and length scales presents a significant challenge when it comes to modeling and simulating flashing sprays [124, 141, 112]. While direct numerical simulation (DNS) allows for modeling the growth and breakup of a small number of bubbles and droplets [83, 32], it becomes unfeasible for macro-scale simulations of an injector. A commonly used approach to simulate sprays on a macroscopic level is to model the continuous or carrier phase on an Eulerian grid and the dispersed phase as Lagrangian particles [108, 142]. This approach has the advantage that no interface has to be resolved between the phases, and the computational grid is much larger than the individual droplets or bubbles. However, it cannot capture the transition of the carrier phase from liquid to vapor during the spray breakup. Further, it requires information about the droplet or bubble size distribution and initial velocity. Another alternative approach involves solving the full set of conservation equations for both phases on an Eulerian grid with suitable mass, momentum, and energy exchange terms [78]. Assuming that the two phases are closely coupled, this can be further simplified by employing a no-slip condition between the phases and solving for a pseudo mixture fluid, with an additional scalar transport equation to distinguish between the two phases, commonly known as the one-fluid model. Various interface-capturing models such as volume of fluid, level-set, or piecewise linear interface capturing (PLIC) can be chosen to resolve the phase interface [38]. However, resolving the interface for the large range of length scales on a macroscopic level requires significant computational effort and is not feasible for the investigated flashing cases. Therefore, droplets or bubbles are modeled on the sub-grid scale, and no interface is resolved [120, 58, 76, 86, 95, 118, 96]. Similar to a diffuse interface approach, this has the benefit that no jump conditions have to be solved at the interface. Further, it offers distinct advantages for compressible flows, such as retaining thermodynamic consistency and capturing the wave speed for a liquid-vapor mixture [119, 64]. Nevertheless, employing the one-fluid methodology entails the significant drawback of losing information about droplet sizes and phase interface area. Yet, these spray characteristics play a pivotal role in comprehending subsequent ignition phenomena for upper-stage rocket engines. With the aim to combine the advantages of the one-fluid model and Lagrangian particles, Vallet et al. [135] incorporated the transport of an interface density scalar, akin to the flame surface density used in combustion simulations, to retain the droplet size for mechanical spray breakup of agricultural sprays. Termed the Eulerian-

Lagrangian spray atomization model (ELSA), this model approach relies exclusively on information from the Eulerian grid, thus circumventing the need to fix the carrier and dispersed phase throughout the simulation. The model of Vallet et al. [135] has then been adapted and refined by several researchers to capture the primary and secondary spray breakup of conventional atomizers [76, 36, 91]. Although initially developed for primary atomization, recent efforts have been made to extend the model to flashing sprays [107, 86]. However, formulating a comprehensive ELSA model that accounts for flashing sprays, grounded on robust physical principles encompassing bubble growth, spray breakup, and droplet evaporation, remains elusive.

Regardless of the choice of the modeling framework, accurately modeling the mass transfer rates for nucleation, bubble growth, and droplet evaporation remains a challenge. Popular models for the mass transfer rate in flashing flows are Hertz-Knudsen relations [32, 31, 87, 33], mass transfer based on the heat transfer coefficients of Adachi et al. [2, 108, 84, 105, 143], and the homogeneous relaxation model (HRM) proposed by Downar-Zapolski [34, 120, 58, 52, 107, 96]. Here, the first two models provide the mass flux per area. Hence, the phase interface area must be known to convert it to a volumetric source. However, the number of droplets or bubbles and their initial diameter are typically unknown [63], and nucleation models are required to estimate the interface area [126, 115]. In addition, the distribution of nucleation sites is required, and the often used simplification of a uniform and constant distribution is not faithfully capturing the flashing behavior [63]. In comparison, the homogeneous relaxation model (HRM) presents a straightforward yet efficacious approach that does not require this information and can be directly applied to one-fluid simulation types. To account for the thermal non-equilibrium conditions in the HRM, the deviation from equilibrium conditions is combined with a relaxation time scale, formulated using empirical coefficients fitted to flashing water experiments [34]. Remarkably, despite its calibration against a single fluid, the HRM has shown broad applicability for various other fluids and flashing conditions with minor or no modification of the model's constants [96, 76, 118, 58, 86].

An additional complexity of flashing sprays is the presence of compressibility effects, which can lead to shocks. Vieira et al. [138] first observed shocks in flashing iso-octane sprays with high ratios of injection to discharge pressures [138]. Subsequently, shocks were also experimentally identified in flashing acetone sprays by Lamanna et al. [73] and in gasoline direct injectors utilizing propane as the working fluid by Poursadegh et al. [104]. The nucleation and bubble growth present within or at the exit of the injector of flashing sprays causes two effects: first, the speed of sound is drastically

reduced compared to the pure liquid or vapor phase [64, 22], and second, the vapor-liquid mixture exits with a higher-than-ambient pressure. Both effects cause the flow to accelerate to supersonic conditions, which is then terminated by a shock system reminiscent of underexpanded gaseous jets [42]. The presence of the shock system can have severe effects on the spray behavior and was found to be the cause of so-called spray collapse in GDI engines [58, 104, 48]. Therefore, for an accurate portrayal of the spray dynamics, it is essential that the numerical model can faithfully represent these transonic effects. Although density-based solvers are typically employed to simulate super- or transonic flows, they are unsuitable for all Mach-Number flow regimes. Thus, to capture the spray dynamics starting from the injector inlet with nearly incompressible liquid to the spray breakup outside of the injector with a fully compressible liquid-vapor mixture, so-called all Mach-Number pressure-based solvers are a promising alternative [52, 48, 59]. For this work, the open-source CFD framework OpenFOAM[®] shall be used for all simulations. However, OpenFOAM does not ship with a compressible two-phase solver with phase change capabilities. While some researchers have extended the OpenFOAM library by adding an all Mach-Number pressure based solver for single phase flows [69], they did not extend it to multiphase flows with phase change. Therefore, based on the existing tools in OpenFOAM, a new solver for compressible flows with phase change had to be developed and implemented in OpenFOAM, which is part of this work.

1.3 Objectives

The extreme conditions present at the injection of cryogenic liquid in space, and the associated experimental challenges have motivated a joint experimental and numerical investigation. Within the collaborative research center Transregio 75 (SFB-TRR 75), the injection of cryogenic nitrogen at upper-stage relevant conditions has been experimentally and numerically investigated in two projects. Hereby, the numerical investigation can shed light upon the flow processes inside and in the vicinity of the injector, which cannot be directly measured in the experiment. On the other side, the experimental investigation, carried out by the German Aerospace Center (DLR) Lampoldshausen, provide a high-quality data set [111] required to validate the developed numerical tools [28].

The aim of this thesis is the numerical investigation of the cryogenic flashing behavior to gain a deeper understanding of the flow processes occurring in the injector and outside, and how they affect the subsequent spray breakup and droplet distribution.

The main objectives of the presented work are as follows:

(1) *Development of a compressible, two-phase solver in OpenFOAM:*

Considering the complex physical process of flash evaporation and the associated numerical challenges, this work's first objective is to develop the required numerical tools, namely a compressible, two-phase solver in OpenFOAM, to simulate cryogenic flashing sprays.

(2) *Investigation of the flow and spray dynamics inside and outside the injector and comparison to experimental data sets:*

The developed two-phase solver shall then be used to investigate the flow and spray behavior of the flashing cryogenic liquid nitrogen, addressing following research questions:

- Does a shock form due to flashing outside of the injector and how does it affect the spray behavior?
- What is the effect of turbulence on the spray behavior? Are simplified 2D simulations sufficient to capture the characteristics of the spray behavior faithfully?

(3) *Expand the existing ELSA model for flashing flows:*

The one-fluid method requires additional models to regain some of the interface surface information, as the phase interface is not resolved. For this purpose, the ELSA model shall be expanded by novel models that account for the surface density production and destruction during flashing based on the physical processes and detailed direct numerical simulations.

1.4 Thesis Outline

The thesis is divided into six chapters, starting with an overview of the fundamentals of flashing sprays, presenting the physical and thermodynamic principles governing flash evaporation in Chapter 2. In the following Chapter 3, the modeling of two-phase flows is elaborated with specific focus on the models employed in this thesis. Chapter 4 provides a in depth inspection how the models are implemented into the open source framework OpenFOAM and the solution procedure chosen for the developed solver. The application of the new solver to different flashing flows and their results are presented in Chapter 5. At last a conclusion and outlook is given in the final Chapter 6.

Chapter 2

Fundamentals of Flashing Sprays

Flashing sprays fundamentally differ from other atomization methods. The energy for the spray breakup is derived from the thermodynamic state of the fluid itself rather than from external forces. It occurs when a sudden pressure drop causes the liquid to expand beyond its saturation conditions to a meta-stable state. Due to the superheated conditions of the liquid, vapor bubbles start to nucleate and rapidly expand and merge, causing the spray to break up. This chapter elaborates on the physical processes characterizing flashing sprays, from nucleation to bubble growth, spray breakup, and final droplet evaporation. It also discusses the transonic behavior associated with flashing sprays.

2.1 Physical and Thermodynamic Processes of Flash Evaporation

Boiling or vaporization of an originally subcooled liquid is practically realized either by isobaric heating or isothermal expansion of the liquid to the saturation line. In the following, only the isothermal expansion is considered; this marks the path A to B in Figure 2.1. If equilibrium conditions can be assumed, the liquid undergoes a phase change, transitioning from the liquid state (point B) to the vapor state (point E). However, barriers to the nucleation of vapor bubbles in the liquid may lead to an expansion of the liquid beyond its saturation point and superheating the liquid [17]. In the context of flashing sprays, this phenomenon is often achieved by the rapid depressurization occurring during the injection of a pressurized liquid into conditions below its saturation pressure, as illustrated by the path A to C in Figure 2.1. The faster the depressurization occurs, the higher the superheat, causing more nucleation, faster bubble growth, and an overall more violent vaporization and spray breakup.

Therefore, a common measure to characterize the strength of flashing sprays is the superheat ratio,

$$R_p = \frac{p_{\text{sat}}(T_l)}{p}, \quad (2.1)$$

which relates the saturation pressure at the liquid temperature to the ambient pressure. However, the degree of superheat is not unlimited, and a thermodynamic limit is given by the spinodal lines, which mark the unstable region. Nevertheless, this theoretical limit is practically not reached for several reasons, including fluid impurities, wall nucleation, dissolved gases, or the practically achievable pressure drop [124]. The initiation of flashing and, with it, the achievable superheat is, therefore rather determined by the point at which random fluctuations on a molecular level cause the formation of stable vapor nuclei [124, 23]. This kinetic limit of superheat is discussed in detail in Section 2.2.

Following the formation of stable vapor nuclei, they start to grow, allowing the metastable liquid to transition to an equilibrium state. Generally, the bubble growth process can be divided into two stages. Initially, bubble expansion is governed by the interplay between surface tension and bubble inertia. Subsequently, as the bubble expands, the surrounding liquid begins to cool, and the dominant factor impeding further growth becomes the conduction of heat to the bubble surface. This marks the transition to the second stage of growth, known as the heat diffusion limit [106, 124].

As bubbles continue to expand, the volume of the bubble-liquid mixture expands until the bubbles coalesce. Typically, this occurs outside of the injector, causing the jet to disintegrate into liquid droplets. Depending on the state of the droplets, they either continue to evaporate until they reach equilibrium conditions or in the case of larger droplets, further nucleation and bubble growth may occur, leading to a violent droplet breakup.

Notably, the distinction between flashing and cavitating flows lies in the outcomes of bubble growth and spray disintegration. In flashing flows, the ambient pressure remains below saturation conditions, fostering bubble expansion, whereas in cavitating flows, pressure recovery at or above the saturation threshold leads to bubble collapse.

2.2 Nucleation of Vapor Bubbles

In a superheated liquid, fluctuations of the fluid properties on a molecular level may cause the formation of vapor nuclei. When these nuclei exceed a critical size, stable vapor bubbles emerge; otherwise, they promptly collapse. The generation of vapor nuclei can be divided into homogeneous nucleation within the liquid and heterogeneous nu-

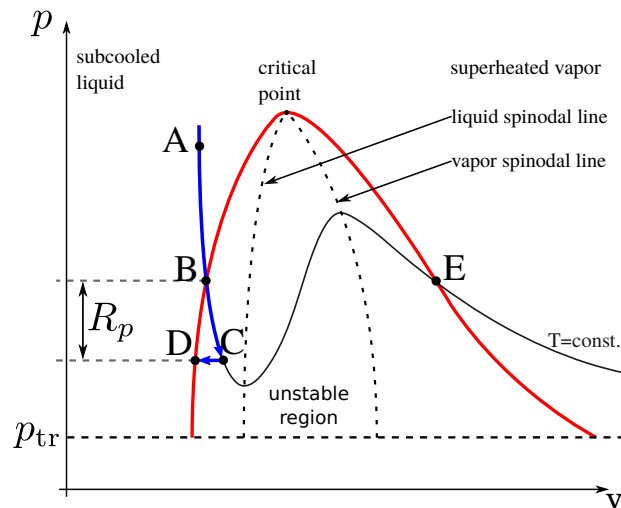


Figure 2.1: Sketch of a p-v diagram with an iso-thermal line.

cleation at the interface between the superheated liquid and a second (typically solid) phase. These general categories of nucleation can be further subdivided, e.g., heterogeneous wall, homogeneous bulk, or heterogeneous bulk nucleation. Independent of homogeneous or heterogeneous nucleation, the basis of the kinetic theory of nucleation is to determine the amount of work required at constant temperature to create a stable nucleus.

2.2.1 Homogeneous nucleation

The origins of classical nucleation theory (CNT) for homogeneous nucleation are attributed to various scholars, including Volmer and Weber [139], Farkas [41], Becker and Döring [12], Zeldovich, and Gibbs [54], as well as Frenkel [43]. In this section, we present a concise derivation of CNT while referring the interested reader to the comprehensive works of Carey [23] and Blander and Katz [17] for an in-depth thermodynamic treatment.

As previously mentioned, the occurrence of stochastic fluctuations can instigate the inception of a vapor bubble. The work to create this vapor bubble with a radius R consists of the generation of surface area and the deposition of the liquid due to the formation of the bubble, expressed as

$$W = 4\pi R^2 \sigma - \frac{4}{3}\pi R^3 \Delta p. \quad (2.2)$$

Here, σ is the surface tension and $\Delta p = p_b - p$ is the pressure difference between the bubble and liquid. Equation (2.2) assumes chemical equilibrium, implying equal temperatures in the vapor and liquid phases ($T_l = T_v$).

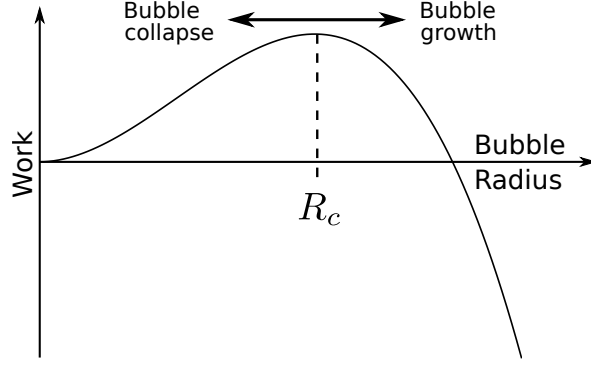


Figure 2.2: Minimum work required to form a vapor bubble of radius R .

The work to create a bubble initially increases until it reaches a maximum, after which it decreases as the bubble expands, as depicted in Figure 2.2. A critical radius R_c marks the size of the minimum stable bubble. Bubbles larger than R_c tend to grow, while those smaller than R_c collapse. Assuming mechanical equilibrium within the vapor bubble, the pressure difference Δp relates to the critical radius through the Young-Laplace equation,

$$\Delta p = \frac{2\sigma}{R_c}. \quad (2.3)$$

Following the derivation of the equilibrium conditions, it can be seen that the pressure p_b within the bubble is slightly less than the saturation pressure $p_{\text{sat}}(T_l)$. The pressure inside the bubble, p_b , can be expressed by integrating and rearranging the Gibbs-Duhem equation, which yields [23]

$$p_b = \exp\left(\frac{p - p_{\text{sat}}(T_l)}{\rho_l (R_u/M) T_l}\right) p_{\text{sat}}(T_l), \quad (2.4)$$

where R_u is the universal gas constant and M the molar mass. Combining Eqs. (2.3) and (2.2) leads then to the formulation of the Gibbs free energy,

$$\Delta G(R_c) = \frac{4}{3}\pi R_c^2 \sigma = \frac{4}{3}\pi \frac{4\sigma^3}{(p_b - p)^2}. \quad (2.5)$$

This energy quantifies the minimum work required to form a stable bubble. At this point, it shall be noted that some researchers have calculated the Gibbs free energy based on the natural logarithm of the superheat ratio, R_p . This formulation, however, stems from the derivation of homogeneous nucleation for subcooled vapor. These two nucleation modes cannot be swapped, and using a model based on R_p is thermodynamically incorrect. For further details, see Appendix A.

As bubbles smaller than the critical radius immediately collapse again, they cannot

grow to stable bubble sizes. Thus, a bubble of size R_c can only be formed through the random fluctuations of the density in the fluid, leading to a temporarily lower than average density in a volume of size R_c . The Gibbs free energy for creating a vapor bubble must therefore be related to the probability of stochastic thermal motion, typically expressed through the kinetic energy of molecules,

$$\frac{\Delta G(R_c)}{k_b T_l}, \quad (2.6)$$

where k_b denotes the Boltzmann constant. Using Eq. (2.6), the nucleation rate per unit volume is [23, 17]

$$J = \frac{N_a \rho_l}{M} \sqrt{\frac{2\sigma}{\pi m_{\text{mol}}}} \exp\left(-\frac{\Delta G(R_c)}{k_b T_L}\right), \quad (2.7)$$

where N_a is the Avogadro number, M the molar mass and m_{mol} refers to the mass of a single molecule. For a detailed derivation of Eq. (2.7) the reader is referred to Carey [23].

Due to the term's strong exponential dependence, the nucleation rate described by Eq. (2.7) behaves like a step function. Hence, combining Eq. (2.7) with a nucleation threshold of e.g., $J > 1 \times 10^{15} \text{ 1/m}^3/\text{s}$ [114], is used to determine the kinetic limit of superheat, beyond which flashing occurs due to homogeneous nucleation.

2.2.2 Heterogeneous nucleation

Heterogeneous nucleation typically occurs at liquid-solid interfaces containing imperfections arising from the manufacturing process. However, in scenarios involving flashing flows, it is often assumed that these surface imperfections remain sufficiently minute, such that the creation of vapor bubbles continues to rely on the stochastic and random nature of density fluctuations [6, 128].

This assumption motivates the introduction of a correction factor, denoted as Ψ , to the classical nucleation theory. The correction factor accounts for the reduction of the critical energy barrier necessary for the formation of stable vapor bubbles [30, 40, 11, 134]. This adjustment leads to the expression for the nucleation rate expressed by

$$J \propto \exp\left(-\frac{\Delta G(R_c)\Psi}{k_b T_L}\right). \quad (2.8)$$

Various approaches exist for determining the value of Ψ . Some researchers have proposed empirical relationships linking Ψ to parameters such as the depressurization rate

or the liquid temperature [6, 40]. Conversely, others have treated Ψ as a model parameter fitted to experimental results [134, 116]. Regardless of the chosen modeling strategy, the value of Ψ remains specific to the particular case under investigation and cannot be readily generalized to diverse fluids or flow conditions [78].

2.3 Bubble Growth

Having established a population of bubble nuclei through the preceding bubble nucleation process, understanding vapor bubble growth becomes paramount. The mathematical description of spherical bubble dynamics in an infinite liquid pool was first described by Rayleigh in 1917 [109]. Although Rayleigh's equation originally neglected surface tension and liquid viscosity, it can be easily extended to include these effects, leading to the well-known Rayleigh-Plesset equation of bubble growth [101, 106],

$$R\ddot{R} + \frac{3}{2}\dot{R}^2 = \frac{1}{\rho_l} \left(p_b - p_l - \frac{2\sigma}{R} - 4\mu_l \frac{\dot{R}}{R} \right), \quad (2.9)$$

with μ_l as the liquid viscosity. In most technical applications, the effect of viscosity can be neglected. Assuming $R(t) \gg R(0)$, Eq. (2.9) can be integrated, yielding [106]

$$\dot{R} = \sqrt{\frac{2}{3} \frac{p_b - p_l}{\rho_l}}. \quad (2.10)$$

Equation (2.10) is commonly referred to as the inertia-limited bubble growth. This equation encapsulates the early phase of bubble expansion dominated by inertial forces. However, as the bubble continues to grow, the impact of heat conduction to the bubble surface gradually becomes more significant, marking the transition to a different growth regime.

The thermally limited growth is dominated by the rate at which heat can be conducted to the bubble surface and is described by

$$L\rho_v(T_{\text{sat}}) \frac{d}{dt} \left(\frac{4}{3}\pi R^3 \right) = -4\pi R^2 q_r. \quad (2.11)$$

Here, L is the latent heat, $\rho_v(T_{\text{sat}})$ the vapor density at saturation condition, and q_r the heat flux to the bubble surface. To determine the heat flux, the temperature difference between the bubble surface and liquid has to be known. Assuming the bubble size attains sufficient magnitude to render the pressure difference between the vapor bubble and liquid negligible (as per Eq. (2.3)), the surface temperature equates to the

saturation temperature, $T_{\text{sat}}(p_l)$. The different conditions in the vapor bubble for the inertia and thermal limited growth are sketched in Figure 2.3.

Using the boundary layer approximation of Plesset and Zwick [102], the bubble growth rate of the thermal limit is given by,

$$\dot{R} = \text{Ja} \sqrt{\frac{3\mathcal{D}_l}{\pi t}}. \quad (2.12)$$

Here, Ja is the Jakob number defined as

$$\text{Ja} = \frac{\rho_l c_{p,l} |T_{\text{sat}}(p_l) - T_l|}{\rho_v L}, \quad (2.13)$$

with $c_{p,l}$ as the liquid heat capacity at constant pressure. The variable \mathcal{D}_l denotes the liquid thermal diffusivity and is defined as

$$\mathcal{D}_l = \frac{\kappa_l}{\rho_l c_{p,l}}, \quad (2.14)$$

and κ_l is the thermal conductivity of the liquid. In the asymptotic limit of $R(t) \gg R(0)$ Eq. (2.12) can be integrated to

$$R(t) = 2\text{Ja} \sqrt{\frac{3\mathcal{D}_l t}{\pi}}. \quad (2.15)$$

Combining Eq. (2.15) with Eq. (2.12) provides a formulation of the bubble growth rate based on the bubble size,

$$R\dot{R} = \frac{12}{\pi} \text{Ja}^2 \mathcal{D}_l. \quad (2.16)$$

It is important to emphasize that Eq. (2.12) and Eq. (2.10) solely represent asymptotic limits of bubble growth. In reality, the bubble growth rate is a combination of both regimes, and an exact calculation requires the combined solution of the Rayleigh-Plesset equation with the energy conservation, e.g., as presented in Lee and Merte [75].

2.4 Breakup of Flashing Sprays

The process of spray breakup, often also referred to as atomization, describes the transformation of the liquid bulk into a dispersed spray of smaller droplets. This process can generally be divided into two key stages: primary and secondary breakup. The primary breakup phase involves the transition from the liquid bulk to a collection of liquid ligaments and discrete droplets. Subsequently, the secondary breakup stage

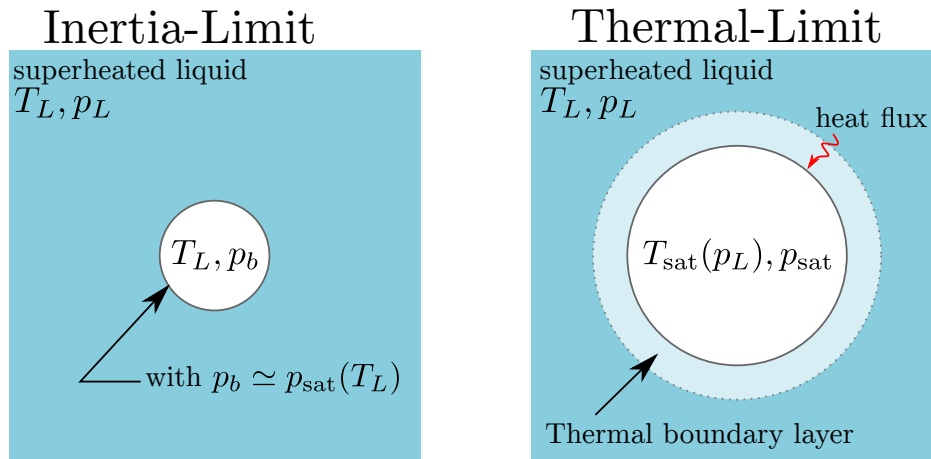


Figure 2.3: Sketch of the inertia and thermal limited bubble growth conditions in the bubble and superheated liquid.

pertains to the further fragmentation of these ligaments or droplets into even finer particles.

2.4.1 Primary spray breakup

Within the context of this work, primary spray breakup is further divided into two categories: aerodynamic and flashing breakup. The first involves mechanically driven processes, where external forces or surface instabilities drive the disintegration of the liquid into droplets. This mechanism encompasses scenarios where the fluid is subjected to external perturbations (e.g.: Kelvin-Helmholtz and Rayleigh-Taylor instabilities), resulting in ligament formation and eventual droplet detachment. The second pathway, characterized as a thermodynamically driven breakup, arises in scenarios such as fully flashing flows. Here, the interplay of thermodynamic forces leads to the initiation of breakup as a consequence of phase change phenomena. Depending on the specific fluid properties and injection conditions, the spray breakup in flashing sprays may span from aerodynamic-dominated breakup to fully flashing scenarios, as depicted in Figure 2.4 for flashing cryogenic nitrogen. Based on the modified Jakob number proposed by Kitamura et al. [65] and a critical Weber number,

$$\text{We} = \frac{\rho_v u^2 R}{2\sigma}, \quad (2.17)$$

Cleary et al. [27] distinguished three separate flashing regimes: aerodynamic dominated breakup, transitional, and fully flashing regime. Studying flashing cryogenic jets, Rees et al. [113] introduced a fourth category, wide flashing, to consider the significant differences in the spray angle of fully flashing sprays. In the aerodynamic dominated

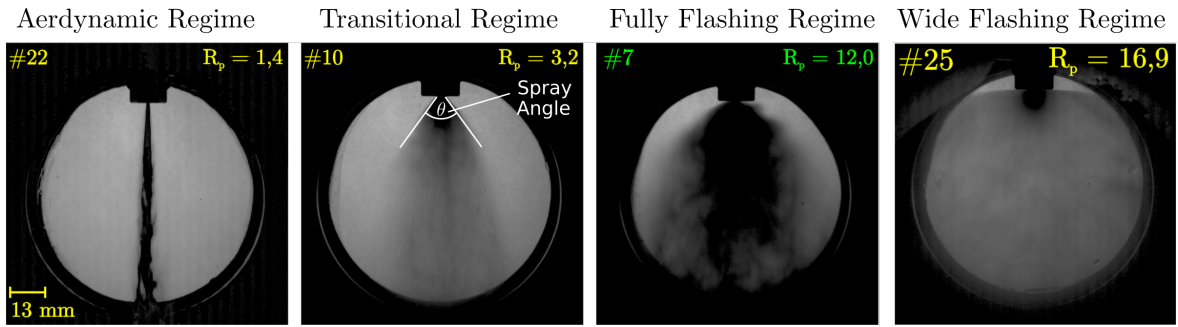


Figure 2.4: Flashing cryogenic nitrogen shadowgraph images, representing the four different flashing regimes according to Cleary et al. [27] and Rees et al. [113].

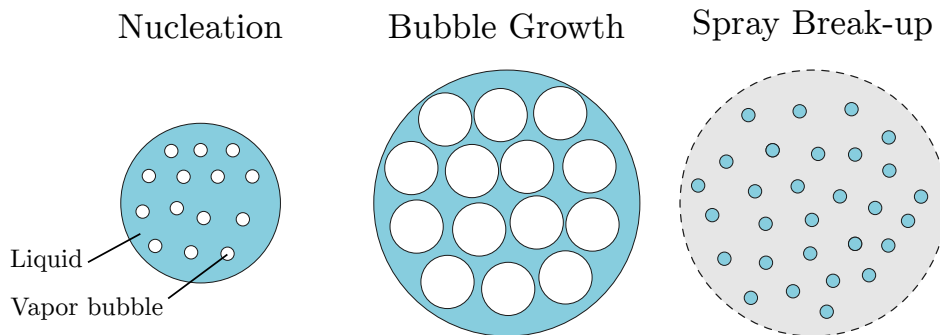


Figure 2.5: Flashing spray breakup through bubble coalescence, depicting the nucleation, bubble growth and spray breakup within a droplet. Inspired by Rees [111].

regime surface instabilities and external forces dominate the spray breakup. Yet, bubble growth and jet shattering may occur, separating this flow regime from a conventional aerodynamic spray breakup [7]. As the degree of superheat increases, phase change phenomena gradually become more prominent in governing spray breakup. Beyond a certain threshold, the spray is considered fully flashing, and spray breakup is determined by the nucleation rate and bubble growth [73, 83]. Considering the flashing regime, Oza and Sinnamon [98] proposed two potential primary spray breakup modes, bubble coalescence and inertial shattering, and one secondary spray breakup mode, micro explosions. In the following, only the two primary spray breakup modes are discussed. The first mode, bubble coalescence, was proposed by Sher and Elata [125] and assumes that spray breakup occurs when an array of spherical bubbles grow until neighboring bubbles touch and the spray transitions from a bubble array in a liquid to droplets in vapor, illustrated in Figure 2.5. This point of spray breakup can be characterized by the void fraction, $\eta = V_v / (V_v + V_l)$, defined as the ratio of bubble vapor volume to the combined volume of bubbles and liquid. With the assumption of spherical bubbles and close-packed spheres, the spray breakup occurs at a void fraction of $\eta = 52.3\%$, which is consistent with experimental observations [77, 125]. The second mode may occur when bubbles start to rapidly grow outside of the injector, and the

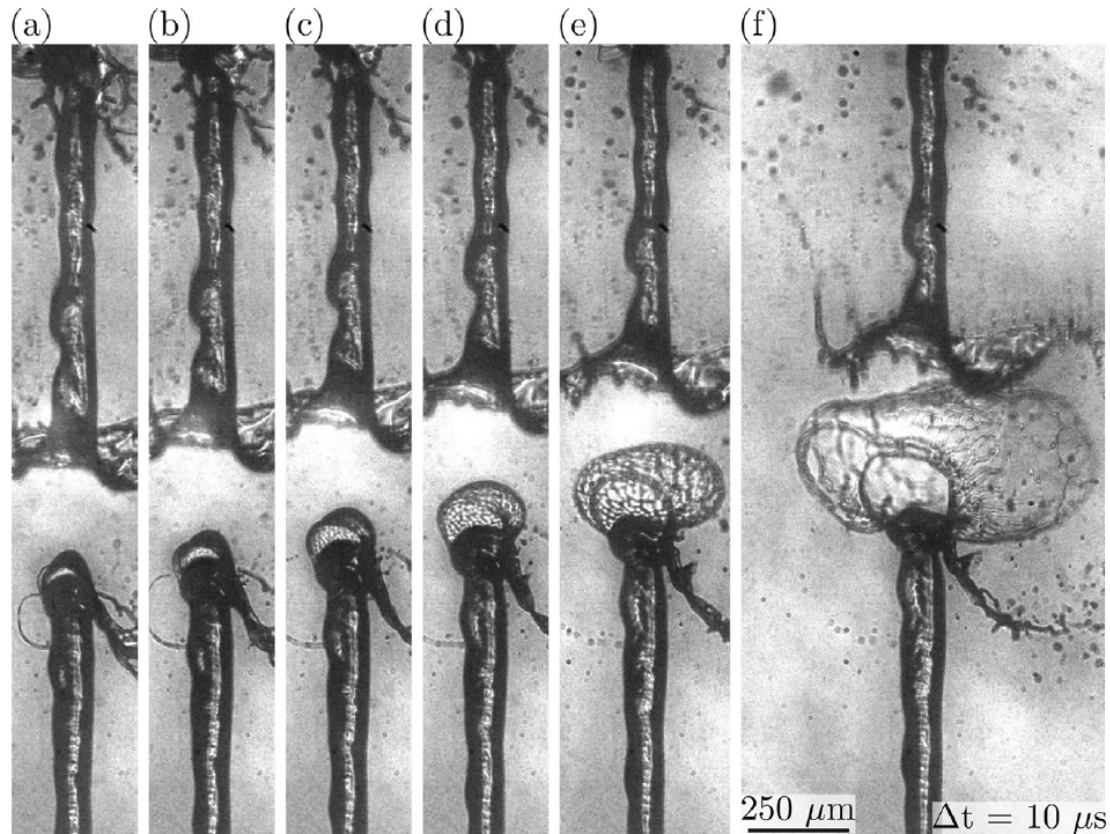


Figure 2.6: Temporal evolution of a bubble growth and shattering of the jet in the transitional flashing regime, captured by Alghamdi et al. [7]. Image taken from Alghamdi et al. [7] with permission of Elsevier.

liquid radial momentum causes a shattering of the jet. An example of this breakup regime could be experimentally visualized by Alghamdi et al. [7] using a long range microscope with up to five million frames per second. Figure 2.6 shows a series of these high resolution images of a lowly superheated spray in the transitional flashing regime, capturing the shattering of the jet.

2.4.2 Secondary spray breakup

Following the primary spray breakup, the generated droplets and liquid ligaments can further disintegrate into smaller droplets, creating so called secondary droplets. Depending on the level of superheat and their size, this disintegration is either driven by thermodynamic processes, such as nucleation and bubble growth, or aerodynamic forces. It is conceivable that droplets are not in thermodynamic equilibrium after the primary spray breakup, and further nucleation of bubbles within the droplet may occur. Following the proposed breakup modes of Oza and Sinnamon [98], this represents the micro explosion mode. This mode assumes that further nucleation and bubble growth

in the previously generated droplets causes their disintegration into smaller secondary droplets. Razzaghi proposed one of the first theoretical models of this spray breakup [110], assuming a bubble growing within the droplet and using the liquid film instability criterion to determine droplet breakup. However, if the droplet is close enough to the kinetic superheat limit such that nucleation occurs, experimental evidence suggests that droplet breakup can be associated when the vapor volume fraction exceeds 50% [77]. Further, Razzaghi postulated that the micro explosion mode generates 1 to 10 secondary droplets, and the droplet size is calculated by solving the mass conservation. Other researchers proposed to use twice as many droplets as bubbles to estimate the droplet number [123, 2]. However, this model is based on the knowledge of the bubble number, which is typically an unknown and either a model or free parameter. To gain further insight into this intricate process, recently numerical studies have been conducted employing DNS of bubble growth and spray breakup [83, 32]. The results of these studies offer two main conclusions. Firstly, only the first few bubble rows at the liquid surface start to grow due to a pressure increase in the center of the liquid [32]. Secondly, the generated droplet size can be attributed to the bubble growth rate when adjacent bubbles merge [83]. However, due to the complexity, no coherent model has yet emerged to determine the droplet size and number distribution after the spray breakup of flashing flows.

In addition to droplet breakup due to nucleation, aerodynamic breakup due to the interplay of stabilizing surface tension and destabilizing hydrodynamic forces on the droplet may occur. The aerodynamic breakup can be categorized by this ratio, expressed through the Weber number defined as

$$\text{We} = \frac{\rho u_{\text{rel}} D}{\sigma}, \quad (2.18)$$

with u_{rel} as the relative velocity of the droplet to the surrounding fluid and D as the droplet diameter. Different breakup modes can be then defined as a function thereof [100]. To maintain focus on the subject matter at hand, we hereby direct the interested reader to the work of Pilch and Erdman [100] for a detailed description of the aerodynamic breakup mechanisms.

2.5 Droplet Evaporation

Once liquid droplets have been created through the primary and secondary spray breakup, these droplets are typically not yet in thermal equilibrium and evaporate further. In contrast to conventional droplet evaporation, the droplet is not heated by

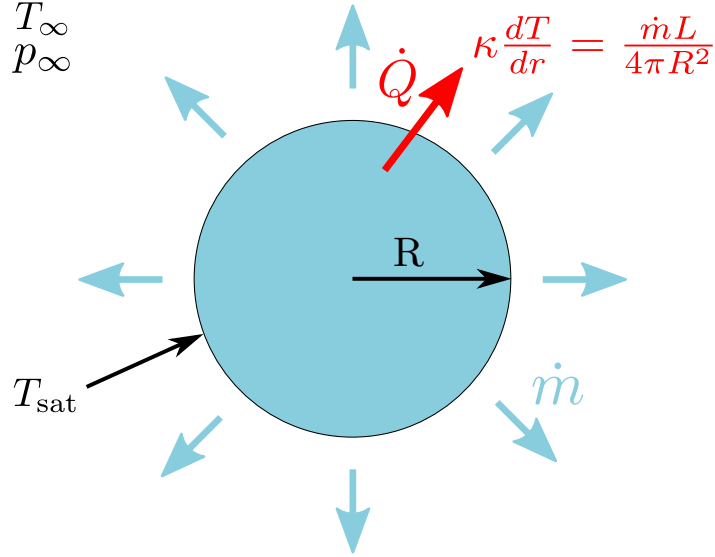


Figure 2.7: Sketch of a flash evaporating droplet.

its surrounding atmosphere. Hence, the heat flux is not directed towards the droplet, as it is assumed for typical models of droplet evaporation, e.g., such as the Abramzon Sirignano model [1]. Therefore, the evaporation rate of flashing droplets is governed by the capability to transport heat from the droplet center to the surface, see Figure 2.7. If radiation and heat convection at the surface is neglected the boundary condition at the droplet surface is

$$\kappa \frac{dT}{dr} = \frac{\dot{m}L}{4\pi R^2}, \quad (2.19)$$

with κ as the thermal conductivity. Modeling the temperature gradient with $dT/dr = (T_l - T_{\text{sat}}(p_\infty))/R$, Adachi et al. [2] derived an empirical correlation for the heat transfer coefficient to determine the mass flux of flash evaporating droplets

$$\dot{m} = \alpha_{sh} \frac{4\pi R^2 \Delta T}{L}, \quad (2.20)$$

with

$$\begin{aligned} \alpha_{sh} &= 0.76\Delta T^{0.26} & 0 \leq \Delta T \leq 5 \\ &= 0.027\Delta T^{2.33} & 5 < \Delta T \leq 25 \\ &= 13.8\Delta T^{0.39} & 25 < \Delta T. \end{aligned}$$

In the work of Adachi et al. [2] the temperature difference is defined as $\Delta T = T_l - T_{\text{sat}}(p_\infty)$, with $T_{\text{sat}}(p_\infty)$ being the saturation temperature at the ambient pressure level.

If the droplet is evaporating in near vacuum conditions several other researchers have

based the droplet evaporation on the diffusion of the vapor away from the surface. Assuming ideal gas conditions, the mass flux is described by Fick's law of diffusion by [Wang2017, 126, 26],

$$\dot{m} = 4\pi R^2 \mathcal{D}_v \frac{M}{R_u} \left(\frac{p_{\text{sat}}(T_s)}{T_s} - \frac{p_\infty}{T_\infty} \right). \quad (2.21)$$

Here, M is the molar mass of the fluid, R_u the universal gas constant and T_s is the temperature at the droplet surface which needs to be determined by solving the energy equation in the droplet with the boundary condition of Eq. (2.19) [26]. Considering convection within the droplet with an effective thermal conductivity, Cheng et al. [26] developed a model that could predict the droplet cool down in good agreement with the experimental data of Shin et al [126]. However, one caveat of the model is the diffusion coefficient \mathcal{D}_v . Typically the diffusion of the vapor to air has been used, however the validity of this assumption for vacuum conditions where only the vapor exists is questionable.

2.6 Transonic Behavior of Flashing Sprays

The rapid phase change and vapor bubble nucleation in the injector of flashing sprays causes the originally liquid spray to exhibit behaviors similar to gaseous sprays, including compressibility effects associated with underexpanded gaseous sprays. Compressibility effects, such as shock structures, have been first observed experimentally for flashing retrograde fluids [70] and recently also for non-retrograde fluids [138, 73, 104]. Two modes of shock structure formation in flashing flows can be distinguished based on the experimental observation. Vieira et al. [138] have observed a liquid core and a surrounding shock structure, which they explained by the rapid evaporation at the liquid surface causing an evaporation wave which then leads to supersonic conditions terminated by the observed shock structure, see Figure 2.8. However, cases without a visible liquid core and shock structures at lower superheat and non-retrograde fluids have been observed [73, 104]. In these cases, it can be assumed that the nucleation and vapor bubble growth within the injector cause the liquid-vapor mix to exit with a higher than ambient pressure. Similar to underexpanded-gaseous sprays, this leads to a rapidly expanding flow, reaching supersonic speeds. Another aspect that has to be considered when studying the transonic behavior of flashing flows is the drastically reduced speed of sound in a gas-liquid mixture [64], compared to the single-phase sound speed. This reduction of the sound speed causes the mixture to go into supersonic

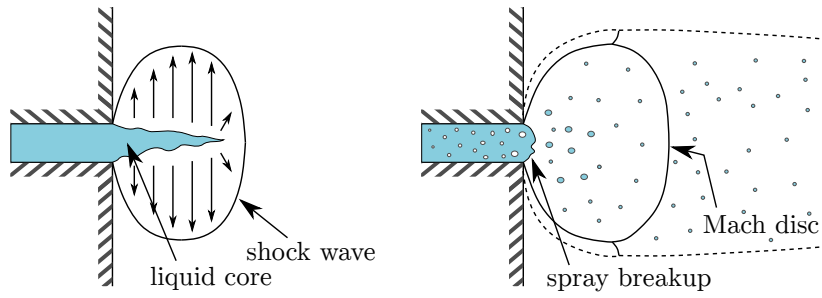


Figure 2.8: Simplified sketch of the shock structure for transonic flashing sprays, (left) for very highly superheated sprays according to Vieira et al. [138] and (right) superheated sprays with spray breakup [73].

conditions significantly sooner than expected for single-phase flows.

Chapter 3

Modeling and Simulation of Two-Phase Flows

Due to the significance of two-phase flows in technical applications, models to simulate these flows have been developed since the beginning of computational fluid dynamics [133]. Several different models and simulation approaches for various two-phase flow conditions have evolved, which can be generally divided into either an Euler-Euler (EE) or Euler-Lagrange (EL) approach. Euler-Lagrange models treat one phase as a continuous solution on an Eulerian grid. In contrast, the second phase is dispersed and treated as discrete particles in a Lagrangian framework. Here, it is assumed that the bubbles, droplets, or solids represented by the particles can be treated as rigid bodies with homogeneous properties within the particle and that they are in a dilute flow. The effect of the flow field around the particles is then subsumed as appropriate forces, e.g., drag, lift, and momentum [22, 122]. This model allows a detailed description of the dispersed particles, given that the underlying assumptions are met.

However, with the aim of simulating the flashing process from the injection of the cryogenic liquid to the final spray with liquid droplets, a method is required that does not fix the dispersed phase, allowing the growth, coalescence, and breakup of the dispersed phase. Hence, the Euler-Euler method, which treats the two-phase flow as interpenetrating continua, is a more suitable choice for this problem. In contrast to the Euler-Lagrange model, the governing equations of the fluid are solved for each phase on the Eulerian grid, and the interactions of the two phases at the interface are represented through suitable exchange terms. Nevertheless, the advantages of the Euler-Euler approach to the Euler-Lagrange are bought with the challenge of describing the jump conditions at the interface.

In contrast to the Euler-Lagrange model, the Euler-Euler approach can be used either

for very detailed simulations, e.g., bubble coalescence, resolving a large degree of flow details, or in the other extreme, it can also be used when not every dispersed particle can be resolved with a feasible computational effort. In the latter case, the individual droplets or bubbles are on a sub-grid scale, and the fluid can be treated as a mixture of the two phases. Therefore, the large scale motions are obtained by averaging and hence neglecting the small scale details [122]. In the latter case, the additional assumption that the two phases are closely coupled and move with the same velocity is often applied, thus removing the need for the momentum exchange terms. Then, only one set of conservation equations for the two-phase mixture has to be solved together with an additional transport equation for the volume fraction. The mixture properties are obtained through an appropriate mixing rule of the two phases.

However, when the interface is no longer directly captured by the Euler-Euler method, the information about the interface surface and droplet or bubble size is lost. To reconstruct this information, an additional transport equation for the surface density, Σ , representing the interface area on the sub-grid level, has been proposed by Vallet et al. [135], called Euler-Lagrange spray atomization (ELSA) model. Here, it shall be reiterated that despite the name, no Lagrangian particles are transported, and only an additional scalar transport equation is solved on the Eulerian grid. This model has then been further expanded and refined by several researchers [76, 36] and even applied with only minor modifications to flashing flows [107, 86]. Yet, the standard ELSA model does not capture the fundamentally different physics of flashing flows compared to a mechanical spray breakup. Therefore, a new ELSA model, based on the physics of flashing sprays, is proposed in this chapter to capture the sub-grid interface of flashing sprays.

The following chapter presents the governing equations of two-phase flows, focusing on the one-fluid method used in this thesis. Following the discussion of the turbulence modeling of the two-phase flow and the averaging of the equations, the additional transport equation for the surface density modeling and the novel models for flashing sprays are presented in Section 3.3. At last, different phase change models used to predict the evaporation rate of flashing flows are discussed.

3.1 Governing Equations

Fluid motion is governed by a set of fundamental equations, consisting of mass, momentum and, in case of compressible flows, energy conservation. These equations provide a comprehensive description of how fluids, whether they are liquids or gases, behave

under the influence of various forces. The set of mass and momentum conservation is also known as the Navier-Stokes equations. However, in the following the term Navier-Stokes equations and governing equations will be used synonymously, referring to the full set of governing equations. The derivation of the Navier-Stokes equations is a well-established topic in the fluid mechanics literature, and the mathematical intricacies behind their development have been extensively documented [137, 22, 122]. Therefore, the differential form of the governing equations for one phase are presented here without further derivation.

The mass conservation in conservative form for one phase, k , is then,

$$\frac{\partial \rho_k}{\partial t} + \nabla \cdot (\rho_k u_k) = \dot{m}, \quad (3.1)$$

with ρ_k and u_k representing the density and velocity of phase k . The source term \dot{m} represents the mass exchange between the two phases at the interface. The momentum equation is given by

$$\frac{\partial \rho_k u_k}{\partial t} + \nabla \cdot (\rho_k u_k u_k) = -\nabla p + \rho_k g + \nabla \cdot \boldsymbol{\tau} + S_m. \quad (3.2)$$

Here, ρg is the gravitational force, $\boldsymbol{\tau}$ represents the viscous stress tensor and S_m the momentum exchange term. For Newtonian fluids, the viscous stress tensor is modeled by relating the dynamic viscosity μ to the velocity gradients,

$$\boldsymbol{\tau} = \mu \left(\frac{\partial u_i}{\partial x_j} + \frac{\partial u_j}{\partial x_i} \right) - \frac{2}{3} \mu \frac{\partial u_k}{\partial x_k} \delta_{ij}. \quad (3.3)$$

The subscripts indicate here the vector components, using the Einstein summation convention and should not be confused with the subscript used to indicate the different phases. Note that the same pressure p is assumed for all phases. Hence an increase of pressure due to surface tension is neglected in the given equation, however, it could be easily extended to include this. The energy equation can be described in several different forms, depending on the definition of the specific energy of the fluid. Here, the energy is expressed as conservation of total enthalpy $e = h + 0.5(u^2)$ [137],

$$\frac{\partial \rho_k e_k}{\partial t} + \nabla \cdot (\rho_k e_k u_k) = \frac{\partial p}{\partial t} - \nabla \cdot q + \boldsymbol{\tau} \nabla (u_k) + S_h, \quad (3.4)$$

with q as the heat flux and S_h representing all source terms including the potential energy as body force.

So far the governing equations presented describe the motion of one phase at an in-

stantaneous point in time and space. While it would be theoretically possible to solve the closed set of equations, it would require a mesh with cell sizes smaller than the smallest length scale of the flow and interface, which is, even with current computational resources, not feasible for most cases. To simplify the equation system, and to allow larger space and time integration, a volume average around a fixed point is applied [122, 22]. The application of the volume average leads to the introduction of the volume fraction,

$$\alpha_k = \frac{V_k}{\sum_k V_k}, \quad (3.5)$$

to the governing equations resulting in,

$$\frac{\partial \alpha_k \rho_k}{\partial t} + \nabla \cdot (\alpha_k \rho_k u_k) = \dot{m}, \quad (3.6)$$

$$\frac{\partial \alpha_k \rho_k u_k}{\partial t} + \nabla \cdot (\alpha_k \rho_k u_k u_k) = \alpha_k (\nabla \cdot \boldsymbol{\tau} - \nabla p) + \alpha_k \rho_k g + S_m, \quad (3.7)$$

$$\frac{\partial \alpha_k \rho_k e_k}{\partial t} + \nabla \cdot (\alpha_k \rho_k e_k u_k) = \frac{\alpha_k \rho_k}{\rho} \left(\frac{\partial p}{\partial t} - \nabla \cdot \mathbf{q} \right) + \alpha_k \boldsymbol{\tau} \nabla (u_k) + S_h. \quad (3.8)$$

Note that the mechanical work and the thermal diffusion in the energy equation are distributed to the phases proportional to their mass fractions. Here, ρ without a subscript represents the mixture density, which is calculated with

$$\rho = \sum_k \alpha_k \rho_k. \quad (3.9)$$

3.1.1 Equation of state

The set of governing equations presented for one phase contains five conservation equations (in three dimensions) but seven unknown variables, namely: ρ , u_x , u_y , u_z , h , T , and p . Therefore, to close the equation system, two additional equations have to be supplied to represent the thermodynamic relationship between the state variables, e.g., the density as a function of pressure and enthalpy as a function of temperature. The relationship between density, temperature, and pressure is expressed with an appropriate choice of the equation of state. The temperature and enthalpy are related by using a typically constant heat capacity factor, c_p , and the total derivative of the enthalpy.

3.1.2 One-fluid model

For closely coupled two-phase mixtures the equation system can be reduced to one set of governing equations with an additional scalar transport equation, typically representing the mass or volume fraction, to distinguish between the two phases. This approach is

commonly referred to as the one-fluid model. With the assumption of a closely coupled two-phase mixture the governing equations of the two-fluid model can be summed up to give the governing equations of the one-fluid model,

$$\frac{\partial \alpha_k \rho_k}{\partial t} + \nabla \cdot (\alpha_k \rho_k u_k) = \dot{m}, \quad (3.10)$$

$$\frac{\partial \rho}{\partial t} + \nabla \cdot (\rho u) = 0, \quad (3.11)$$

$$\frac{\partial \rho u}{\partial t} + \nabla \cdot (\rho u u) = (\nabla \cdot \boldsymbol{\tau} - \nabla p) + \rho g, \quad (3.12)$$

$$\frac{\partial \rho e}{\partial t} + \nabla \cdot (\rho e u) = \left(\frac{\partial p}{\partial t} - \nabla \cdot q \right) + \boldsymbol{\tau} \nabla(u). \quad (3.13)$$

Variables without a subscript, e.g., the density ρ , represent the properties of the two-phase mixture. The mixture velocity u is related to the velocity of the phase u_k through the relative velocity u_{rel} between the two phases,

$$u_k = u + (1 - \alpha_k) u_{\text{rel}}. \quad (3.14)$$

A detailed derivation of the velocity of center of volume can be found in Appendix B. This relative velocity has to be modeled and is used in the volume of fluid approach to avoid the numerical diffusion of the phase interface. However, as for the investigated flashing cases the phase interface is on the sub-grid scale, a no-slip assumption is applied which then results in $u_k = u$.

3.1.3 Interface tracking techniques

The precise tracking of the phase interface between two immiscible fluids holds significant importance in a range of technical and engineering applications, including extraction, chemical process engineering, and separation processes [55]. In the realm of multiphase flows, several methods have been established, including marker-and-cell (MAC), level-set, and constrained interpolation profile (CIP). In this context, we will briefly introduce two commonly used models within the one-fluid framework [55, 37, 38].

The first model employs a geometric reconstruction technique known as Piecewise Linear Interface Construction (PLIC) to determine the position of the interface surface within each computational cell. PLIC calculates a planar surface within each cell, ensuring that the volume enclosed by this surface and the cell accurately represents the volume fraction, α . A visual representation of this concept can be seen in Figure 3.1. Particular for 3D simulations, a main challenge lies in determining the surface

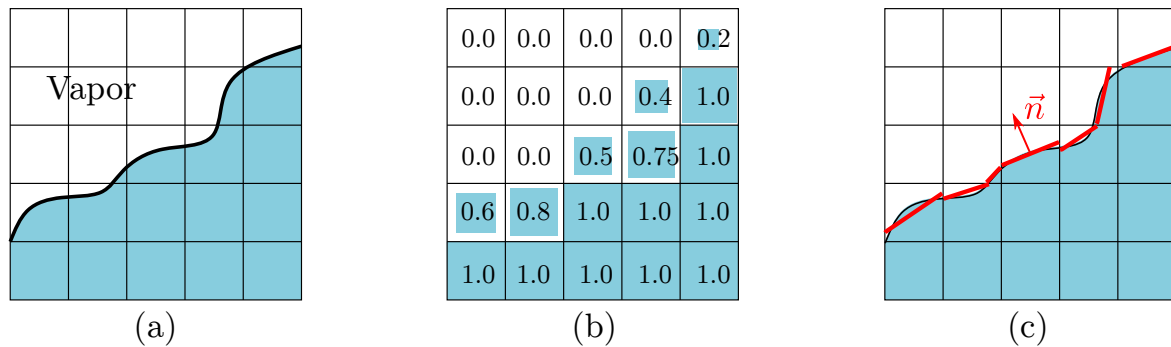


Figure 3.1: Sketch of the real liquid-vapor interface (a), representation of the volume of fluid field (b), and the interface reconstruction with PLIC (c).

normal vector and establishing the surface position within the cell while maintaining second-order accuracy to conserve mass [37]. Nevertheless, PLIC is a highly accurate and widely used method that inherently handles situations involving the breakup and merging of bubbles or droplets [55, 37].

The second method uses the relative velocity u_{rel} resulting from the volume averaging, see Eq. (3.14), to compress and avoid the smearing of the interface. Therefore, this velocity is called in the following compression velocity u_{Γ} . This idea was initially introduced by Jasak and Weller [62] in a technical paper and later implemented by Rusche [117]. The compression velocity is described with

$$u_{\Gamma} = K_C n^* \max \frac{|n^* u|}{|S|^2}, \quad (3.15)$$

where K_C is a model constant, n^* the normalized interface surface vector determined from the volume fraction gradient, and S the surface area of the cell face. An advantage of this method lies in its simplicity of implementation and computation, while still achieving acceptable accuracy, provided that the Courant number remains low.

3.2 Turbulence Modeling

The governing equations, as derived in the preceding section, offer a fundamental framework applicable to both laminar and turbulent flows, provided that the numerical methods can resolve all relevant scales. In contrast to laminar flows, which can be resolved with relative computational ease, turbulent flows pose a formidable challenge due to the impracticality of fully resolving their smallest flow structures in most practical scenarios. Consequently, direct numerical simulations (DNS) which resolve all turbulent scales are used for investigation of detailed, small scale phenomena, often confined to academic investigations. However, in many engineering and scientific ap-

plications, resolving every turbulent fluctuation in time and space is not essential for addressing practical questions. This realization has led to the adoption of the Reynolds decomposition method for state variables, decomposing the variable in a time averaged and fluctuating part, also called Reynolds averaging. For any state variable Φ the decomposition is then

$$\Phi = \bar{\Phi} + \Phi' \quad \text{with} \quad \bar{\Phi} = \frac{1}{\Delta t} \int_0^{\Delta t} \Phi(t) dt.$$

The overbar denotes the time averaged variable and the prime denotes the fluctuations. It is important to note that the time averaging pertains to the turbulent time scale, hence the slowest fluctuations caused by the largest eddies and is valid for steady flows [137]. In case of time varying flows, an ensemble average of instantaneous events of repeated identical experiments is taken. For variable density flows it is common to use a density weighted averaging to avoid modeling the additional terms arising from the correlation of the velocity and density fluctuations. This averaging procedure is called Favre averaging and is defined as

$$\tilde{\Phi} = \frac{\overline{\rho\Phi}}{\bar{\rho}}, \quad (3.16)$$

and the fluctuations are denoted with double primes,

$$\Phi'' = \Phi - \tilde{\Phi}. \quad (3.17)$$

It is noteworthy to mention that a two-phase flow using a mixture approach always resembles a variable density flow, even if the phase densities themselves are considered constant. Therefore, Favre averaging should be applied to the governing equations even if no additional compressibility effects appear in the flow field [15].

Applying the Reynolds decomposition to the governing equations of the one-fluid approach follows the same principle as for single phase flows, and is extensively documented in the literature [137, 103, 122]. The Favre averaged set of governing equations of the one-fluid method is then,

$$\frac{\partial \tilde{\alpha}_k \bar{\rho}_k}{\partial t} + \nabla \cdot (\tilde{\alpha}_k \bar{\rho}_k \tilde{u}_k) = -\nabla \cdot (\overline{\rho_k \alpha_k'' u_k''}) + \bar{m}, \quad (3.18)$$

$$\frac{\partial \bar{\rho}}{\partial t} + \nabla \cdot (\bar{\rho} \tilde{u}) = 0, \quad (3.19)$$

$$\frac{\partial \bar{\rho} \tilde{u}}{\partial t} + \nabla \cdot (\bar{\rho} \tilde{u} \tilde{u}) = (\nabla \cdot \bar{\tau} - \nabla \bar{p}) - \nabla \cdot (\overline{\rho u'' u''}) + \bar{\rho} g, \quad (3.20)$$

$$\frac{\partial \bar{\rho} \tilde{e}}{\partial t} + \nabla \cdot (\bar{\rho} \tilde{e} \tilde{u}) = \left(\frac{\partial \bar{p}}{\partial t} - \nabla \cdot \bar{q} \right) - \nabla \cdot (\overline{\rho u'' e''}) + \tau \nabla \cdot (\tilde{u}). \quad (3.21)$$

The primary challenge in solving the averaged equations lies in modeling the emerging correlations among fluctuations in the mass, momentum, and energy conservation, $\overline{\rho_k \alpha_k'' u_k''}$, $\overline{\rho u'' u''}$ and $\overline{\rho u'' e''}$. In general, three distinct modeling approaches can be distinguished. First, there is the aforementioned DNS method, which resolves all turbulent structures, thus eliminating the need for modeling unclosed terms. Secondly, the Reynolds averaged Navier Stokes (RANS) method, which focuses on the mean flow properties and where all turbulent structures are modeled. Lastly, the large eddy simulation (LES) concept offers a compromise between RANS and DNS. The idea of LES is to resolve the large turbulent structures in time and space, while the smaller structures, which exhibit a more universal behavior [137], are modeled. This is achieved by applying a spatial filtering operation on the governing equations, with a defined spatial filter width. This averaging procedure can be applied in the same way as the presented Reynolds average, with the distinction, that the averaging operator represents a spatial and not a time average. Hence, a conceptual distinction between RANS and LES lies in their treatment of unclosed terms; RANS employs a time average for all turbulent scales, while LES utilizes a spatial average for modeling only sub-grid terms.

3.2.1 RANS/LES turbulence models

Turbulence modeling has been a fundamental part of CFD since the beginning, and various turbulence models for different flow aspects have been developed. However, despite best efforts, no general purpose model has emerged and the choice of the turbulence model has to be appropriate for the investigated case. In the following, turbulence modeling in the context of RANS and LES are discussed.

RANS turbulence models

Most of the common RANS turbulence models are based on the Boussinesq hypothesis, relating the Reynolds stresses to the mean rates of deformation [137, 103] by

$$-\overline{\rho u' u'} = \rho \nu_t \left(\frac{\partial \bar{u}_i}{\partial x_j} + \frac{\partial \bar{u}_j}{\partial x_i} \right) - \frac{2}{3} \rho k_t \delta_{ij}, \quad (3.22)$$

where k_t is the turbulent kinetic energy $k_t = 0.5 \left(\sum \overline{u_i'^2} \right)$ and δ_{ij} is the Kronecker delta. The term ν_t is the kinematic turbulent viscosity and a model parameter. To close the

turbulent transport of a scalar, e.g., energy, species mass fraction, or volume fraction, a simple yet widely adopted approach is the gradient diffusion hypothesis [103]. In analogy to the turbulent momentum transport, the turbulent transport of a scalar is proportional to the mean gradients,

$$-\rho\overline{u'\Phi'} = \rho\Gamma_t\nabla\overline{\Phi}. \quad (3.23)$$

Here, Γ_t denotes the turbulent diffusivity, and it is generally assumed to be in close approximation to the turbulent viscosity. This motivates the introduction of a turbulent Prandtl number,

$$\text{Pr}_t = \frac{\nu_t}{\Gamma_t}, \quad (3.24)$$

which is often assumed to be around unity. Therefore, the primary task in all turbulence models founded on the Boussinesq hypothesis is the computation of the turbulent viscosity, ν_t .

Over the last few decades, a variety of turbulence models, differing in computational complexity, have been developed. These models are derived either algebraically (e.g., mixing length models) or by solving one or more additional transport equations (e.g., Spalart-Allmaras, k- ϵ , k- ω models). To reiterate, no general purpose turbulence model for all flow scenarios exists. However, the k- ω SST (Shear Stress Transport) model of Menter [93, 92] has demonstrated broad applicability in both free-stream and wall-bounded flows. Therefore, in this work, it is employed for the majority of RANS simulations. The concept behind the k- ω SST model involves blending between the k- ϵ model in the free stream and the k- ω model in the wall-near region. For a comprehensive understanding of the k- ω SST model and common turbulence models, a detailed exposition can be found in the work by Argyropoulos et al. [9] and in the literature sources cited [137, 103].

LES turbulence models

The difficulty of deriving a general purpose RANS turbulence model roots in modeling all turbulent scales, even though larger scales are strongly effected by the geometry of the domain, boundary conditions and body forces [137]. In contrast, the small turbulent scales are assumed to exhibit a more universal, isotropic behavior, motivating the LES approach of resolving the larger structures while modeling the small sub-grid structures. It shall be noted here that the LES model is derived independent of the numerical method or grid size used, thus 'filtered' and 'residual' are the correct terms. However, in practice the cell size serves as an implicit filter width, $\Delta = \sqrt[3]{\Delta_x\Delta_y\Delta_z}$,

hence here the terminology of resolved quantities and unresolved sub-grid fluctuations is used in the following. An LES is typically considered to be sufficiently resolved if 80% of the turbulent energy is directly captured. For free shear flows it is cost-efficient to resolve 80% of the turbulent energy in the complete computational domain. However, for wall bounded flows, resolving the turbulent structures becomes more expensive and scales with the Reynolds number with about $\propto \text{Re}^{1.8}$ [25, 103]. Therefore, LES can be divided into wall-resolving and wall-modeled LES, where in the latter case, a suitable wall model is applied, and 80% of the turbulent energy is only resolved in the bulk flow.

Applying the spatial filtering to the governing equations results in additional unclosed terms, similar to the Reynolds averaged equations. However, in addition to the Reynolds stresses, the spatial filtering results in additional terms due to the difference of spatial and time averaging, called Leonard's stress and cross stresses. Yet, most of the sub-grid turbulence models assume that the sum of all turbulent stresses can be described by the Boussinesq hypothesis, leading to a formulation analogous to the Reynolds averaging,

$$-\rho \overline{u'v'} = \mu_{\text{sgs}} \left(\frac{\partial \bar{u}_i}{\partial x_j} + \frac{\partial \bar{u}_j}{\partial x_i} \right) - \frac{2}{3} \rho k_t \delta_{ij}. \quad (3.25)$$

In analogy to RANS models, a turbulent (dynamic) sub-grid viscosity or eddy viscosity, μ_{sgs} , has to be computed.

A variety of LES eddy viscosity models have been developed in the last decades of which the Smagorinsky model [129] is a simple yet often applied model. The Smagorinsky model computes the eddy viscosity based on the filter width, Δ , and the resolved strain tensor \tilde{S} , leading to the following equation

$$\mu_{\text{sgs}} = \rho (C_S \Delta)^2 \sqrt{2 \tilde{S}_{ij} \tilde{S}_{ij}}, \quad (3.26)$$

with

$$\tilde{S}_{ij} = \frac{1}{2} \left(\frac{\partial \tilde{u}_i}{\partial x_j} + \frac{\partial \tilde{u}_j}{\partial x_i} \right). \quad (3.27)$$

The parameter C_S is a model constant and is approximately $C_S \approx 0.18$ [97]. While the Smagorinsky model in its pure form is a very simple and easy to implement model it has several disadvantages. One significant disadvantage of the Smagorinsky model for the investigated cases in this work is that the turbulent viscosity does not vanish at a no-slip boundary condition, e.g., walls. To account for this erroneous behavior,

damping functions to correct the viscosity have been introduced [136, 53]. However, the damping functions do not reproduce the viscosity scaling at the wall and may lead to numerical instabilities for complex geometries [97]. This gave rise to develop a new model that accounts for the turbulent viscosity behavior at walls, called wall-adapting local eddy-viscosity (WALE) [97], which does not suffer from these problems. The interested reader can find a detailed derivation and motivation for this model in Nicoud et al. [97].

A significant challenge of determining the quality of an LES in practice is determining the amount of resolved turbulent energy. Typically no reference DNS case or experimental data exists which would allow a direct comparison and the amount of resolved turbulent energy is computed from the filtered values [24, 66]. Further, the numerical dissipation introduced by the numerical methods can be in the order of the modeled turbulent viscosity or, in cases of transonic flows, even outweigh them [3, 61, 45]. This gave rise to a new class of LES, so called implicit LES (ILES). ILES uses the numerical dissipation of the scheme, which are typically dependent on the flux limiter used, to model the turbulent viscosity implicitly. Hence, no additional turbulence model is required [61, 45]. However, this class of LES requires that the introduced numerical dissipation of the scheme is well understood for all transport equations. Further, the numerical dissipation does not vanish at the wall [35]. Therefore, selecting a suitable turbulent sub-grid model and minimizing the numerical dissipation seems more appropriate for a complex flow with varying numerical schemes, as it is typically found in CFD simulations.

3.2.2 Turbulence modeling of two-phase flows

The turbulence models presented in the previous section are derived for single phase flows. In the context of multiphase flows, turbulence of the continuous and dispersed phase has to be considered [122]. However, for one-fluid simulations with a diffused interface, as considered in this work, a general convention on how to accurately model turbulence has not yet been found [68]. Therefore, these flows are often treated as variable density flows, for which turbulence modeling is available and commonly used in the literature [59, 86, 95, 118]. Hence, standard turbulence models available in OpenFOAM are used within this work to model the turbulence for the one-fluid model.

3.3 Surface Density Modeling for Flashing Sprays

The standard ELSA model as it has been introduced by Vallet et al. [135] and expanded by Lebas et al. [74] models the aerodynamic spray breakup where shear forces and turbulence are the dominating factors. However, flashing sprays are characterized by nucleation, bubble growth, merging, and succeeding spray breakup, which are based on fundamentally different physical processes. An ELSA model for flashing sprays should account for these processes, hence requiring a novel set of source terms. This affects in particular the source terms for the so-called dense region of the spray with $\alpha_l > 0.5$. In this region, the standard ELSA approach assumes that the surface density is initialized by the first wrinkles in the jet surface, based on the turbulent length scale, once it exits the injector. The evolution of the surface wrinkling is then modeled based on the turbulent kinetic energy [74]. However, for flashing flows nucleation and bubble growth is present within the jet and may already appear within the injector. Therefore, a new initialization term that accounts for the nucleating bubbles and a source term describing the spray breakup is required. In the dilute region of the spray where only droplets are present, the standard source terms considering droplet collision/coalescence, breakup and secondary breakup have to be expanded by a term accounting for the continuous evaporation of the droplets. With these considerations in mind, the novel surface density transport equation reads,

$$\begin{aligned} \frac{\partial \Sigma}{\partial t} + \nabla \cdot (\Sigma u) = & \quad \Psi [S_{\text{init}} + S_{\text{BrkUp}}] \\ & + (1 - \Psi) [S_{\text{evap,dilute}} + S_{\text{turb,dilute}} + S_{\text{2ndBrk}}], \end{aligned} \quad (3.28)$$

with $\Sigma = \frac{A_l}{V}$ representing the mean interfacial area per unit volume, and $\Psi(\alpha)$ represents here a phase indicator function based on the volume fraction. The first term on the RHS of Eq. (3.28), S_{init} , describes the creation of surface density due to nucleation and bubble growth. The second term, S_{BrkUp} , represents the creation of surface density due to the spray breakup, encompassing the merging of the bubbles, breakup of the lamellae, and formation of the first droplets [83]. The source terms for the dilute region include the evaporation of droplets, $S_{\text{evap,dilute}}$, the collision/coalescence of droplets due to turbulence, $S_{\text{turb,dilute}}$, and secondary breakup based on the relative velocity of the two phases, S_{2ndBrk} .

The indicator function used in Eq. (3.28) differs slightly from the indicator function proposed by Lebas et al. [74]. Here the assumption is made that the spray breakup has fully occurred for a volume fraction of the closest sphere packing, $V_v/V \approx 0.74$ yielding a liquid volume fraction of $\alpha_l = 0.26$. The blending to the dense treatment of bubble

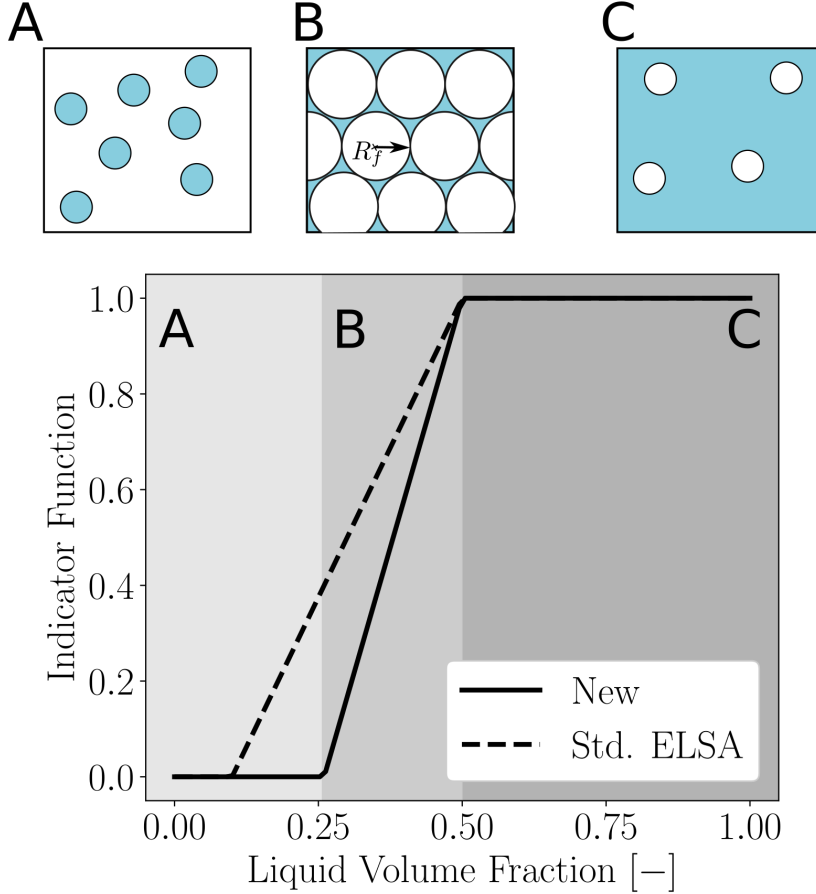


Figure 3.2: Indicator function and comparison of dense spray turbulent source term modeling for surface density transport. The qualitative spray bubble/droplet morphology for each region of the liquid volume fraction is sketched above, blue is liquid and white represents vapor. The radius of the bubbles when they merge and the spray breakup occurs is marked with R_f .

growth and coalescence for a liquid volume fraction larger than 0.5 shall be described by

$$\Psi(\alpha_l) = \begin{cases} \alpha_l < 0.26; & 0 \\ 0.26 \leq \alpha_l \leq 0.5; & \frac{\alpha}{0.24} - \frac{0.52}{0.48} \\ \alpha_l > 0.5; & 1 \end{cases}$$

The difference between the new indicator function to the standard ELSA model and a sketch of the different regimes is shown in Figure 3.2.

3.3.1 Principal model design of the source terms

With the exception of the initial source term, the source term's modeling follows the principal design proposed by Lebas et al. [74] in which the surface density is relaxed

towards a so-called equilibrium value, Σ^{eq} , with a given relaxation time τ ,

$$S_{\Sigma} = \frac{C}{\tau} \Sigma \left(\frac{\Sigma^{\text{eq}} - \Sigma}{\Sigma^{\text{eq}}} \right). \quad (3.29)$$

Here, C is a modeling constant and is typically set to unity unless otherwise noted. The different source terms for the spray breakup, droplet evaporation, droplet collision and coalescence, or secondary breakup then only differ in their relaxation time and equilibrium value. Therefore, for each source term, it is necessary to model an equilibrium surface density and relaxation time.

The equilibrium surface density value is obtained by relating it to the modified Weber number definition,

$$\text{We}^* = \frac{E_{\text{kin}}}{E_{\text{surf}}} = \frac{\rho u_c^2 \mathcal{L}}{12\sigma}, \quad (3.30)$$

with a characteristic density ρ , velocity u_c , and length scale \mathcal{L} . By setting the characteristic length scale to the Sauter mean diameter of the dispersed phase the Weber number can be related to the surface density,

$$\begin{aligned} \mathcal{L} &= D_{32} = 6 \frac{V_d}{A_d} \\ &= \frac{6\alpha}{\Sigma}, \end{aligned} \quad (3.31)$$

with V_d as the volume and A_d as the area of the dispersed phase. Replacing the characteristic length in Eq. (3.30) with Eq. (3.31) gives then an expression for the equilibrium surface density,

$$\Sigma^{\text{eq}} = \frac{\alpha \rho u_c^2}{2\sigma \text{We}^{\text{eq}}}. \quad (3.32)$$

Here, We^{eq} is the so-called equilibrium Weber number and is a model parameter. In conclusion, the choice of the characteristic velocity and relaxation time are the main modeling parameter to distinguish between the different source terms. The equilibrium Weber number is set often around unity and can be seen as a fine-tuning parameter in comparison to the velocity scale and relaxation time.

3.3.2 Source terms for flashing sprays in the dense region

In contrast to an aerodynamic spray breakup, the first interface area is generated in flashing sprays by nucleating bubbles. This behavior is captured by the initializing source term, S_{init} , which defines a minimum surface density Σ_{min} , towards which the

surface density relaxes with a relaxation time τ based on the bubble growth rate,

$$S_{\text{init}} = \frac{1}{\tau} (\Sigma_{\text{min}} - \Sigma), \quad (3.33)$$

with

$$\tau = \frac{R_f}{\frac{\partial R_f}{\partial t}}. \quad (3.34)$$

Here, the bubble growth rate is based on the so called final bubble radius, R_f , which is defined as the bubble radius at merging of the bubbles directly prior to spray breakup [83]. The minimum surface density is determined with the final bubble radius, R_f , and the definition of the Sauter mean diameter of Eq. (3.31),

$$\Sigma_{\text{min}} = \frac{3(1 - \alpha_l)}{R_f}. \quad (3.35)$$

Note that the minimum surface density describes the interface area right before spray breakup, hence with bubbles as the dispersed phase. Thus, the vapor volume fraction $\alpha_v = 1 - \alpha_l$ is used to calculate the Sauter mean diameter.

The bubble growth rate in Eq. (3.34) is modeled using the heat diffusion limit of Prosperetti [106],

$$\frac{\partial R}{\partial t} = \frac{12}{\pi} \frac{\kappa \text{Ja}^2}{\rho_l c_p R}. \quad (3.36)$$

Here, the Jakob number, Ja, is defined as

$$\text{Ja} = \frac{\rho_l c_p (T_l - T_{\text{sat}}(p))}{\rho_v L}, \quad (3.37)$$

with L representing the latent heat. It is important to highlight that this term describes the surface density generation due to nucleation and bubble growth, but not due to the merging of the bubbles and the resulting spray breakup. The surface density generation due to spray breakup is described in the next paragraph.

Once the bubbles have grown to a size that they touch and merge, the spray breakup is initiated [82, 83, 32]. Depending on the bubble Weber and Ohnesorge number different breakup regimes can be identified [82]. In a detailed DNS study, Loureiro et al. [83] have found that the dynamics of the bubbles prior to merging or more precisely, the growth rate at the time of merging, is one main parameter that determines the spray breakup process. Hence, the bubble growth rate at the time of merging is selected as the characteristic velocity scale to model the equilibrium surface density. This is in

contrast to the standard ELSA model, which uses the turbulent kinetic energy as a velocity scale to model the surface density in the dense spray region.

The equilibrium surface density value is then obtained from

$$\Sigma_{\text{ev}}^{\text{eq}} = \frac{\rho_l \alpha \dot{R}_f^2}{2 \text{We}_{\text{ev}}^{\text{eq}} \sigma}, \quad (3.38)$$

where $\text{We}_{\text{ev}}^{\text{eq}}$ is again a model parameter. Even though the bubble growth rate is used here, the generated surface density represents the spray breakup and the generation of the droplets and not the bubbles [81, 83]. Loureiro et al. [83] have studied the bubble growth and spray breakup behavior of flashing cryogenic oxygen and provided a theoretical estimate for the resulting droplet diameter,

$$D_{\text{ref}} = \frac{8\sigma}{\rho_l \dot{R}_f^2}. \quad (3.39)$$

With $D_{32} = \frac{6\alpha}{\Sigma}$ we get

$$\Sigma = \frac{3\rho_l \alpha \dot{R}_f^2}{4\sigma}. \quad (3.40)$$

Combining Eq. (3.38) with Eq. (3.40) gives the equilibrium Weber number for flashing cryogenic flows as $\text{We}_{\text{ev}}^{\text{eq}} = 2/3$. Detailed DNS indicated, however, that a correction factor is needed and the resulting droplet diameter after spray breakup can be approximated by [83],

$$D = 0.294 \sqrt{\text{We}_b} D_{\text{ref}}. \quad (3.41)$$

Hence, the corrected Weber number is

$$\text{We}_{\text{ev,corr}}^{\text{eq}} = 0.294 \sqrt{\text{We}_b} \text{We}_{\text{ev}}^{\text{eq}}, \quad (3.42)$$

and is implemented in the ELSA model using a corresponding pre-factor to the uncorrected equilibrium surface density,

$$\Sigma_{\text{ev,corr}}^{\text{eq}} = \frac{3.4}{\sqrt{\text{We}_b}} \Sigma_{\text{ev}}^{\text{eq}}. \quad (3.43)$$

The bubble Weber number, We_b , is here defined according to Loureiro et al. [83] with

$$\text{We}_b = \frac{2R_f \rho_l \dot{R}_f^2}{\sigma}. \quad (3.44)$$

The final source term for the surface density is then given by

$$S_{\text{evap,dense}} = \frac{1.0}{\tau} \Sigma \left(\frac{\Sigma_{\text{ev,corr}}^{\text{eq}} - \Sigma}{\Sigma_{\text{ev,corr}}^{\text{eq}}} \right). \quad (3.45)$$

The time scale, τ , is the same as for the initialization term and given by Eq. (3.34).

3.3.3 Estimating the final bubble merging radius

It is evident that a suitable estimate of the final bubble radius, R_f , is essential to get valid results and for the model to have predictive capabilities. Starting from the critical radius of bubble nuclei, R_{crit} , the final bubble radius can be described as a multiple of R_{crit} ,

$$R_f^* = \frac{R_f}{R_{\text{crit}}}. \quad (3.46)$$

This normalized bubble radius, R_f^* , can be estimated as [83]

$$R_f^* = \left(\frac{4}{3} \pi n_b R_{\text{crit}}^3 \left[\frac{1}{\eta} - 1 + \frac{\rho_v}{\rho_l} \right] \right)^{-1/3}. \quad (3.47)$$

The parameter n_b and η are the bubble number density and the vapor volume fraction at merging. Here, the densest packing of spheres with $\eta = 0.74$ is assumed, consistent to the assumption made for the indicator function Ψ . Note that this equation respects the decrease in bubble number density due to spatial expansion of the fluid volume during bubble growth. The main challenge is to determine the bubble number density n_b . Often, the homogeneous nucleation model from the classical nucleation theory (CNT), such as the one presented by Blander et al. [17] or Carey [23], is selected in the literature to estimate the nucleation rate for flashing flows [73].

However, these models predict zero nucleation for the conditions present in the investigated cryogenic liquid nitrogen cases of this thesis. This insufficiency of theoretical models is a well-known phenomenon despite the apparent flashing behavior of the spray [78]. One uncertainty of the physical properties in the CNT is the determination of the surface tension, σ , which appears in the third order in the exponential term (cf. Eq. (2.7)). It is known that the surface tension is a function of the bubble radius and cannot be neglected, particularly in the range of the critical radius [132]. Although correction factors such as $\sigma_{\text{corr}} \approx 0.8\sigma$ have been suggested for cavitation bubbles [21], they are not sufficient to shift the onset of flashing to match experimental results and a much larger reduction of the factor of around 8 would be needed. In addition, changes in surface tension would still not change the nucleation rates very strong sensitivity on

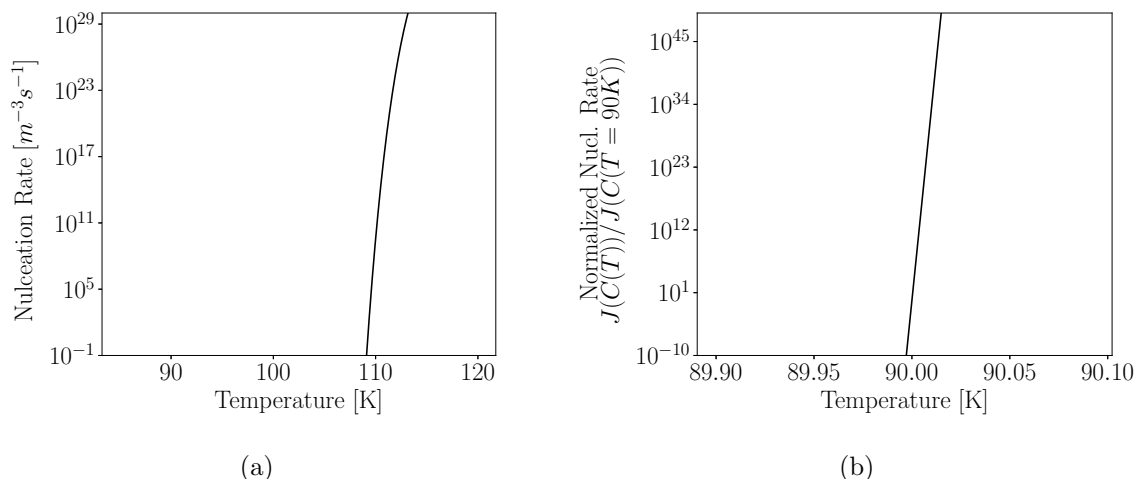


Figure 3.3: (a) Nucleation rate predicted by CNT for cryogenic nitrogen for $p = 15\,000$ Pa. (b) Normalized homogeneous nucleation rate predicted by CNT.

temperature. This is shown in Figure 3.3 where the nucleation rate predicted by the CNT model for the cryogenic nitrogen is plotted. On the right, the nucleation rate, J , is normalized by its value at $T=90$ K. It clearly shows how even minor changes in the temperature lead to an extreme increase or decrease of J due to its exponential temperature dependence. Further, the superheat limit when homogeneous nucleation occurs is predicted at a liquid temperature of about 110 K, which is significantly higher than the observed flashing behavior of liquid nitrogen at $T = 90$ K [52].

The discrepancy between the theoretical model and the experimental observation indicates the importance of a different nucleation mechanism, namely heterogeneous nucleation [46, 78, 79, 134, 71, 6]. To account for this behavior, some researchers have added a correction factor to the exponential term of the nucleation model [78, 134, 6]. The obvious disadvantage is that the newly introduced parameter has to be matched to experiments and lacks any predictive capability. Independent of this correction factor, the homogeneous nucleation model exhibits an extremely strong sensitivity towards the relevant input parameters for the thermodynamic conditions typical for flash evaporation. Within a certain range, small pressure and temperature variations around the bubble trigger huge jumps in nucleation rates such that the homogeneous nucleation model effectively acts like an on/off switch (see also Figure 3.3) and is unlikely to capture the physics of the onset of bubble nucleation and its variation with surrounding thermodynamic conditions, namely the temperature, correctly.

In addition to homogeneous nucleation, heterogeneous nucleation can occur at the liquid-solid interface of the wall and within the fluid, see Section 2.2.2. The heterogeneous wall nucleation requires knowledge about the wall roughness or structure to

determine the nucleation rate [126]. Further, the hydrophilic properties of the wall affect the heterogeneous and bulk nucleation in the flow as well [46]. The heterogeneous bulk nucleation is typically modeled by adding a correction factor to the classical nucleation theory, as has been indicated above. The correction factor significantly alters the equation and can be of the order of 1×10^{-6} [78]. Due to these complex, and often unknown, interactions we propose here to use the amount of dissolved gases as an estimation parameter [90, 71]. Typically, working fluids or fuels in technical applications are not pure substances but contain potential nucleation sites, such as dissolved gases. This aspect is often not considered in numerical applications, and pure fluids are assumed despite all indications that impurities serve as nucleation kernels [71, 90]. Due to the significant difference of $\Delta T \approx 20$ K to the superheat limit predicted by CNT for the investigated cryogenic nitrogen cases, we estimate that the majority of the nucleating bubbles are dissolved gas molecules [71]. Hence, the bubble number density is calculated with

$$n_b = \frac{3\alpha_d}{4\pi R_{\text{crit}}^3}, \quad (3.48)$$

where α_d represents the amount of dissolved gas in the fluid and R_{crit} the critical radius, which describes the minimum stable vapor bubble size in a superheated liquid [23] (cf. Section 2.2.1). Combining Eqs. (3.48) and (3.47) gives then

$$R_f^* = \left(\alpha_d \left[\frac{1}{\eta} - 1 + \frac{\rho_v}{\rho_l} \right] \right)^{-1/3}, \quad (3.49)$$

which is independent of the critical radius. Due to the randomized distribution of the nucleating bubbles, however, an equidistant spacing of bubbles cannot be assumed. Hence, bubbles will coalesce before the final spray breakup, which reduces the bubble number at merging [83]. The mean distance between the bubbles can be estimated with probabilistic methods, e.g., of Bhattacharyya et al. [14], which states that the mean distance between the bubbles is about half to an equidistant spacing. However, as the bubble number density, n_b , is affecting the final bubble merging radius, R_f , with the cubed root $R_f \propto \sqrt[3]{1/n_b}$, a reduction of two is not significantly affecting the results. Therefore, as the number of bubbles at merging cannot be exactly determined and considering the uncertainties of the model, the simpler approach with an equidistant spacing of Eq. (3.49) is used. In addition to R_f^* , the critical radius has to be determined to calculate the final bubble merging radius R_f , see Eq. (3.46). With the Young-Laplace equation (cf. (2.3)) and the expression for the bubble vapor pressure of Eq. (2.4) the critical radius is

$$R_c = \frac{p_b - p}{2\sigma}. \quad (3.50)$$

3.3.4 Droplet evaporation in the dilute spray regime

In the dilute spray region droplets have formed and continue to evaporate, which results in a decrease in the surface density, described by

$$\frac{\partial \Sigma}{\partial t} = \frac{4}{d\rho_l} \frac{\partial}{\partial t} (n_d m_d). \quad (3.51)$$

Here, n_d is the droplet number density and m_d is the mass of one droplet [kg]. Hence, this time derivative represents the change of droplet mass per volume. Replacing the diameter with the description of the Sauter mean diameter then gives,

$$\frac{\partial \Sigma}{\partial t} = \frac{2}{3\alpha\rho_l} \Sigma \underbrace{\frac{\partial}{\partial t} (n_d m_d)}_{\dot{m}}. \quad (3.52)$$

Multiple models exist to approximate droplet evaporation for flashing flows. However, for a correct prediction of the droplet diameter the evolution of the surface density must match the change in volume fraction. Therefore, the same evaporation model for the dilute phase must be chosen for the surface density and volume fraction transport. Suitable phase change models for flashing flows are presented in the next Section 3.4.

The modified surface density transport equation together with the proposed modifications of the source terms is called the flashing liquid atomization model (FLAM) to distinguish it from the standard ELSA model.

3.4 Phase Change Models

The precise simulation of flashing flows requires the accurate modeling of the mass transfer rate, \dot{m} , which is integral throughout the entire process, spanning from bubble nucleation to droplet evaporation. The understanding and modeling of these mass transfer rates are imperative for gaining insights into the complex dynamics of flashing flows. In this section, three widely recognized models for the mass transfer rate are presented and discussed in terms of their respective merits and drawbacks. This exploration commences with an examination of the Hertz-Knudsen relations, a model grounded in statistical thermodynamics [32, 31, 87]. Subsequently, a method reliant on an empirical heat transfer coefficient for mass transfer modeling is discussed. Lastly, attention is directed towards the homogeneous relaxation model (HRM), as originally proposed by Downar-Zapolski et al. [34].

3.4.1 Hertz-Knudsen model

The Hertz-Knudsen model, rooted in the kinetic theory of gases and based on Knudsen [67] and Hertz's [60] foundational works, describes mass exchange at the phase interface. In the following, a short overview of the model and its derivation is presented. For an in-depth understanding and comprehensive derivation of the model, we refer the reader to the detailed review and summary provided by Persad et al. [99].

The Hertz-Knudsen equation can be derived from statistical thermodynamics by approximating the velocity of the vapor molecules with the Maxwell-Boltzmann distribution function. With this, a collision frequency of vapor molecules with the interface can be derived,

$$j = p_s(T) \sqrt{\frac{M}{2\pi R_u T^{\text{eq}}}}. \quad (3.53)$$

Here, j describes the net flux of vapor molecules at equilibrium conditions with T^{eq} as the equilibrium temperature. Further, as equilibrium conditions are assumed the net flux of condensation and evaporation is zero.

In the case of evaporation this obviously is untrue, yet this derivation is still used to describe the mass flux of evaporation by subtracting the condensation from the evaporation flux and using an interface temperature. In addition, to reach a better agreement with experimental results Knudsen has added an evaporation, λ_e , and condensation, λ_c , coefficient leading to the final Hertz-Knudsen equation,

$$\dot{m}'' = \sqrt{\frac{M}{2\pi R_u}} \left(\lambda_e \frac{p_s(T)}{\sqrt{T_l^I}} - \lambda_c \frac{p}{\sqrt{T_v^I}} \right). \quad (3.54)$$

Here, T_l^I and T_v^I denote interface temperatures on the liquid and vapor sides and the double prime that this is a mass flux per unit area.

The problem arises now to determine the two modeling coefficients, λ_e and λ_c . The first issue is that the two coefficients cannot be determined with this single equation, which is why often both model coefficients are set constant and equal, $\lambda_c = \lambda_e$. Secondly, the two interface temperatures have to be determined and, in analogy to the model coefficient, an equal interface temperature on both sides is assumed, $T_l^I = T_v^I$. However, experimental studies have found a temperature jump at the interface of several Kelvin over just a few molecules, thus challenging the assumption of the thermal equilibrium condition. Moreover, finding a common evaporation or condensation coefficient has proven elusive, with experimentally or numerically determined values varying across several orders of magnitude for the same fluid [99]. Consequently, these coefficients appear highly case-dependent, undermining their predictive capability within

the model.

Further, the model results in a flux per unit area which requires the interface area, A_I , to be converted to a mass flux per volume to be applicable for the one-fluid method. However, the interface area is typically an unknown in a one-fluid, two-phase simulation and has to be modeled. Some researchers use a constant empirical factor of $A_I = n_d * \pi D^2$ with a nucleation density of $1 \times 10^{13}/\text{m}^3$ and a bubble radius of 1×10^{-6} m based on cavitating flows [31, 87, 88, 63]. However, the fixed diameter and number density is in contrast to the rapid bubble growth and merging during flash evaporation. In addition these settings are used for bubble growth and droplet evaporation alike. Hence, while providing satisfactory results for some cases, it introduces significant modeling, undermining the otherwise thermodynamic founded modeling approach of the Hertz-Knudsen model.

3.4.2 Adachi model

While the Hertz-Knudsen model can be applied to growing vapor bubbles in the superheated liquid as well as the evaporating droplets, the model of Adachi et al. [2], as presented in Section 2.5, focuses on the evaporation rate of superheated droplets. Therefore, it is of particular interest for Lagrangian based methods [108, 84, 105, 143] but has also been applied to Euler-Euler based simulations [Kapusta2021]. In addition, similar to the Hertz-Knudsen model, a number density must be assumed or modeled to derive a mass flux per unit volume required for the volume fraction transport.

3.4.3 Homogeneous relaxation model

The homogeneous relaxation model (HRM), originally proposed by Bilicki and Kestin [16], is an empirically derived model which encapsulates the full flashing process from nucleation to spray breakup. The idea of the HRM is to extend the homogeneous equilibrium model (HEM) to account for the finite time required for the flashing process by introducing a relaxation time denoted as Θ . The change in the mass fraction χ_l is then expressed as the deviation to equilibrium conditions divided by the relaxation time,

$$\frac{D\chi_l}{Dt} = \frac{\dot{m}_l}{\rho} = \frac{\chi_l^{\text{eq}} - \chi_l}{\Theta}. \quad (3.55)$$

For an infinitely small relaxation time the model would retain the HEM approach, whereas a relaxation time towards infinity represents the homogeneous frozen model, where the time scale of the flow velocity is much faster than the time scale of evapora-

tion. The equilibrium mass fraction χ_l^{eq} is determined by

$$\chi_l^{\text{eq}} = \frac{h - h_{\text{SG}}(p)}{h_{\text{SL}}(p) - h_{\text{SG}}(p)}, \quad (3.56)$$

with h denoting the mixture enthalpy and $h_{\text{SG}}(p)$ the saturation state of liquid and vapor (subscript SL and SG). This formulation differs slightly from the one given in the literature of Downar-Zapolski et al. [34], as there the vapor mass fraction χ_v has been used. Based on the liquid mass fraction the mixture enthalpy is expressed by

$$h = \chi_l h_l(p, T) + (1 - \chi_l) h_{\text{SG}}(p). \quad (3.57)$$

Substituting h in Eq. (3.56) with Eq. (3.57) leads to:

$$\frac{D\chi}{Dt} = -\chi \frac{h_l(p, T) - h_{\text{SL}}(p)}{h_{\text{SG}}(p) - h_{\text{SL}}(p)} \frac{1}{\Theta}. \quad (3.58)$$

In some cases, the fluid is expanded below the triple point pressure, and no saturation conditions can be calculated for this pressure value. Therefore, the pressure to calculate the saturation conditions is limited to the triple point value to allow the computation of the phase change in these instances.

Downar-Zapolski et al. [34] derived an empirical formulation of the relaxation time Θ by fitting the evaporation rate to flashing water experiments, providing a high and low pressure fit of the relaxation time,

$$\text{low pressure fit:} \quad \Theta = \Theta_0 \alpha_v^\beta \left(\frac{p_{\text{sat}}(T_L) - p}{p_{\text{sat}}} \right)^\lambda, \quad (3.59)$$

$$\text{high pressure fit:} \quad \Theta = \Theta_0 \alpha_v^\beta \left(\frac{p_{\text{sat}}(T_L) - p}{p_c - p_{\text{sat}}} \right)^\lambda. \quad (3.60)$$

Here, $p_{\text{sat}}(T_l)$ is the saturation pressure based on the liquid temperature, p_c the pressure at the critical point and Θ_0 , β , and λ are empirical coefficients. Despite being fitted to flashing water experiments, the description of the relaxation time derived by Downar-Zapolski et al. [34] has shown a wide range of applicability for several technical applications, fluids, and thermodynamic conditions [96, 76, 118, 58, 86, 120].

The significant advantage of the HRM, compared to the previous two models, is that no additional modeling for the interface area is required. The HRM already returns the mass flow rate as change per volume which is the native format required for the Euler-Euler, one-fluid, simulation. Further, the full process of nucleation to spray breakup is covered by this single model.

Chapter 4

Solving the Equation System in OpenFOAM

Solving the presented set of equations for the one-fluid model with phase change for flashing flows is a challenging task, and the solution accuracy and numerical stability are significantly affected by the implementation details. This chapter presents a novel compressible two-phase solver for flashing flows in the open source framework OpenFOAM[®] (for Open source Field Operation And Manipulation). At first, a short introduction to the OpenFOAM framework is given, followed by a discussion of different solution methods for sub- and transonic flows. In the third section, the implementation of the governing equations presented in the previous Chapter 3 is given. The last chapter then discusses the implementation of the equation of state with tabulated properties.

4.1 OpenFOAM

OpenFOAM[®] is a free and open-source toolbox for solving numerical problems, first published by OpenCFD in 2004 and licensed under the GNU General Public License version 3. Since then, it has been continuously developed and expanded and is now the leading open-source CFD platform. Currently, three main distributors and developers of OpenFOAM exist OpenCFD, CFD Direct, and Wikki Ltd. For this work, mainly the OpenFOAM version v2012 of OpenCFD, part of the ESI group, is used, while early results are obtained with the OpenFOAM 5.x version from CFD Direct.

OpenFOAM employs a finite volume approach to solve partial differential equations on unstructured grids with polyhedral cells. Its object-oriented programming in C++ provides a powerful code basis for researchers to write customized solvers while building

on the existing tool set. Despite numerous standard OpenFOAM solvers, it does not include a solver for compressible two-phase flows with phase change. Therefore, a key part of this work is the development and implementation of a solver that can solve cryogenic flashing flows, called `compressiblePhaseChangeFoam`.

4.2 Solution Methods for Sub- and Transonic Flows

The governing equations in Chapter 3 are presented with the density as an independent variable and pressure as a dependent variable, which is computed based on the equation of state. Methods that adhere to this discretization approach are commonly referred to as *density-based* methods. This approach is favored in cases of transonic or supersonic flows due to the strong coupling between density and pressure. However, for low Mach numbers or incompressible flows, the problem arises that an independent variable no longer determines the pressure as the time derivative in the mass conservation vanishes. Further, the difference between acoustic and convective wave speeds makes the equation system increasingly stiff and difficult to solve [18]. One common method to solve this problem is to couple the momentum and mass conservation equations to derive a Poisson equation for the pressure. This approach then solves for the pressure, and the density is determined from the equation of state. Consequently, this method is called *pressure-based* approach. In OpenFOAM all standard CFD solvers, except for `rhoCentralFoam`, which however is strongly coupled to the perfect gas assumption [69], follow the pressure-based approach.

Considering the aim of solving the injection process of cryogenic liquid from pure liquid to the spray breakup and droplets, the solution method should be able to solve near incompressible flows in the injector, where pure liquid is present, and highly compressible regions, e.g., during the spray breakup. Therefore, the pressure-based approach is selected, and by considering the pressure-density coupling, it is expanded to applications of high Mach number flows.

4.2.1 Pressure-velocity solution algorithm

To solve transient, compressible flows, OpenFOAM employs a so-called PIMPLE algorithm, which is a combination of the well-known PISO (pressure implicit with splitting of operators) and SIMPLE (semi-implicit method for pressure-linked equations) algorithms [56]. A detailed explanation of the PISO and SIMPLE algorithms can be found in Versteeg et al. [137]. The conceptual idea of the PIMPLE algorithm is to achieve time steps with a CFL number much larger than one by finding a steady-state solu-

tion for the current time step. This is achieved by wrapping the PISO algorithm in a SIMPLE loop. In OpenFOAM, the notation inner and outer loops is used, where inner loops refer to the number of times the pressure equation is solved and outer loops to the SIMPLE iterations, see also Figure 4.1.

4.3 Implementation of the Governing Equations

In this section, the implementation in OpenFOAM of the governing equations introduced in the one-fluid approach and the surface density transport equation from Chapter 3, utilizing a pressure-based solution approach is presented.

4.3.1 Volume fraction transport

The liquid mass conservation of Eq. (3.18) is first written in non-conservative form for the liquid phase to derive a transport equation of the volume fraction, α_l ,

$$\bar{\rho}_l \frac{\partial \tilde{\alpha}_l}{\partial t} + \tilde{\alpha}_l \frac{D\bar{\rho}_l}{Dt} + \bar{\rho}_l \nabla \cdot (\tilde{\alpha}_l \tilde{u}) = \bar{m} - \nabla \cdot (\overline{\rho_l \alpha_l'' u''}). \quad (4.1)$$

Following the approach of Anez et al. [8] the turbulent contributions can be modeled with a gradient diffusion approach,

$$(\overline{\rho_l \alpha_l'' u''}) = (\bar{\rho}_l \widetilde{\alpha_l'' u''}) = -\bar{\rho}_l \left(\frac{\nu_t}{Sc_t} \nabla \tilde{\alpha}_l \right), \quad (4.2)$$

with Sc_t as the turbulent Schmidt number. For the following derivations all properties represent averaged properties, as during the simulation only averaged properties are calculated and stored. Further, to allow some short-hand notation we define the material derivative of an averaged property as

$$\frac{D\bar{\Phi}}{Dt} = \frac{\partial \bar{\Phi}}{\partial t} + \tilde{u} \cdot \nabla \bar{\Phi} \quad (4.3)$$

and

$$\bar{\rho} \frac{D\tilde{\Phi}}{Dt} = \frac{\partial \bar{\rho} \tilde{\Phi}}{\partial t} + \nabla \cdot (\bar{\rho} \tilde{u} \tilde{\Phi}). \quad (4.4)$$

It shall also be noted, that the mean of composed variables, such as the mixture density or mass fraction are calculated with the mean of the individual components,

$$\bar{\rho} = \bar{\rho}_l \tilde{\alpha}_l + \bar{\rho}_v \tilde{\alpha}_v, \quad (4.5)$$

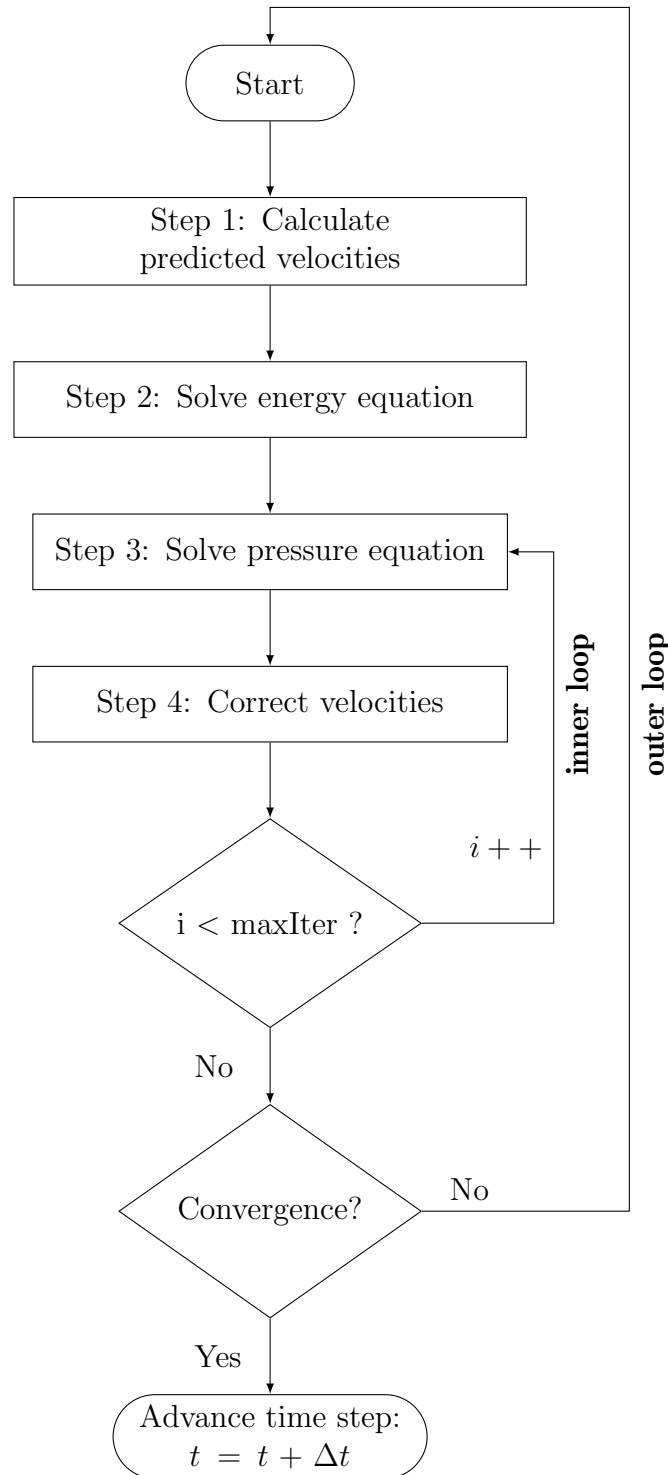


Figure 4.1: Flow chart of the PIMPLE algorithm for a compressible flow. Based on the standard `rhoPimpleFoam` solver of OpenFOAM.

and

$$\bar{\chi}_k = \frac{\bar{\rho}_k \widetilde{\alpha}_k}{\bar{\rho}}. \quad (4.6)$$

To account for the density changes due to temperature and pressure variations, the density in the material derivative is expressed by a linear compressibility model,

$$\bar{\rho} = \rho_0 + \bar{\psi} \bar{p}, \quad (4.7)$$

where $\bar{\psi} = \frac{\partial \bar{\rho}}{\partial \bar{p}}$ is the compressibility. With this, the transport equation reads,

$$\frac{\partial \widetilde{\alpha}_l}{\partial t} + \frac{\widetilde{\alpha}_l}{\bar{\rho}_l} \left(\bar{\psi}_l \frac{D\bar{p}}{Dt} + \bar{p} \frac{D\bar{\psi}_l}{Dt} \right) + \nabla \cdot (\widetilde{\alpha}_l \tilde{u}) = \nabla \cdot \left(\frac{\nu_t}{Sc_t} \nabla \widetilde{\alpha}_l \right) + \frac{\bar{m}}{\bar{\rho}_l}. \quad (4.8)$$

So far, the transport equation does not include information about the second phase, which, however, is important to capture the compressible behavior in the vapor. To include this information, the compressibility term in Eq. (4.8) is replaced by adding the Eq. (4.8) for the two phases together and using that $\alpha_l = 1 - \alpha_v$, which leads to

$$\begin{aligned} \nabla \cdot \tilde{u} + \frac{\bar{\psi}_l}{\bar{\rho}_l} \frac{D\bar{p}}{Dt} + \frac{\bar{p}}{\bar{\rho}_l} \frac{D\bar{\psi}_l}{Dt} = \\ \widetilde{\alpha}_v \left(\frac{\bar{\psi}_v}{\bar{\rho}_v} - \frac{\bar{\psi}_l}{\bar{\rho}_l} \right) \frac{D\bar{p}}{Dt} - \widetilde{\alpha}_v \left(\frac{\bar{p}}{\bar{\rho}_v} \frac{D\bar{\psi}_v}{Dt} - \frac{\bar{p}}{\bar{\rho}_l} \frac{D\bar{\psi}_l}{Dt} \right) - \bar{m} \frac{\bar{\rho}_l - \bar{\rho}_v}{\bar{\rho}_l \bar{\rho}_v}. \end{aligned} \quad (4.9)$$

Inserting Eq. (4.9) into Eq. (4.8) gives then the final transport equation for the liquid volume fraction,

$$\begin{aligned} \frac{\partial \widetilde{\alpha}_l}{\partial t} + \nabla \cdot (\widetilde{\alpha}_l \tilde{u}) - \nabla \cdot \left(\frac{\nu_t}{Sc_t} \nabla \widetilde{\alpha}_l \right) = \widetilde{\alpha}_l \left[\widetilde{\alpha}_v \left(\frac{\bar{\psi}_v}{\bar{\rho}_v} - \frac{\bar{\psi}_l}{\bar{\rho}_l} \right) \frac{D\bar{p}}{Dt} \right] \\ + \widetilde{\alpha}_l \left[\widetilde{\alpha}_v \left(\frac{\bar{p}}{\bar{\rho}_v} \frac{D\bar{\psi}_v}{Dt} - \frac{\bar{p}}{\bar{\rho}_l} \frac{D\bar{\psi}_l}{Dt} \right) \right] \\ + \widetilde{\alpha}_l \nabla \cdot (\tilde{u}) + \frac{\bar{m}}{\bar{\rho}_l} \left(1 + \widetilde{\alpha}_l \left(\frac{\bar{\rho}_l - \bar{\rho}_v}{\bar{\rho}_v} \right) \right). \end{aligned} \quad (4.10)$$

The first term on the RHS of the equation accounts for the change in density due to pressure changes, and the second term accounts for the change in density due to temperature changes. That the second term describes the changes due to temperature becomes apparent if the compressibility is expressed for a perfect gas with $\psi = 1/(RT)$.

4.3.2 Coupling momentum and mass conservation - pressure equation

To derive the Poisson equation for the pressure, the velocity in the mass conservation equation is replaced by the discretized flux from the momentum equation,

$$\frac{\partial \rho}{\partial t} + \nabla \left(\rho \left[\frac{H(u)}{a_p} - \frac{\nabla p}{a_p} \right] \right) = 0, \quad (4.11)$$

where a_p are the diagonal coefficients of the velocity matrix and $H(u)$ sums up the off-diagonal coefficients multiplied by the velocity of the neighboring cells, the unsteady part, and all sources except the pressure gradient, see also Appendix D.1.1. This is the standard pressure equation of OpenFOAM for compressible flow, e.g., in `rhoPimpleFoam`, and its subsonic and transonic treatment is given in Appendix D. However, the solution of this equation leads to a mass flux,

$$(\rho u)_f = \left(\frac{\rho}{a_p} H(u) \right)_f - \left(\frac{\rho}{a_p} \nabla p \right)_f, \quad (4.12)$$

with the subscript f denoting the value at the cell faces, hence the flux over the cell boundaries. Yet, a volume flux is required for the volume fraction transport equation. Further, the effect of the phase change on the pressure and density is currently hidden inside the density derivative. Therefore, the averaged mass conservation, see Eq. (3.19), is first expanded to exclude the density from the divergence term,

$$\frac{\partial \bar{\rho}}{\partial t} + \bar{\rho} \nabla \cdot \tilde{u} + \tilde{u} \cdot \nabla \bar{\rho} = 0, \quad (4.13)$$

which can also be expressed as

$$\frac{D\bar{\rho}}{Dt} + \bar{\rho} \nabla \cdot \tilde{u} = 0. \quad (4.14)$$

For a general case, the total derivative of the density is derived in the work of Bilicki et al. [16] as a function of the mass fraction χ , pressure p , and enthalpy h respectively temperature T ,

$$\frac{D\bar{\rho}}{Dt} = \underbrace{\left(\frac{\partial \bar{\rho}}{\partial \bar{\chi}} \right)_{p,T}}_{\text{Evaporation}} \frac{D\bar{\chi}}{Dt} + \underbrace{\left(\frac{\partial \bar{\rho}}{\partial \bar{p}} \right)_{\chi,T}}_{\text{Compressibility}} \frac{D\bar{p}}{Dt} + \underbrace{\left(\frac{\partial \bar{\rho}}{\partial \bar{T}} \right)_{\chi,p}}_{\text{Temperature}} \frac{D\bar{T}}{Dt}. \quad (4.15)$$

The first term is the effect of evaporation on the mixture density, the second considers

the compressibility of the density, and the last term takes the effect of changing temperature into account. In the following the modeling of the three individual contributions is described.

Phase change: The effect of the phase change on the pressure is modeled with the term,

$$\left(\frac{\partial \bar{\rho}}{\partial \bar{\chi}} \right)_{p,h} \frac{D\bar{\chi}}{Dt}.$$

The first term is the derivation of the density in respect to the mass fraction for constant enthalpy and pressure. The second term is expressed, following the HRM model of Sec. 3.4.3, by the mass change,

$$\frac{D\bar{\chi}}{Dt} = \frac{\bar{m}}{\bar{\rho}}. \quad (4.16)$$

As the mixture density changes with the pressure, the source term can be linearized through a Taylor expansion [120],

$$M(\bar{p}^*) + \frac{\partial M(\bar{p}^*)}{\partial \bar{p}} \times (\bar{p}^{k+1} - \bar{p}^*) \quad (4.17)$$

with

$$M \equiv \left(\frac{\partial \bar{\rho}}{\partial \bar{\chi}} \right)_{p,h} \frac{\bar{m}}{\bar{\rho}}. \quad (4.18)$$

Here, the superscript $*$ denotes the already calculated properties and $k+1$ the implicit calculated values of the current time step, see also Appendix D. The final, linearized description of the phase change source term is then

$$\left(\frac{\partial \bar{\rho}}{\partial \bar{\chi}} \right)_{p,h} \frac{D\bar{\chi}}{Dt} = \left[\bar{\rho} \frac{\bar{\rho}_l - \bar{\rho}_v}{\bar{\rho}_v} \right] \left(\frac{\bar{m}}{\bar{\rho}_l} + \frac{1}{\bar{\rho}_l} \frac{\partial \bar{m}}{\partial \bar{p}} \times (\bar{p}^{k+1} - \bar{p}^*) \right). \quad (4.19)$$

Compressibility: The compressibility of the mixture,

$$\left(\frac{\partial \bar{\rho}}{\partial \bar{p}} \right)_{x,T}, \quad (4.20)$$

is expressed through the following mixture rule [22],

$$\frac{\partial \bar{\rho}}{\partial \bar{p}} = \bar{\rho} \sum_{i=1}^N \left(\frac{\tilde{\alpha}_i}{\bar{\rho}_i} \left(\frac{\partial \bar{\rho}}{\partial \bar{p}} \right)_i \right), \quad (4.21)$$

where N is the number of phases. This expression is also referred to as Wood's formula [22, 104, 119] and a detailed derivation is given in Appendix C.

Temperature: The same derivation as for the compressibility can be made for the change of density with temperature, which yields,

$$\left(\frac{\partial \bar{\rho}}{\partial \bar{T}}\right)_{p,\chi} \frac{D\bar{T}}{Dt} = \bar{\rho} \sum_{i=1}^N \left(\frac{\tilde{\alpha}_i}{\bar{\rho}_i} \left(\frac{\partial \bar{\rho}}{\partial \bar{T}}\right)_i \frac{D\bar{T}}{Dt}\right) \quad (4.22)$$

Assuming a linear compressibility model, $\bar{\rho} = \rho_0 + \bar{\psi}\bar{p}$, the effect of temperature on each phase can be described with,

$$\begin{aligned} \left(\frac{\partial \bar{\rho}_i}{\partial \bar{T}}\right)_{p,\chi} \frac{D\bar{T}}{Dt} &= \left(\frac{\partial \bar{\psi}_i \bar{p}}{\partial \bar{T}}\right)_{p,\chi} \left(\frac{\partial \bar{T}}{\partial t} + \tilde{u} \cdot \nabla \bar{T}\right) \\ &= \bar{p} \left[\frac{\partial \bar{\psi}_i}{\partial t} + \tilde{u} \cdot \nabla \bar{\psi}_i\right] \\ &= \bar{p} \frac{D\bar{\psi}_i}{Dt}. \end{aligned} \quad (4.23)$$

Using this in Eq. (4.22) yields

$$\left(\frac{\partial \bar{\rho}}{\partial \bar{T}}\right)_{p,\chi} \frac{D\bar{T}}{Dt} = \bar{\rho} \cdot \bar{p} \left[\frac{\tilde{\alpha}_l}{\bar{\rho}_l} \frac{D\bar{\psi}_l}{Dt} + \frac{\tilde{\alpha}_v}{\bar{\rho}_v} \frac{D\bar{\psi}_v}{Dt}\right]. \quad (4.24)$$

Final pressure equation: To derive the final pressure equation, the velocity in Eq. (4.14) is replaced with the discretized flux of the momentum equation,

$$\tilde{u} = \left[\frac{H(\tilde{u})}{a_p} - \frac{\nabla \bar{p}}{a_p}\right]. \quad (4.25)$$

Further, the terms for the compressibility and the effect of changing temperature of Eqs. (4.24) and (4.21) can be combined to yield

$$\left(\frac{\tilde{\alpha}_l}{\bar{\rho}_l} \frac{D\bar{\psi}_l \bar{p}}{Dt} + \frac{\tilde{\alpha}_v}{\bar{\rho}_v} \frac{D\bar{\psi}_v \bar{p}}{Dt}\right) + \frac{1}{\bar{\rho}} \left(\frac{\partial \bar{\rho}}{\partial \bar{\chi}}\right)_{p,T} \frac{D\bar{\chi}}{Dt} + \nabla \cdot \left(\frac{H(\tilde{u})}{a_p} - \frac{\nabla \bar{p}}{a_p}\right) = 0. \quad (4.26)$$

Comparing the final pressure equation, Eq. (4.26), to a conventional pressure equation for compressible flows in OpenFOAM reveals two major differences. First, the density is excluded from the Laplacian and velocity divergence term, which consequently leads to a volume flux instead of a mass flux, see also Eq. (4.25). Secondly, the velocity is only replaced with Eq. (4.25) in the divergence term and not in the material derivatives

to avoid additional non-linear terms. Replacing the velocity in all terms with the discretized momentum equation and using the linear compressibility model to replace the compressibility with the density, the standard pressure equation can be recovered. However, this would hide the effect of the compressibility of the individual phases and their implicit treatment, leading to numerical unfavorable conditions.

4.3.3 Energy equation

Conventionally, the one-fluid approach solves for a common mixture temperature of both phases. However, a significant temperature difference between the superheated liquid and the vapor at saturation conditions exists for flashing flows and should be represented in the equation system [52]. Therefore, a rather unconventional approach is chosen for the newly developed `compressiblePhaseChangeFoam` solver. The enthalpy of both phases is transported individually to capture the significant temperature differences.

The enthalpy transport equation of Eq. (3.8) with $e_k = h_k + 0.5u^2$, is first written in the non-conservative form by expanding the first two terms resulting in

$$\alpha_k \rho_k \frac{De_k}{Dt} + \left[\frac{\partial \alpha_k \rho_k}{\partial t} + \nabla \cdot (\alpha_k \rho_k u) \right] e_k = \left(\frac{\partial p}{\partial t} - \nabla q \right) \frac{\alpha_k \rho_k}{\rho} + S_e. \quad (4.27)$$

The term in the angular brackets is the mass change, \dot{m} , as seen in Eq. (3.1), and represents the energy of the liquid that has evaporated. Neglecting the kinetic energy of the evaporated liquid and dividing the equation with the mass fraction $\chi_k = (\rho_k \alpha_k) / \rho$ then gives,

$$\rho \frac{Dh_k}{Dt} + \rho \frac{DK}{Dt} = \left(\frac{\partial p}{\partial t} - \nabla \cdot q \right) + \frac{\rho}{\rho_k \alpha_k} [S_e - \dot{m} h_k]. \quad (4.28)$$

Here K is used as a shorthand notation for the kinetic energy, $K = 0.5u^2$. Note that the division with the mass fraction is strictly only valid when there is also the phase present within the cell, thus $\alpha_k > 0$. However, it is still solved on the complete grid, which requires some careful numerical handling to avoid division by zero and instabilities.

Assuming that the vapor is generated at the saturation conditions of the surrounding pressure, the source term is

$$S_e = \dot{m} h_{SG}(p). \quad (4.29)$$

It shall be emphasized at this point that the enthalpy $h_{SG}(p)$ and not the evaporation enthalpy $h_{fg} = h_{SG}(p) - h_l$ is used because S_e represents the energy that is now stored in the vapor phase and not the energy required to transform liquid to vapor. Further, here the convention is made that the mass flux \dot{m} always represents the change in the

liquid mass. Hence, the mass flux has to be applied with a negative sign for the vapor phase.

Modeling the heat transfer

The heat transfer q in the energy equation is modeled with Fourier's law of heat conduction [137],

$$q = -\kappa \nabla T, \quad (4.30)$$

with κ as the heat conductivity. However, as the energy equation is solved for the enthalpy and not the temperature, it is useful to replace the term with the solved variable. To achieve this, the total derivative of the enthalpy can be used,

$$dh = \underbrace{\left(\frac{\partial h}{\partial T}\right)_p}_{c_p} dT + \left(\frac{\partial h}{\partial p}\right)_T dp. \quad (4.31)$$

The first term of the equation is typically referred to as constant heat capacity c_p and is a fluid property. The second term is for an ideal gas zero, however, for a real gas it has to be considered. Using the definition of the entropy combined with the thermodynamic chain rule and the Maxwell relations, the heat flux can be expressed with simple to compute terms as

$$q = -\kappa \left(\frac{1}{c_p} \nabla h + \frac{1}{c_p} \left[v - vT \sqrt{\frac{\psi(c_p - c_v)}{T}} \right] \nabla p \right). \quad (4.32)$$

A detailed derivation of the heat flux can be found in Appendix E.

The low ambient pressure at high altitudes and in the experimental chamber of the cases investigated justifies an ideal gas assumption. However, the equally low temperatures go against the ideal gas assumption of low pressure and high temperature. Therefore, the real gas representation of the heat flux, Eq. (4.32), has been implemented in the solver. It was found that including the real gas effects in the heat flux did not affect the results in a measurable way, which justified the use of the ideal gas assumption and a simplified heat flux expression with,

$$q = -\frac{\kappa}{c_p} \nabla h, \quad (4.33)$$

for all simulation results presented in this thesis.

Turbulence modeling

Applying the Favre averaging to the enthalpy transport equations yields for both phases,

$$\bar{\rho} \frac{D\tilde{h}_l}{Dt} + \bar{\rho} \frac{D\tilde{K}}{Dt} = \left(\frac{\partial \bar{p}}{\partial t} + \nabla \cdot \left(\frac{\kappa}{c_p} \nabla \tilde{h}_l \right) \right) - \nabla \cdot (\overline{\rho u'' h_l''}) + \frac{\bar{\rho}}{\bar{\rho}_l \tilde{\alpha}_l} \bar{m} \left[h_{\text{SG}}(p) - \tilde{h}_l \right]. \quad (4.34)$$

$$\bar{\rho} \frac{D\tilde{h}_v}{Dt} + \bar{\rho} \frac{D\tilde{K}}{Dt} = \left(\frac{\partial \bar{p}}{\partial t} + \nabla \cdot \left(\frac{\kappa}{c_p} \nabla \tilde{h}_v \right) \right) - \nabla \cdot (\overline{\rho u'' h_v''}) - \frac{\bar{\rho}}{\bar{\rho}_v \tilde{\alpha}_v} \bar{m} \left[h_{\text{SG}}(p) - \tilde{h}_v \right]. \quad (4.35)$$

The turbulent contributions are closed with the Reynolds analogy used in Eq. (4.2) and presented in Section 3.2,

$$\overline{\rho u'' h_k''} = - \left(\frac{\mu_t}{\text{Pr}_t} \nabla \tilde{h}_k \right). \quad (4.36)$$

4.3.4 Surface density transport equation

A general expression of the averaged surface density transport equation is,

$$\frac{\partial \bar{\Sigma}}{\partial t} + \nabla \cdot (\bar{\Sigma} \tilde{u}) + \nabla \cdot (\bar{\Sigma} \tilde{u} - \bar{\Sigma} \tilde{u}) = \bar{S}_\Sigma, \quad (4.37)$$

where S_Σ constitutes all source terms of bubble growth, spray breakup, droplet evaporation and collision/coalescence. The unclosed term $(\bar{\Sigma} \tilde{u} - \bar{\Sigma} \tilde{u})$ appearing on the LHS represents the difference between the mixture and interface velocity and is closed in analogy to the volume fraction transport with the gradient diffusion approach [8, 135],

$$\bar{\Sigma} \tilde{u} - \bar{\Sigma} \tilde{u} = - \frac{\nu_t}{\text{Sc}_t} \nabla \bar{\Sigma}. \quad (4.38)$$

Notes to Favre averaging: It shall be noted that a rigorous approach to average the surface density transport equation results in a Reynolds averaged velocity, \bar{u} , which is inconsistent with the Favre averaged velocity, \tilde{u} , used in the mass, momentum, and energy equation. Two main approaches to resolve this issue can be identified in the literature. Lebas et al. [74] proposed to replace the surface density Σ with a density-weighted surrogate variable $\Omega = \Sigma/\rho$, which then allows to write the transport equation with the mixture density in the derivatives, resulting in a typical Favre averaged transport equation. Other researchers have used the Favre averaged velocity for the transport of Σ directly, thus replacing $u = \tilde{u}$, leading to $\tilde{\tilde{u}} = \tilde{u}$ [121, 86, 36]. Further,

the solution of the pressure equation, as presented in Section 4.3.2, returns a volume flux. While it is possible to reconstruct a mass flux, $(\rho u)_f$, it introduces new numerical uncertainties by interpolating the densities to the cell faces. Therefore, the modeling choice of using the Favre averaged velocity in the transport of the surface density is selected.

4.4 Thermophysical Properties and Equation of State

In order to solve the governing equations, the chosen thermodynamic model must not only provide an equation of state for the pressure-density coupling but also possess the capability to represent both the superheated state and saturation conditions accurately. While OpenFOAM offers a versatile thermodynamic library, no standard model that fulfills the requirements exists. To overcome this limitation, a novel thermodynamic library is developed, which introduces a new set of functions providing access to the saturation conditions. Further, for the computation of the thermophysical data, including the superheated state, the state-of-the-art thermodynamic library CoolProp [13] based on Helmholtz-energy-explicit solutions, is selected. Nevertheless, performing real-time calculations of fluid properties such as density or the temperature-enthalpy lookup for each cell and time-step is prohibitively time-consuming. To address this issue, a pre-calculation and tabulation approach is implemented for the necessary data sets, combined with linear or bi-cubic interpolation to obtain intermediate values. It is important to note that the normalized root mean square (NRMS) error resulting from interpolation is less than 5×10^{-5} for vapor properties and less than 8×10^{-9} for liquid properties. Therefore, the use of tabulated properties is justified, considering the simultaneous significant computational speed up of factor 50.

Chapter 5

Simulation of Cryogenic Flashing Nitrogen

In Chapter 3, the theoretical framework for modeling flashing flows is presented, while Chapter 4 details the implementation of these models within a newly devised compressible, two-phase solver featuring phase change capabilities in the OpenFOAM platform. The resulting solver, called *compressiblePhaseChangeFoam*, can now be applied to the flashing cryogenic liquid nitrogen test cases experimentally examined at the DLR Lampoldshausen to investigate the flow and spray dynamics inside and outside of the injector. In the context of this investigation, four consecutive journal publications have been published, exploring the flashing behavior of cryogenic liquid nitrogen and the effect of shocks in flashing sprays. In these papers, the objectives listed in the Chapter 1 are successively addressed. To reiterate, the objectives are:

- (1) Development of a compressible, two-phase solver in OpenFOAM.
- (2) Investigation of the flow and spray dynamics inside and outside the injector and comparison to experimental data sets.
- (3) Expand the existing ELSA model for flashing flows.

The first objective of this work, developing a compressible two-phase solver for flashing cryogenic flows, has already been addressed in the previous chapters. Nonetheless, it is important to highlight that the development of a novel computational fluid dynamics (CFD) solver extends beyond the mere implementation of governing equations. It involves a thorough validation process to establish the accuracy and reliability of the solver within the specific context of this study. The validation of the solver is addressed in the first paper, Gärtner et al. [52], validating its capability to accurately capture shocks in flashing flows and predict the spray angle. In addition, the effect of the shock on the flow pattern is discussed. The second paper, Gärtner et al. [48], explores

the behavior of flashing sprays in the context of gasoline direct injection (GDI) with 3D RANS, emphasizing the significant effect shock structures associated with flashing sprays can have on the flow and spray pattern. While not focusing on cryogenic liquids, it provides insight into shock interactions of flashing flows, which is important for subsequent work focusing on a typical injector array used in a rocket engine. The third paper, Gärtner et al. [51], highlights the effects of 3D LES modeling compared to 2D RANS, investigating the spray dynamics and droplet movement. The development of the novel ELSA model introduced in Section 3.3 is presented in the fourth paper, Gärtner et al. [49], and validated with 2D RANS compared to three cases of flashing cryogenic nitrogen with different superheat ratios. Further, it is compared to other standard ELSA models of the literature, showcasing the importance of the novel source terms introduced in this work.

Paper 1:

The validation of the developed solver, *compressiblePhaseChangeFoam*, has been addressed in the publication Gärtner et al. [52]. First, the capability to capture the transonic effects of flashing flows was validated by comparison to flashing acetone experiments conducted by Lamanna et al. [73], where unambiguous measurements of the location of the shock exist. The experimental setup consists of a diesel injector with a diameter of 150 μm and an aspect ratio of $L/D = 6$ with a constant injection pressure of 10 bar and an outlet pressure of 60.8 mbar. Five distinct cases, varying in inlet temperature and superheat ratio (R_p), ranging from $T_{\text{inj}} = 311$ K with $R_p = 8.7$ to $T_{\text{inj}} = 373$ K and $R_p = 61$, were investigated. Prior to investigating the transonic effects of the flashing acetone, the unconventional use of two separate energy equations for each phase was examined. Despite significant differences in vapor and liquid temperatures, choosing between a single mixture temperature and two separate phase temperatures did not influence the resulting velocity field and shock position. The marginal impact of the modeling choice for energy transport is attributed to the strong dependence of modeling parameters on the liquid temperature and the fact that only pure gas phase values, such as density, depend on the vapor temperature. Nevertheless, the additional computational effort is very moderate, and therefore, the two-equation model for energy transport has been used for all further simulations. The comparison of the lateral expansion of the shock wave for the five investigated cases showed a very good agreement with the experimental data. Further, the spray angle could be matched for cases of higher superheat. This behavior is expected, as the homoge-

neous nucleation model is not well suited for low superheat ratios with more dominant heterogeneous nucleation and an intact liquid core at the injector exit. With these results, it can be concluded that the solver can accurately capture the transonic effects associated with flashing flows.

Subsequently, the solver was applied to three cases of flashing cryogenic liquid nitrogen, which were experimentally investigated at the test bench M3.3 at the German Aerospace Center (DLR) Lampoldshausen. The injection conditions of the three cases are listed in Table 5.1, and a detailed description of the experimental setup is found in Rees [111]. In addition to the capability to capture compressible effects, the phase change model has to be validated for the investigated cases. Notably, two of the investigated cases have a chamber pressure below the triple point of nitrogen, necessitating the constrain of the saturation pressure to the triple point value, see also Section 3.4.3. Validation of the default high-pressure fit coefficients of the HRM model was accomplished by comparing the mass flow rate through the injector between the experiment and the simulation. The agreement in mass flow rates attests to the accuracy of the standard literature parameters in capturing flashing behavior within the injector. A parameter study further supports this result, revealing that modifications significantly affect the mass flow rate without altering the qualitative spray behavior outside the injector.

Table 5.1: Boundary values for the cryogenic nitrogen jet.

Case	T_{inj} [K]	p_{inj} [Bar]	R_p [-]	Ja [-]
LN2-1	82.3	8.1	11.7	0.17
LN2-2	89.7	4.4	48.1	0.25*
LN2-3	95.6	6.2	188.6	0.31*

The experimental shadowgraph images revealed stationary or slightly upstream floating dark regions approximately 20 to 30D downstream of the injector. While these alone lack conclusive interpretation, a comparison with numerical results exposed a recirculation zone forming in this region as is shown in Figure 5.1¹. This recirculation arises from the interaction between the low velocity in the spray core and the high velocities of the slipstream downstream of the Mach disc. It differs from recirculation directly after the Mach disc in underexpanded gaseous flows, the existence of which is debated in the literature [127, 39, 44]. However, it requires further investigation to estimate the numerical contribution to the observed phenomena and will be addressed

¹The cases LN2-1 and LN2-2 were recalculated for this image with the, at the time of writing, newest version of the solver (579dd3) using the adaptive mesh refinement method of blastAMR and the linear upwind scheme for the divergence operators.

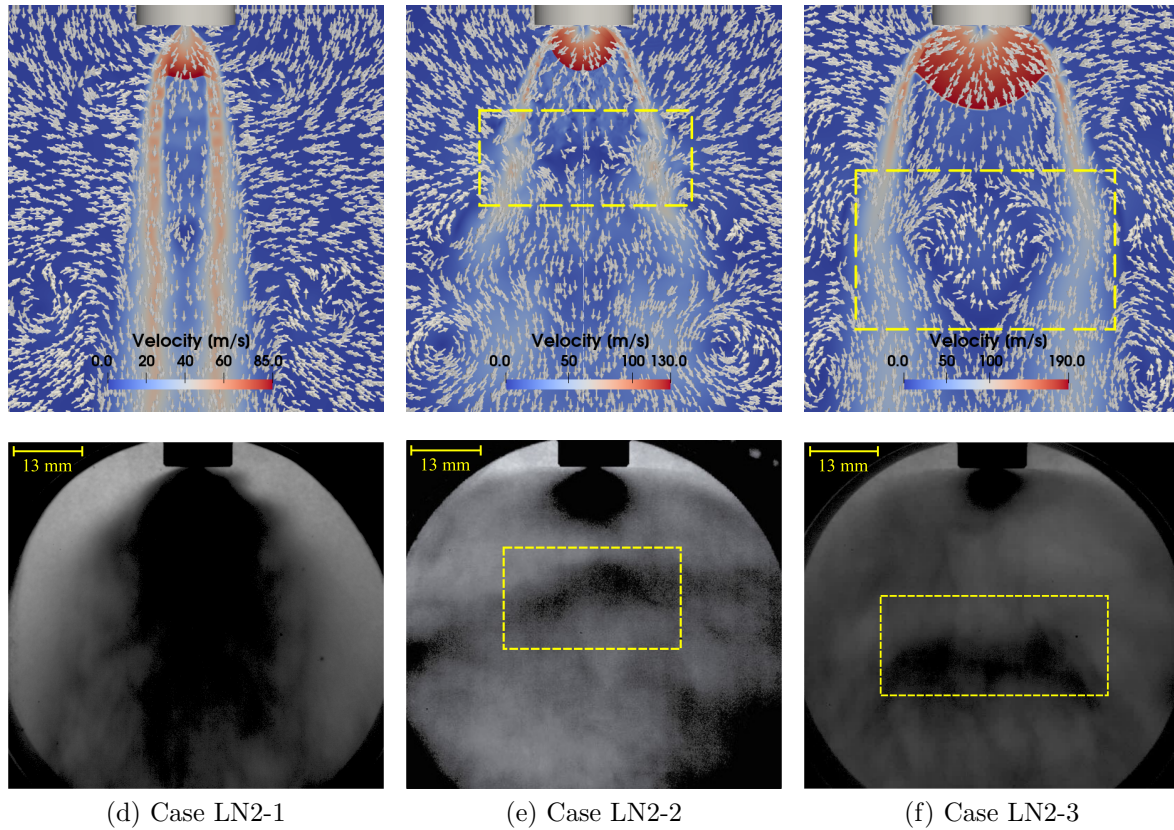


Figure 5.1: Velocity contour plot of the nitrogen spray compared to the shadowgraph images. The velocity direction is visualized in the simulation with white arrows, and the recirculation zone is marked with a yellow box.

in the following publications. Nevertheless, the presence of these observed dark structures in the experimental shadowgraph images suggests the existence of shocks, even when not directly visible, due to the high optical density near the injector exit.

Paper 2:

In the investigation presented by Gärtner et al. [48], the study focuses on shocks and their influence on spray collapse in the context of flashing flows with 3D unsteady RANS simulations. Two distinct configurations were examined: a single-hole injector and the eight-hole spray G configuration from the engine combustion network (ECN). A comparison of predictions of fully flashing *n*-hexane sprays in a single-hole injector with simulations by Guo et al. [57], who used the commercial CFD software CONVERGE, served as an additional validation case for the developed solver presented in Chapter 4. The comparison demonstrated that the solver could faithfully reproduce the results when matching the inlet conditions. Systematically varying chamber pressure and injection temperature revealed that the chamber pressure predominantly dictated

the position of the Mach disk, while the injection temperature primarily influenced the increase in velocity and the extension of the shock wave. Consequently, the conventional parameter R_p , commonly employed to characterize flashing behavior, was found inadequate for unambiguously describing the dynamics of the jet or subsequent spray collapse.

To explore the shock interaction arising from opposing plumes and the three-dimensional effects induced by neighboring injector holes, the study analyzed the spray G configuration of ECN. Three cases were examined: the standard G2 case with slightly superheated iso-octane and two propane cases exhibiting pronounced spray collapse behavior. Comparison of simulation results for the G2 spray with extinction imaging demonstrated a general trend match, with discrepancies observed in the x-y plane perpendicular to the spray axis. Notably, the simulation predicted individual plumes, contrasting with the experimental observation of the eight plumes forming a ring structure. This divergence was attributed to the simplified numerical setup, wherein the simulation employed iso-octane throughout the domain, while the experiment involved nitrogen in the chamber. Nevertheless, this discrepancy did not compromise the interpretation of spray dynamics in the presence of shock structures.

Given the inadequacy of the superheat ratio R_p as a criterion for spray collapse, a new characteristic number, D_n , was proposed by Lacey et al. [72]. Analysis of the first propane case (case Propane-A in [48]) indicated that the reflected shocks of opposing plumes did not merge, contrary to expectations, as the D_n value of 0.95 fell below the threshold of 1.0. In the second case, with a D_n of 1.27, the reflected shocks interacted and merged into a central Mach disk, aligning with the anticipated behavior suggested by the characteristic number D_n .

The results align with the findings of Guo et al. [58], underscoring that the merging of reflected shocks due to the underexpanded vapor jet leads to spray collapse by shielding the low-pressure cell at the center of the spray from ambient conditions. This behavior is shown in Figure 5.2, which shows the time development of the pressure field and shock system. At first, the individual plumes form a first and second pressure cell, as also observed for single-hole injectors. However, as the shock system expands, the reflected shocks of the individual plumes merge and form a third pressure cell in the center of the spray, which causes the observed spray to collapse.

Consequently, $D_n \geq 1$ emerges as a reliable estimate for predicting spray collapse, though not a necessary criterion. This conclusion is further reinforced by the experimental investigation of Poursadegh et al. [104], where spray collapse occurred for D_n values below 1.0. Moreover, the observed spray patterns and radially squeezed-out

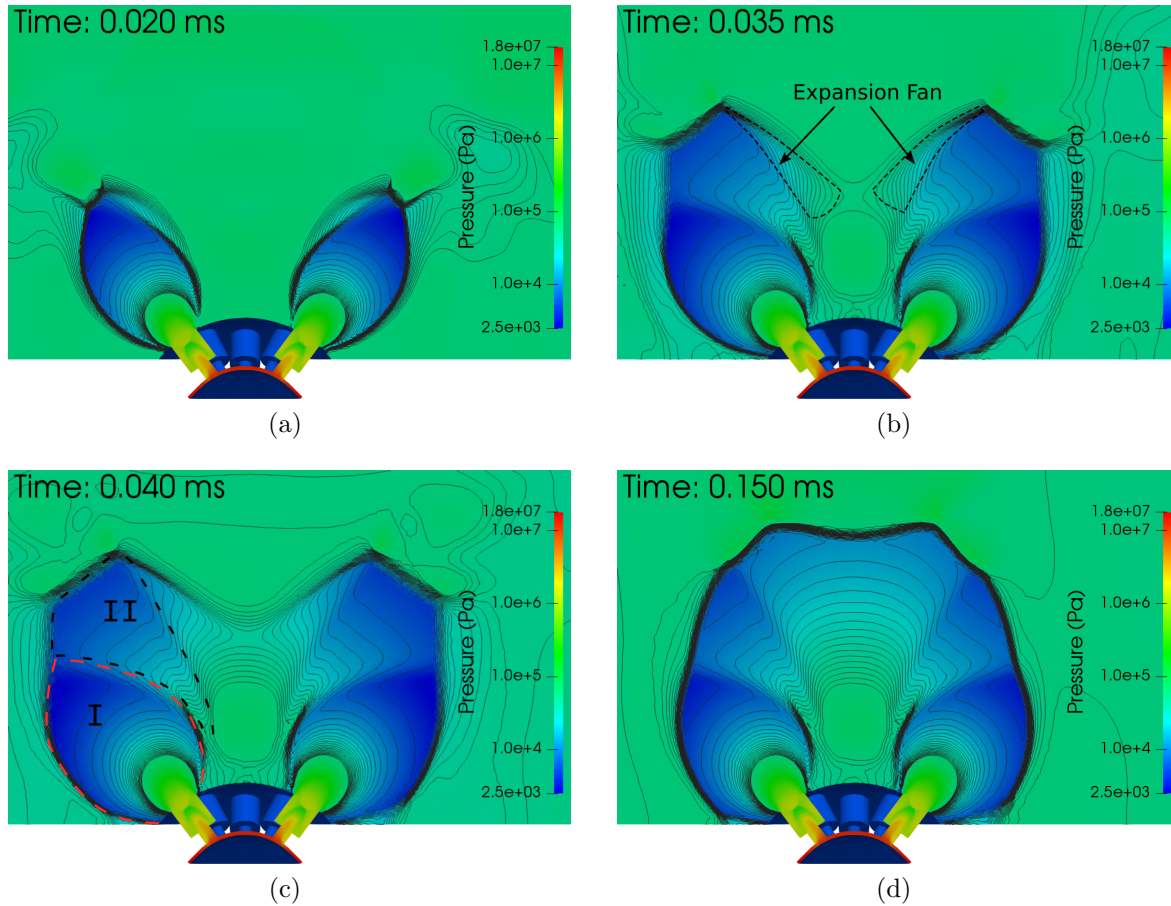


Figure 5.2: Logarithmic pressure contour for the case of Propane-B for different time steps: (a) 0.020 ms, (b) 0.035ms, (c) 0.040 ms and (d) 0.150 ms. The formed pressure cells are marked in (c) with Roman numerals I and II.

fluid correlate well with experimental results.

In summary, the proposed notion of underexpanded vapor jet plumes interacting between opposing injector holes receives numerical support. Additionally, the assertion by Guo et al. [58] regarding an isolated low-pressure region in the center causing spray collapse is corroborated by the results of the propane cases. Moreover, the paper demonstrates the applicability of the developed solver to 3D simulations.

Paper 3:

In the preceding publications, the capabilities of the developed solvers in accurately capturing compressible flashing behavior in both 2D and 3D configurations have been demonstrated, addressing this thesis's first and second objectives. In the following study, three-dimensional effects on the spray dynamics inside and outside the injector were further explored for case LN2-2 investigated with 2D RANS in Paper 1 [52].

Additionally, the impact of more detailed turbulence modeling was explored through large eddy simulation (LES). To facilitate reliable LES application in the context of flashing flows, a novel weighted essentially non-oscillatory (WENO) scheme developed for OpenFOAM [50] has been employed, meeting the demands of low dissipation rates and the ability to resolve discontinuities, such as shocks.

The influence of resolving turbulent eddies on the injector's evaporation rate was investigated by comparing 3D LES results with 2D RANS simulations from [52]. The findings revealed that the 3D LES generates more vapor due to turbulent eddies at the wall, a larger separation zone at the injector inlet, and increased vapor transport toward the injector's center. Despite variations in vapor distributions between the two simulation types, the overall mass flow shows only a marginal 3.6% difference due to an increased velocity of the LES in the near-wall region. Therefore, while 2D RANS accurately predicts general characteristics of mass flow rate and bulk velocity, it lacks the capacity for a detailed examination of vapor/liquid distribution within the injector.

In the initial 2D RANS investigation outlined in Paper 1 [52], the comparative analysis was limited to qualitative shadowgraph images. Now, the more recently available experimental droplet size and velocity measurements permit a quantitative comparison of experiment and simulation. Figure 5.3a shows the mean LES velocity and overlaid the measured droplet velocities of the experiment. It shows that the spray velocities of the one-fluid solver matched the measured droplet velocities well in the slipstream of the shock but were much lower than the measured values in the spray center just downstream of the shock front. This discrepancy can be explained by the experimentally measured droplet size distribution, which indicates that not all droplets are small enough to follow the gas flow perfectly, thereby violating the no-slip assumption of the one-fluid model. To investigate the behavior of these larger droplets, additional one-way coupled particles were injected and tracked for a more meaningful comparison between experiments and simulations. These particles were injected with the droplet size distribution measured closest to the injector and the local velocity of the one fluid solution. The tracked particles provide good approximations of the experimental values in the spray center and the slipstream, showing that the droplets follow the gas flow with a delay of about 10 to 20 D, depending on the droplet size. This also matches with the velocity drop between 20 to 30 D in the experimental data, see Figure 5.3b.

However, the recirculation zone observed in the first paper could not be reproduced by 3D LES, and it is likely that an inverse energy cascade wrongly causes the strong recirculation in 2D due to the missing vortex stretching effects. Nonetheless, smaller eddies and zones of low axial velocity continued to be present in the 3D simulation

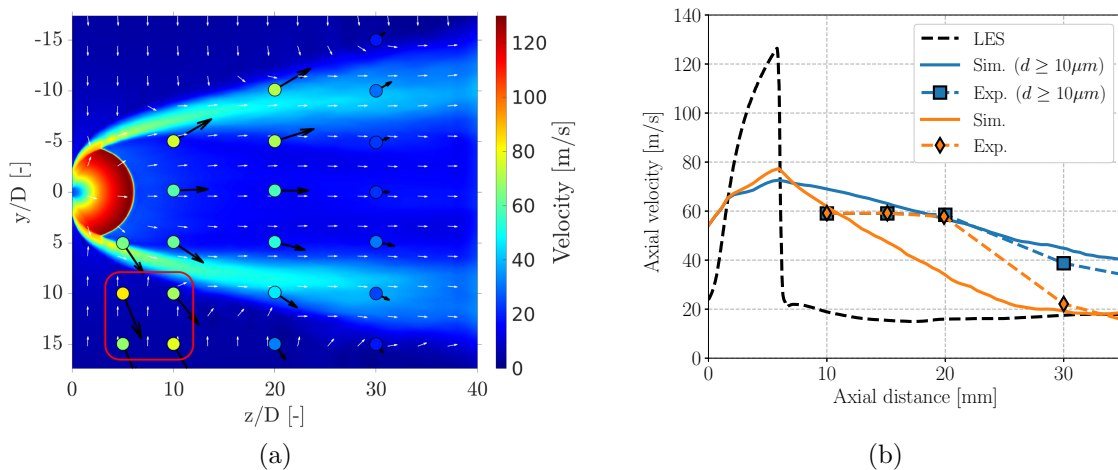


Figure 5.3: (a) Mean velocity of the LES compared to the experimentally measured droplet velocities marked as circles with a scaled velocity vector in black. The white arrows represent the flow direction of the LES solution. The red marked region denotes experimental measurement points with only a few valid measurements, resulting in a low statistical relevance. (b) Axial velocity of the one-fluid solution (LES), the experimental data (Exp) and sampled particles (Sim), as well as conditioned velocities for droplets larger than $10\mu\text{m}$.

in the same region, and the region could be identified as a suitable location for spray ignition in upper-stage rocket engines burning conventional fuels.

In summary, the 2D RANS can capture the overall characteristics of the spray dynamics, matching mass flow rate and spray angle. However, it overpredicts the recirculation downstream of the shock front due to missing three-dimensional effects. Further, resolving the larger eddies is required for a more detailed prediction of the vapor distribution within the injector, yet not affecting the overall mass flow rate significantly. While the one-fluid model cannot capture the behavior of the larger particles, it produces the correct velocity field for smaller droplets and the vapor phase, which governs the movement of the larger particles.

Paper 4:

In the conventional one-fluid model featuring a sub-grid scale phase interface, a notable limitation is the inherent loss of information pertaining to the surface interface. Addressing this limitation, Chapter 3 has introduced the flashing liquid atomization model (FLAM), an extension to the standard Eulerian-Lagrangian spray atomization (ELSA) model for flashing flow, to recover the surface density. The development and verification of this model is the focus of the fourth and last publication presented in

this thesis, addressing the third and final objective. In Gärtner et al. [49] the standard ELSA model, developed for aerodynamic spray breakup, was first presented and implemented into the developed solver *compressiblePhaseChangeFoam* of Chapter 4. The implementation of the standard model has then been validated by comparison to the work of Ménard et al. [91], which has also been used as a reference case for the ELSA model of Lebas et al. [74]. After the implementation of the standard model has been verified, the novel FLAM model detailed in Section 3.3 is implemented in the same solver. A critical parameter within the FLAM model is the bubble number density or, alternatively, the radius of merging bubbles. As discussed in Section 3.3, the homogeneous nucleation model fails to provide a valid prediction for the bubble number density. Instead, the experiment's measured purity of liquid nitrogen is employed to compute the bubble merging radius R_f^* using Eq. (3.49). The newly developed FLAM model was then applied to a reference case of flashing cryogenic nitrogen, where the axial distribution of the Sauter mean droplet diameter was measured. Figure 5.4a compares the measured droplet diameters with the Sauter mean diameter calculated from the surface density model on the central axis, showing a good agreement between the predicted droplet diameter of the model and the experimental data. Further, the development of the surface density along the spray axis followed the trend of flashing spray breakup observed in DNS [83] and provides a prediction of the spray breakup location.

Comparisons with the standard ELSA model and another ELSA model from the literature highlight their inability to predict the substantial increase in surface density resulting from flashing spray breakup, see Figure 5.4b. Consequently, these models were unable to provide a valid prediction of the mean droplet diameter. Thus, the results underscore the ability of the newly developed model to predict the surface generation of flashing cryogenic sprays and emphasize the importance of basing source term models on the underlying physical processes driving surface generation. The model's sensitivity to the two main model parameters was investigated in a parameter study, showing that the uncertainties of the parameter selection are in the range of experimental uncertainty. Hence, the model is, within reason, robust to changes in the modeling parameters. Further, the assumptions made to determine the model parameters are justified.

At last, the FLAM model was applied to two other cases of flashing cryogenic nitrogen with a varying superheat ratio while keeping the model parameters constant. It was found that the model could predict the decrease of the droplet diameter with increasing superheat ratio and that the predicted droplet sizes were in the range of the experi-

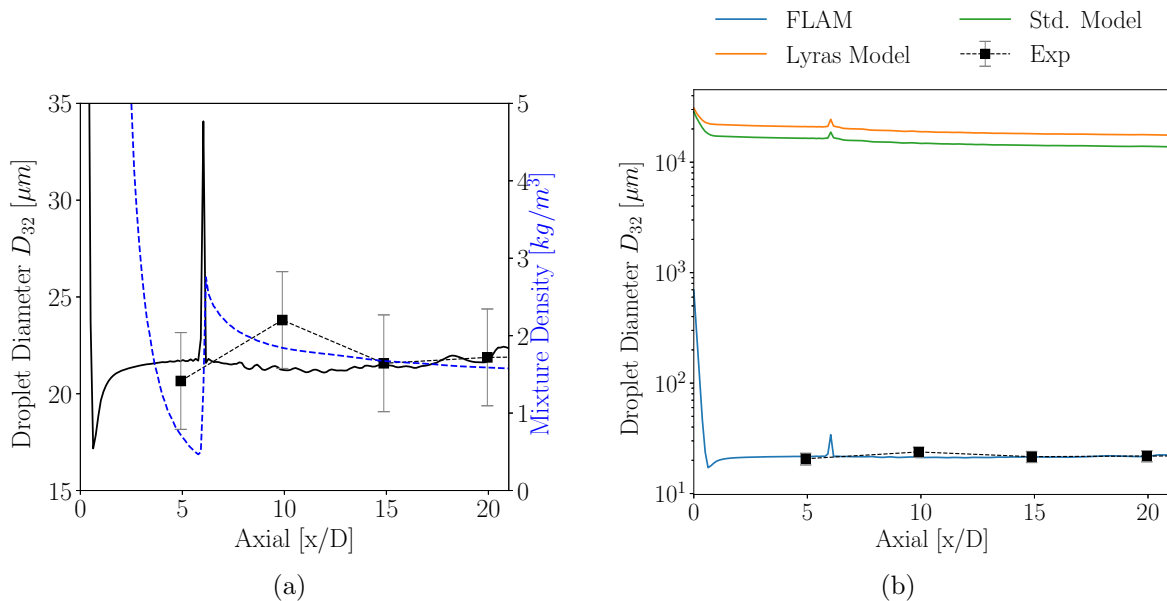


Figure 5.4: (a) Mean Sauter diameter, D_{32} , with the model parameters $R_f^* = 140$, $We_{ev}^{eq} = 0.66$. Subfigure (b) shows a comparison of the new FLAM model to the standard ELSA model (green line) and the ELSA model for flashing sprays proposed by Lyras et al. [86] (orange line).

mentally measured values. In addition, it supports the claim to use the dissolved gases to predict the nucleation rate in comparison to other nucleation models, which would predict significantly different bubble number densities for the three investigated cases. In conclusion, the model has shown its applicability for flashing cryogenic nitrogen cases for different superheat ratios and can be considered verified for 2D RANS. However, further test cases with different fluids and flashing conditions would be beneficial to determine the model's capabilities and limitations. In addition, the model's application to high-fidelity simulations with 3D domains and LES modeling has to be tested and is part of future work.

Summary

In the four papers [52, 48, 51, 49], a novel compressible, one-fluid solver for cryogenic flashing liquids is presented and validated for 2D RANS, 3D RANS and LES cases. Its capability to capture the transonic effects and phase change of flashing flows has been proven for different fluids and conditions. A qualitative comparison of experimental shadowgraph images with simulation results exposed a recirculation zone in the same location where indicators for a negative axial velocity have been observed. A succeeding quantitative comparison of measured droplet velocities with 3D LES revealed that

larger droplets would not follow the gas flow, violating the no-slip assumption of the model. However, the gas dynamics are captured, which governs, in combination with the droplet's inertia, the movement of the larger particles. Lastly, the loss of surface interface information inherent to the one-fluid model has been overcome by introducing a new ELSA model for flashing sprays. Finally, potential future work to further validate and improve the models has been identified and is discussed in Chapter 6.

Paper 1:

Title: Numerical and Experimental Analysis of Flashing Cryogenic Nitrogen

Authors: Jan Wilhelm Gärtner
Institute for Combustion Technology (ITV),
University of Stuttgart, Stuttgart, Germany

Andreas Kronenburg
Institute for Combustion Technology (ITV),
University of Stuttgart, Stuttgart, Germany

Andreas Rees
Institute of Space Propulsion,
German Aerospace Center (DLR), Hardthausen, Germany

Joachim Sender
Institute of Space Propulsion,
German Aerospace Center (DLR), Hardthausen, Germany

Michael Oswald
Institute of Space Propulsion,
German Aerospace Center (DLR), Hardthausen, Germany

Grazia Lamanna
Institute of Aerospace Thermodynamics,
University of Stuttgart, Stuttgart, Germany

Journal: International Journal of Multiphase Flow

Volume: 130

Pages: 103360

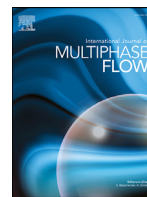
Author Contributions:

- Programming (100%)
- Data generation (50%)
- Scientific originality (30%)



Contents lists available at ScienceDirect

International Journal of Multiphase Flow

journal homepage: www.elsevier.com/locate/ijmulflow

Numerical and experimental analysis of flashing cryogenic nitrogen

Jan Wilhelm Gärtner^a, Andreas Kronenburg^{a,*}, Andreas Rees^b, Joachim Sender^b, Michael Oschwald^b, Grazia Lamanna^c^aInstitute for Combustion Technology, University of Stuttgart, Herdweg 51, Stuttgart 70174, Germany^bInstitute of Space Propulsion, German Aerospace Center (DLR), Langer Grund, Hardthausen 74239, Germany^cInstitute of Aerospace Thermodynamics, University of Stuttgart, Pfaffenwaldring 31, Stuttgart 70569, Germany

ARTICLE INFO

Article history:

Received 22 January 2020

Revised 18 May 2020

Accepted 25 May 2020

Available online 4 June 2020

Keywords:

Flash boiling

HRM Model

Spray structure

ABSTRACT

The development of new upper orbit thrusters using cryogenic propellants requires an improved understanding of the dynamics of oxidizer and fuel injection at near vacuum conditions before ignition. Due to the low ambient pressure, the propellants enter a superheated state and flash evaporation occurs. Flash boiling of cryogenic liquid nitrogen is studied experimentally on the newly developed test bench at DLR Lampoldshausen and numerically with a newly developed OpenFOAM© solver. Here, a one-fluid approach is selected where phase properties, such as density, enthalpy and saturation conditions are determined with the thermodynamic library CoolProp and tabulated before runtime. The phase change is modeled by the homogeneous relaxation model. For highly superheated jets the flow becomes supersonic and forms a shock after the injector outlet. The solver is validated with the aid of flashing acetone spray experiments where the shock structures are more clearly visible. The results show that the developed solver is capable to predict the all important gas dynamics by matching shock structure and spray angle to the experiment. The experiments using cryogenic liquid, however, do not reveal any shock structures but regions with low negative axial velocities can be identified on the jet centerline. A comparison with the simulations now demonstrates that shocks continue to persist but the respective shadowgraph signals may be obscured in these flows. The joint experimental and numerical study thus provides a consistent understanding of the observed flow features that govern the fluid dynamics and jet breakup of cryogenic flashing flows.

© 2020 Elsevier Ltd. All rights reserved.

1. Introduction

Novel developments of environmentally friendly orbital maneuvering systems aim at replacing conventional hypergolic propellants such as hydrazin and its derivatives with less harmful and operationally safer alternatives that include conventional fuels like hydrogen, methane and kerosene. One of the major characteristics for these engines is their intermittent use for in-space maneuvering procedures, and the future use of non-hypergolic conventional fuels requires a better understanding of the process of injection and ignition under the extreme conditions that prevail in space. The typically cryogenic propellant is injected prior to ignition into a near vacuum which leads to a superheated state of the fuel and a rapid and strong evaporation. This strong and nearly instant evaporation of the liquid is called flash evaporation or flash boiling. The flashing process presents a multi-scale problem of bubble nucleation in the range of nanometers, of bubble growth, breakup and

coalescence at a macroscale and lastly of evaporating droplets at a micrometer scale (Sher et al., 2008; Witlox et al., 2007).

These large ranges of length and time scales pose significant challenges for modeling and simulation. Resolving all scales for a simulation of the complete combustion chamber is currently not feasible at reasonable computational costs. Therefore, bubble nucleation, growth and the formed droplets are typically not resolved and they need to be modeled at the subgrid-scale. Once the droplets are formed, they constitute a dispersed phase. They are then simulated through an Euler-Lagrange approach in which the droplets are tracked as Lagrangian particles and the vapor is treated as a continuous phase on an Eulerian grid (Yeoh and Tu, 2010). However, prior to the spray breakup the liquid forms a continuous phase and a Lagrangian treatment of the liquid is less suitable. In this case, an alternative approach where the full set of conservation equations is solved for both phases and the phases are coupled through momentum exchange terms may be more feasible. This poses, the additional challenge of modeling the momentum exchange for the transition of a liquid jet to droplets. Assuming that the two phases are closely coupled and thus move at

* Corresponding author.

E-mail address: andreas.kronenburg@itv.uni-stuttgart.de (A. Kronenburg).

the same velocity allows for a simplified treatment, the so-called one-fluid approach, where only one set of conservation equations needs to be solved and the fluid properties are determined through an appropriate mixing rule. The different phases are then distinguished through a volume fraction. The reduction to one set of conservation equations assumes a zero slip velocity between the two phases and that both phases experience a common pressure and mixture temperature.

All approaches require modeling of the phase change. An early model to describe evaporation within the context of a one-fluid model is the homogeneous equilibrium model, which assumes liquid and vapor to be in thermal equilibrium (Bilicki and Kestin, 1990). For flashing flows, however, the fluid is certainly not in equilibrium and the liquid is in a metastable state. The homogeneous relaxation model (HRM) can capture these regimes as it relates the evaporation rate to the deviation of the vapor quality or mass fraction χ from its respective equilibrium value and a relaxation time Θ (Bilicki and Kestin, 1990). A description for the relaxation time can be found in the work of Zapolski et al. (Downar-Zapolski et al., 1996) in which it is fitted with empirical parameters to flashing water flow experiments.

The HRM model has been used by several authors to simulate flashing liquids for varying environmental conditions and technical applications. Schmidt et al. (2010) developed a one-fluid solver in OpenFOAM using the HRM model to predict the water discharge through short nozzles. This solver is then used in the work of Lee et al. (2009) to simulate flashing of JP8 jet fuel to predict the mass flow and estimate the potential of flashing on the spray breakup and mixing. Neroorkar et al. (2011) used the incompressible version of Schmidt et al.'s (Schmidt et al., 2010) OpenFOAM implementation to simulate the flashing of fuels in a swirl injector, comparing the spray angle to experiments. In the work of Lyras et al. (2017) the high pressure fit of the HRM model is used to compute the flow of cryogenic liquid nitrogen through sharp-edged orifices, showing that the model can capture the mass flow rate accurately. The HRM model has also been used successfully in the commercial code CONVERGE (Saha et al., 2016; Guo et al., 2019; Saha et al., 2017) to predict flashing for gasoline direct injection engines. Saha et al. (2017) estimated the effect of the HRM model coefficients on flashing gasoline and concluded that the default values give reasonable results for fluids other than water. Yet, the model parameters may need adjustment depending on the studied flashing regime. Independent of the specific values of the parameters, it is apparent that the HRM model is applicable for the prediction of the phase change of flashing liquids for varying conditions and fluids in a one-fluid modeling approach.

Another aspect of fully flashing jets is the existence of shocks and their effects on the flow. Shocks in flashing flows and their effects have been observed in retrograde fluids (Kurschat et al., 1992; Vieira and Simoes-Moriera, 2007) and more recently also in non-retrograde fluids (Lamanna et al., 2014; Mansour and Müller, 2019). Similar to underexpanded gaseous jets, the vapor generated by the flashing exits the injector at a much higher pressure than the far field value due to choking. This leads to a rapidly expanding flow outside the injector. Supersonic speeds are reached due to the concomitant increase of local flow velocities and the reduction of local speed of sound in a two phase mixture compared to the respective single phase values. The sonic velocity for a mixture can be surprisingly low, for example an air/water mixture at standard temperature and pressure has a sonic velocity of about 20 m/s compared to the individual pure phase sonic velocities of 300 m/s and 1500 m/s, respectively (Michaelides et al., 2017). If supersonic velocities are reached, the gas flow velocity is reduced downstream through a system of shocks. However, these shocks are difficult to measure through common shadowgraph methods and numerical methods can help to shed light on the existence and location

of shocks. Guo et al. (2019) used the commercial code CONVERGE and the HRM model to simulate flashing gasoline direct injection and detected a barrel shock and Mach disk. Yet, the shock size and position have not been validated by comparison with experimental results and the accuracy of the simulations is uncertain.

The present work introduces a new compressible solver based on the standard OpenFOAM solver compressibleInterFoam with some features integrated from interPhaseChangeFoam. It aims at validated predictions of the key hydrodynamic features of cryogenic liquid jets injected into combustion chambers under relevant conditions for orbital maneuvering systems. The key features include shock position and size that determine the liquid jets dispersion in the domain. A first validation includes a comparison with flashing acetone sprays (Lamanna et al., 2014) where the shock structures could easily be measured. For the predictions of cryogenic liquids, that are the primary focus of this work, the computational study is complemented by experiments at the DLR Lampoldshausen. Previous experiments of LOX flash boiling (De Rosa et al., 2006; Lamanna et al., 2015) revealed some operational limitations of the existing test bench in terms of control and adjustment of the injection temperature. Here, we present new data from a new cryogenic test bench (called M3.3) with a unique temperature controlled injection system that ensures cryogenic spray injection under high-altitude conditions at a desired and reproducible nozzle exit temperature. Three cases are investigated by shadowgraph images, and they provide the conditions for all our computations with cryogenic liquids.

2. Derivation of governing equations

The one-fluid approach uses the governing equations for mass, momentum and energy known from single phase flow with an additional transport equation for the volume fraction,

$$\frac{\partial \overline{\rho_L \tilde{\alpha}}}{\partial t} + \nabla \cdot (\overline{\rho_L \tilde{\alpha} \tilde{\mathbf{u}}}) + \nabla \cdot (\overline{\rho_L \alpha_L'' \mathbf{u}''}) = \tilde{m}_L, \quad (1)$$

$$\frac{\partial \overline{\rho \tilde{\mathbf{u}}}}{\partial t} + \nabla \cdot (\overline{\rho \tilde{\mathbf{u}} \tilde{\mathbf{u}}}) = -\nabla \tilde{p} + \overline{\rho} \mathbf{g} + \nabla \cdot \tilde{\boldsymbol{\tau}}_t, \quad (2)$$

$$\frac{\partial \overline{\rho e}}{\partial t} + \nabla \cdot (\overline{\rho e \tilde{\mathbf{u}}}) = \frac{\partial \tilde{p}}{\partial t} - \nabla \cdot (\tilde{k}_{\text{eff}} \nabla \tilde{T}) + \nabla \cdot (\tilde{\mathbf{u}} \cdot \tilde{\boldsymbol{\tau}}_t) + \tilde{S}_e, \quad (3)$$

with $e = h + \frac{1}{2} \mathbf{u}^2$ where $\alpha = V_L/V$, ρ , ρ_L , p , \mathbf{u} , $\boldsymbol{\tau}_t$, h , \mathbf{g} , S_e are the volume fraction, mixture density, liquid density, pressure, mixture velocity vector, turbulent viscous stress tensor, mixture enthalpy, gravity and energy source or sink terms, respectively. The term \tilde{m}_L denotes the mass exchange across the phase interface through evaporation. The fluid properties of the transported pseudo-fluid, such as the mixture density ρ , are obtained through volume averaging of the individual phase values. Subscripts 'L' and 'G' indicate liquid and gas phase properties, while no subscript refers to mixture properties. The overbar represents Reynolds averages of the density field while tildes and double prime superscripts denote Favre averages and fluctuations around these averages, respectively.

The turbulent contributions for the momentum and energy equation are included in the turbulent viscous stress $\boldsymbol{\tau}_t$ and turbulent conductivity k_t . For the transport of the volume fraction the additional term $\nabla \cdot (\overline{\rho_L \alpha_L'' \mathbf{u}''})$ is modeled with a gradient diffusion assumption,

$$-\nabla \cdot (\overline{\rho_L \alpha_L'' \mathbf{u}''}) = \overline{\rho_L} \nabla \cdot \left(\frac{\nu_t}{Sc_t} \nabla \tilde{\alpha}_L \right). \quad (4)$$

Here, ν_t is the turbulent viscosity and Sc_t the turbulent Schmidt number. In the following overbar and tilde will be omitted in the equations for better readability.

To account for compressibility effects, a compressibility $\psi = \frac{\partial \rho}{\partial p}$ is introduced and the density's dependence on pressure is expressed by a linear model, $\rho = \rho_0 + \psi p$. Inserting this expression into the volume fraction equation yields

$$\frac{\partial \alpha_L}{\partial t} + \frac{\alpha_L}{\rho_L} \left(\psi_L \frac{Dp}{Dt} + p \frac{D\psi_L}{Dt} \right) + \nabla \cdot (\alpha_L \mathbf{u}) = \nabla \cdot \left(\frac{\nu_t}{Sc_t} \nabla (\alpha_L) \right) + \frac{\dot{m}_L}{\rho_L}. \quad (5)$$

To include information of the second phase in the equation, the compressibility term is replaced by summing Eq. (5) over the two phases and using $\alpha_L = 1 - \alpha_G$. This gives,

$$\nabla \cdot \mathbf{u} + \frac{\psi_L}{\rho_L} \frac{Dp}{Dt} + \frac{p}{\rho_L} \frac{D\psi_L}{Dt} = \alpha_G \left(\frac{\psi_G}{\rho_G} - \frac{\psi_L}{\rho_L} \right) \frac{Dp}{Dt} - \alpha_G \left(\frac{p}{\rho_G} \frac{D\psi_G}{Dt} - \frac{p}{\rho_L} \frac{D\psi_L}{Dt} \right) - \dot{m}_L \frac{\rho_L - \rho_G}{\rho_L \rho_G}. \quad (6)$$

Inserting Eq. (6) into Eq. (5) gives the final volume fraction equation,

$$\begin{aligned} & \frac{\partial \alpha_L}{\partial t} + \nabla \cdot (\alpha_L \mathbf{u}) - \nabla \cdot \left(\frac{\mu_t}{Sc_t} \nabla \alpha \right) \\ &= \alpha_L \alpha_G \left[\left(\frac{\psi_G}{\rho_G} - \frac{\psi_L}{\rho_L} \right) \frac{Dp}{Dt} + \left(\frac{p}{\rho_G} \frac{D\psi_G}{Dt} - \frac{p}{\rho_L} \frac{D\psi_L}{Dt} \right) \right] \\ &+ \alpha_L \nabla \cdot (\mathbf{u}) + \frac{\dot{m}_L}{\rho_L} \left(1 + \alpha_L \left(\frac{\rho_L - \rho_G}{\rho_G} \right) \right). \end{aligned} \quad (7)$$

2.1. Pressure equation

The implementation of the governing equations is discussed in the context of an OpenFOAM implementation, where a pressure based approach is used to ensure conservation of mass. In the following, a suitable pressure equation is derived to include the compressible effects of a two phase flow. The general pressure equation is formulated as

$$\nabla \cdot \left(\frac{\nabla p}{a_p} \right) - \nabla \cdot \left(\frac{H(\mathbf{u})}{a_p} \right) = \frac{1}{\rho} \frac{D\rho}{Dt}, \quad (8)$$

where a_p represents the diagonal terms of the momentum equation and $H(\mathbf{u})$ the off-diagonal component. First, the total derivative of the density is introduced as in the work of Bilicki and Kestin (1990) where ρ is a function of the mass fraction $\chi = m_L/m$, pressure p , and enthalpy h (or temperature T),

$$\frac{D\rho}{Dt} = \underbrace{\left(\frac{\partial \rho}{\partial \chi} \right)_{p,T}}_{\text{evaporation}} \frac{D\chi}{Dt} + \underbrace{\left(\frac{\partial \rho}{\partial p} \right)_{\chi,T}}_{\text{compressibility}} \frac{Dp}{Dt} + \underbrace{\left(\frac{\partial \rho}{\partial T} \right)_{\chi,p}}_{\text{temperature}} \frac{DT}{Dt}. \quad (9)$$

The first term accounts for the effect of evaporation on the mixture density, the second considers the compressibility of the mixture density, and the last term modifies density due to changes in temperature. The compressibility of the mixture is expressed through (Brennen, 2005)

$$\frac{\partial \rho}{\partial p} = \sum_{i=1}^N (\rho_i \alpha_i) \sum_{i=1}^N \left(\frac{\alpha_i}{\rho_i} \left(\frac{\partial \rho}{\partial p} \right)_i \right). \quad (10)$$

In analogy to Eq. (10) the thermal expansion of the mixture is,

$$\frac{\partial \rho}{\partial T} = \sum_{i=1}^N (\rho_i \alpha_i) \sum_{i=1}^N \left(\frac{\alpha_i}{\rho_i} \left(\frac{\partial \rho}{\partial T} \right)_i \right). \quad (11)$$

Inserting the linear compressibility $\rho = \rho_0 + \psi p$ in Eq. (11) the effect of the temperature is expressed as,

$$\left(\frac{\partial \rho}{\partial T} \right) \frac{DT}{Dt} = \rho p \left[\frac{\alpha_L}{\rho_L} \frac{D\psi_L}{Dt} + \frac{\alpha_G}{\rho_G} \frac{D\psi_G}{Dt} \right]. \quad (12)$$

Combining Eq. (12) and Eq. (10) the final pressure equation is given by,

$$\nabla \cdot \left(\frac{\nabla p}{a_p} \right) - \nabla \cdot \left(\frac{H(\mathbf{u})}{a_p} \right) = \frac{1}{\rho} \left(\frac{\partial \rho}{\partial \chi} \right)_{p,T} \frac{D\chi}{Dt} + \frac{\alpha_L}{\rho_L} \frac{D\psi_L p}{Dt} + \frac{\alpha_G}{\rho_G} \frac{D\psi_G p}{Dt}. \quad (13)$$

This pressure equation differs from the compressible formulation of Schmidt et al. (2010) who have neglected the effect of changing temperature on the flow. This is, however, important if transonic behavior is to be approximated accurately.

2.2. Energy equation

In the one fluid approach, the energy of the mixture is represented by a common temperature T . This avoids a jump condition at the phase interface as it would be present for the enthalpy. Therefore, the energy conservation equation (Eq. (3)) can be rewritten for each phase as,

$$\begin{aligned} \alpha_L \rho \frac{DT}{Dt} + \frac{\alpha_L}{c_{p,L}} \rho \frac{DK}{Dt} &= \left(\frac{\partial p}{\partial t} + \nabla \cdot (k_L \nabla T) \right) \frac{\alpha_L}{c_{p,L}} \\ &+ \frac{\alpha_L}{c_{p,L}} \dot{m}_L h_G - \frac{\rho}{\rho_L c_{p,L}} \dot{m}_L h_L \end{aligned} \quad (14)$$

and

$$\alpha_G \rho \frac{DT}{Dt} + \frac{\alpha_G}{c_{p,G}} \rho \frac{DK}{Dt} = \left(\frac{\partial p}{\partial t} + \nabla \cdot (k_G \nabla T) \right) \frac{\alpha_G}{c_{p,G}} - \frac{\alpha_G}{c_{p,G}} \dot{m}_G h_G, \quad (15)$$

where K represents the kinetic energy. The mechanical work and the thermal diffusion are distributed to the phases in proportion to their mass fractions. Further, the source term of Eq. (3) was replaced by,

$$S_{e,L} = -S_{e,G} = \frac{\alpha_L \rho_L}{\rho} \dot{m}_L h_G. \quad (16)$$

Here, it is also assumed that the energy required for the phase change is drawn from both phases weighted by their respective mass fraction. Combining Eqs. (14) and (15) gives the final energy equation,

$$\begin{aligned} \rho \frac{DT}{Dt} + \left(\frac{\alpha_L}{c_{p,L}} + \frac{\alpha_G}{c_{p,G}} \right) \left(\rho \frac{DK}{Dt} - \frac{\partial p}{\partial t} \right) \\ = (\alpha_L \nabla \cdot (\gamma_{\text{eff,L}} \nabla T) + \alpha_G \nabla \cdot (\gamma_{\text{eff,G}} \nabla T)) \\ - \frac{\rho}{\rho_L c_{p,L}} \dot{m}_L h_L + \dot{m}_L h_G \left(\frac{\alpha_L}{c_{p,L}} + \frac{\alpha_G}{c_{p,G}} \right), \end{aligned} \quad (17)$$

with γ_{eff} being the effective thermal conductivity divided by the heat capacity, $\gamma_{\text{eff}} = (k + k_t)/c_p$.

The use of Eq. (17) provides the standard procedure for flashing flows using the one-fluid approach, but the assumption of one common temperature for the liquid and vapor phase may not be a suitable choice. Assuming the vapor is generated at saturation conditions of the surrounding pressure, the saturation temperature is much lower than the liquid temperature. Thus, two separate phase temperatures instead of one mixture temperature may be more adequate. Here, we therefore test an alternative modeling approach where the energy equations for the liquid and the vapor phases are not combined. They are solved independently and are coupled with each other through the energy source terms. As the energy equation of each phase is solved separately the advantage of using temperature instead of enthalpy ceases to exist (see above) and the enthalpy equations are solved directly,

$$\rho \frac{Dh_L}{Dt} + \rho \frac{DK}{Dt} = \left(\frac{\partial p}{\partial t} + \nabla \cdot (k_L \nabla T_L) \right) + \frac{\rho}{\rho_L \alpha_L} \dot{m}_L (h_{SG}(p) - h_L) \quad (18)$$

and

$$\rho \frac{Dh_G}{Dt} + \rho \frac{DK}{Dt} = \left(\frac{\partial p}{\partial t} + \nabla \cdot (k_G \nabla T_G) \right) + \frac{\rho}{\rho_G \alpha_G} \dot{m}_L (h_G - h_{SG}(p)). \quad (19)$$

The derivation for these equations is given in Appendix A.

2.3. HRM Model

The mass transfer, \dot{m}_L , is modeled with the homogeneous relaxation model (HRM), which has been originally developed by Downar-Zapolski et al. (1996). This empirical model describes the change of mass fraction χ as being proportional to the difference between the local and the equilibrium conditions as well as a relaxation time Θ , which depends on the pressure difference and the volume fraction,

$$\Theta = \Theta_0 \left(\frac{\rho_L - \rho}{\rho_L - \rho_v} \right)^\beta \left(\frac{p_s(T) - p}{p_c - p_s(T)} \right)^\lambda. \quad (20)$$

Here, $\Theta_0 = 3.84 \times 10^{-7}$ s, $\beta = -0.54$, $\lambda = -1.76$ and p_c is the critical pressure of the fluid. The exponents are empirical values determined by comparison of simulations with flashing water experiments (Downar-Zapolski et al., 1996). There, the mass fraction was based on the vapor mass. Here, the mass fraction is based on the liquid mass χ , as defined above, and not on the vapor mass which requires a modification of the expression for the equilibrium mass fraction,

$$\bar{\chi} = \frac{h - h_{SG}(p)}{h_{SL}(p) - h_{SG}(p)}. \quad (21)$$

where h is the mixture enthalpy, $h = \chi h_L(p, T) + (1 - \chi) h_{SG}(p)$, $h_{SL}(p)$ is the saturation enthalpy of the liquid and $h_{SG}(p)$ the saturation enthalpy of the vapor for the given pressure p . With these definitions (Eqs. (20) and (21)) the homogeneous relaxation model is given by

$$\frac{D\chi}{Dt} = -\chi \frac{h_L(p, T) - h_{SL}(p)}{h_{SG}(p) - h_{SL}(p)} \frac{1}{\Theta} = \frac{\dot{m}_L}{\rho}. \quad (22)$$

Note, that \dot{m}_L has the units kg/(s. m³) which corresponds to a conventional notation for a finite volume approach.

The enthalpy difference is the driving force for flash-boiling and we therefore modify here the definition of the Jakob number,

$$Ja = \frac{h_L(p, T) - h_{SL}(p)}{h_{SG}(p) - h_{SL}(p)}, \quad (23)$$

the homogeneous relaxation model can be rewritten as,

$$\frac{D\chi}{Dt} = -\chi Ja \frac{1}{\Theta}, \quad (24)$$

with Ja indicating the evaporation potential of the liquid. A second characteristic number is the superheat commonly defined as the pressure ratio $R_p = p_{sat}/p$. The superheat is used to describe flashing flows and to characterize the strength of the evaporation. Thus, a higher value indicates a more rapid evaporation process. To show the effect of R_p on the relaxation time in Eq. (20) more clearly, $p_{sat} \ll p_c$ is assumed for simplicity. Then the relaxation time can be expressed as,

$$\Theta = \Theta_0 \left(\frac{\rho_L - \rho}{\rho_L - \rho_v} \right)^{-0.54} \left(\frac{p R_p}{p_c} \right)^{-1.76}, \quad (25)$$

and it is now apparent that a higher superheat leads to a reduction of the relaxation time and thus to a more rapid and stronger evaporation predicted by the HRM model.

3. Validation with acetone sprays

The validation of the compressible solver requires experiments, where shock structures are clearly visible and where unambiguous measurements of the location of the shock exist. These conditions are given in the experiments by Lamanna et al. (2014), who conducted a series of acetone spray experiments under flashing and transient conditions. The experimental setup consists of a diesel injector with a diameter of 150 μ m and an aspect ratio $L/D = 6$. The

Table 1

Boundary value of the acetone jet case.

Case	T_{inj} [K]	T_∞ [K]	R_p [-]	Ja [-]
Ac-1	311	293	8.7	0.17
Ac-2	327	293	15.4	0.23
Ac-3	343	293	26.1	0.30
Ac-4	350	293	32.3	0.32
Ac-5	373	293	61.0	0.42

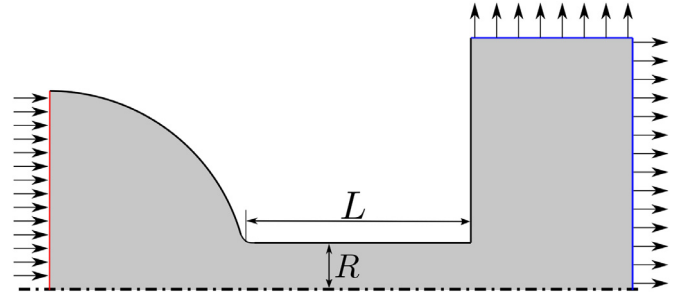


Fig. 1. Computational domain of the acetone spray.

acetone is injected with an injection pressure of 10 bar at varying temperatures, such that the liquid reaches superheated conditions for the outlet pressure of 60.8 m bar. In the following, 5 cases with varying inlet temperatures are examined as is detailed in Table 1.

Fig. 1 shows a sketch of the computational two-dimensional wedge domain. The domain is meshed with 300 000 structured hexahedron cells with a cell size of 2.5 μ m at the injector outlet. A coarser mesh of 135000 cells has also been used for grid independence studies. Prediction of velocity, mass fraction and temperature are insensitive to the spatial resolution, however, the curvature of the shock is somewhat underresolved on the coarse mesh, as is evidenced by small velocity fluctuations. Differences are limited to the shock front and as the spurious disturbances disappear for the fine mesh, only these results are reported here. The boundaries are placed sufficiently far away from the injector outlet and inlet such that there are no direct effects of the boundary on the flow. At the inlet the boundary value of the volume fraction is set to 0.999 to represent nucleation sites in the liquid for the HRM model. A value smaller than unity is needed as Θ tends to infinity for $\alpha = 1$, but the exact value (values for $\alpha \in [0.999, (1 - 10^{-15})]$ were tested) is of no importance as all results reported here are insensitive to the exact initialization of α . The pressure uses a total pressure boundary condition for the inlet and the non-reflective wave transmissive boundary condition at the outlet. As the Y^+ value ranges from 1 to 6 a wall function based on the Spalding's law is used to model the wall flow. Variation of Y^+ has shown no significant influence on the solution, indicating that the wall model is applicable for this case.

The required fluid properties such as density, viscosity or enthalpy are calculated with the thermodynamic library CoolProp (Bell et al., 2014) before the simulation and are stored in lookup tables. During run time the required properties are taken from the table and intermediate values are obtained through linear interpolation. This replaces the equation of state implementations in OpenFOAM to allow for correct calculation of metastable conditions at an acceptable computational cost. For the divergence schemes the normalized variable diminishing scheme MUSCL is used except for the volume fraction transport which uses the van-Leer TVD scheme. Additionally, all gradients use the cell limited scheme. The residual is set to 1×10^{-9} and convergence of the outer loop is achieved for an initial residual of 1×10^{-3} . For the PIMPLE loop 3 PISO iterations are used and convergence is typically reached after 4 to 5 outer iterations. The turbulence is modeled

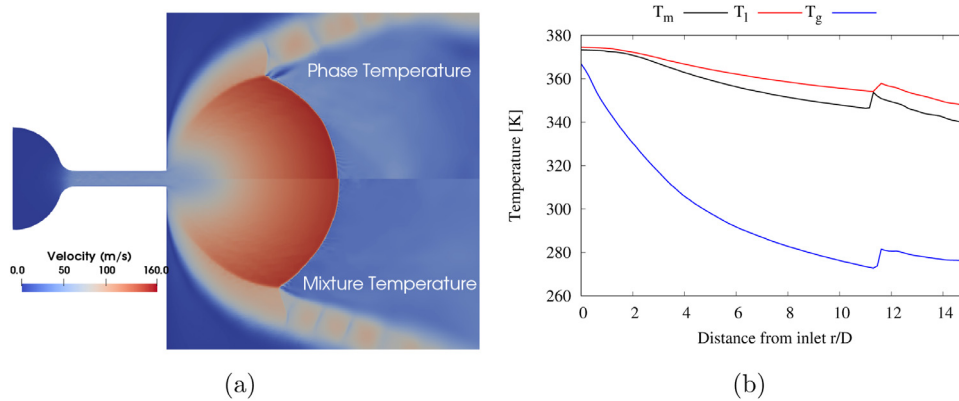


Fig. 2. Comparison of the mixture temperature approach with solving the phase temperatures individually for acetone case Ac-5. Figure (a) shows the velocity profile for the two cases and (b) the temperature profiles along the centerline axis with T_m as the mixture, T_l liquid and T_g vapor temperature.

with the $k-\omega$ SST model, which is suitable for adverse pressure gradients present at the wall after the injector exit. To guarantee the stability of the implicit-explicit MULES solver used for the volume fraction transport, the maximum Courant number is set to 0.9.

3.1. Effect of using a mixture temperature

In Section 2 it is hypothesized that the use of a single mixture temperature for flashing flows may not be the best modeling choice. To test the effect of this assumption on the solution, case Ac-5 is simulated using the mixture temperature assumption (standard approach) as well as solving the energy for each phase separately (alternative approach). Fig. 2(a) compares the velocity for the two approaches. It shows that both models give similar results for the velocity field, despite large differences in the vapor and liquid temperature, as seen in Fig. 2(b). Further, and with the exception of the pure gas phase values such as the density, all model parameters depend on the liquid temperature only. This explains why the difference in the simulation results for the overall spray angle and velocity are not significant. Yet, the additional computational effort is very moderate and solving the two energy equations independently is advised to get more correct values for the liquid and gas properties. Therefore, all following simulations are carried out using the alternative approach (Eqs. (18) and (19)).

The velocity fluctuations leading to a regular, cellular structure in periphery of the jet resemble Mach-diamonds in over-expanding jets. When a flow is over-expanded, the gas pressure within the wake is lower than that of the ambient which causes compression of the flow. The compression can then result in a pressure increase above that of the ambient in the subsonic stream. Now, the flow expands again and accelerates to reduce the pressure. The fluid may yet again overexpand reaching a pressure level below the ambient conditions. The difference between the internal and external pressures reduces each time the flow passes through one of these compression/expansion processes. The process repeats itself until the pressure of the supersonic flow equals the pressure of the subsonic environment resulting in the cellular structure observed in Fig. 2(a).

3.2. Results for model validation

For the validation of the solver with the acetone spray the spray angle and lateral shock expansion are examined. In the work of Lamanna et al. (2014) a correlation for the spray parameters and the lateral expansion of the shock wave is given by,

$$\log\left(\frac{R}{D}\right) = 0.2755 \log(X) - 0.3087 \quad (26)$$

with

$$X = \frac{p_{\text{sat}}(T_{\text{inj}})}{p_c} \left(\frac{p_{\text{inj}}}{p_{\infty}}\right)^2 \frac{L}{D}. \quad (27)$$

The spray angle β is calculated by

$$\tan\left(\frac{\beta(x)}{2}\right) = \frac{y(x)}{\Delta x}, \quad (28)$$

where x is the distance to the injector exit and $y(x)$ the radial distance of the spray from the centerline. This definition reflects the fact that, in flash-boiling experiments, the spray cone angle has not a unique value, but it varies along the spray axis. In the simulation the edge of the spray is determined through the Laplacian of the mixture density, $\nabla \cdot (\nabla \rho)$. This value is chosen since a shadowgraph method measures the Laplacian of the refractive index which is proportional to the density integrated along the line of sight (Panigrahi and Muralidhar, 2012). As only 2D simulations are performed the integration is omitted.

Fig. 3 shows the Mach Number and the Laplacian of mixture density (left) and for comparison the experimental image with an overlaid Mach number isoline of $Ma=1$ (right) of case Ac-5. The lateral expansion of the shock wave is marked by the green line in Fig. 3(a). In Fig. 3(a) two barrel shocks and a bow shock are visible. After the first barrel shock the flow is still supersonic and at a lower pressure than the far field value of the vacuum chamber. This leads to the second barrel shock over which the flow decelerates to subsonic velocity and matches the far field pressure. Since the bow shock is normal to the flow velocity the flow directly transitions from the supersonic conditions upstream to subsonic flow downstream. As a consequence a subsonic region with low velocity is enclosed by a supersonic flow with a higher velocity. Further, the isoline shows a nearly perfect agreement of the bow shock in the shadowgraph image. In addition the shock outline matches with the spray contour. Fig. 4 shows the normalized shock wave expansion for cases Ac-2 to Ac-5 alongside the correlation of Eq. (26) and the experimental results marked by green triangles. Case Ac-1 is excluded in this analysis as the superheat is too low to form a visible shock system and an unambiguous comparison for model validation would not be possible. The results show good agreement between the experimental and simulation data. Case Ac-2 deviates most from the given correlation function. Note that its X value obtained from Eq. (27) is also below the lowest measured value and that the closest experimentally measured value shows a similar deviation from the correlation function. The results match the trends seen in the experiments, indicating that the linear correlation may not hold for these low pressure ratios. With these results it can be concluded that the solver can accurately capture transonic behavior of the fully flashing flow.

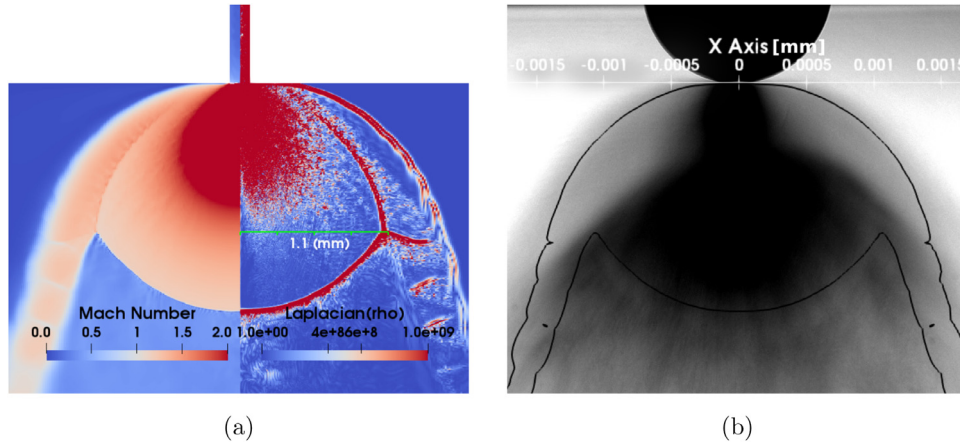


Fig. 3. Simulation results of case Ac-5 showing the Laplacian of the mixture density and Mach Number in (a). The experimental shadowgraph image is overlaid with the isolate for $Ma = 1$ of the simulation in (b).

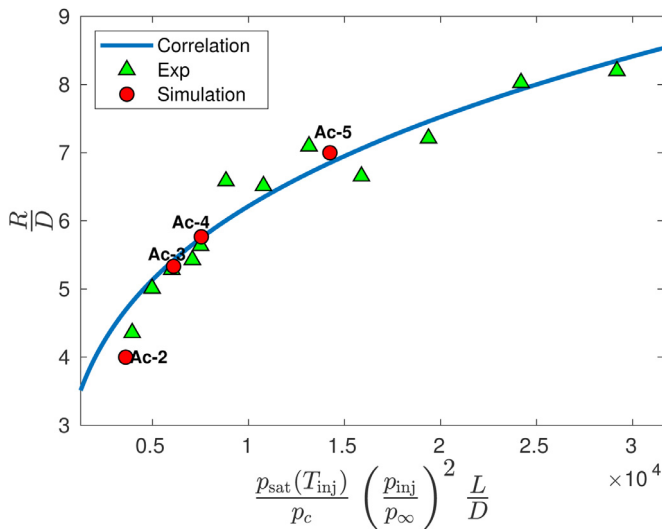


Fig. 4. Normalized lateral expansion of the shock wave versus the inlet conditions. The experimental results are marked with green triangles and the simulation data by red circles. The cases are denoted with Ac-2, Ac-3, etc. Experimental values and correlation is taken from Lamanna et al. (2014). (For interpretation of the references to colour in this figure legend, the reader is referred to the web version of this article.)

In Fig. 5 the shadowgraph image of the experiment is combined with a contour plot of the predicted mass fraction. In cases Ac-1 and Ac-2 a liquid core can be seen in the shadowgraph image. This region at the centerline of the jet indicates that nucleation and bubble growth at the injector wall is dominating over the nucleation in the center of the jet. When the liquid jet then exits the injector the core stays intact and the bubbles at the jet exterior burst (Park and Lee, 1994). This behavior of an intact liquid core with heterogeneous nucleation and bubble growth at the injector wall and at the exterior liquid-vapour interface of the jet cannot be captured with the homogeneous nucleation and evaporation assumptions used for the HRM model. For cases Ac-3 to Ac-5 with a higher superheat such a liquid core is not present and the expansion of the jet compared to the simulation improves, as now the assumption of homogeneous nucleation and evaporation becomes valid. A comparison of the spray angle shows that the HRM overpredicts the spray angles for cases Ac-1 and Ac-2, if the liquid core is taken as a measure, while for cases Ac-4 and Ac-5 the predicted expansion matches the measurements. This result is

consistent with the notion of the predominance of homogeneous nucleation for the latter cases. Still, the expected trend of a sharp rise in spray angle for the transition of the onset of flashing to fully flashing is represented with the simulation results as well. Here it shall be noted that the slight discrepancy in the angle of cases Ac-4 and Ac-5 are not surprising given the uncertainty in the modeling of non-equilibrium flash-boiling. For example, a slight difference in the calculation of the vapor fraction leads to a different exit Mach number (and pressure ratio), which changes the gas dynamics of the under-expanded jets. Furthermore, sharp corners at the nozzle exit can act as additional loci of heterogeneous nucleation, leading to a finer distribution of droplets surrounding the main jet core.

From these results we can conclude that the solver's capability to accurately approximate compressibility under flashing conditions is validated and can now be applied to predict flash boiling of cryogenic liquids.

4. Investigation of flashing cryogenic nitrogen

To investigate flashing of cryogenic liquids the numerical approach introduced in Section 3 is now adapted to the test bench conditions and complemented by the analysis of novel experiments conducted at DLR Lampoldshausen. For the first test campaigns cryogenic liquid nitrogen is chosen as test fluid as the use of liquid oxygen poses additional safety risks. Note that similar trends are expected for liquid oxygen and nitrogen since their fluid properties are close.

4.1. Experimental setup

The newly designed test bench M3.3 consists of three main systems, as depicted in Fig. 6: the media supply and pressurization system, the cryogenic temperature adjustment and injection system (CTAIS) and the vacuum system. The CTAIS consists of a double-walled and vacuum-insulated pressure tank filled with liquid and gaseous nitrogen (GN2), see Figs. 6(a) and 6(c). By an evacuation or pressurization of the GN2 phase in the pressure tank the fluid is cooled down or heated up, respectively. Inside the pressure tank is the complete feed and injection system with the test fluid, liquid nitrogen (LN2), which consists of a 0.5 l run-tank, a coriolis mass flowmeter upstream of the injector, the injector unit with a pneumatic run valve and the injector nozzle, see Fig. 6(b). That means that all these sub-systems are completely surrounded by the cooling medium nitrogen to provide a homogeneous temperature distribution from the run-tank to the injector nozzle. To provide the injection parameters a Pt100A temperature sensor and

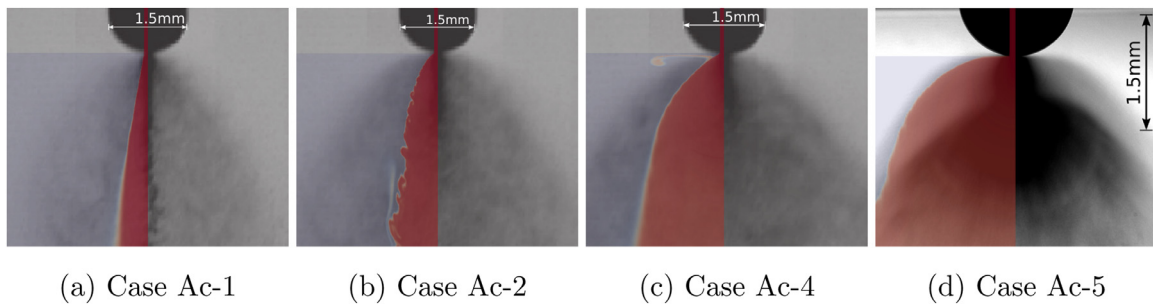


Fig. 5. Overlay of shadowgraph images and the mass fraction for flashing acetone. The superheat ratio increases from left to right. Equally, the homogeneous nucleation rate increases and with it the validity of the HRM model..

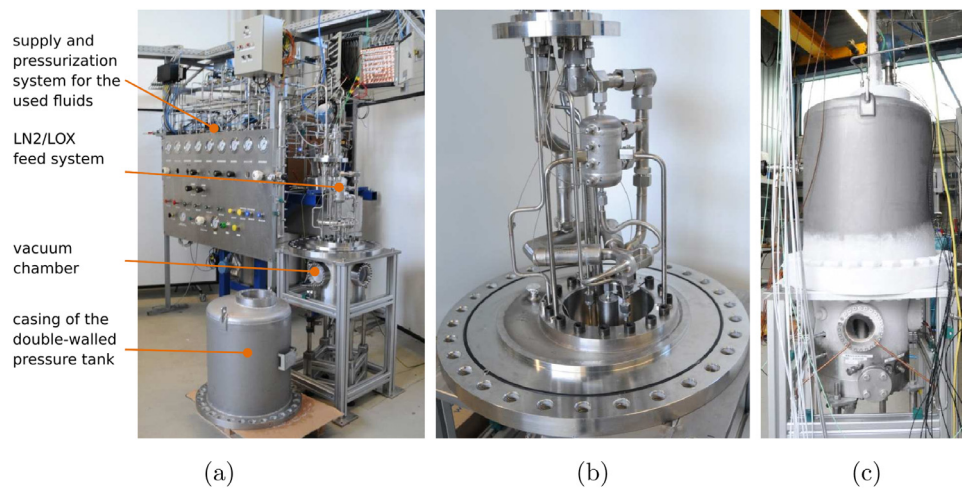


Fig. 6. Test bench M3.3 with supply and pressurization system, open CTAIS and vacuum system (a); open CTAIS with run tank, pneumatic run valve, injector unit and sensors in-between (b); chilled-down test bench M3.3 in operation mode (c).

Table 2

Components of optical shadowgraph set-up.

Component	Manufacturer	Type
Xenon light source	Müller Elektrik & Optik	SVX 1450 & LAX 1450
Camera lens	Tamron	A061 AF28-300mm
Camera	Photron	Fastcam SA-X

a dynamic pressure sensor 601A by Kistler are each installed about 30 mm upstream of the injector nozzle exit. In this study a single injector with a diameter of $D_{inj} = 1\text{ mm}$ and a length-to-diameter ratio $L/D = 2,9$ was used.

In the first run-in, tests it was shown that the system is capable of keeping the injection temperature T_{inj} constant during the whole injection time of about 2 s, that the injection temperature is reproducible in the range of $\pm 0,6\text{ K}$ for each test run and that the temperature distribution is homogeneous in the whole test fluid feed line. A more detailed description of the test bench M3.3 can be found in the studies of Rees et al. (2019a,b).

4.1.1. High-speed shadowgraph

To visualize the injected LN2 sprays the optical technique of backlight shadowgraph is used by illuminating the sprays through one of the four optical accesses of the vacuum chamber. As can be seen in Fig. 7 the high-speed camera, which was set to 10000 fps with a frame size of 1024×1024 pixels and an exposure time of $97\ \mu\text{s}$, is positioned at the opposite optical access of the chamber. The focus of the lens is set to the plane of symmetry of the injector at atmospheric conditions before starting the chill-down of the test bench. Further details of the optical setup are listed in Table 2.

4.2. Experimental results

Some flow "anomalies" are observed in the experiments shown in Fig. 8. They are highlighted by the yellow boxes at a constant position in the four shadowgraph frames. Each frame belongs to the same fully flashing liquid nitrogen spray, the sequence is taken with a time step of 0,1 ms. The spray has an injection temperature of $T_{inj} = 90,5\text{ K}$, an injection pressure of $p_{inj} = 5,5 \times 10^5\text{ Pa}$ and a degree of superheat $R_p = 69$. Video analysis shows that the dark structure close to the upper edge of the yellow box is nearly motionless or is even slightly floating towards the injector. These regions indicate the presence of a recirculation. The shadowgraph images alone do not provide proof of its existence, but additional PDA measurements were reported in Rees et al. (2019a). These measurements demonstrated - for the first time - the existence of negative velocities in cryogenic flash-boiling sprays and include some preliminary analysis of the most likely droplet sizes and their correlation with velocities. An explanation why negative velocities occur can be based on the isooctane and acetone experiments presented in Lamanna et al. (see Figs. 14 and 15 in Lamanna et al. (2014)). They observed shocks and behind the Mach disk, a recirculation zone is created. This leads to the attainment of high local supersaturated conditions and hence to the re-condensation of the fuel. As pointed out in Lamanna et al. (2014), at near vacuum conditions, the amount of refraction caused by the shock structure is generally weak and requires extremely long exposure times to be detectable by standard CCD cameras. This is the reason why the shock structure is not visible in the LN2 shadowgrams due to the selected frame rate and short exposure.

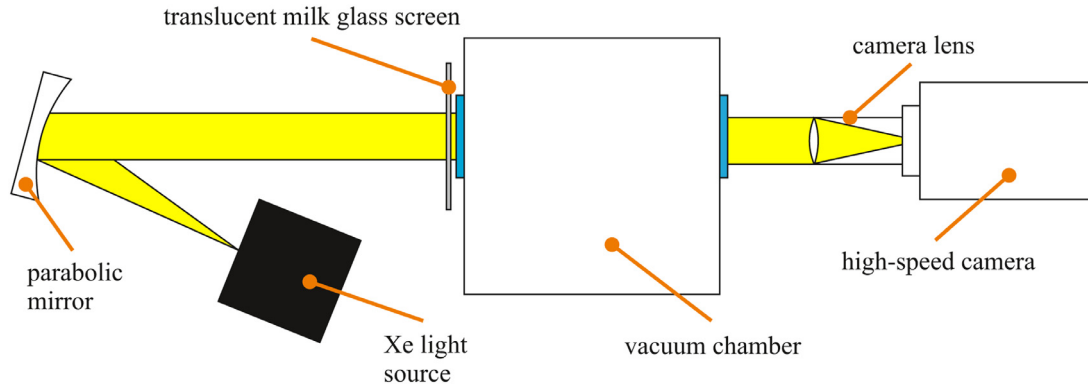


Fig. 7. Scheme of the optical set-up for high-speed backlight shadowgraph at test bench M3.3.

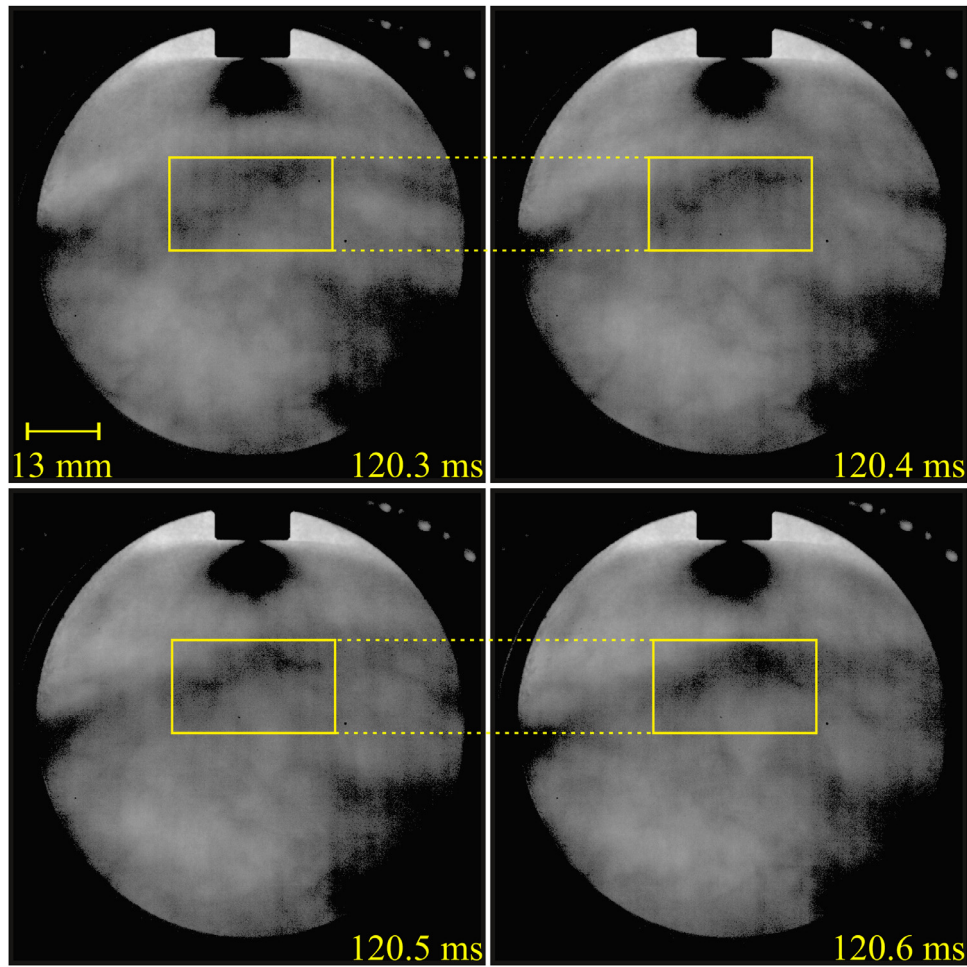


Fig. 8. Fully flashing LN2 spray at different times after injection start at $T_{inj} = 90,5 \text{ K}$, $p_{inj} = 5,5 \times 10^5 \text{ Pa}$ and $D_{inj} = 1,0 \text{ mm}$.

Table 3
Boundary values for the cryogenic nitrogen jet.

Case	T_{inj} [K]	p_{inj} [Bar]	R_p [-]	Ja [-]
LN2-1	82.3	8.1	11.7	0.17
LN2-2	89.7	4.4	48.1	0.25*
LN2-3	95.6	6.2	188.6	0.31*

To corroborate whether a similar phenomenology is also responsible for a possible recirculation in cryogenic flash-boiling sprays, the three cases selected in Table 3 are examined. For the

cases LN2-2 and LN2-3 the pressure inside the test chamber is below the triple point value ($p_t = 126 \text{ mBar}$). This, does not necessarily imply that the liquid instantly freezes but it may stay in a superheated state and continue to evaporate until the droplet interface temperature drops below the sublimation line and the droplet freezes. Yet, whether this case appears depends on the initial liquid temperature and residence time of the droplet in the observation window. Independent of the occurrence of freezing, these pressure conditions require minor adaptations of the numerical approach: such low pressure conditions do not allow for direct evaluation of the Jakob number needed for the HRM model, since no satura-

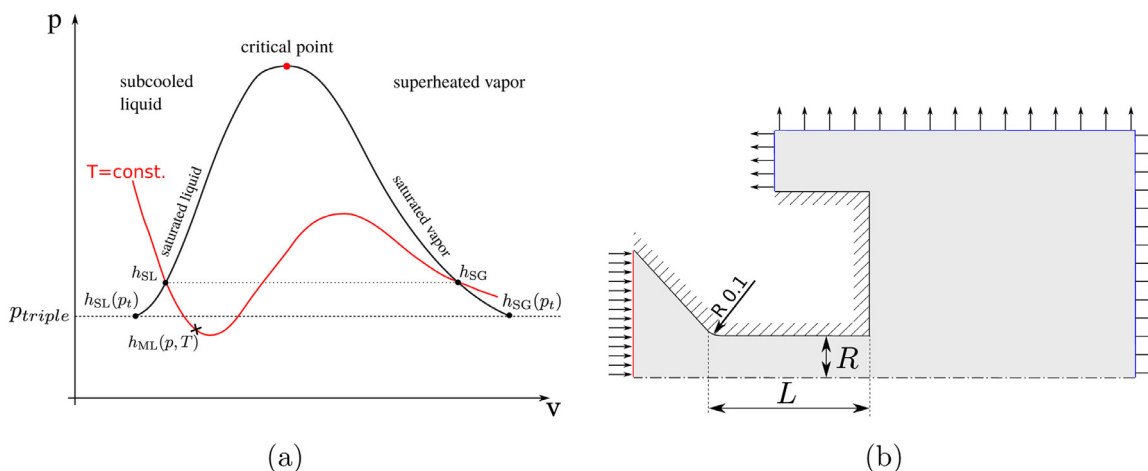


Fig. 9. Sketch of P-V diagram for the case of superheated liquid below the triple point (a) and sketch of the computational 2D wedge domain of the injector as well as vacuum chamber for the cryogenic LN2 spray (b).

tion enthalpy values can be calculated for pressure below the triple point.

As the temperature and pressure at the droplet interface are unknown two bounding cases for the saturation conditions can be formulated. The first limiting case is given by vapor being generated at the saturation condition of the bulk liquid temperature ($T_L > T_L^s$). The second limiting case is given by the pressure limit, thus the vapor is generated at saturation conditions of the triple point pressure. These bounding conditions are depicted in Fig. 9(a). To avoid any inconsistencies of the HRM model between cells slightly above and below the triple point the pressure limit is chosen here and the saturation values are determined at the triple point pressure, thus $h_{SL}(p < p_t)$ becomes $h_{SL}(p_t)$. This is also used to compute the Jakob number in Table 3.

4.3. Simulation setup

Fig. 9(b) shows the computational 2D wedge domain for the nitrogen spray. A structured hexahedron mesh is used with 931 000 cells and a cell size of $10 \mu\text{m}$ at the injector outlet. The numerical settings are the same as for the acetone case, with the exception that the TVD limited linear scheme is used. This scheme is used as the MUSCL scheme leads to numerical instabilities for case LN2-2 at the shock front.

4.4. Simulation results of the velocity field

Fig. 10 shows the velocity fields for the three test cases. Similar to the acetone spray a shock front is visible shortly after the injector exit. In addition to the shock, a region of low velocity can be examined about 20D to 30D downstream of the injector. This region is a result of the low velocity after the shock interacting with the high velocity stream at the edge of the jet. Due to this shear layer, a recirculation zone is formed. The bottom row of Fig. 10 shows the shadowgraph images of the three cases. The observed motionless region is marked with a yellow square for the cases LN2-2 and LN2-3. A comparison with the velocity contour from the simulation shows that the dark regions in the shadowgraph match with the recirculation zones in the simulation. This is also visualized for case LN2-3 by velocity vectors in Fig. 11. Here, the vectors represent the flow direction but not the magnitude of the velocity. We can now conclude with the help of our corresponding computer simulations that a shock must be present even though the measurements do not give direct evidence of its existence. The shock is hidden in the shadowgraph images, but the

observed motionless, dark regions further downstream provide, in conjunction with the simulations, a consistent understanding of the fluid dynamics of the LN2 flashing jets. It is also noted here that the experiments indicate some low frequency pulsation. This is also observed in the computations where the recirculation zone eventually collapses and re-establishes itself. As the frequency is low such a collapse is observed but a quantitative analysis of the dynamics is - due to excessive run times - difficult to achieve and beyond the scope of the paper.

4.5. Comparison of the mass flow rates

Additional to the shadowgraph images the computed mass flow rates are compared with the experiment. The mass flow rates are determined by the injection pressure and the evaporation within the injector. They are not imposed as inflow velocities at the boundaries but result from the computations and can therefore be used as an additional quantity to validate the HRM model. Fig. 12 shows the measured mass flow rates for the experiments and simulations. As we solve a transport equation for the volume fraction and not for total mass, the solver is not strictly mass conserving and an error shall be estimated. To determine this error the mass fluxes through the inlet and through two planes, one within the injector and one within the flashing chamber, are calculated for LN2-3. The mass flux error is always below 3% and shall be understood as an instantaneous maximum. The average value is difficult to determine as the flow does not reach a truly stationary state. Independent of the exact value, however, these small mass deficiencies are not expected to unduly affect any of the dynamics associated with the thermodynamics of flash-boiling that drive jet expansion, and the qualitative expansion characteristics reported here will not change. For case LN2-1 with the lowest superheat the mass flow of the simulation is too large compared with the experiment which suggests that the modeled evaporation of the liquid nitrogen is not strong enough. As the jet spreading is also too small it is possible that the standard HRM model constants are not suitable for this case and need adjustment. For the latter two cases the mass flow rates of the experiments and simulations match within the measurement uncertainty of about 1.8 g/s. For these two cases it is noted that, despite the large difference of the injection pressure, the mass flow rates predicted by the simulations are quite similar. This can be explained by taking the pressure difference (Δp) between the injection pressure p_{inj} and the saturation pressure $p_{sat}(T_{inj})$ which is for the two cases 887 m bar and 542 m bar, respectively. Noting that the pressure difference for case LN2-3 is

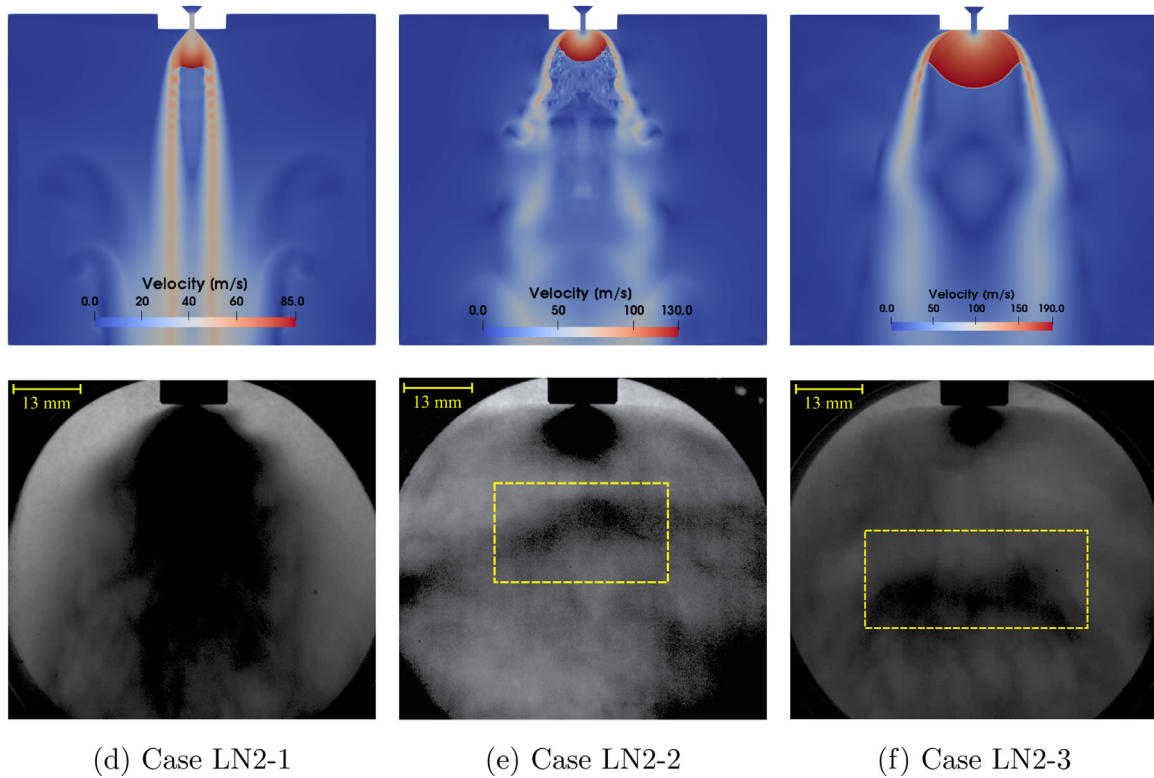


Fig. 10. Velocity contour plot of the nitrogen spray compared to the shadowgraph images.

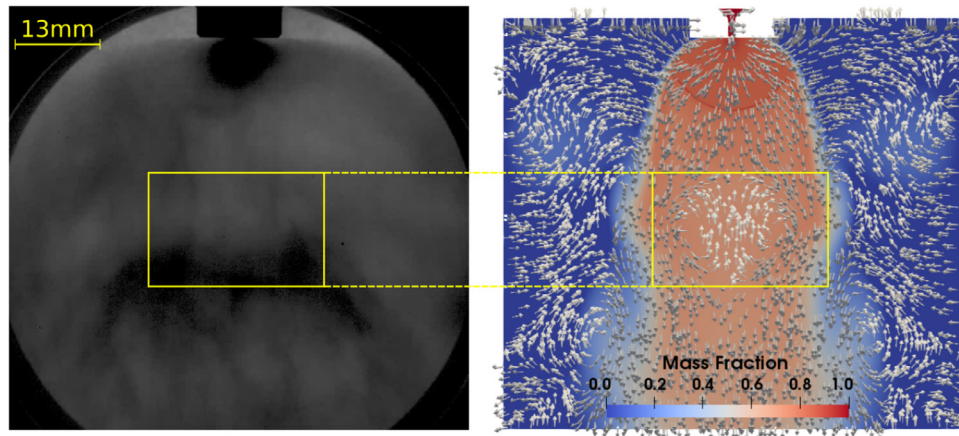


Fig. 11. Shadowgraph image of case LN2-3 compared to the mass fraction field and the velocity vectors. The position of the recirculation zone seen in the simulation is marked through the yellow box. (For interpretation of the references to colour in this figure legend, the reader is referred to the web version of this article.)

actually smaller than that for case LN2-2 and using $\dot{m} \propto \sqrt{\Delta p}$ the smaller mass flux can be explained. The experiments show different trends. This can be attributed to the experimental uncertainties, as exact flow rates are difficult to measure. Further interpretation of the differences may be futile as the computed results are within this uncertainty range. Lastly, a qualitative comparison of shadowgraph and simulation shows that the initial 180° spray angle does not persist to the edges of the domain and that the overall spray spreading is larger in the experiment than in the simulation. To this point the default model coefficients of the HRM model as reported by Downar-Zapolski et al. (1996) have been used. However, it is reasonable to assume that the model constants may need adjustment, which is a common procedure in the literature (Guo et al., 2019) since the water experiments may not represent the flashing characteristics of all other fluids sufficiently well.

4.6. HRM Model coefficients

As the spreading of the jet is underpredicted in the simulations an increase of the modeled evaporation mass flux \dot{m}_l may lead to improvements. This increase can be achieved by a decrease of the relaxation time Θ and is tested for case LN2-3 (see Eq. (22)). Firstly, the constant Θ_0 is modified which can be seen as a shift of the phase change function. We reduced its value by more than one order of magnitude to $\Theta_0 = 1.0 \times 10^{-9}$ s. This specific value is chosen here to provide a significant change of the model parameter, but it is noted that Guo et al. (2019) used the same value to simulate flashing behavior of diesel injectors. Further, the exponent of the superheat, λ , is adjusted from -1.76 to -1.0 as this parameter represents the local thermodynamic conditions and the physical properties of the fuel (Saha et al., 2017). Fig. 13 shows a

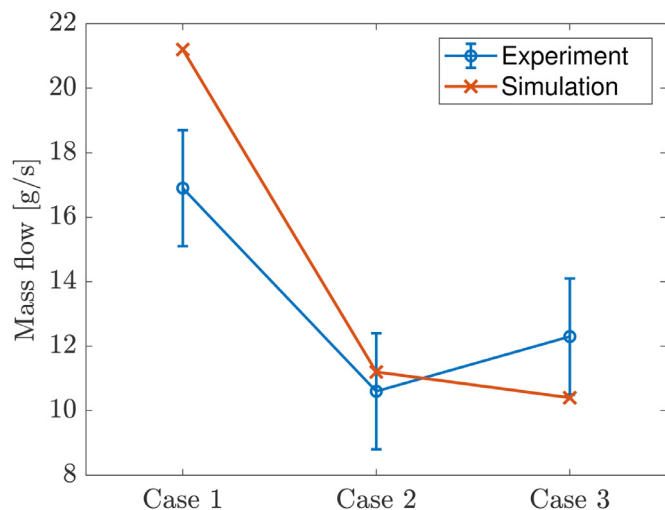


Fig. 12. Comparison of mass flow of the experiment and simulation for liquid nitrogen. Measurement uncertainties are marked by the error bars.

comparison of the velocity contours for the original model coefficients and the modification. As expected the decrease of the relaxation time Θ leads to a stronger evaporation and higher velocities. However, the total spreading of the jet and expanse of the shock front do not change notably. Examining the mass flow rate shows, that the change of the HRM model leads to a significant reduction of over 25% to 6.65 g/s for the change of Θ_0 and to 7.76 g/s for the change of the exponent λ . As the change of the evaporation strength does not lead to a notable increase of the jet spreading or shock expansion and the original model coefficients of Downar-Zapolski et al. (1996) give better results with respect to the mass flow, it can be concluded that the original coefficients present a decent fit for the HRM model.

It therefore seems that the modeled evaporation is not the cause for the disparities of the jet spreading between the simulation and the experiment. We can only hypothesize here, but one possible cause might be the no-slip assumption between the phases. Within the injector, we can expect that the no-slip assumption does not introduce notable errors. The one-momentum equation merely enforces no-slip conditions within one computational cell, but slip velocities between different cells are possible. Therefore, a possible vapor layer at the wall (indicated by liquid volume fractions $\alpha < 0.5$) can be separated from the bulk liquid (with average $\alpha > 0.75$) by a cell face with the different cells featuring different velocities. Within the liquid core inside the injector the momentum is determined by the liquid (the liquid mass

fraction is above 99%) and slip between the bubbles and the liquid is not expected (Sher et al., 2008). This is different downstream of the injector exit where a clear separation of phases or flow regimes by different cells is not possible. Here, the assumption of no-slip is only valid if the droplets generated through flash evaporation are small enough and follow the gas stream. However, larger droplets of up to 50 μm have also been observed in the experiments (Rees et al., 2019a) and Stokes numbers much larger than one are expected. These droplets will not follow the gas flow at the barrel shock front, violating the no slip assumption. Their inertia will drive them along their radial trajectories and may explain why the shadowgraph images show larger spreading than the computations predict. It must be noted, however, that these first PDA measurements do not provide droplet size distributions and more measurements are needed for an unambiguous assessment of this hypothesis.

5. Conclusions

Flash boiling of cryogenic nitrogen sprays has been investigated by a joint experimental and numerical study. The experiments were conducted at the newly developed test bench M3.3 and provide shadowgraph images of flashing jets with well defined boundary conditions for the simulation. For the simulations a fully compressible multiphase solver based on OpenFOAM has been developed and validated. The phase change is modeled with the homogeneous relaxation model. The code is validated against flashing acetone sprays where shock structures are clearly visible and allow for an unambiguous comparison of the major flow features caused by compressible gas dynamics effects. The solver can predict the lateral expansion of the shock wave, proving that the gas dynamic effects are correctly implemented. Secondly, comparison of the jet spray angles show the limitation of the chosen modeling approach for low superheat ratios R_p . This behavior is expected and can be explained by the choice of the evaporation model. Additionally, using one momentum equation requires that there is no slip velocity between the phases in one cell and forces acting at the jet's interface cannot be captured. Yet, for higher superheats these assumptions can be made and the simulations agree very well with experiments for the shock expansions and the spray angles.

In the shadowgraph images of the nitrogen spray stationary or upstream floating dark regions have been observed. The images alone do not allow for a conclusive interpretation, and this study now provides an excellent example of the complementary nature of experiments and numerics that is needed to explain the observed phenomena. The floating dark regions are located at about 20 to 30 diameters downstream of the injector exit where the simulations predict recirculation zones. The simulations indicate the

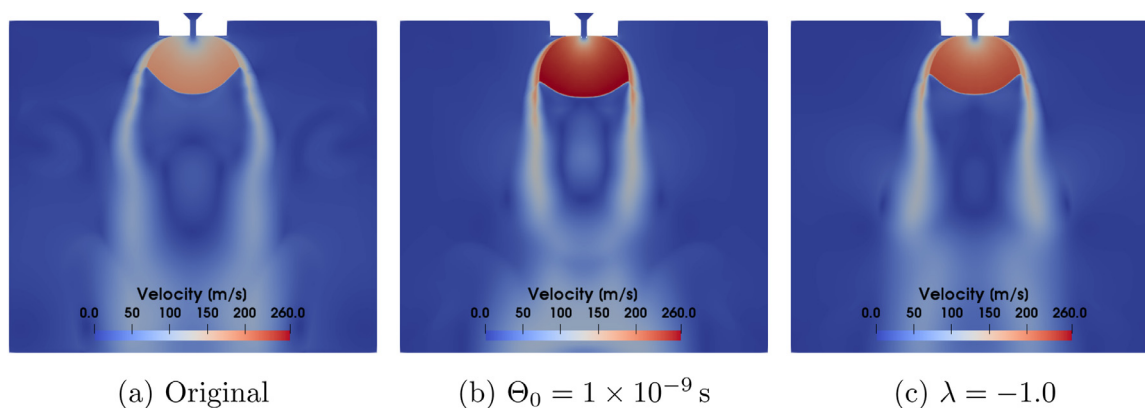


Fig. 13. Velocity contour for case LN2-3 using varying HRM model coefficients. (a) shows the original HRM model, (b) with $\Theta_0 = 1 \times 10^{-9}$ s and (c) with $\lambda = -1.0$.

existence of a shock that causes a low velocity area surrounded by a high speed flow which leads to recirculation on the centerline. The latter can be made responsible for the darker area in the shadowgraph images.

The mass flow rate of the simulation and the experiment match for the cases with a higher superheat within the measurement accuracy. Also, an initial 180° spray angle is seen for the fully flashing nitrogen cases. However, the radial expansion is too small compared to the shadowgraph image. Parameter studies with respect to modeling parameters of the evaporation model demonstrated that standard parameters as used in the literature provide the overall best agreement with measurements.

Future work will therefore focus, from the experimental side, on the analysis of specific droplet data like size and velocity and, from the numerical side, on the development of an improved phase change model that accounts for local effects of bubble growth as investigated in Dietzel et al. (2019).

Declaration of Competing Interest

The authors declare that they have no known competing financial interests or personal relationships that could have appeared to influence the work reported in this paper.

Acknowledgements

The authors thank the German Research Foundation (DFG) for financial support of the project within the collaborative research center SFB-TRR 75, Project number 84292822. The authors also thank for the access to the supercomputer ForHLR funded by "The Ministry of Science, Research and the Arts Baden-Württemberg" fund the super computer resources.

Appendix A. The derivation of the Enthalpy Equations

The energy conservation for one phase is given by

$$\frac{\partial \alpha_1 \rho_1 e}{\partial t} + \nabla \cdot (\alpha_1 \rho_1 \mathbf{e} \mathbf{u}) = \left(\frac{\partial p}{\partial t} - \nabla \cdot \mathbf{q} \right) \frac{\alpha_1 \rho_1}{\rho} + S_e, \quad (\text{A.1})$$

with e being the total energy $e = h + K$ and K being the kinetic energy $K = 0.5|\mathbf{u}|^2$. The heat transfer is modeled using Fourier's law with the specific thermal conductivity k , viz.

$$-\nabla \cdot \mathbf{q} = \nabla \cdot (k \nabla T). \quad (\text{A.2})$$

The mechanical work and the thermal diffusion are distributed to the phases proportional to their mass fractions. Additionally, the effect of shear on the mechanical work is neglected. Expanding the first two terms provides an expression with the phase mass outside of the derivative,

$$\alpha_L \rho_L \frac{D(h_L + K)}{Dt} + \left[\frac{\partial \alpha_L \rho_L}{\partial t} + \nabla \cdot (\alpha_L \rho_L \mathbf{u}) \right] e_L = \left(\frac{\partial p}{\partial t} + \nabla \cdot (k_L \nabla T_L) \right) \frac{\alpha_L \rho_L}{\rho} + S_e. \quad (\text{A.3})$$

Further multiplication with the inverse mass fraction $\frac{\rho}{\rho_L \alpha_L}$ gives,

$$\rho \frac{Dh_L}{Dt} + \rho \frac{DK}{Dt} + \left[\frac{\partial \alpha_L \rho_L}{\partial t} + \nabla \cdot (\alpha_L \rho_L \mathbf{u}) \right] \frac{\rho}{\rho_L \alpha_L} e_L = \left(\frac{\partial p}{\partial t} + \nabla \cdot (k_L \nabla T_L) \right) + \frac{\rho}{\rho_L \alpha_L} S_e \quad (\text{A.4})$$

The term in the angular brackets is the change of liquid mass \dot{m}_L , as seen in Eq. (1).

Assuming that the vapor is generated at saturation conditions of the surrounding pressure, the source terms from Eqs. (A.4) and (1) are related by

$$S_e = \dot{m}_L h_{SG}(p). \quad (\text{A.5})$$

Note that here the enthalpy $h_{SG}(p)$ and not the evaporation enthalpy $h_{fg} = h_{SG}(p) - h_{SL}$ is used, because S_e represents the energy that is now stored in the vapor phase and not the energy required to transform liquid to vapor. Neglecting the change of kinetic energy K of e_L on the LHS of Eq. (A.4) then gives the enthalpy equations presented in Section 2.2,

$$\rho \frac{Dh_L}{Dt} + \rho \frac{DK}{Dt} = \left(\frac{\partial p}{\partial t} + \nabla \cdot (k_L \nabla T_L) \right) + \frac{\rho}{\rho_L \alpha_L} \dot{m}_L (h_{SG}(p) - h_L), \quad (\text{A.6})$$

and for the second phase

$$\rho \frac{Dh_G}{Dt} + \rho \frac{DK}{Dt} = \left(\frac{\partial p}{\partial t} + \nabla \cdot (k_G \nabla T_G) \right) + \frac{\rho}{\rho_G \alpha_G} \dot{m}_L (h_G - h_{SG}(p)). \quad (\text{A.7})$$

References

- Bell, I.H., Wronski, J., Quoilin, S., Lemort, V., 2014. Pure and pseudo-pure fluid thermophysical property evaluation and the open-source thermophysical property library coolprop. *Industrial & Engineering Chemistry Research* 53 (6), 2498–2508. doi:10.1021/ie4033999.
- Bilicki, Z., Kestin, J., 1990. Physical aspects of the relaxation model in two-phase flow. *Proceedings of the Royal Society of London A: Mathematical, Physical and Engineering Sciences* 428 (1875), 379–397. doi:10.1098/rspa.1990.0040.
- Brennen, C.E., 2005. *Fundamentals of multiphase flow*. Cambridge university press.
- De Rosa, M., Sender, J., Zimmermann, H., Oschwald, M., 2006. Cryogenic spray ignition at high altitude conditions. In: 42nd AIAA/ASME/SAE/ASEE Joint Propulsion Conference & Exhibit.
- Dietzel, D., Hitz, T., Munz, C.-D., Kronenburg, A., 2019. Numerical simulation of the growth and interaction of vapour bubbles in superheated liquid jets. *Int. J. Multiphase Flow* 121, 103112. doi:10.1016/j.ijmultiphaseflow.2019.103112.
- Downar-Zapolski, P., Bilicki, Z., Bolle, L., Franco, J., 1996. The non-equilibrium relaxation model for one-dimensional flashing liquid flow. *Int. J. Multiphase Flow* 22 (3), 473–483. doi:10.1016/0301-9322(95)00078-X.
- Guo, H., Li, Y., Wang, B., Zhang, H., Xu, H., 2019. Numerical investigation on flashing jet behaviors of single-hole GDI injector. *Int. J. Heat Mass Transf.* 130, 50–59. doi:10.1016/j.ijheatmasstransfer.2018.10.088.
- Kurschat, T., Chaves, H., Meier, G., 1992. Complete adiabatic evaporation of highly superheated liquid jets. *J. Fluid Mech.* 236, 43–59.
- Lamanna, G., Kamoun, H., Weigand, B., Manfretti, C., Rees, A., Sender, J., Oschwald, M., Steelant, J., 2015. Flashing behavior of rocket engine propellants. *Atomization Sprays* 25 (10), 837–856.
- Lamanna, G., Kamoun, H., Weigand, B., Steelant, J., 2014. Towards a unified treatment of fully flashing sprays. *Int. J. Multiphase Flow* 58, 168–184. doi:10.1016/j.ijmultiphaseflow.2013.08.010.
- Lee, J., Madabhushi, R., Fotache, C., Gopalakrishnan, S., Schmidt, D., 2009. Flashing flow of superheated jet fuel. In: *Proceedings of The Combustion Institute*, 32, pp. 3215–3222.
- Lyras, K., Dembele, S., Vyazmina, E., Jallais, S., Wen, J., 2017. Numerical simulation of flash-boiling through sharp-edged orifices. *International Journal of Computational Methods and Experimental Measurements* 6, 176–185. doi:10.2495/CMEM-V6-N1-176-185.
- Mansour, A., Müller, N., 2019. A review of flash evaporation phenomena and resulting shock waves. *Exp. Therm. Fluid Sci.* 107, 146–168. doi:10.1016/j.expthermflusci.2019.05.021.
- Michaelides, E.E., Crowe, C.T., Schwarzkopf, J.D., 2017. *Multiphase flow handbook*, 2nd CRC Press, Taylor & Francis Group.
- Neroorkar, K., Gopalakrishnan, S., R. O. Grover, J., Schmidt, D., 2011. Simulation of flash boiling in pressure swirl injectors. *Atomization Sprays* 21, 179–188.
- Panigrahi, P.K., Muralidhar, K., 2012. Laser Schlieren and Shadowgraph. In: *Schlieren and Shadowgraph Methods in Heat and Mass Transfer*. Springer, pp. 23–46.
- Park, B.S., Lee, S.Y., 1994. An experimental investigation of the flash atomization mechanism. *Atomization Sprays* 4 (2), 159–179.
- Rees, A., Araneo, L., Salzmänn, H., Kurudzija, E., Suslov, D., Lamanna, G., Sender, J., Oschwald, M., 2019. Investigation of velocity and droplet size distributions of flash boiling LN₂-jets with phase doppler anemometry. In: *ILASS-Europe 2019, 29th Annual Conference on Liquid Atomization and Spray Systems*.
- Rees, A., Salzmänn, H., Sender, J., Oschwald, M., 2019. Investigation of flashing LN₂-jets in terms of spray morphology, droplet size and velocity distributions. In: *8th European Conference for Aeronautics and Space Sciences*.
- Saha, K., Som, S., Battistoni, M., 2017. Investigation of homogeneous relaxation model parameters and their implications for gasoline injectors. *Atomization Sprays* 27 (4), 345–365.

- Saha, K., Som, S., Battistoni, M., Li, Y., Quan, S., Kelly Senecal, P., 2016. Modeling of internal and near-nozzle flow for a gasoline direct injection fuel injector. *J. Energy Resour. Technol.* 138 (5). doi:[10.1115/1.4032979](https://doi.org/10.1115/1.4032979).
- Schmidt, D., Gopalakrishnan, S., Jasak, H., 2010. Multidimensional simulation of thermal non-equilibrium channel flow. *Int. J. Multiphase Flow* 36, 284–292.
- Sher, E., Bar-Kohany, T., Rashkovan, A., 2008. Flash-boiling atomization. *Prog. Energy Combust. Sci.* 34 (4), 417–439. doi:[10.1016/j.pecs.2007.05.001](https://doi.org/10.1016/j.pecs.2007.05.001).
- Vieira, M.M., Simoes-Moriera, J.R., 2007. Low-pressure flashing mechanisms in isooc-tane liquid jets. *J. Fluid Mech.* 572, 121–144. doi:[10.1017/S0022112006003430](https://doi.org/10.1017/S0022112006003430).
- Witlox, H., Harper, M., Bowen, P., Cleary, V., 2007. Flashing liquid jets and two-phase droplet dispersion: II. comparison and validation of droplet size and rainout formulations. *J. Hazard. Mater.* 142 (3), 797–809. doi:[10.1016/j.jhazmat.2006.06.126](https://doi.org/10.1016/j.jhazmat.2006.06.126).
- Yeoh, G.H., Tu, J., 2010. *Computational techniques for multi-phase flows: basics and applications*. Butterworth-Heinemann, Oxford.

Paper 2:

Title: Numerical Investigation of Spray Collapse in GDI with OpenFOAM

Authors: Jan Wilhelm Gärtner
Institute for Combustion Technology (ITV),
University of Stuttgart, Stuttgart, Germany

Ye Feng
Institute for Combustion Technology (ITV),
University of Stuttgart, Stuttgart, Germany

Andreas Kronenburg
Institute for Combustion Technology (ITV),
University of Stuttgart, Stuttgart, Germany

Oliver T. Stein
Institute for Combustion Technology (ITV),
University of Stuttgart, Stuttgart, Germany

Journal: Fluids

Year: 2021

Volume: 6


Pages: 104

Author Contributions:

- Programming (90%)
- Data generation (75%)
- Scientific originality (40%)

Article

Numerical Investigation of Spray Collapse in GDI with OpenFOAM

Jan Wilhelm Gärtner, Ye Feng , Andreas Kronenburg * and Oliver T. Stein

Institute for Combustion Technology, University of Stuttgart, Herdweg 51, 70174 Stuttgart, Germany; jan-wilhelm.gaertner@itv.uni-stuttgart.de (J.W.G.); st159621@stud.uni-stuttgart.de (Y.F.); o.stein@itv.uni-stuttgart.de (O.T.S.)

* Correspondence: kronenburg@itv.uni-stuttgart.de

Abstract: During certain operating conditions in spark-ignited direct injection engines (GDI), the injected fuel will be superheated and begin to rapidly vaporize. Fast vaporization can be beneficial for fuel–oxidizer mixing and subsequent combustion, but it poses the risk of spray collapse. In this work, spray collapse is numerically investigated for a single hole and the spray G eight-hole injector of an engine combustion network (ECN). Results from a new OpenFOAM solver are first compared against results of the commercial CONVERGE software for single-hole injectors and validated. The results corroborate the perception that the superheat ratio R_p , which is typically used for the classification of flashing regimes, cannot describe spray collapse behavior. Three cases using the eight-hole spray G injector geometry are compared with experimental data. The first case is the standard G2 test case, with iso-octane as an injected fluid, which is only slightly superheated, whereas the two other cases use propane and show spray collapse behavior in the experiment. The numerical results support the assumption that the interaction of shocks due to the underexpanded vapor jet causes spray collapse. Further, the spray structures match well with experimental data, and shock interactions that provide an explanation for the observed phenomenon are discussed.

Keywords: GDI; spray collapse; shock interaction; flash boiling; HRM Model



Citation: Gärtner, J.W.; Feng, Y.; Kronenburg, A.; Stein, O.T. Numerical Investigation of Spray Collapse in GDI with OpenFOAM. *Fluids* **2021**, *6*, 104. <https://dx.doi.org/10.3390/fluids6030104>

Academic Editor: Markus Klein

Received: 2 February 2021

Accepted: 1 March 2021

Published: 4 March 2021

Publisher's Note: MDPI stays neutral with regard to jurisdictional claims in published maps and institutional affiliations.



Copyright: © 2021 by the authors. Licensee MDPI, Basel, Switzerland. This article is an open access article distributed under the terms and conditions of the Creative Commons Attribution (CC BY) license (<https://creativecommons.org/licenses/by/4.0/>).

1. Introduction

Fuel direct injection (GDI) in spark-ignited engines has become a widely used method in the automotive industry to improve engine efficiency and to reduce CO₂ emissions. The advantages of direct injection include, but are not limited to, controlled fuel-to-air ratios during cranking and cold start, lower operating break specific fuel consumption, higher compression ratios and increased engine efficiency [1]. In recent years, liquid pressurized gas (LPG) internal combustion engines have been emerging as a suitable alternative to conventional gasoline engines and have become common in many regions of the world. While LPG offers many advantages over refinery gasoline, such as a higher compression ratio and lower specific CO₂ emissions, it has a significantly higher saturation pressure. Therefore, the fuel is injected in a superheated condition for several engine operating conditions that are typical for direct injection. In the superheated state, vapor bubbles nucleate within the jet and start to grow rapidly, leading to a disintegration of the jet and a fine dispersed cloud of droplets. This process is commonly referred to as flash boiling and often characterized by the superheat ratio of the saturation to ambient pressure, $R_p = p_{\text{sat}}/p$. While flash boiling can help to improve the vaporization process and reduce the droplet size, adverse effects such as spray collapse may occur [2–4]. Spray collapse is a result of plume-to-plume interaction [2,4,5], with a significantly increased penetration length and decreased spray angle, which negatively impacts engine performance and emissions. Even though flashing occurs in a wider range of operating conditions for LPG, higher hydrocarbons experience flashing as well and may also be subject to spray collapse.

Flashing in direct injection engines has been studied by several authors. Zeng et al. [2] experimentally studied the spray morphology of several gasoline-like fluids such as ethanol, methanol or *n*-hexane with an eight-hole industry grade injector with a nominal spray angle of 60°. The authors concluded that spray collapse occurs at superheat ratios greater than $R_p = 3.33$. However, this threshold disregards the injector geometry, which plays an important role in determining the onset of spray collapse. The fact that the injector geometry, especially the number of bores, affects the spray collapse was first reported by Weber and Leick [6]. This work was continued by Lacey et al. [4] who investigated propane and iso-octane for the spray G configuration of the engine combustion network (ECN) with a nominal spray angle of 80°. They found that R_p cannot serve as a general threshold value for spray collapse and that rather the combination of geometric parameters with an adiabatic expansion process gives a criterion for spray collapse. It is therefore assumed that the flow is choked within the injector and that the subsequent expansion of the under-expanded gaseous jet causes spray collapse, if the two opposite plumes touch. Payri et al. [7], however, observed spray collapse for iso-octane in a supercritical regime; thus, flashing cannot be the cause of spray collapse.

Flash boiling in GDI engines has been studied numerically by multiple researchers including Guo et al. [5], Saha et al. [8], Rachakonda et al. [9], Devassy et al. [10], Mohapatra et al. [11]. Saha et al. [12] investigated the applicability of the homogeneous relaxation model of Downar-Zapolski et al. [13] to the modeling of the phase change. They concluded that the general model parameters originally fitted to water are in good agreement and can be used to simulate flashing in GDI. Devassy et al. [10] used a Hertz–Knudsen relationship with an empirical nucleation model to simulate flash boiling in the spray G case of ECN, showing that this model is applicable for the modeling of flashing in GDI injectors. However, only one case was considered, and spray collapse was not discussed. A general comparison of different CFD software tools and modeling approaches has been summarized in Mohapatra et al. [11], concluding that the choice of the evaporation model does not significantly affect the mass flow rate through the nozzle but that rather the general numerical modeling is important to correctly capture the injection process. In Guo et al. [5] the interaction of two plumes of a two-hole injector was studied. They focused on the resulting shock structures of the flashing jet after the exit of the injector. Similar to underexpanded gaseous jets, a shock system formed outside of the injector, and the authors stated that the interaction of the shocks caused a low-pressure region in the center of the spray, resulting in spray collapse. In a successive study, the same authors investigated the spray collapse of propane using a spray G injector [14]. They concluded that spray collapse is caused by the shock interactions of neighboring plumes, which isolate the low-pressure region in the center of the spray from the ambient conditions. However, their work focused on significantly lower injection pressures than those investigated in this work. As the injection pressure has a strong influence on the spray characteristics of flashing flows, different shock structures can be expected [15,16].

The presence of shocks in flashing flows was also shown experimentally by Lamanna et al. [17] for flashing acetone sprays and numerically for flashing cryogenic nitrogen sprays by Gärtner et al. [18]. Poursadegh et al. [16] visualized the shock structures for spray collapse in an ECN injector for the supercritical injection of propane using near-nozzle Schlieren images. A low-pressure region in the center of the spray was also considered as the cause of spray collapse in the work of Rachakonda et al. [19]. However, Rachakonda et al. [19] did not mention the cause of the low-pressure region or the developing shock structures. Possibly, the coarse grid of only 1.4 million cells did not allow the resolution of these structures.

In this work, the cause of spray collapse due to flashing and the proposed idea of shock interaction for high injection pressures are investigated. Further, the capability of R_p to describe flashing spray behavior is challenged by simulating two cases with the same R_p value but different injection temperatures. The simulations are conducted with an in-house code based on OpenFOAM [20], which uses a one-fluid approach together

with the homogeneous relaxation model (HRM) to model the two phase flow. The solver has already been applied successfully to cases of flash boiling cryogenic nitrogen and acetone [18]. At first, the solver is applied to the single injector case of Guo et al. [21] to validate the solver for GDI applications and to investigate the mesh effects. In a second step, three cases using the spray G configuration are simulated, and plume-to-plume shock interaction is studied.

2. CFD Modeling

To simulate flashing, a compressible one-fluid in-house solver based on the OpenFOAM -v5.x [20] compressibleInterFoam code was developed. This solver has already been applied successfully to flashing cryogenic liquids and has been validated to predict shock size and position correctly [22]. The solver uses a one-fluid approach and therefore solves the equation for the transport of a liquid volume fraction in addition to the mass, momentum and energy equations. The set of governing equations to solve is therefore as follows:

$$\frac{\partial \bar{\rho}_1 \tilde{\alpha}}{\partial t} + \nabla \cdot (\bar{\rho}_1 \tilde{\alpha} \tilde{\mathbf{u}}) + \nabla \cdot (\overline{\rho_1 \alpha_1'' \mathbf{u}''}) = \tilde{m}_1, \quad (1)$$

$$\frac{\partial \bar{\rho} \tilde{\mathbf{u}}}{\partial t} + \nabla \cdot (\bar{\rho} \tilde{\mathbf{u}} \tilde{\mathbf{u}}) = -\nabla \bar{p} + \bar{\rho} \mathbf{g} + \nabla \cdot \tilde{\boldsymbol{\tau}}_t, \quad (2)$$

$$\bar{\rho} \frac{D \tilde{h}_l}{Dt} + \bar{\rho} \frac{D \tilde{K}}{Dt} = \left(\frac{\partial \bar{p}}{\partial t} + \nabla \cdot (k_{l, \text{Eff}} \nabla \tilde{T}_l) \right) + \frac{\bar{\rho}}{\bar{\rho}_1 \tilde{\alpha}_1} \dot{m}_1 (h_{\text{SG}}(p) - \tilde{h}_l), \quad (3)$$

$$\bar{\rho} \frac{D \tilde{h}_g}{Dt} + \bar{\rho} \frac{D \tilde{K}}{Dt} = \left(\frac{\partial \bar{p}}{\partial t} + \nabla \cdot (k_{g, \text{Eff}} \nabla \tilde{T}_g) \right) + \frac{\bar{\rho}}{\bar{\rho}_g \tilde{\alpha}_g} \dot{m}_1 (\tilde{h}_g - h_{\text{SG}}(p)), \quad (4)$$

where $\alpha = V_l/V$, ρ , ρ_l , p , \mathbf{u} , K , $\boldsymbol{\tau}_t$, h , k_{Eff} , g , are the volume fraction, mixture density, liquid density, pressure, mixture velocity vector, kinetic energy, turbulent viscous stress tensor, mixture enthalpy, effective thermal conductivity and gravity, respectively. The overbar represents Reynolds averages of the density field, while tildes and double prime superscripts denote Favre averages and fluctuations around these averages, respectively. Variables with the subscripts “l” and “g” refer to the fluid properties of the respective phase, while properties without an index are volume-averaged quantities. Contrary to typical one-fluid implementations, the developed solver solves the energy equation of each phase separately, therefore allowing a temperature difference between the two phases [18]. The turbulent contributions for the enthalpy transport equations are included in the effective thermal conductivity using

$$\nabla \cdot (k_{g, \text{Eff}} \nabla \tilde{T}) = \nabla \cdot \left(\left(\frac{\mu}{\text{Pr}} + \frac{\mu_t}{\text{Pr}_t} \right) \nabla \tilde{h} \right), \quad (5)$$

where μ_t is the turbulent viscosity and Pr_t is the turbulent Prandtl number. The same modeling approach is chosen for the volume fraction transport, and further details about the implementation can be found in [18]. The use of an Euler–Euler approach with the transport of a volume fraction allows for a simple treatment of the transition of the pure liquid region in the injector to the vapor droplet mixture in the final spray. However, as no phase interface is resolved, effects such as droplet/bubble drag and slip velocities between the phases are neglected. This also holds for any microscopic effects such as nucleation, bubble growth and details on spray break-up. After spray break-up, no information on the droplet size distribution exists, and interactions between the phases may not be well modeled. The admittedly simple implementation used here is, however, a proven method to simulate the behavior of flashing spray and capture the characteristics of the flow such that qualitative—and to a certain degree also quantitative—agreement with experiments is observed [8,14,23–26]. More advanced models such as Euler–Lagrange coupling [27], interface tracking with surface density modeling [19] and general LES simulations [28] were also applied to the simulation of GDI injectors. The coupling of Eulerian and La-

grangian simulations allowed for a more detailed spray treatment; however, only the slightly superheated spray G case was considered [27]. Surface density modeling was used for Euler–Euler descriptions and gave the additional information of the mean droplet diameter or spray shape. However, surface density provided additional information only and did not feed back information for the mass, momentum, energy conservation or phase change equations. Thus, flow dynamics were not affected by the more sophisticated description of the two-phase flow. Lastly, the LES simulation of Befrui et al. [28] for a GDI injector used sharp interface tracking, but this approach is not suitable to model flashing behavior.

Throughout this work, the turbulent viscosity μ_t is modeled with the $k-\omega$ shear stress transport (SST) model. This turbulence model is suitable for adverse pressure gradients at the wall and to model flow separation. Further, the $k-\epsilon$ turbulence model was also tested, and it was found that the choice of turbulence model has no significant effect on the results.

Phase Change Modeling

The phenomenon of flash boiling poses a multi-scale problem, ranging from bubble nuclei at the nanoscale via bubbles in the micrometer range to bubble coalescence and spray break-up at the macro scale [29,30]. Due to this large-scale separation, it is not possible to resolve the bubble or droplet interface and to simulate all scales for any relevant engineering problem. Thus, the phase change has to be modeled using the resolved scales available. Over time, several models have emerged to simulate flash boiling in a one-fluid approach, notably the Hertz–Knudsen model and the homogeneous relaxation model (HRM). While the pure Hertz–Knudsen model is based on fundamental physical principles, it requires the knowledge of the correct interface temperatures, which are not available in simulations in which the bubble or droplet interfaces are not resolved [31]. Further, information about the interface area or droplet/bubble number density is required to get the total mass flux. In contrast, the HRM model by Downar-Zapolski et al. [13] relates the phase change to the deviation of the liquid mass fraction, χ , to its respective equilibrium value and a relaxation time Θ which depends on the pressure difference and the volume fraction,

$$\Theta = \Theta_0 \left(\frac{\rho_l - \rho}{\rho_l - \rho_g} \right)^\beta \left(\frac{p_s(T) - p}{p_c - p_s(T)} \right)^\lambda \quad (6)$$

where p_c is the critical pressure and the coefficients $\Theta_0 = 3.84 \times 10^{-7}$ s, $\beta = -0.54$, $\lambda = -1.76$ represent the high-pressure fit to the flashing water experiments. The final expression for the phase change with χ as the liquid mass fraction is then

$$\frac{D\chi}{Dt} = -\chi \frac{h_1(p, T) - h_{SL}(p)}{h_{SG}(p) - h_{SL}(p)} \frac{1}{\Theta} = \frac{\dot{m}_1}{\rho} \quad (7)$$

We re-iterate here that the current one-fluid implementation using the HRM approach is unable to account for any microscopic effects such as local homogeneity within the two phases, including their local temperatures and pressures, bubble and droplet sizes, which will, on a microscopic scale, determine the evaporation rates and thus spray break-up and jet spreading. Despite these shortcomings, HRM has been successfully applied to simulate flashing fluids in various conditions and applications [8,23,24,26]. Further, the empirical coefficients are applicable for a wide range of fluids and superheat conditions, and it is noted here that for cavitating nozzles, the flow is close to thermal equilibrium such that the HRM approach gives phase change rates of the order of the homogeneous equilibrium model (HEM) [32]. This is in agreement with the work of Guo et al. [5] who used a lower Θ_0 constant to simulate flashing *n*-hexane in GDI injectors, effectively implying a relaxation time in the range of nanoseconds, and the work of Mohapatra et al. [11], in which the homogeneous equilibrium model (HEM) gave the same results as the HRM model. Thus, as the HRM model uses only information of the resolved scales and is a proven method, it is used here to model the phase change.

3. Single Hole Injector

The general setup is first validated by comparison with the numerical work of Guo et al. [21]. In their work, a modified version of a commercial five-hole injector using *n*-hexane as a fluid is investigated. One injector bore is considered, with a nominal spray angle of 60° , and the geometry is shown in Figure 1. As only one injector bore is simulated, this case allows for meshes with a reduced cell number compared with the full eight-hole spray G injector. Therefore, this case is also used to investigate the effects of the mesh as well as the injection temperature and ambient pressure on spray and flow dynamics.

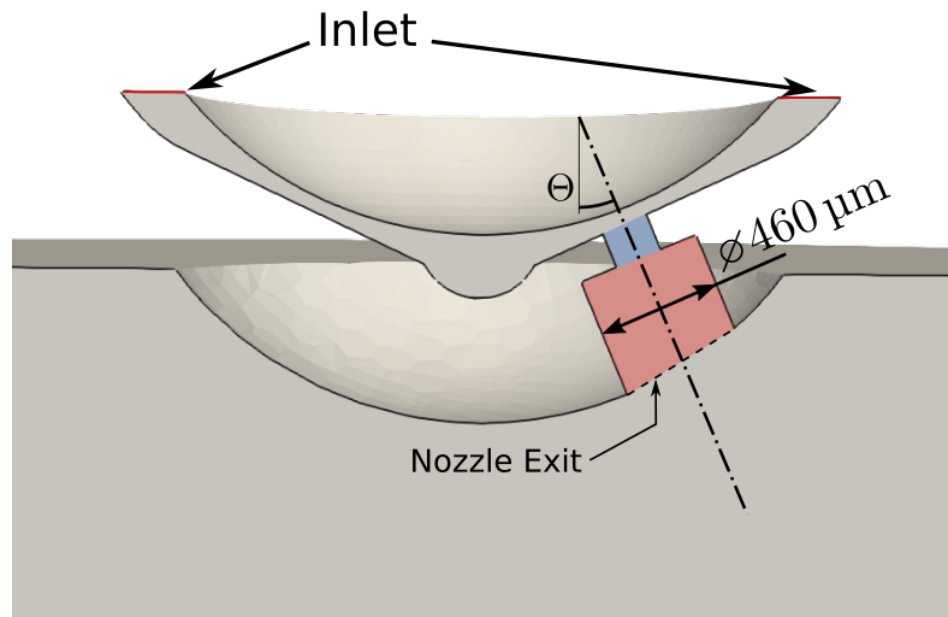


Figure 1. Single-hole domain test case. The inner bore and counter bore are marked with a blue and red box, respectively.

For the reference case, the authors used the commercial software CONVERGE 2.3 [33] to simulate the flashing flow together with the HRM model for the phase change and adaptive mesh refinement to capture the shock structures. In contrast to the standard HRM model, the Θ_0 constant was modified and set to 1×10^{-9} s, while keeping the exponents of the high-pressure fit of Downar-Zapolski et al. [13]. To compare the results of the OpenFOAM solver, the same settings for the HRM model were selected. For the discretization scheme, first-order temporal discretization was used together with a hybrid scheme switching between a central differencing and upwind approach depending on a shock sensor [34] for the momentum equation. The reference solution with CONVERGE used a second-order temporal discretization and a second-order upwind scheme. A second-order backwards Euler method cannot be used with the OpenFOAM solver due to the implementation of the volume fraction transport equation, which requires an explicit flux correction [18]. Therefore, for the sake of stability, all presented results used first-order Euler time discretization. The mesh was generated with the OpenFOAM tool snappyHexMesh using a mesh size of $15.625 \mu\text{m}$ in the injector and in the jet, including the shock front. The mesh size was the result of a previous mesh study [35]; in addition, the cell size was smaller than the value of $17.5 \mu\text{m}$ suggested by Saha et al. [36] and in the range of the smallest mesh size of $12.5 \mu\text{m}$ used for the reference computations by Guo et al. [21].

Table 1 lists the three cases, which are compared to the results of Guo et al. [21] using the injection temperature of 403 K. In these simulations, the inlet pressure was reduced, as for an injection pressure of 10 MPa, the velocity and pressure at the inlet of the injector were above the reported values of the reference cases. As the details of the geometry upstream of the injector bore were not known, the adjustment of the injection pressure seemed to be

justified to match the same pressure and velocity values at the entrance of the inner bore of the injector between the simulations and the reference.

Table 1. Test cases for the single-hole injector.

Case	P_{inj} [MPa]	T_{inj} [K]	P_{amb} [kPa]	T_{amb} [K]	R_p
nHexane-A	7.5	403	101	300	4.49
nHexane-B	7.5	403	60	300	8.31
nHexane-C	7.5	403	20	300	24.9

3.1. Discussion of the Results

Inside the inner bore and in the upstream regions of the counter bore of the injector, most of the liquid vaporized, thus increasing the pressure and leading to an underexpanded gaseous jet leaving the injector. The vapor therefore exited the injector with a pressure above the ambient conditions, leading to an expansion and acceleration of the fluid to supersonic conditions. The supersonic vapor flow was then terminated by a complex shock system [37]. For the case nHexane-A, this is depicted in Figure 2, showing the outer barrel shock as well as the formed Mach disk with its reflected shocks.

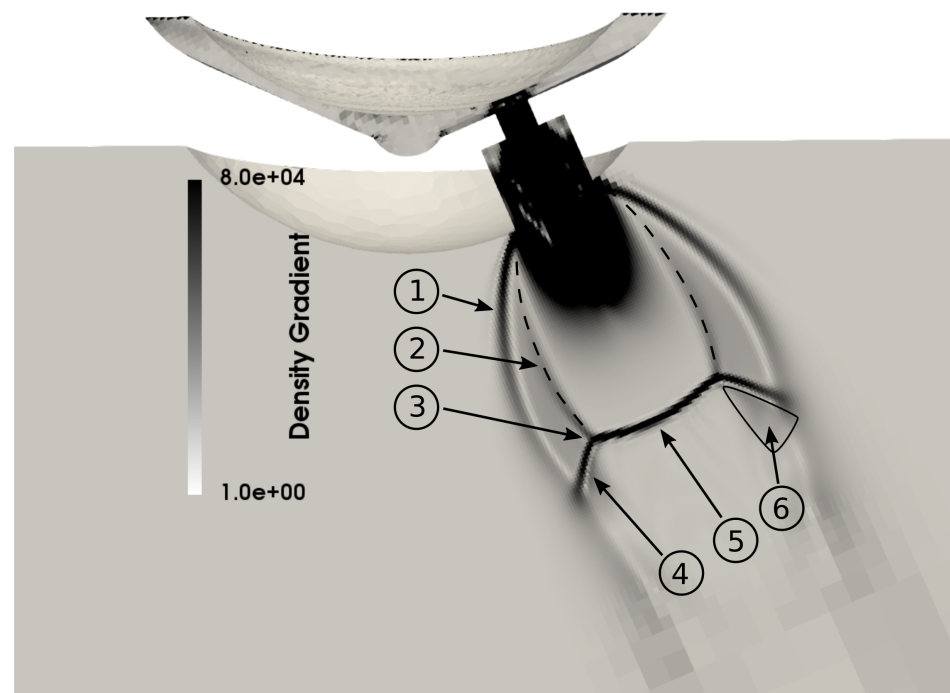


Figure 2. Shock system for the case of nHexane-A visualized by the density gradient magnitude. (1) Constant pressure streamline or barrel shock, (2) intercepting shock, (3) triple point, (4) reflected shock, (5) Mach disk, (6) slip stream [37].

To compare the data to the reference, the velocity magnitude along the centerline of the injector axis is plotted in Figure 3. This shows that the trend between both simulations was matched and that the same conditions within the injector and at the outlet could be reproduced. Further, it validated the OpenFOAM implementation and its capability to predict the shock structures of fully flashing jets correctly.

3.2. Effects of Injection Pressure and Temperature

Figure 3 also shows that, with increasing back pressure, the shock front terminating the gas expansion moves upstream and the maximum velocity is decreased at the same time. However, the acceleration up to the shock front is the same for all three cases. The effect of the injection temperature on the velocity is plotted in Figure 4a with a fixed back pressure

of 101 kPa. From the results, it is apparent that the injection temperature mainly affected the acceleration of the flow. The increase of pressure in the injector seen in Figure 4b was due to the higher saturation pressure for higher injection temperatures. Inside the injector, the liquid evaporated and the pressure correspondingly increased, therefore decreasing the evaporation speed until an equilibrium between pressure increase and evaporation speed was established. Thus, for a higher injection temperature (and a higher saturation pressure), the pressure increased in the injector.

We can conclude that the injection temperature mainly affects the velocity gradient in the supersonic region whereas the ambient pressure determines the position of the shock front. Further, this means that cases with the same R_p value do not give the same velocity profiles, as a lower ambient pressure with a lower injection temperature can give the same R_p value as a case with higher injection temperature and ambient pressure. The variable R_p is thus not sufficient to characterize the flow dynamics in the combustion chamber.

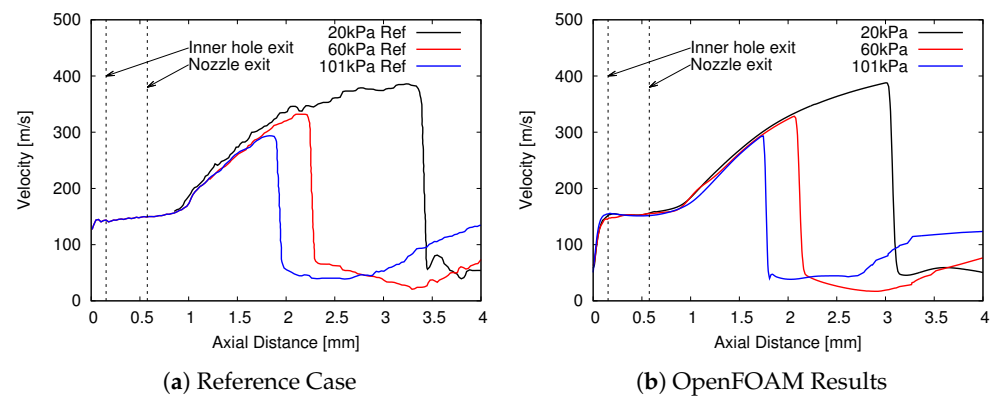


Figure 3. Velocity magnitude for the single-hole injector with *n*-hexane. Reference solution of Guo et al. [21] is shown in (a).

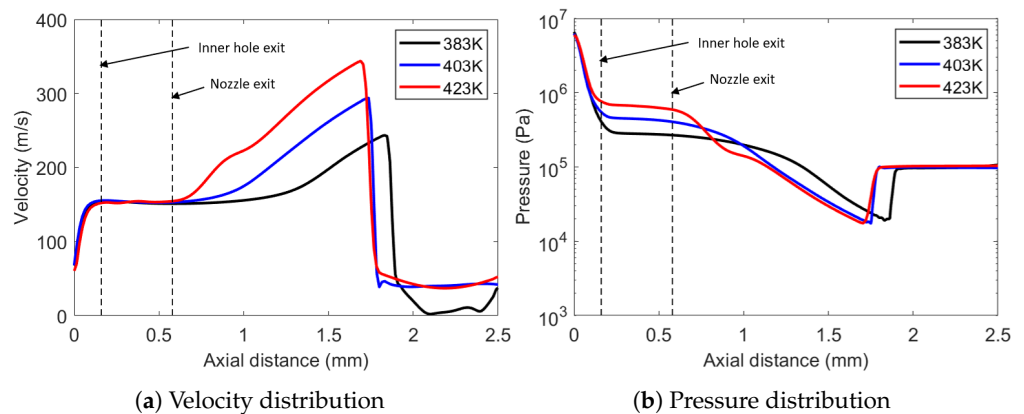


Figure 4. Effect of injection temperature on the spray development.

4. Simulation of Eight-Hole Spray G Configuration

In the previous section, the results of the OpenFOAM solver were compared and validated against the CFD code CONVERGE. Then, the solver was applied to three test cases using the spray G configuration defined by the ECN network (see Table 2). The first case was the standard G2 test case, which was only slightly superheated. The two propane cases were taken from Lacey et al. [4] and showed full spray collapse behavior in the experiment.

Table 2. Boundary conditions for the test cases for the spray G configuration.

Case	Fluid	P_{inj} [MPa]	T_{inj} [K]	P_{amb} [kPa]	T_{amb} [K]	R_p
IsoOctane-A (G2)	Iso-octane	20	363.0	50	293	1.5
Propane-A	Propane	20	363.0	100	293	26.3
Propane-B	Propane	20	363.0	53	293	70.8

4.1. Mesh Generation

On the ECN website, a mesh is provided. However, the mesh resolution outside the injector with a cell size greater than $42\ \mu\text{m}$ is too coarse to capture the flashing and shock structures accurately. Further, the domain size of about 7 mm in diameter is too small to include the complete shock structure. Therefore, a new mesh was generated with the automatic grid generator GMSH. This tool has the advantage of smooth mesh gradings as opposed to tools such as snappyHexMesh or cfMesh, which use refinement levels and have a cell size jump at the refinement boundaries. The Frontal–Delaunay meshing algorithm was chosen for 2D and 3D meshing as the advanced Frontal–Delaunay for quads algorithm gave invalid cells [38]. The mesh for the propane cases is displayed in Figure 5, showing that a smooth transition of cell size and refinement in the supersonic region was achieved. Inside the inner bore, where most of the liquid evaporated under fully flashing conditions, the cell size was set to $12.5\ \mu\text{m}$ in accordance with the results of the single-hole injector. The location of the shock position was first approximated by preliminary simulations with a coarse mesh. Subsequent mesh refinement in the regions of interest provided the final grid used to obtain the results presented here. While the complete 3D mesh was used for the two propane cases, the iso-octane case was simulated with only three injectors and a cyclic boundary condition. Due to the relatively low superheat ratio of this case, no spray collapse was expected, and therefore simulating only a segment of the domain was justified.

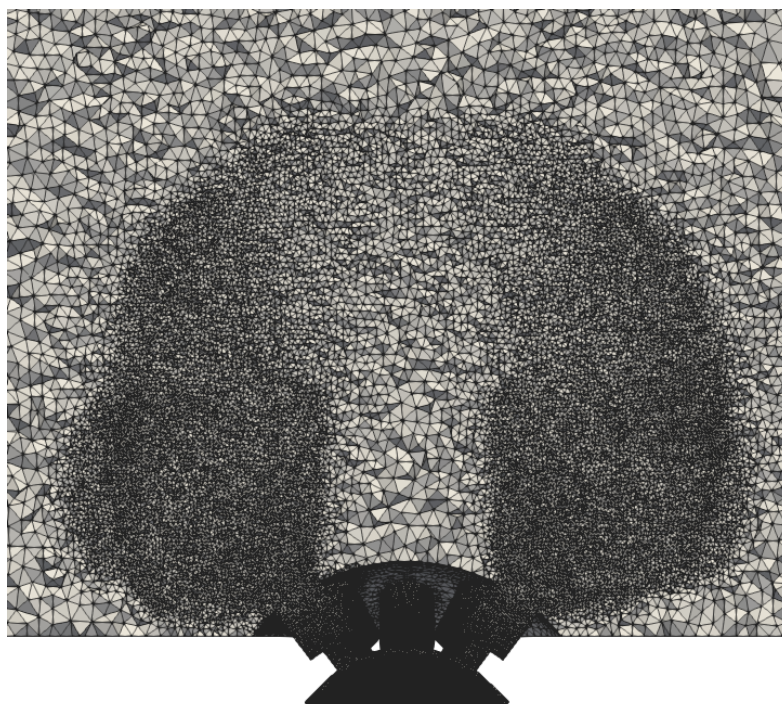


Figure 5. Mesh used for the simulation of propane spray G cases. Cell refinement at the expected shock front by prior simulations with a coarse grid.

4.2. IsoOctane Case A

Experimental data sets for the case of IsoOctane-A are available on the ECN web page. In the work of Hwang et al. [39], extinction imaging was used together with a tomographic reconstruction to get a 3D image of the projected liquid volume fraction. Figure 6 shows the experimentally measured liquid volume fraction of the experiment at the y - z plane and the x - y plane at 10 mm downstream of the injector. The iso-contour line for a volume fraction of $\alpha = 5 \times 10^{-4}$ is drawn in red for the experimental data; the simulation results are represented by the blue dotted line using the original HRM model constants and by the black line for the numerical results with the HRM model using the modified constants, $\Theta_0 = 1$ ns.

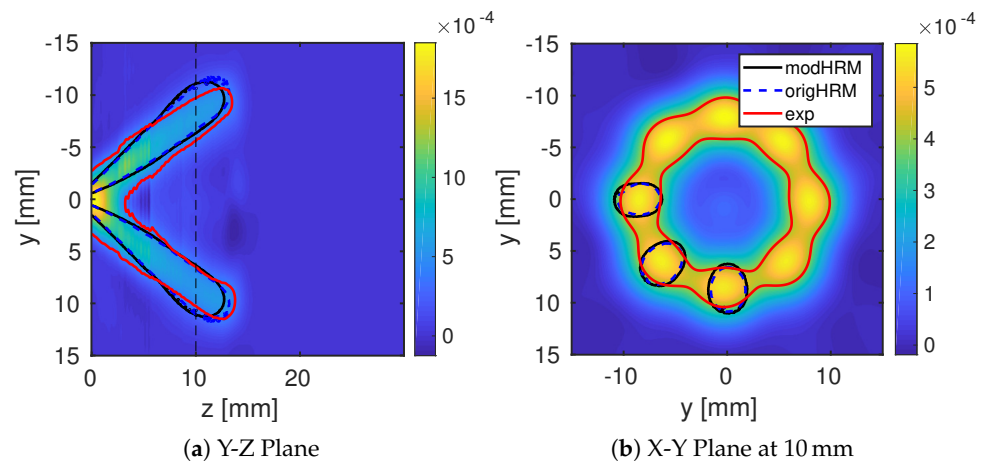


Figure 6. Liquid volume fraction distribution for the case IsoOctane-A as measured in the experiment. Experimental data are taken from Hwang et al. [39], and the iso-contour for volume fraction $\alpha = 5 \times 10^{-4}$ is shown in black for the homogeneous relaxation model (HRM) model with modified constants, with a blue dotted line for the original HRM model and red for the experimental results.

The cut in the axial y - z plane shows that the liquid penetration length, cone angle and the outer contour were in agreement with the experimental data. Further, the increase of the evaporation rate by adjusting the relaxation time did not significantly change the results. This is in agreement with the findings of Mohapatra et al. [11], who showed that the choice of the evaporation model did not significantly affect the mass flow rate of injection. For the x - y plane, the experimental results indicate that all jets fused into one ring. This is different from the numerical results, which predicted individually detectable plumes. It is difficult to identify a specific reason for this difference. The injection conditions and the resulting subsonic spray correctly prevented spray collapse, while the accurate prediction of spray expansion in the y - z plane suggested the accurate modeling of the evaporation rate. A possible cause could be the difference in setup between the experiment and the simulation. In the experiment, the chamber was filled with nitrogen, whereas the simulation assumed a single component solution and sets the gas to iso-octane vapor. However, iso-octane has a density about five times higher than that of nitrogen, which affects the momentum exchange between the spray and the surrounding gas. In addition, the experimental data included some inaccuracies as well. For example, the quality of the data depends on the accuracy of the estimated droplet size, which was assumed to be $7 \mu\text{m}$, as measured in the experiments performed at General Motors and Shanghai Jiao Tong University using phase-doppler interferometry (PDI) [40]. However, the experiments were conducted for the spray G configuration and not the evaporating G2 configuration. Further, artifacts in the measurement and reconstruction relatively close to the injector were reported by Hwang et al. [39]. The authors mentioned that no individual plumes were detectable for positions closer than 5 mm. In conclusion a mix of several possible reasons may contribute to the deviation of the simulation results from the experiment in

the x–y plane. The matching angle and spreading of the spray in the cross-sectional y–z cut, as well as the comparison of the evaporation model variations, show that the chosen set-up and modeling are generally applicable for the spray G case.

4.3. Spray Collapse Due to Shock Interaction

The two propane cases investigated experimentally exhibited spray collapse behavior, as evident in Lacey et al. [4]. Spray collapse is here defined as a significantly decreased spray angle and increased liquid penetration length compared to a conventional non-flashing spray. This is clearly visible in Figure 7, which shows three cases of flashing propane injection from the experiments [4]. The first case in picture (a) is a slightly superheated spray with an R_p of 9.38, which has a wide spray angle and a short liquid penetration length. The second image (b) corresponds to the case of Propane-A of this paper and shows a significantly reduced spray angle as well as an increased liquid penetration length. The last image shows the case of Propane-B with an even further increased liquid penetration length.

In their study, the authors introduced a new criterion for spray collapse due to flashing, called D_n . This criterion can be determined analytically with the assumption of a homogeneous equilibrium inside the injector and an isentropic expansion from the liquid fuel in the rail system to the nozzle throat with a succeeding adiabatic but non-isentropic expansion to the chamber pressure. For further details on how to compute the value, readers are referred to Lacey et al. [4]. If the plumes are modeled as stream tubes, the plume diameter, $d_{c,fuel}$, can be calculated. This plume diameter is then related to a collapse diameter, $d_{collapse}$, calculated from the pitch circle diameter, d_{cc} , of the injector nozzle holes and the orifice angle Θ , as visualized in Figure 8. Thus, severe spray collapse occurs for cases in which the collapse diameter is equal to or greater than the distance between the nozzles expressed by $d_{collapse}$; i.e., $D_n = d_{c,fuel}/d_{collapse} \geq 1$. In summary, spray collapse occurs if the shocks of opposing plumes touch. In the following section, the spray development of the shock structures and the cause of the spray collapse are numerically investigated for a case slightly below and another case above this threshold, as the experimental techniques do not allow the visualization of the shock structures in fully flashing flows.

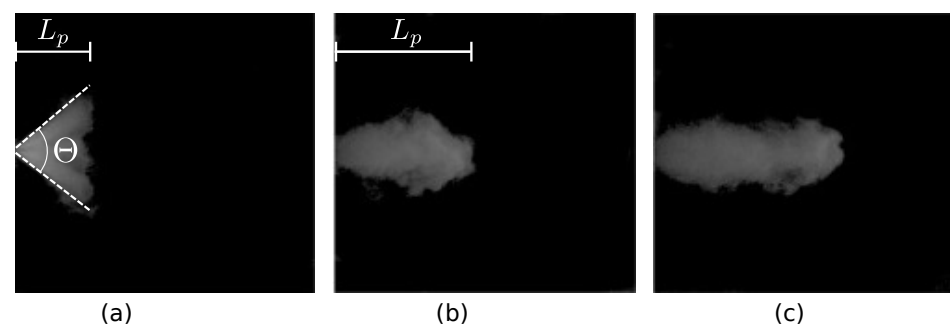


Figure 7. Mie-scattering images at 500 μ s after injection start: (a) shows a slightly evaporating case ($R_p = 9.38$), (b) the case of Propane-A and (c) the case of Propane-B. The liquid penetration length L_p is marked in the images (a,b). Reprinted from Lacey et al. [4] with permission from Elsevier.

The case of Propane-A is studied first, with a value of $D_n = 0.95$ [4]. Figure 9 shows in the left column the development of the velocity magnitude in a central plane at different time steps. Shortly after the start of injection, a shock system with a diamond structure was formed, which is typical for moderately underexpanded jets [37] (see Figure 9a). As the spray developed further and more liquid was transported to the counter bore of the injector, the strength of the evaporation increased and the pressure correspondingly rose, leading to a highly underexpanded jet. The reflected shocks in the perpendicular x–y plane began to interact with neighboring plumes, and the Mach disk shrunk, forming the reflected shock seen in Figure 9b. This created a low-pressure region in the center of the spray, pulling the plumes towards the center. In Figure 9c, the reflected shocks of the opposing plumes came

close to each other but did not merge into one central Mach disk as was expected due to the analytical threshold value. However, the superheat was high enough that the spray angle collapsed and the liquid penetration length increased compared to the non-collapsed case in Figure 7a. The increase in liquid penetration length can be explained by the altered focus of the major mass flow and thus the momentum along the centerline in the axial direction.

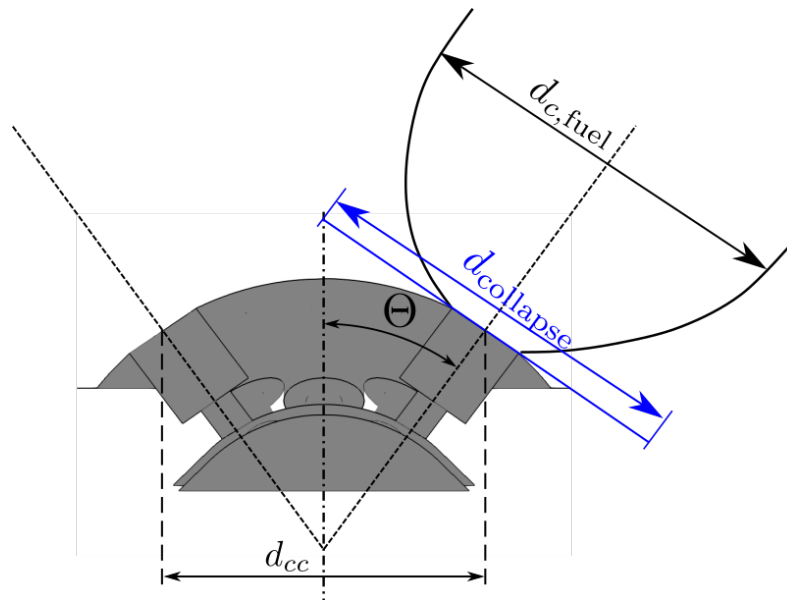


Figure 8. A simplified view of the injector with a pitch circle diameter d_{cc} and the fuel expansion $d_{c,fuel}$ [4].

The second case, Propane-B, had a lower chamber pressure and thus a higher superheat. As a result, stronger shocks and a faster development of the spray collapse were expected. This can be seen in the right column of Figure 9, which shows the velocity magnitude development for this case. In Figure 9e, after $20 \mu s$, the spray was already in a highly underexpanded state and corresponded to the situation in Figure 9b of case A at $100 \mu s$. Figure 9f marks the beginning of the spray collapse, when the reflecting shocks of the opposing plumes began to form. In comparison to the case of Propane-A, the reflected shocks in Figure 9g began to interact and merge into one new Mach disk, pulling the plumes even closer together. The final steady state, with a Mach disk in the center of the spray, is depicted in Figure 9h. The liquid penetration length of case Propane-B was even further increased in the experiment compared to the case of Propane-A, which can be explained by the reduced spray diameter, the faster formation of the shock structure and thus the further focusing of the momentum along the centerline of the spray. Therefore, the criterion of $D_n \geq 1$ for severe spray collapse can be seen as a sufficient but not necessary measure to predict spray collapse. These findings are supported by the results of Guo et al. [14]. There, a case similar to Propane-B was simulated, featuring the same level of superheat R_p but a much lower injection pressure. In this case, the spray showed shock structures of a highly underexpanded jet without the merging of the reflective shocks or a central Mach disk, while still resulting in spray collapse.

Figure 10 shows the pressure development up to $150 \mu s$. In Figure 10a, it can be seen that the initial shock structure of a moderately underexpanded jet began to form a reflected shock. Here, one pressure cell can be identified, as for single-hole injectors. With increasing time, a second pressure cell with a slightly higher pressure than the first cell formed out of the reflected shocks and the expansion fan. This is in accordance with the findings of Guo et al. [5] for a two-hole injector. Figure 10c shows the onset of the shock merging in the center to form a third pressure cell and with it the Mach disk. This is different to the results for the two-hole injector, in which only two pressure cells were found that had originated from the merging of the reflected shocks.

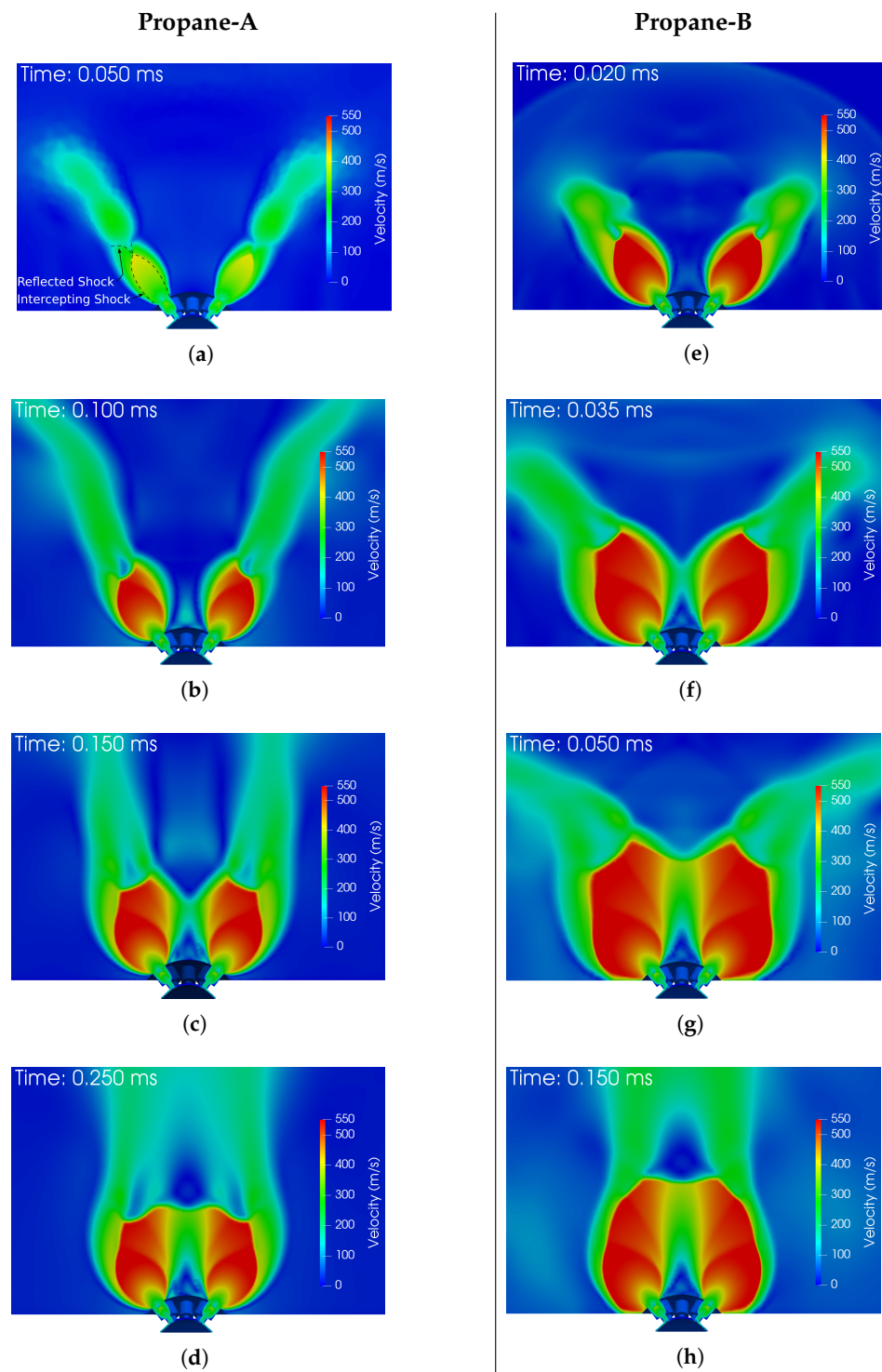


Figure 9. Velocity magnitude for different times for the case of Propane-A in the left column (subfigures (a)–(d)) and Propane-B in the right column (subfigures (e)–(h)).

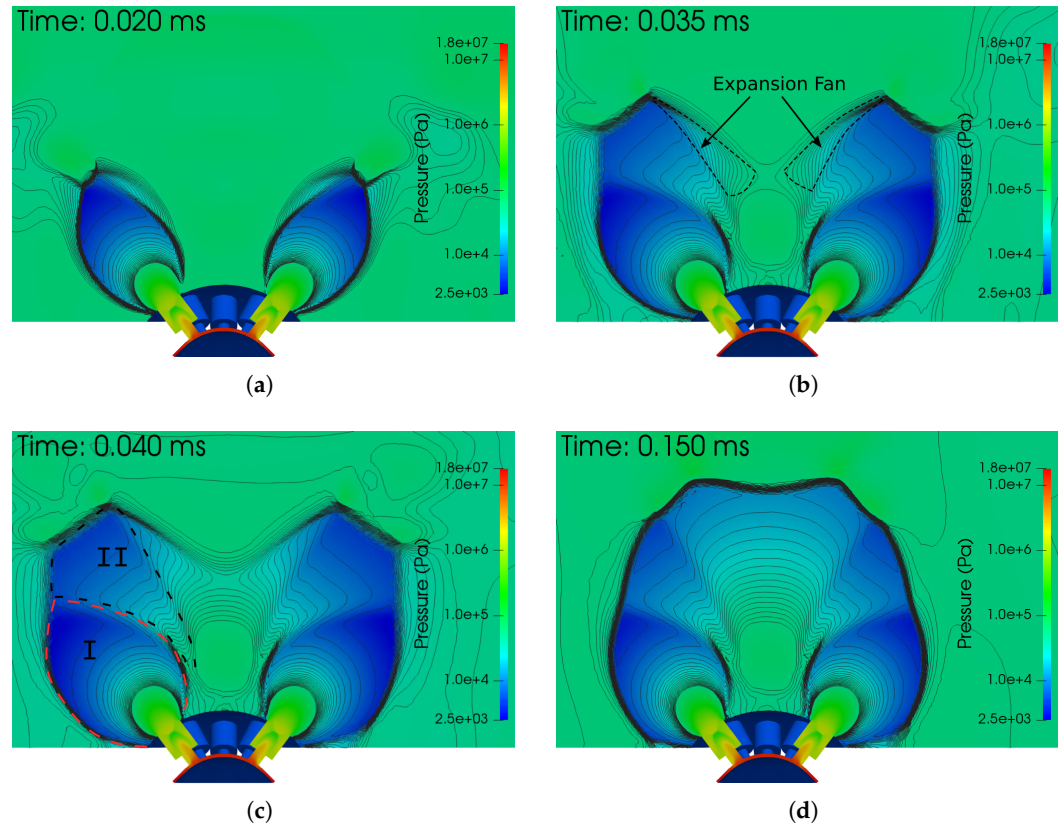


Figure 10. Logarithmic pressure contour for the case of Propane-B for different time steps: (a) 0.020 ms, (b) 0.035 ms, (c) 0.040 ms and (d) 0.150 ms. The formed pressure cells are marked in (c) with Roman numerals I and II.

In conclusion, the prediction of merging shocks of opposing plumes using D_n is corroborated. However, $D_n \geq 1$ cannot be understood as providing a strict limit, as both cases show spray collapse behavior despite being below and above this threshold. It should be noted that the evaporation rates and thus jet expansion predicted by the HRM approach greatly depend on the relaxation times, which in turn are given by the HRM coefficients. The latter have not been further investigated, therefore adding some uncertainty to the numerical results. These constraints in the interpretation of our results should be considered in the light of the experimental study by Poursadegh et al. [16] who showed that spray collapse was found for a D_n as low as 0.8, thus supporting the claim that $D_n \geq 1$ is a useful estimate but not a unique threshold value. The faster merging and reduced spray diameter of the spray for the second case can explain the increased liquid penetration length. However, the description here with the pressure cells is a two-dimensional view only. While the central pressure cell with the Mach disk is common to all injectors, the other two cells are present for each injector and also form more cells between two neighboring injectors.

4.4. Shock Interaction of Neighboring Plumes

The highly three-dimensional structure of the shock system is apparent in Figure 11a. It shows the strong interaction between neighboring plumes and the resulting reflected shocks, as well as the slip stream between two injectors. To visualize the shock structure inside the spray, Figure 11b shows the density gradient at a cross-sectional plane 0.65 mm above the injector and at the x - z and y - z planes. The first pressure cell of Figure 10c is shown in light blue. Further, the three-dimensional view shows that the low-pressure cell that formed in the center of the spray was shielded from the ambient conditions by the merging of the reflected shocks of neighboring injectors. This formed a closed shock front

around the low-pressure core, providing a suitable explanation as to why spray collapse occurred even though case Propane-A had a value of D_n below one. Therefore, these results support the findings of Guo et al. [14] who stated that spray collapse occurs if the shock structures of neighboring plumes interact, merge and thus isolate the low-pressure cell in the center of the spray from the ambient conditions. A possible modification of D_n to include this information could be to relate the fuel expansion diameter $d_{c,fuel}$ not to the distance of opposing plumes but to that of neighboring plumes instead. However, the modification and successful validation of this parameter is beyond the scope of this work.

The intercepting shocks of neighboring plumes lead to a compression of the flow between two injector holes and thus a higher pressure, as shown in Figure 12a. A sketch of the shock system is shown in Figure 12b. It shows the Mach disk of the shock system of each injector, marked with M, the incident shock AB and the resulting Mach stem BC as well as the reflective shock R. The change in the flow direction through the incident shock AB is also visible in the velocity vectors of Figure 13. The flow through the Mach disk, M, changes mainly in the axial direction, which is perpendicular to the observed plane and thus not visible. However, in the 3D view of Figure 11a, the change is clearly visible on the left side. In contrast, the flow through the Mach stem and the slip stream are not directed axially. The resulting mass flux is clearly visible in the mass fraction contour plots of Figure 13, forming radially stretched fingers. The curling of the flow at the end of these fingers is due to the large velocity gradients between the slip stream and the surrounding flow, which form Kelvin–Helmholtz instabilities. To conclude, the shock wave system can explain the radial profiles that have been observed in experiments of Zhang et al. [41]. Despite these radial streams, most of the mass is directed into the axial direction and focused into a rather narrow region on the centerline, therefore leading to the increased liquid penetration length.

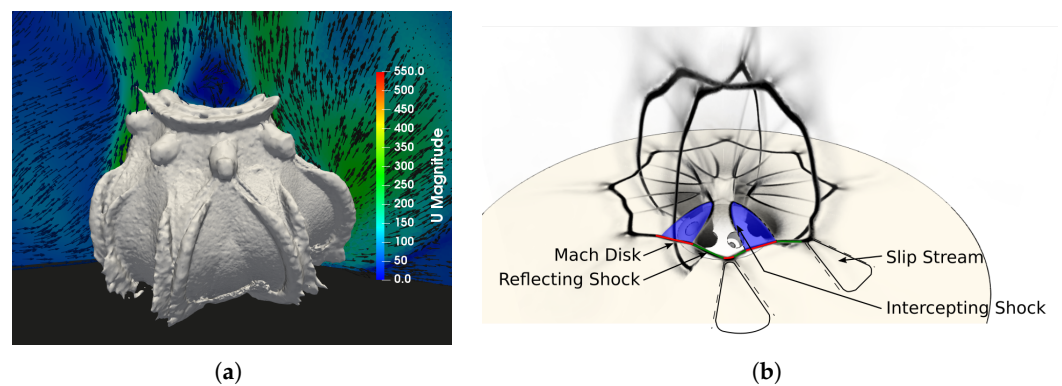


Figure 11. (a) Three-dimensional iso-contour of the density gradient for the case of Propane-B at 150 μ s. The left side shows a cut through an injector and the right side shows a cut between two injector bores. (b) Density gradient contour for the case of Propane-B; the first pressure cell is colored in light blue.

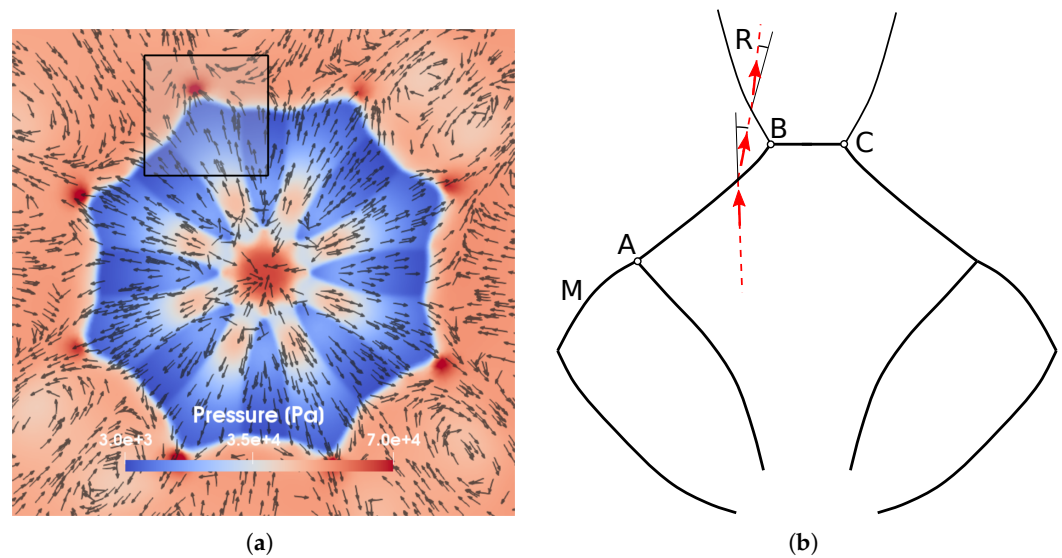


Figure 12. (a) Pressure distribution at a plane 0.65 mm above the injector and 2D velocity vector. (b) Schematic drawing of the shock system for the marked area in (a) showing the velocity vector through the incident shock wave AB. The reflective shock is marked with R and the Mach disk with M.

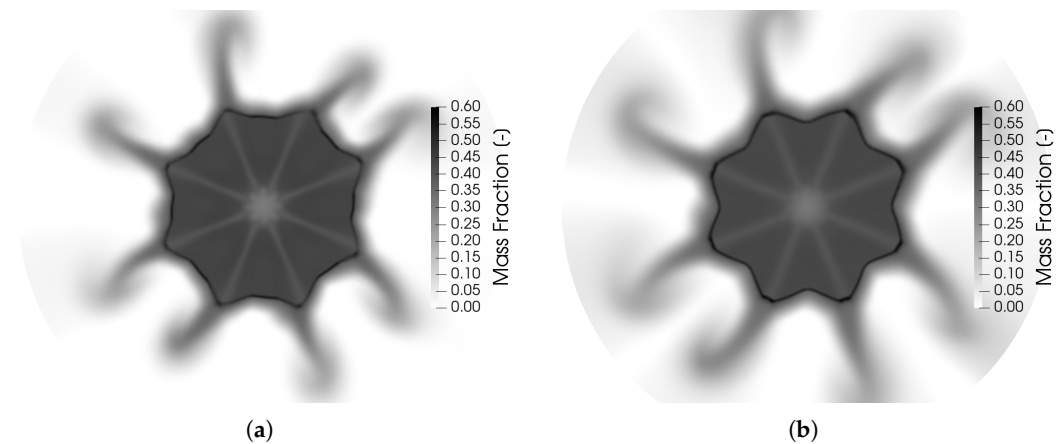


Figure 13. Liquid mass fraction contour at x-y plane at 0.65 mm (a) and 1.5 mm (b) above the injector.

5. Conclusions and Outlook

In this work, severe spray collapse due to flashing was investigated numerically for single and multi-hole injectors with different fluids. The numerical solver was based on OpenFOAM, and its suitability for predicting injection processes under conditions relevant for direct injection gasoline engines was demonstrated. The solver was validated by the comparison of predictions of fully flashing *n*-hexane sprays in a single-hole injector with simulations by Guo et al. [21], who used the commercial CFD software CONVERGE. The comparison of the two solvers showed that the OpenFOAM solver can reproduce the results if inlet conditions are matched. Varying the chamber pressure and injection temperature showed that the position of the Mach disk was mainly determined by the chamber pressure, whereas the increase of velocity and also the extension of the shock wave was predominantly set by the injection temperature. Therefore, the value R_p , which is typically used to describe flashing, could not be used here to unambiguously describe the behavior of the jet or later spray collapse. To investigate the shock interaction of both the opposing plumes and also the three-dimensional effect caused by neighboring injector holes, the spray G configuration of ECN was analyzed. Here, three cases were studied:

first, the standard G2 case with slightly superheated iso-octane; second, two propane cases which showed severe spray collapse behavior. The simulation results of the G2 spray were compared with extinction imaging, showing that the general trend was matched [39]. Deviations from the experimental results were found in the x - y plane perpendicular to the spray axis. In the experiments, the results showed that the eight plumes formed a ring structure, whereas the simulation predicted individual plumes. This was possibly due to the simplified numerical setup, as the simulation used iso-octane throughout the domain, in contrast to the experiment, in which the chamber was filled with nitrogen; however, this does not affect the interpretation of spray dynamics due to shock structures.

As the superheat ratio R_p cannot give a criterion for spray collapse, a new characteristic number, D_n , was proposed by Lacey et al. [4]. The first propane case results, for Propane-A, showed that the reflected shocks of opposing plumes did not merge as would be expected, since the value of D_n of 0.95 was below the threshold value of 1.0. In the second case with a D_n of 1.27, the reflected shocks of opposing plumes interacted and merged into one central Mach disk. Thus, the shock structures of the two propane cases showed the expected behavior indicated by the characteristic number D_n . Our results support the findings of Guo et al. [14]; i.e., that the merging of the reflected shocks due to the underexpanded vapor jet causes the collapse of the spray, by shielding the low-pressure cell in the center of the spray from the ambient conditions. Thus, $D_n \geq 1$ can be seen as a good estimate but not a necessary criterion for spray collapse. This result is supported by the experimental investigation of Poursadegh et al. [16], where spray collapse occurred for values of D_n below 1.0. Further, the spray patterns and the radially squeezed-out fluid are in agreement with experimental results.

In conclusion, the proposed idea of the interaction of underexpanded vapor jet plumes of opposing injector holes was numerically supported. Further, the finding of Guo et al. [14] that an isolated low-pressure region in the center of the spray causes spray collapse was confirmed by the results of the propane cases. Further investigations of the flow behind the shock system would be required to get a holistic view of the spray behavior and to give a quantitative prediction of the liquid penetration length. In addition, future work may investigate the transition of the spray towards spray collapse, as the new characteristic number, D_n , can be seen as a sufficient but not necessary criterion to predict spray collapse.

Author Contributions: Conceptualization, J.W.G. and A.K.; methodology, J.W.G., Y.F. and A.K.; software, J.W.G.; validation, J.W.G. and Y.F.; formal analysis, J.W.G. and Y.F.; investigation, J.W.G. and Y.F.; resources, A.K.; data curation, J.W.G.; writing—original draft preparation, J.W.G.; writing—review and editing, A.K. and O.T.S.; visualization, J.W.G.; supervision, A.K. and O.T.S.; project administration, A.K. and O.T.S.; funding acquisition, A.K. All authors have read and agreed to the published version of the manuscript.

Funding: The project is funded by the collaborative research center SFB-TRR75, Project number 84292822 and supported by the supercomputer forHLR funded by the Ministry of Science, Research and the Arts of Baden-Württemberg and by the Federal Ministry of Education and Research.

Institutional Review Board Statement: Not applicable.

Informed Consent Statement: Not applicable.

Data Availability Statement: The data and numerical tools presented in this study are available on reasonable request from the corresponding author.

Acknowledgments: The authors thank the German Research Foundation (DFG) for financial support of the project within the collaborative research center SFB-TRR 75, Project number 84292822. The authors also are grateful for the access to the supercomputer ForHLR funded by the Ministry of Science, Research and the Arts Baden-Württemberg and by the Federal Ministry of Education and Research.

Conflicts of Interest: The authors declare no conflict of interest.

References

1. Zhao, F.; Lai, M.C.; Harrington, D.L. Automotive spark-ignited direct-injection gasoline engines. *Prog. Energy Combust. Sci.* **1999**, *25*, 437–562. [CrossRef]
2. Zeng, W.; Xu, M.; Zhang, G.; Zhang, Y.; Cleary, D.J. Atomization and vaporization for flash-boiling multi-hole sprays with alcohol fuels. *Fuel* **2012**, *95*, 287–297. [CrossRef]
3. Montanaro, A.; Allocca, L. Flash Boiling Evidences of a Multi-Hole GDI Spray under Engine Conditions by Mie-Scattering Measurements. *SAE Tech. Pap.* **2015**. [CrossRef]
4. Lacey, J.; Poursadegh, F.; Brear, M.J.; Gordon, R.; Petersen, P.; Lakey, C.; Butcher, B.; Ryan, S. Generalizing the behavior of flash-boiling, plume interaction and spray collapse for multi-hole, direct injection. *Fuel* **2017**, *200*, 345–356. [CrossRef]
5. Guo, H.; Li, Y.; Xu, H.; Shuai, S.; Zhang, H. Interaction between under-expanded flashing jets: A numerical study. *Int. J. Heat Mass Transf.* **2019**, *137*, 990–1000. [CrossRef]
6. Weber, D.; Leick, P. Structure and Velocity Field of Individual Plumes of Flashing Gasoline Direct Injection Sprays. In Proceedings of the ILASS Europe, 26th Annual Conference on Liquid Atomization and Spray Systems, Bremen, Germany, 8–10 September 2014. [CrossRef]
7. Payri, R.; Salvador, F.J.; Martí-Aldaraví, P.; Vaquerizo, D. ECN Spray G external spray visualization and spray collapse description through penetration and morphology analysis. *Appl. Therm. Eng.* **2017**, *112*, 304–316. [CrossRef]
8. Saha, K.; Som, S.; Battistoni, M.; Li, Y.; Pomraning, E.; Senecal, P.K. Numerical Investigation of Two-Phase Flow Evolution of In- and Near-Nozzle Regions of a Gasoline Direct Injection Engine During Needle Transients. *SAE Int. J. Engines* **2016**, *9*, 1230–1240. [CrossRef]
9. Rachakonda, S.K.; Wang, Y.; Schmidt, D. Flash-Boiling Initialization for Spray Simulations Based on Parametric Studies. *At. Sprays* **2018**, *28*. [CrossRef]
10. Devassy, B.; Benković, D.; Petranovic, Z.; Edelbauer, W.; Vujanovic, M. Numerical Simulation of Internal Flashing in a GDI Injector Nozzle. In Proceedings of the 29th European Conference on Liquid Atomization and Spray Systems, Paris, France, 2–4 September 2019.
11. Mohapatra, C.K.; Schmidt, D.P.; Sforozo, B.A.; Matusik, K.E.; Yue, Z.; Powell, C.F.; Som, S.; Mohan, B.; Im, H.G.; Badra, J.; et al. Collaborative investigation of the internal flow and near-nozzle flow of an eight-hole gasoline injector (Engine Combustion Network Spray G). *Int. J. Engine Res.* **2020**. [CrossRef]
12. Saha, K.; Som, S.; Battistoni, M. Investigation of Homogeneous Relaxation Model Parameters and their Implications for Gasoline Injectors. *At. Sprays* **2017**, *27*, 345–365. [CrossRef]
13. Downar-Zapolski, P.; Bilicki, Z.; Bolle, L.; Franco, J. The non-equilibrium relaxation model for one-dimensional flashing liquid flow. *Int. J. Multiph. Flow* **1996**, *22*, 473–483. [CrossRef]
14. Guo, H.; Nocivelli, L.; Torelli, R. Numerical study on spray collapse process of ECN spray G injector under flash boiling conditions. *Fuel* **2021**, *290*, 119961. [CrossRef]
15. Guo, H.; Nocivelli, L.; Torelli, R.; Som, S. Towards understanding the development and characteristics of under-expanded flash boiling jets. *Int. J. Multiph. Flow* **2020**, *129*, 103315. [CrossRef]
16. Poursadegh, F.; Lacey, J.S.; Brear, M.J.; Gordon, R.L.; Petersen, P.; Lakey, C.; Butcher, B.; Ryan, S.; Kramer, U. On the phase and structural variability of directly injected propane at spark ignition engine conditions. *Fuel* **2018**, *222*, 294–306. [CrossRef]
17. Lamanna, G.; Kamoun, H.; Weigand, B.; Steelant, J. Towards a unified treatment of fully flashing sprays. *Int. J. Multiph. Flow* **2014**, *58*, 168–184. [CrossRef]
18. Gärtner, J.W.; Kronenburg, A.; Rees, A.; Sender, J.; Oswald, M.; Lamanna, G. Numerical and experimental analysis of flashing cryogenic nitrogen. *Int. J. Multiph. Flow* **2020**, *130*, 103360. [CrossRef]
19. Rachakonda, S.K.; Paydarfar, A.; Schmidt, D.P. Prediction of spray collapse in multi-hole gasoline direct-injection fuel injectors. *Int. J. Engine Res.* **2019**, *20*, 18–33. [CrossRef]
20. The OpenFOAM Foundation Ltd. OpenFOAM. 2021. Available online: <https://openfoam.org/> (accessed on 16 February 2021).
21. Guo, H.; Li, Y.; Wang, B.; Zhang, H.; Xu, H. Numerical investigation on flashing jet behaviors of single-hole GDI injector. *Int. J. Heat Mass Transf.* **2019**, *130*, 50–59. [CrossRef]
22. Gärtner, J.W.; Rees, A.; Kronenburg, A.; Sender, J.; Oswald, M.; Loureiro, D. Large Eddy Simulation of Flashing Cryogenic Liquid with a Compressible Volume of Fluid Solver. In Proceedings of the 29th European Conference on Liquid Atomization and Spray Systems, Paris, France, 2–4 September 2019.
23. Neroorkar, K.; Gopalakrishnan, S.; Grover, R.O., Jr.; Schmidt, D. Simulation of flash boiling in pressure swirl injectors. *At. Sprays* **2011**, *21*, 179–188. [CrossRef]
24. Schmidt, D.; Gopalakrishnan, S.; Jasak, H. Multidimensional simulation of thermal non-equilibrium channel flow. *Int. J. Multiph. Flow* **2010**, *36*, 284–292. [CrossRef]
25. Lyras, K.; Dembele, S.; Wen, J.X. Numerical simulation of flashing jets atomisation using a unified approach. *Int. J. Multiph. Flow* **2018**, *113*. [CrossRef]
26. Lyras, K.; Dembele, S.; Vyazmina, E.; Jallais, S.; Wen, J. Numerical simulation of flash-boiling through sharp-edged orifices. *Int. J. Comput. Methods Exp. Meas.* **2017**, *6*, 176–185. [CrossRef]
27. Saha, K.; Quan, S.; Battistoni, M.; Som, S.; Senecal, P.K.; Pomraning, E. Coupled Eulerian Internal Nozzle Flow and Lagrangian Spray Simulations for GDI Systems. *SAE Tech. Pap.* **2017**. [CrossRef]

28. Befrui, B.; Corbinelli, G.; Spiekermann, P.; Shost, M.; Lai, M.C. Large Eddy Simulation of GDI Single-Hole Flow and Near-Field Spray. *SAE Int. J. Fuels Lubr.* **2012**, *5*, 620–636. [[CrossRef](#)]
29. Sher, E.; Bar-Kohany, T.; Rashkovan, A. Flash-boiling atomization. *Prog. Energy Combust. Sci.* **2008**, *34*, 417–439. [[CrossRef](#)]
30. Witlox, H.; Harper, M.; Bowen, P.; Cleary, V. Flashing liquid jets and two-phase droplet dispersion: II. Comparison and validation of droplet size and rainout formulations. *J. Hazard. Mater.* **2007**, *142*, 797–809. [[CrossRef](#)] [[PubMed](#)]
31. Persad, A.H.; Ward, C.A. Expressions for the Evaporation and Condensation Coefficients in the Hertz-Knudsen Relation. *Chem. Rev.* **2016**, *116*, 7727–7767. [[CrossRef](#)] [[PubMed](#)]
32. Schmidt, D.P.; Rakshit, S.; Neroorkar, K. Thermal and inertial equilibrium in small, high-speed, cavitating nozzle simulations. In Proceedings of the 11th International Annual Conference on Liquid Atomization and Spray Systems 2009, ICLASS 2009, Vail, CO, USA, 26–30 July 2009.
33. Richards, K.J.; Senecal, P.K.; Pomraning, E. CONVERGE 2.3. *Converg. Sci.* **2020**.
34. Ducros, F.; Ferrand, V.; Nicoud, F.; Weber, C.; Darracq, D.; Gacherieu, C.; Poinso, T. Large-eddy simulation of the shock/turbulence interaction. *J. Comput. Phys.* **1999**, *152*, 517–549. [[CrossRef](#)]
35. Feng, Y. Numerical Investigation of GDI Injectors and Shock Interactions. Ph.D. Thesis, University of Stuttgart, Stuttgart, Germany, 2020.
36. Saha, K.; Som, S.; Battistoni, M.; Li, Y.; Quan, S.; Kelly Senecal, P. Modeling of Internal and Near-Nozzle Flow for a Gasoline Direct Injection Fuel Injector. *J. Energy Resour. Technol.* **2016**, *138*. [[CrossRef](#)]
37. Franquet, E.; Perrier, V.; Gibout, S.; Bruel, P. Free underexpanded jets in a quiescent medium: A review. *Prog. Aerosp. Sci.* **2015**, *77*, 25–53. [[CrossRef](#)]
38. Remacle, J.F.; Henrotte, F.; Carrier Baudouin, T.; Geuzaine, C.; Béchet, E.; Mouton, T.; Marchandise, E. A frontal delaunay quad mesh generator using the L_∞ norm. In Proceedings of the 20th International Meshing Roundtable, IMR 2011, Paris, France, 23–26 October 2011; pp. 455–472. [[CrossRef](#)]
39. Hwang, J.; Weiss, L.; Karathanassis, I.K.; Koukouvinis, P.; Pickett, L.M.; Skeen, S.A. Spatio-temporal identification of plume dynamics by 3D computed tomography using engine combustion network spray G injector and various fuels. *Fuel* **2020**, *280*, 118359. [[CrossRef](#)]
40. Engine Combustion Network. Primary Spray G Datasets. 2021. Available online: <https://ecn.sandia.gov/gasoline-spray-combustion/target-condition/primary-spray-g-datasets/> (accessed on 16 February 2021)
41. Zhang, G.; Xu, M.; Zhang, Y.; Zhang, M.; Cleary, D.J. Macroscopic characterization of flash-boiling multihole sprays using planar laser-induced exciplex fluorescence. part II: Cross-sectional spray structure. *At. Sprays* **2013**, *23*. [[CrossRef](#)]

Paper 3:

Title: Investigating 3-D Effects on Flashing Cryogenic Jets with Highly Resolved LES

Authors: Jan Wilhelm Gärtner
Institute for Combustion Technology (ITV),
University of Stuttgart, Stuttgart, Germany

Andreas Kronenburg
Institute for Combustion Technology (ITV),
University of Stuttgart, Stuttgart, Germany

Andreas Rees
Institute of Space Propulsion,
German Aerospace Center (DLR), Hardthausen, Germany

Michael Oswald
Institute of Space Propulsion,
German Aerospace Center (DLR), Hardthausen, Germany

Journal: Flow, Turbulence and Combustion

Year: 2023

Author Contributions:

- Programming (100%)
- Data generation (75%)
- Scientific originality (40%)



Investigating 3-D Effects on Flashing Cryogenic Jets with Highly Resolved LES

Jan Wilhelm Gärtner¹ · Andreas Kronenburg¹ · Andreas Rees² · Michael Oswald²

Received: 10 February 2023 / Accepted: 25 August 2023
© The Author(s) 2023

Abstract

For the development of upper stage rocket engines with laser ignition, the transition of oxidizer and fuel from the pure cryogenic liquid streams to an ignitable mixture needs to be better understood. Due to the near vacuum conditions that are present at high altitudes and in space, the injected fuel rapidly atomizes in a so-called flash boiling process. To investigate the behavior of flashing cryogenic jets under the relevant conditions, experiments of liquid nitrogen have been performed at the DLR Lampoldshausen. The experiments are accompanied by a series of computer simulations and here we use a highly resolved LES to identify 3D effects and to better interpret results from the experiments and existing 2D RANS. It is observed that the vapor generation inside the injector and the evolution of the spray in the combustion chamber differ significantly between the two simulation types due to missing 3D effects and the difference in resolution of turbulent structures. Still, the observed 3D spray dynamics suggest a suitable location for laser ignition that could be found in regions of relative low velocity and therefore expected low strain rates. Further, measured droplet velocities are compared to the velocities of notional Lagrangian particles with similar inertia as the measured droplets. Good agreement between experiments and simulations exists and strong correlation between droplet size and velocity can be demonstrated.

Keywords Flashing · LES · Cryogenic liquids · Compressible two-phase flow

✉ Andreas Kronenburg
andreas.kronenburg@itv.uni-stuttgart.de

Jan Wilhelm Gärtner
jan-wilhelm.gaertner@itv.uni-stuttgart.de

¹ Institute for Combustion Technology, University of Stuttgart, Pfaffenwaldring 31, Stuttgart 70569, Germany

² Institute of Space Propulsion, German Aerospace Center (DLR), Langer Grund, Hardthausen 74239, Germany

1 Introduction

The aspiration to develop environmentally friendly and lighter upper stage rocket engines leads to continuing attempts to replace hydrazine and its derivatives with more conventional fuels, such as methane, kerosene, or hydrogen. As these fuels are not hypergolic, fuel replacement strategies must be combined with a lightweight ignition technique, such as laser ignition (Manfretti and Kroupa 2013). Before ignition, the fuel is injected into near vacuum conditions present at high altitudes and in space, causing the fluid to transit into a superheated state and resulting in rapid and strong evaporation. This process is typically referred to as flash boiling or flash evaporation. A well-based understanding of this complex physical process is required to achieve a successful ignition under these extreme conditions. The modeling and simulation of flashing sprays poses a significant challenge due to the inherent multi-scale problem caused by bubble nucleation in the range of nanometers, bubble growth, breakup and coalescence with scales at a macroscale and the resulting droplets at a micrometer scale (Sher et al. 2008; Witlox et al. 2007; Rees et al. 2020). While DNS simulations of single aspects, such as bubble growth, are possible (Loureiro et al. 2020), resolving all scales within one simulation is not feasible with current computational resources. Hence, bubble nucleation, growth, breakup, and droplets are typically not resolved and have to be modeled. After the spray breakup, the droplets constitute a disperse phase which is typically simulated by Lagrangian particles, whereas the continuous phase, here the vapor, is modeled on an Eulerian grid (Yeoh and Tu 2010). However, prior to spray breakup, the liquid is the continuous phase and the vapor bubbles can be treated as Lagrangian particles. Further, a continuous and separate discrete phase cannot be defined during spray breakup. To avoid the challenge of switching the phases for the Lagrangian treatment and the difficult spray breakup region, an alternative approach where the full set of conservation equations are solved for each phase on an Eulerian grid is more feasible. Often, the additional assumption that vapor and liquid are closely coupled and move with the same velocity is applied, thus removing the need for the momentum exchange terms. Then, only one set of conservation equations for the vapor-liquid mixture has to be solved together with an additional transport equation for the volume fraction. The mixture properties are obtained through an appropriate mixing rule of the two phases. This so called one fluid model is commonly applied to solve two phase sprays and jets for flashing conditions (Schmidt et al. 2010; Guo et al. 2020; Lee et al. 2009; Lyras et al. 2017; Mohapatra et al. 2020; Saha et al. 2017; Neroorkar et al. 2011). Independent of the modeling framework, phase change and nucleation has to be modeled. A simple and early model to describe the phase change is the homogeneous equilibrium model (HEM), which assumes that the vapor and liquid are always in a thermodynamic equilibrium (Bilicki and Kestin 1990). However, this model requires the assumption of an infinite fast relaxation time towards equilibrium conditions, whereas the main aspect of flashing flows is that the liquid is in a superheated, meta-stable state, which is not in equilibrium (Sher et al. 2008). To account for the finite time required to reach equilibrium conditions, the HEM model has been expanded to include a relaxation time, resulting in the homogeneous relaxation model (HRM) (Bilicki and Kestin 1990). A description of the relaxation time, based on flashing water experiments, has been found by Downar-Zapolski et al. (1996). Despite the fit on flashing water experiments, the proposed model has shown wide applicability for various fluids and conditions with only minor modifications of the empirical coefficients (Saha et al. 2017; Lee et al. 2009; Guo et al. 2020). Further, the HRM model does not require detailed information about the interphase surface, which distinguishes it from other

models such as the Hertz-Knudsen model (Persad and Ward 2016). The one fluid model, combined with the HRM model, has already been successfully applied to simulate flashing flows for various fluids and conditions, inside and outside the injector (Schmidt et al. 2010; Guo et al. 2020; Lee et al. 2009; Lyras et al. 2017; Mohapatra et al. 2020; Saha et al. 2017; Neroorkar et al. 2011).

In addition to the complex physics of the flashing process, compressibility effects may alter the flow dynamics as shocks can be observed in flashing sprays (Lamanna et al. 2014; Vieira and Simoes-Moriera 2007; Poursadegh et al. 2017). Similar to gaseous underexpanded flows, the evaporation inside the injector causes the vapor-liquid mixture to exit with a higher than ambient pressure, leading to an acceleration of the vapor into supersonic conditions, which is terminated by a shock system (Franquet et al. 2015). The presence of shocks was corroborated by experimental studies of a short converging nozzle with iso-octane as the working fluid (Vieira and Simoes-Moriera 2007). Further, shocks were observed for flashing acetone sprays by Lamanna et al. (2014) and also for propane using a gasoline direct injector (GDI) by Poursadegh et al. (2017). It is therefore essential to include the compressibility effects in the simulation of flashing sprays to capture the gas dynamics correctly, e.g., for GDI systems, the resulting shocks and their interaction is a crucial aspect to explain behaviors such as spray collapse (Gärtner et al. 2021; Guo et al. 2021; Lacey et al. 2017).

To understand the behavior of flashing cryogenic liquids, experiments with cryogenic nitrogen at conditions present at high altitudes have been performed at the DLR Lampoldshausen, providing shadowgraph images, droplet velocities, and droplet size distributions (Rees et al. 2019, 2020). A joint numerical-experimental study attempted to explain nearly motionless or slightly upstream floating dark structures that were observed in the experiment. 2D RANS simulations identified a recirculation zone about 20D downstream of the injector, which seemingly explained the experimental observations. To investigate the effect of turbulence modeling as well as potentially missing 3D effects in existing 2D simulations, a 3D LES of the same setup is presented here. Previously, only shadowgraph images had been available for a qualitative comparison of the flow structures. With the more recently availability of experimental droplet measurements a quantitative comparison of the simulation and experiment is possible. This allows for a validation of our simulation models and an improved analysis of the flow behavior. This work discusses the effects and associated restrictions of 2D implementations within the injector, see Sect. 4.2, as well as on the recirculation zone, see Sect. 4.4. The flow behavior inside the combustion chamber and particularly the quantitative comparison of droplet velocities and simulation results are presented in Sect. 4.3. In addition, one-way coupled Lagrangian particles, representing the measured droplet size distribution, are added to the simulation to investigate the correlation between droplet size and velocity in comparison to the LES results. A better understanding of the flow dynamics in flashing cryogenic jets is achieved, which may aid the identification of suitable ignition locations for combustible mixtures. These findings aid the development of novel upper stage rocket engines.

2 Numerical Modeling

The accurate numerical solution of the two phase flow with phase change and the faithful capture of transonic effects is challenging. Typically, density-based solvers coupled with suitable Riemann solvers are chosen to compute transonic flows and to resolve the shock front.

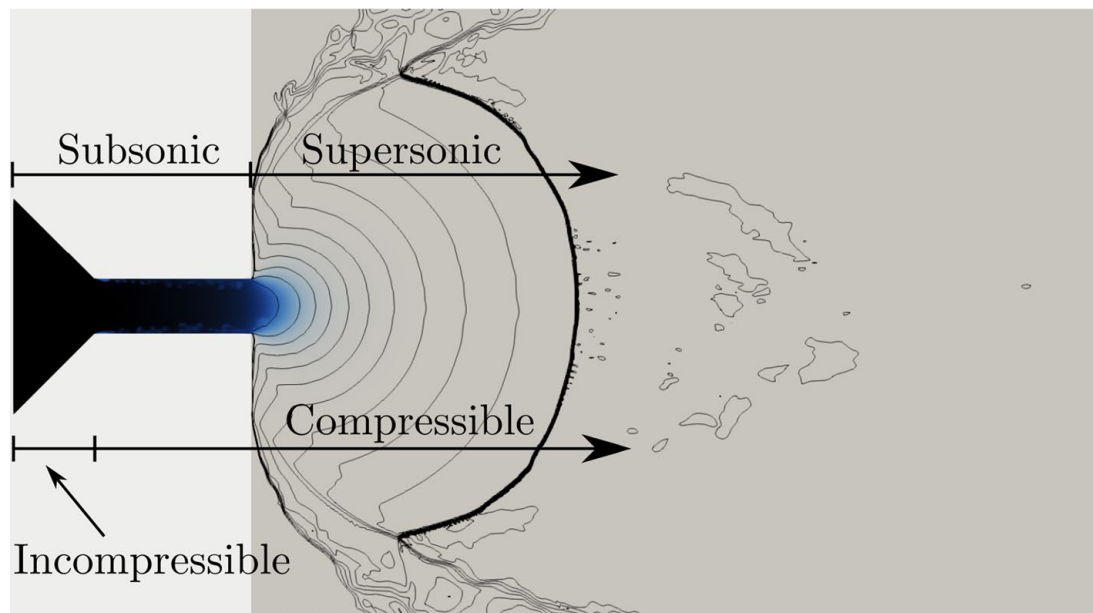


Fig. 1 Simulation regime of sub- to supersonic as well as incompressible to compressible flow for the case of flashing cryogenic liquid nitrogen. The background color is the liquid volume fraction and the black lines are velocity magnitude iso contours

However, these kinds of solvers are not well suited for subsonic regimes. To overcome this problem, a pressure based, hybrid approximate Godunov-type solver has been developed by Kraposhin et al. (2015, 2018). It can be applied to a wide range of Mach numbers as well as non-ideal gas conditions. This technique has also been applied to a two phase solver (UniCFD 2021). One disadvantage is that the solver requires the phases to be compressible and that phase change is currently not included. With the aim of simulating the complete injection process of pure liquid at the injector inlet, the vapor bubble-liquid mixture in the injector, and the spray in the chamber, not only subsonic and supersonic regions are crossed but also a transition of nearly incompressible fluid to the compressible mixture occurs. This is illustrated in Fig. 1.

Due to these reasons, a compressible, pressure-based, two-phase solver with phase change has been developed in OpenFOAM, which solves the compressibility of each phase separately. This solver has already been successfully applied to simulate flashing sprays in different conditions using a RANS based approach (Gärtner et al. 2020, 2021). Further, its capability to predict shock size and position correctly could be validated with flashing acetone experiments, for which unambiguous measurements of the shock front exist (Gärtner et al. 2020). In contrast to typical one fluid approaches, the solver uses separate energy transport equations for both phases. This separation of the two phases is required due to the significant temperature differences between the two phases at the same location (Gärtner et al. 2020). With this adaptation the governing equation system is given by,

$$\frac{\partial \overline{\rho_L \tilde{\alpha}}}{\partial t} + \nabla \cdot (\overline{\rho_L \tilde{\alpha} \tilde{u}}) + \nabla \cdot (\overline{\rho_L \alpha'' u''}) = \tilde{m}_L, \quad (1)$$

$$\frac{\partial \overline{\rho \tilde{u}}}{\partial t} + \nabla \cdot (\overline{\rho \tilde{u} \tilde{u}}) = -\nabla \bar{p} + \bar{\rho} g + \nabla \cdot \tilde{\tau}_L, \quad (2)$$

$$\begin{aligned} \bar{\rho} \frac{D\tilde{h}_L}{Dt} + \bar{\rho} \frac{DK}{Dt} &= \left(\frac{\partial \bar{p}}{\partial t} + \nabla \cdot (k_{L,\text{Eff}} \nabla \tilde{T}_L) \right) \\ &+ \frac{\bar{\rho}}{\bar{\rho}_L \tilde{\alpha}_L} \dot{m}_L (h_{\text{SG}}(p) - \tilde{h}_L), \end{aligned} \quad (3)$$

$$\begin{aligned} \bar{\rho} \frac{D\tilde{h}_G}{Dt} + \bar{\rho} \frac{DK}{Dt} &= \left(\frac{\partial \bar{p}}{\partial t} + \nabla \cdot (k_{G,\text{Eff}} \nabla \tilde{T}_G) \right) \\ &+ \frac{\bar{\rho}}{\bar{\rho}_G \tilde{\alpha}_G} \dot{m}_L (\tilde{h}_G - h_{\text{SG}}(p)), \end{aligned} \quad (4)$$

where the volume fraction α is defined as $\alpha = V_L/V$. The variables ρ and p are density and pressure with the overbars denoting Reynolds averages. Further, \mathbf{u} , K , $\boldsymbol{\tau}_t$, h , k_{Eff} , g represent the mixture velocity vector, kinetic energy, turbulent viscous stress tensor, enthalpy, effective thermal conductivity and gravity, respectively. The tildes and double prime superscripts denote Favre averages and their fluctuations, whereas overbars denote Reynolds averages. The subscripts “L” and “G” refer to the fluid properties of the respective phase, subscripts “SG” and “SL” denote saturation conditions of the gas or liquid at the given pressure level, while properties without an index are volume-averaged quantities. The turbulent contributions of the sub-grid stresses in the momentum equation are included in the turbulent viscous stress $\boldsymbol{\tau}_t$. For the energy equation, the effective conductivity $k_{\text{Eff}} = k_t + k$ is the sum of laminar and turbulent conductivities. Here, the turbulent conductivity is calculated with the turbulent Prandtl number, Pr_t ,

$$k_t = \rho \frac{\nu_t}{\text{Pr}_t}, \quad (5)$$

set for all simulations to 1.0. For the transport of the volume fraction the additional term $\nabla \cdot (\overline{\rho_L \alpha_L'' \mathbf{u}''})$ is modeled with a gradient diffusion assumption (Anez et al. 2019),

$$-\nabla \cdot (\overline{\rho_L \alpha_L'' \mathbf{u}''}) = \bar{\rho}_L \nabla \cdot \left(\frac{\nu_t}{\text{Sc}_t} \nabla \tilde{\alpha}_L \right). \quad (6)$$

Here, ν_t is the turbulent viscosity and Sc_t the turbulent Schmidt number, which is set to $\text{Sc}_t = 0.5$ (Tominaga and Stathopoulos 2007). A detailed derivation of the equation system is found in Gärtner et al. (2020). In the following the overbars and tildes will be omitted in the equations to improve the readability.

In the LES implementation, the turbulent viscosity, ν_t , is modeled with the Wall-Adapting Local Eddy-viscosity model (WALE), which is based on the square of the velocity gradient tensor (Nicoud and Ducros 1999). This model accounts for the turbulent viscosity behavior at the wall and has shown to be superior to the wall damped Smagorinsky model when applied to variable density flows (Huang et al. 2021).

To solve the coupled equation system, the mass and momentum equation are combined to derive a pressure equation,

$$\nabla \cdot \left(\frac{\nabla p}{a_p} \right) - \nabla \cdot \left(\frac{H(\mathbf{u})}{a_p} \right) = \frac{1}{\rho} \frac{D\rho}{Dt}. \quad (7)$$

The variable, a_p represents the diagonal terms of the momentum equation and $H(\mathbf{u})$ the off-diagonal component. The total derivative of the density requires the compressibility of the mixture, which is expressed by Brennen (2005),

$$\left(\frac{\partial \rho}{\partial p}\right) = \sum_{i=1}^N (\rho_i \alpha_i) \sum_{i=1}^N \left(\frac{\alpha_i}{\rho_i} \left(\frac{\partial \rho}{\partial p}\right)_i\right). \quad (8)$$

From Eq. (8), it is already apparent that the compressibility of the mixture is significantly higher than the individual components. This results in a lower speed of sound, such that velocities of 50 ms^{-1} and below can lead to supersonic conditions (Karplus 1958). This reduction of the speed of sound is the cause for the observed shock structures of flashing sprays for comparable low gas flow velocities.

The empirical homogeneous relaxation model (HRM) is chosen to model the mass transfer, \dot{m}_L . This model describes the change of mass fraction, χ , as being proportional to the difference to equilibrium conditions combined with a relaxation time, Θ , (Downar-Zapolski et al. 1996)

$$\frac{D\chi}{Dt} = -\chi \frac{h_L(p, T) - h_{SL}(p)}{h_{SG}(p) - h_{SL}(p)} \frac{1}{\Theta} = \frac{\dot{m}_L}{\rho}. \quad (9)$$

Here, χ is the mass fraction, h_L the enthalpy of the superheated liquid, h_{SG} and h_{SL} the saturation conditions at the current pressure p . The relaxation time is based on a constant factor Θ_0 , the void fraction, ϵ , and the normalized pressure difference, ψ ,

$$\Theta = \Theta_0 e^{\beta} \psi^{\lambda}, \quad (10)$$

$$\epsilon = \left(\frac{\rho_L - \rho}{\rho_L - \rho_v}\right), \quad (11)$$

$$\psi = \left(\frac{p_s(T) - p}{p_c - p_s(T)}\right), \quad (12)$$

with $p_s(T)$ denoting the saturation pressure and p_c the critical pressure of the fluid. The high-pressure fit coefficient for Θ_0 and the exponents β and λ of Downar-Zapolski et al. (1996) have shown in previous works a good agreement with the flashing behavior of cryogenic liquid nitrogen Gärtner et al. (2020). Therefore, the high-pressure fit coefficients of $\Theta_0 = 3.84 \times 10^{-7}$, $\beta = -0.54$, and $\lambda = -1.76$ are selected for this work.

3 LES Case Setup

The computational domain consists of the injector with a conus as well as the combustion chamber, see Fig. 2. Here we define, the origin of the coordinate system to be at the injector outlet and the z -axis corresponding with the axial direction of the injector. The injector has to be included for a faithful approximation of the well defined boundary conditions of the experiment, which provide mass flow rate, injection pressure as well as temperature at the injector inlet (Rees et al. 2020). The injection and boundary conditions are listed in Tables 1 and 2. Further, it can be assumed that at the injector inlet the nitrogen is still pure liquid. The initial conditions assume that the inlet conditions prevail in the entire injector.

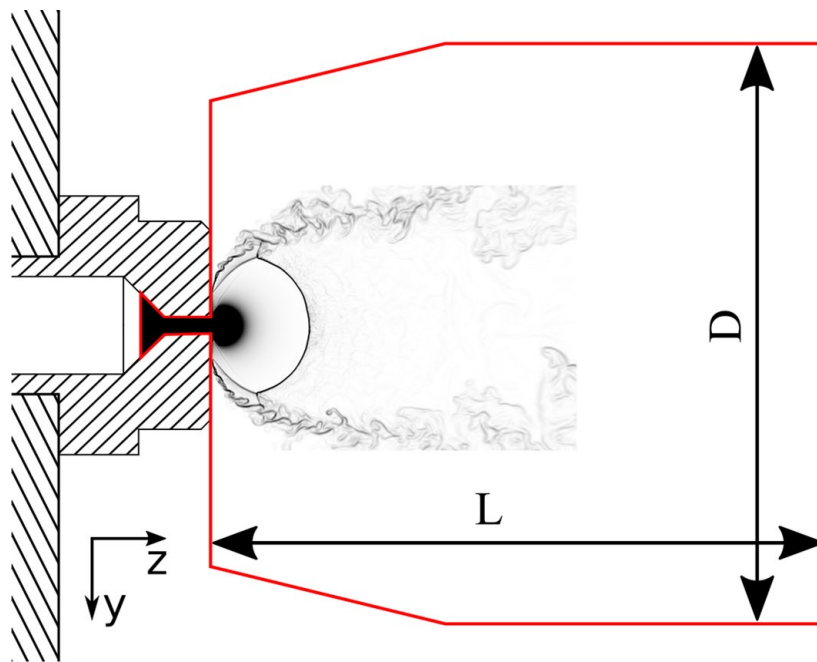


Fig. 2 Sketch of the injector with the computational domain marked by a red boundary. The spray with its shock system is outlined by the density gradient

Table 1 Injection conditions of the experiment

Parameter	Value	Unit
Inj. temperature	89.7 ± 0.6	K
Inj. pressure	$(4.4 \pm 0.4) \times 10^5$	Pa
Chamber pressure	7300 ± 2700	Pa
Mass flow rate	10.6 ± 1.7	g s^{-1}
Inj. volume fraction	0.999	–
Injector diameter	1.0	mm
L/D	2.9	–
R_p	46.8	–
$p_{\text{sat}}(T_{\text{inj}})$	351000	Pa

Table 2 Boundary conditions of the simulation domain

Boundary	Variable	Boundary condition
Inlet	p	Total pressure
	T	Fixed value
	U	Time varying fixed value
Outlet	p	Total pressure
	T	Zero gradient (outflow)
	U	Fixed value (inflow)
	U	Pressure based flux calculation
Wall	p	Zero gradient
	T	Zero gradient
	U	No slip

Table 3 Domain size and mesh resolution

	Mesh size	Cell size (μm)			
		Injector		Shock	
		Axial	Radial	Axial	Radial
Coarse	40×10^6	21	10	37	10
Medium	67×10^6	14	13	25	13
Fine	80×10^6	14	10	25	10

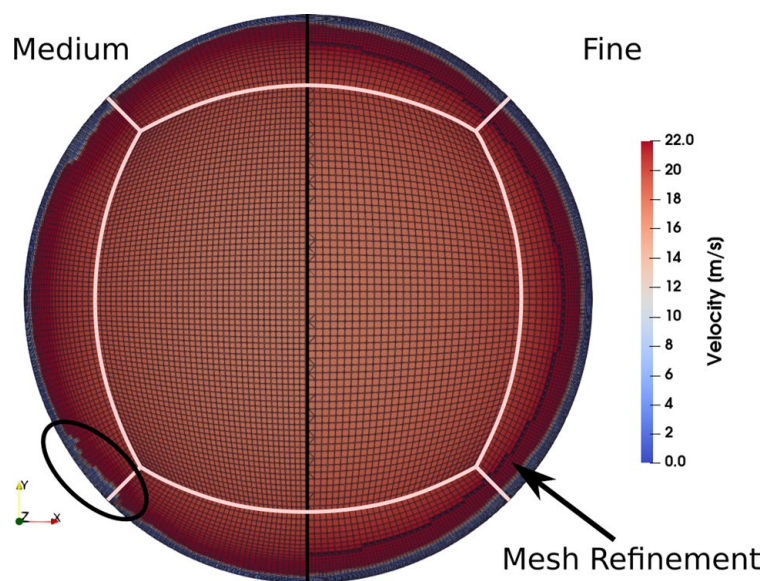


Fig. 3 Visualization of the mesh and velocity magnitude at the transition from injector cone to pipe for the medium and fine mesh. For the medium mesh the spurious flow, which appear at the block mesh boundary between the circumferential blocks around the core, is circled. The white lines represent the block mesh boundaries

At the start of the simulation, the domain size can be reduced to only include the injector and a small part of the combustion chamber. With simulation progress the domain size is adapted until the final dimensions of 35 mm diameter and a length of $L = 40$ mm are reached. To check the mesh dependency of the solution, three meshes with 40, 67, and 80 million cells are tested, see Table 3. While no significant changes of velocity, vapor distribution, and LES quality (defined by the ratio of resolved to total turbulent kinetic energy) could be found in the chamber, a mesh refinement of the boundary layer at the injector wall (leading to the setup with 80 m cells) is needed to prevent spurious flows at block mesh boundaries, see Fig. 3. The largest mesh is therefore used for the averaging of the LES field. In analogy to experimental data, time is reported as time after start of injection (SOI). To resolve the shocks present for this flashing flow (Gärtner et al. 2020) with an LES suitable accuracy, the WENO scheme is chosen to discretize the momentum, energy and volume fraction transport equation (Gärtner et al. 2020). To ensure stability of the equation system a maximum Courant number of $Co = 0.85$ is set, which results in a time step of about $2E-8$ s. Further, the OpenFOAM PIMPLE algorithm is used with five outer iterations to reach convergence of the governing equation system.

4 Results and Discussion

In the following section the results of the LES are presented and compared to 2D RANS simulations and the experimental data. The section is split into four parts, firstly validating the phase change model by comparison of the mass flow rate with experiments, secondly investigating the effect of turbulent eddies on the vapor distribution in the injector, thirdly the dynamic behavior of the spray in the combustion chamber and lastly investigating the dark structures in the shadowgraph images at locations at about 20 to 30D downstream of the injector.

4.1 Validation of HRM Model Parameters

For a quantitative comparison of the experiment to the simulation, the mass flow rate through the injector is chosen, as it develops freely and is subject to the known pressure boundaries. In addition, the mass flow rate is directly affected by the evaporation rate inside the injector. Therefore it is a suitable quantity to validate the HRM model parameters. To include the turbulent inflow condition, a time-variant input, sampled from a highly resolved LES of the pipe and conus leading up to the injector, is used. To fix the velocity as well as the pressure at the inlet boundary is numerically unstable. Hence, while solving the momentum predictor step, the pressure boundary at the inlet is treated as zero gradient. The pressure equation then uses the total pressure boundary condition and does not force the velocity flux, calculated from the predictor step, to the velocity boundary. This mimics the fixed flux extrapolated pressure boundary condition of OpenFOAM without relying on a Neumann boundary condition. This process is required as the pressure information of the outlet boundary cannot travel upstream to the inlet due to the supersonic shock developing in the chamber.

The mass flow rate is measured at the inlet patch of the simulation using the liquid density at the given pressure and temperature value. After the end of the start up phase of the simulation, the mass flow rate is constant over time at 10.4 g s^{-1} , which is slightly below the target value of 10.6 g s^{-1} . However, considering the comparable large experimental uncertainty of 1.77 g s^{-1} it is well within the expected bounds. Further, the transition radius of cone to injector pipe affects the separation zone and, with it, the mass flow rate. Compared to the simulation, minor manufacturing uncertainties could also lead to a slight difference between the simulation and the target value.

4.2 Effect of Turbulence Modeling in the Injector

To compare the effect of dimensionality and the associated effect on the representation of turbulent structures in the injector, the 3D LES results are compared to a 2D RANS simulation using the same numerical settings and a comparable mesh resolution. Figure 4a shows the instantaneous liquid volume fraction for the LES (top) and the RANS result (bottom). The separation zone at the inlet is larger for the LES and more vapor is generated and then distributed further into the center of the injector by turbulent eddies. A comparison of the mean volume fraction (solid line) and velocity (dashed line) as a function of the normalized radial position is shown in Fig. 4b. The radial distribution of the mean properties confirm the finding from the instantaneous view that more liquid is evaporated and transported further into the injector center. Even though the vapor distributions vary between the two

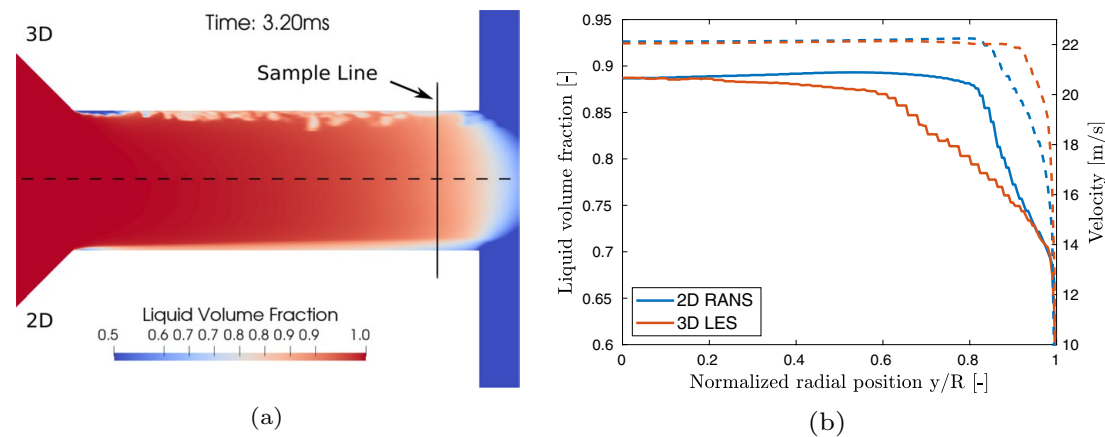


Fig. 4 **a** Instantaneous liquid volume fraction in the injector for the 3D (top) and 2D (bottom) simulation. The sample line for Fig. 4 is marked by a black line. **b** Mean liquid volume fraction (solid line) and velocity (dashed line) plotted at $x/D = 2.6$ after the injector inlet for the 2D RANS and 3D LES

simulation types, the overall mass flow varies only by 3.6% due to an increased velocity of the LES in the near wall region. This shows that resolving the large eddies affects the vapor and velocity distribution significantly inside the injector and that a simpler RANS model is not sufficient to study the injector behavior in detail.

4.3 Spray Dynamics in the Combustion Chamber

Due to the optical dense area close to the injector exit and the challenging experimental conditions, it is not possible to get quantitative data of the spray break-up process after the injector exit and only qualitative shadowgraph images are available for comparison, see Fig. 5b. Further downstream of the injector, however, where a more dilute regime can be observed, quantitative measurements of droplet characteristics are possible. Droplet velocities and size distributions are provided downstream of the injector in Rees et al. (2020) and allow for a qualitative and quantitative comparison of simulations with measurements in the combustion chamber. In Fig. 5a the mean velocity distribution at the center plane of the spray is compared to the measured droplet velocities and Fig. 5b shows an experimental shadowgraph image. In the slip stream predictions are quite good but the velocities in the spray center do not match in regions close to the injector. After 20 mm the simulation results are in better agreement with the measured droplet velocities. Close to the injector outlet less than 100 Doppler bursts were detected, hence favoring larger and faster droplets. Due to the low statistics in this region the points in the range of $10 \leq y \leq 15$ and $0 \leq z \leq 10$ are excluded from the following analysis, marked by a red square in Fig. 5a. We note that the one fluid method imposes the assumption that the two phases have no relative velocities. The droplet size distributions provided by the PDA measurements suggest however, that the droplets generated by the spray may be too large to fully follow the gas flow. To investigate the behavior of the droplets, passive particles are injected into the simulation at positions where the liquid volume fraction is between 1 to 5%. The particles are initialized with the local velocity value and initial droplet sizes are sampled from the measured size distribution at $y = 0$ and $z = 10$ mm that is depicted in Fig. 6. After injection the particle size is fixed and only the drag force is acting on the particles given by the standard sphere drag model (Putnam 1961)

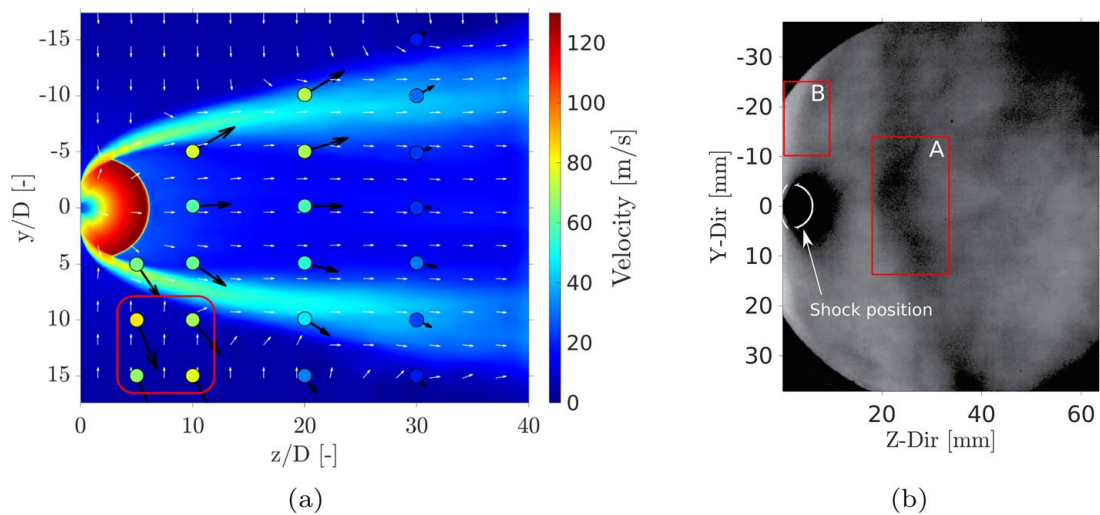
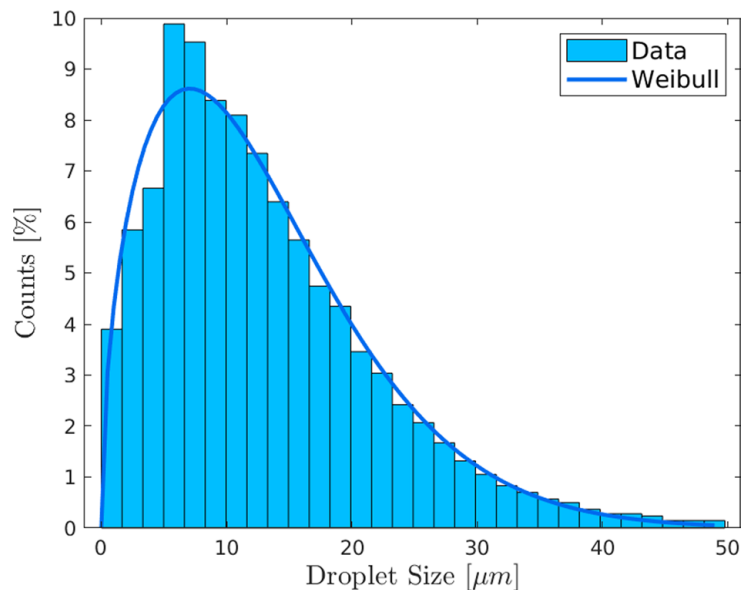


Fig. 5 **a** Mean velocity of the LES compared to the experimentally measured droplet velocities marked as circles with a scaled velocity vector in black. The white arrows represent the flow direction of the LES solution. **b** Experimental shadowgraph image of the spray, adapted from Gärtner et al. (2020) with permission of Elsevier

$$C_D = \frac{24}{Re} + \frac{24}{6} Re^{-1/3}. \quad (13)$$

The particle velocity field is time and space averaged, with an averaging interval of 0.7 ms and spatial averaging in circumferential direction. For the averaging procedure all particles are tracked and given a unique ID to avoid duplicate counts of the same particle in one averaging bin. Figure 7 shows that the particle velocities match well with the experimental data for the values in the slip stream and at 10 mm downstream of the injector. In addition, the velocity direction of the particle data is displayed as white arrows with the same scaling for the velocity magnitude as used for the experimental data set, showing good agreement of the predicted and measured particle flow directions. Positions relatively

Fig. 6 Experimental droplet size distribution measured at $z = 10$ mm with a Weibull fit



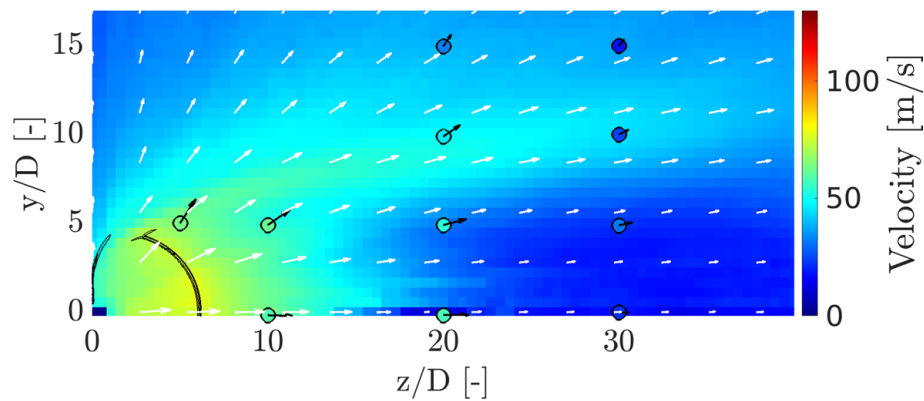


Fig. 7 Velocity of the one-way coupled particles of the simulation projected onto a 2D plane compared to the measured droplet velocities. The white arrows denote the velocity magnitude and direction of the particles in the simulation and the black arrows represent magnitude and direction of the experimental measured droplets

far upstream ($z = [5, 10]$) and away from the center line ($y = [10, 15]$) are excluded. The data quality of the experiment at these positions is, to reiterate, poor as only a low two digit number of Doppler bursts were detected (Rees et al. 2020), and it is likely that a bias for larger particles with higher inertia and larger radial velocities exist for this part of the domain.

A quantitative comparison of the experimentally measured velocity magnitude with the LES and particle data at the axial positions $z/D = [5, 10, 20, 30]$ is given in Fig. 8. Due to the circumferential averaging of the particle data, only results for the positive y -axis are presented for the particles. Further, as experimental points at $y/D = [10, 15]$ and $z/D = [5, 10]$ are excluded, only one measurement point remains closest to the injector at $z/D = 5$. The line plots confirm the finding of Fig. 5a, that the LES results (blue line) match well in the slipstream and further downstream, whereas close to the injector and the center line, they significantly deviate. In contrast, the particle data (red line) matches well with the experimental measurements, as observed in Fig. 7.

The correlation of droplet size and velocity is also visible in Fig. 9, which shows the axial velocity of the one fluid solution (black line), the mean particle velocity (simulation - orange line) and the mean droplet velocity (experiments - orange symbols) along the centerline taking averages from the entire particle and droplet populations. Note that the simulated values are an integrated average of all particles found in a radius of 2 mm around the centerline. This is due to the circumferential averaging, which is needed as the zero volume of the centerline itself prevents sampling and a finite cross-section needs to be defined to have a significant number of particles in each averaging bin. The figure also shows a conditioned velocity for the particle population with diameters larger than $10 \mu\text{m}$ (blue line). Measured data also include droplet velocities averaged from droplets larger than $10 \mu\text{m}$ only and they are indicated here by the blue square symbols. The conditioned (large droplet) velocities of the experiments agree very well with the corresponding (large particle) simulated data. Due to the larger mass and momentum of these droplets they decelerate more slowly than the smaller droplets. The computed velocity of the total particle population, however, decreases much faster and reaches the value of the gas-phase velocity after 20 mm. The difference between the mean particle velocity and the measured droplet values at 15 mm and 20 mm is likely to be due to a bias for larger droplets in the measurements. The experiments recorded fewer than 100

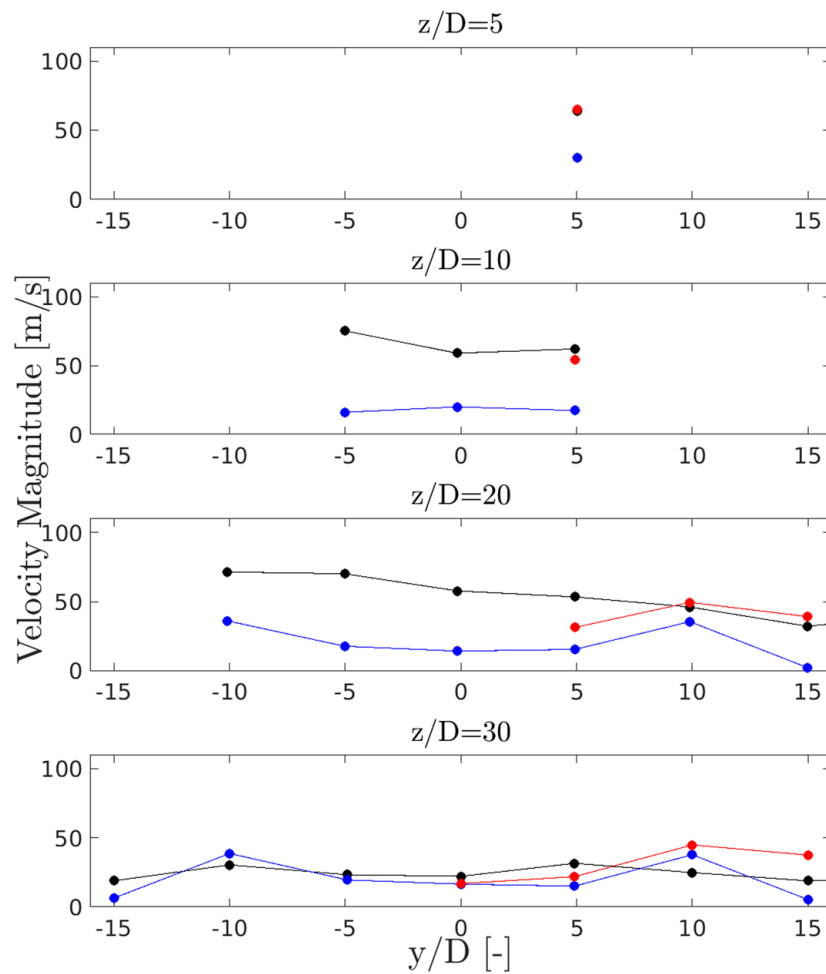
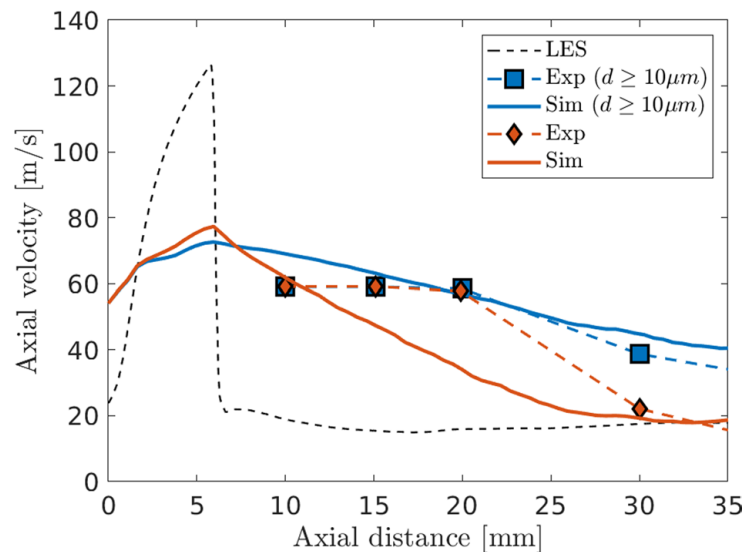


Fig. 8 Quantitative comparison of the experimentally measured velocity magnitude (black line) with the mean LES results (blue line) and particle data (red line) at different axial positions, z/D , as function of the radial distance, y/D

Fig. 9 Axial velocity of the one fluid solution (LES), the experimental data (Exp) and sampled particles (Sim), as well as a conditioned velocities for droplets larger than $10\ \mu\text{m}$



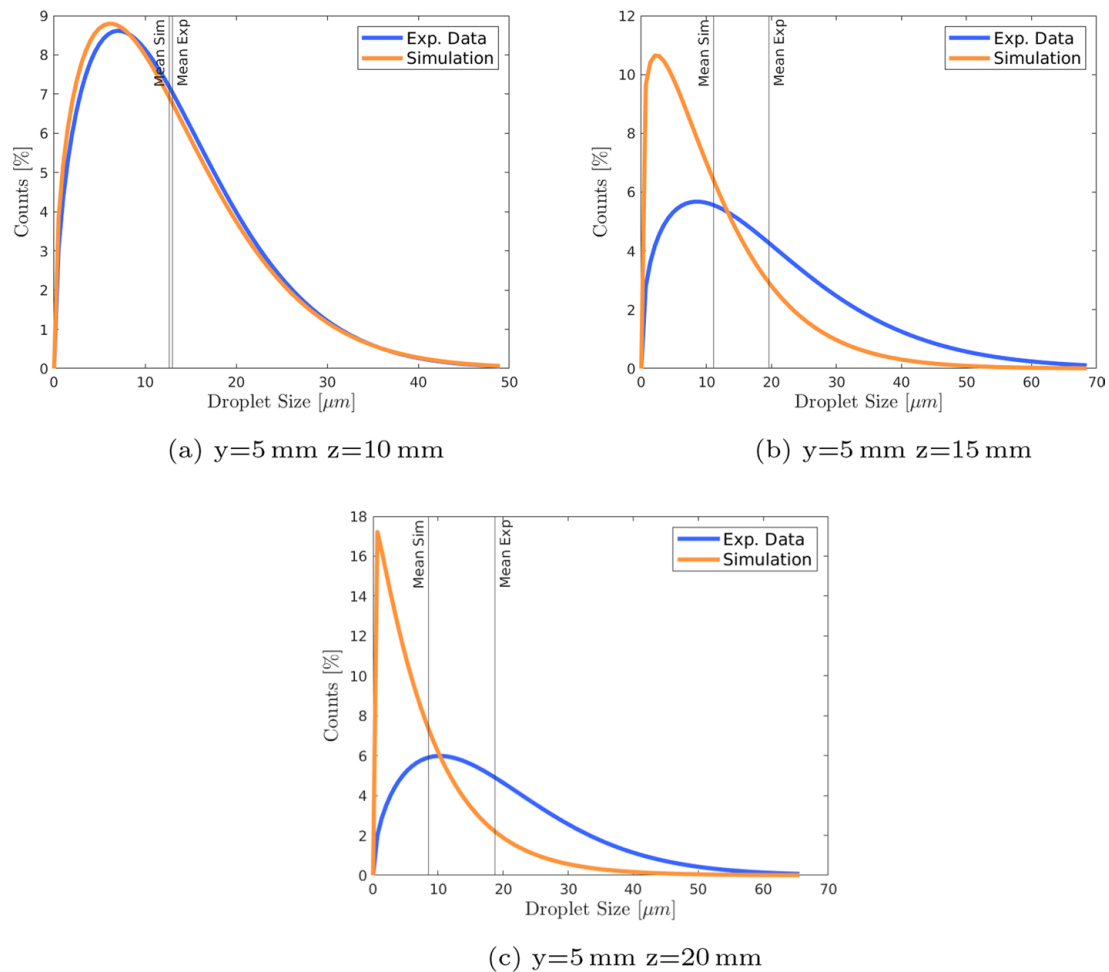


Fig. 10 Droplet size distribution measured in the experiment at $z = 10, 15, 20$ mm compared to the particle size distribution in the simulation

droplets at measurement locations close to the injector with $z \leq 20$ mm and a bias for large droplets was observed (Rees et al. 2020). This bias can also be observed in the droplet size distributions at the axial locations of 10, 15, and 20 mm downstream of the injector as shown in Fig. 10. For the locations at 10 mm to 20 mm the experimentally measured mean droplet size increases which is due to the mentioned bias in the measurement, whereas the particle size distribution is shifted slightly towards smaller particles. However, this shift in particle size distribution is not due to evaporation, as the particle size is fixed at the injection, but due to larger particles having a higher inertia and thus continuing to travel radially outwards out of the averaging volume used for circumferential averaging.

These results show that droplets with larger diameters do not follow the gas flow perfectly and that they reach the gas flow velocity only with a delay at about 20 mm to 40 mm downstream of the injector. The exact position depends on the droplet size. Further, larger droplets will travel beyond the extent of the shock size which also explains why the one fluid simulation does not predict a transport of liquid into the regions close to the injector but far away from the centerline (marked as area B in Fig. 5b). The good agreement between the size conditioned particles and the experimental data suggests that the underlying velocity field is correct. As they are only affected by the drag force, that the gas flow

exerts on the particles. Further, one-way coupling as effectuated here, seems justified as the volume fraction is about 1% after the spray break-up and the small droplets will not significantly affect the gas flow velocity. Therefore, these results do not invalidate the one-fluid solution used to calculate the underlying velocity field but rather demonstrate, that only the motion of the smaller droplets and the gas phase is captured accurately. Capturing the dynamics of larger droplets will, however, require a more detailed approach, such as a combined Euler-Lagrange approach.

4.4 Recirculation Zone

In the shadowgraph images of the experiment nearly motionless or slightly upstream floating structures can be found at about 20D to 30D downstream of the injector (Gärtner et al. 2020), see marked area A in Fig. 5b. A 2D RANS study of this case has shown that a recirculation zone develops in this region which could explain the observed behavior. The 3D LES, however, does not develop such a pronounced recirculation zone as can be seen in Fig. 11a, which shows the instantaneous pressure field in the center plane for the 3D and 2D simulations together with the velocity displayed as vector glyphs and colored by the axial velocity component. To improve clarity of presentation the pressure and velocity values are clipped. Instead of a recirculation zone, smaller regions with low axial velocity are present. They have been marked as area 'C' in Fig. 11a. The reason for this mismatch between the two simulation types can be found in the 3D effects and circumferential inhomogeneity that cannot be captured in the 2D simulation. In the 2D simulations, the recirculation originates from a velocity eddy that is created by the alternating low and high pressure pattern in the slip stream which causes the flow to rotate in a counter clockwise direction. This eddy then increases in magnitude by the large shear velocities between the slip stream and core velocity pushing it towards the center line of the spray, where it stays stationary for a short period. While the low/high pressure pattern also exists in the 3D LES, it is not as pronounced and distinctly separated as in the 2D RANS simulation. Further analysis of the pressure pattern in a cross-section at 8 mm downstream of the injector

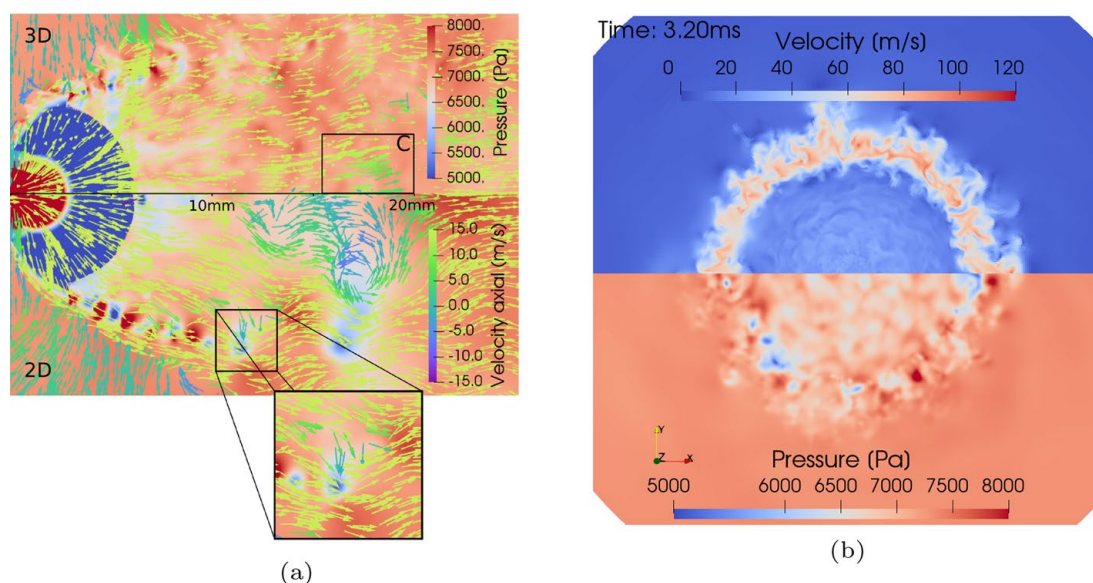


Fig. 11 **a** Pressure and axial velocity displayed as vector glyphs for 3D and 2D simulations. **b** cross sectional view of the instantaneous velocity and pressure for the 3D LES 8 mm downstream of the injector

helps to explain the differences. We note a clear circumferential variation of pressure and velocity and fluid elements transporting mass into the low pressure regions can "escape" in lateral direction such that large eddies, as observed in the 2D simulations, cannot build up. This 2D effect seems very similar to the well known inverse energy cascade that is characteristic for 2D shear layer simulations, where a roll-up of the initial eddies can be observed. Thus, the existence of the rather strong recirculation zone in 2D appears to be related to the simplified representation of turbulence and the omission of the vortex stretching effect that leads to a decay of large vortex structures, prevents roll-up and the propagation of negative velocities towards the centerline. As a result we observe in the 3D LES small separated regions of low axial velocity in the range of 15 to 30D, but no contiguous recirculation area is present. In terms of combustor development, we can still identify the spray center at around 20D as a suitable location for mixture ignition as the low axial velocities will reduce strain on the ignition kernel, prevent immediate extinction and allow a fully burning flame to stabilize itself.

5 Conclusion

High order LES of flashing cryogenic nitrogen are performed. The simulations are carried out by a compressible, one fluid-two phase solver developed in OpenFOAM using the homogeneous relaxation model to describe phase change. The phase change model and its parameters have been validated by comparison with the measured mass flow rate through the injector. The effect of resolving turbulent eddies on the evaporation rate in the injector is investigated by comparing the results to 2D RANS simulations. The results show that more vapor is generated for the 3D LES due to turbulent eddies at the wall, a larger separation zone at the injector inlet and that more vapor is transported toward the center of the injector. The spray velocities in the combustion chamber of the one fluid solver match the measured droplet velocities well in the slip stream of the shock but are much lower than the measured values in the spray center just downstream of the shock front. The measured droplet size distributions indicate that not all droplets are small enough to follow the gas flow perfectly and additional one-way coupled particles are injected and tracked for a more meaningful comparison between experiments and simulations. These particles are injected with the droplet size distribution measured closest to the injector and the local velocity of the one fluid solution. The tracked particles provide good approximations of the experimental values in the spray center and in the slip stream, showing that the droplets follow the gas flow with a certain delay of about 10 to 20 D depending on the droplet size. This also matches with the velocity drop between 20 to 30D in the experimental data. Additional analysis of shadowgraph images revealed motionless structures which were explained by a recirculation zone found in previous 2D RANS simulations. This recirculation zone could not be reproduced by 3D LES and it is likely that the strong recirculation in 2D is wrongly caused by an inverse energy cascade since vortex stretching effects are omitted here. However, smaller eddies and zones of low axial velocity continue to be present in the 3D simulation in the same region, and the region can be identified as a suitable location for spray ignition in upper stage rocket engines burning conventional fuels.

Author Contributions All authors contributed to the study conception and design. Material preparation and computations were performed by Jan Gärtner, experiments were conducted by Andreas Rees. Data comparison was led by Jan Gärtner. The first draft of the manuscript was written by Jan Gärtner and all authors commented on previous versions of the manuscript. All authors read and approved the final manuscript.

Funding Open Access funding enabled and organized by Projekt DEAL. This research is funded by Deutsche Forschungsgemeinschaft (DFG, German Research Foundation) within the project SFB-TRR 75, project number 84 292 822. Further, this work was performed on the HoreKa supercomputer funded by the Ministry of Science, Research and the Arts Baden-Württemberg and by the Federal Ministry of Education and Research.

Declarations

Conflict of interest The authors declare that no competing interests as defined by Springer, or other interests that might be perceived to influence the results and/or discussion reported in this paper exist.

Ethical approval Not applicable.

Informed consent Not applicable.

Open Access This article is licensed under a Creative Commons Attribution 4.0 International License, which permits use, sharing, adaptation, distribution and reproduction in any medium or format, as long as you give appropriate credit to the original author(s) and the source, provide a link to the Creative Commons licence, and indicate if changes were made. The images or other third party material in this article are included in the article's Creative Commons licence, unless indicated otherwise in a credit line to the material. If material is not included in the article's Creative Commons licence and your intended use is not permitted by statutory regulation or exceeds the permitted use, you will need to obtain permission directly from the copyright holder. To view a copy of this licence, visit <http://creativecommons.org/licenses/by/4.0/>.

References

- Anez, J., Ahmed, A., Hecht, N., et al.: Eulerian–Lagrangian spray atomization model coupled with interface capturing method for diesel injectors. *Int. J. Multiph. Flow* **113**, 325–342 (2019)
- Bilicki, Z., Kestin, J.: Physical aspects of the relaxation model in two-phase flow. *Proc. R. Soc. Lond. A: Math. Phys. Eng. Sci.* **428**(1875), 379–397 (1990)
- Brennen, C.E.: *Fundamentals of Multiphase Flow*. Cambridge University Press, Cambridge (2005)
- Downar-Zapolski, P., Bilicki, Z., Bolle, L., et al.: The non-equilibrium relaxation model for one-dimensional flashing liquid flow. *Int. J. Multiph. Flow* **22**(3), 473–483 (1996)
- Franquet, E., Perrier, V., Gibout, S., et al.: Free underexpanded jets in a quiescent medium: A review. *Prog. Aerosp. Sci.* **77**, 25–53 (2015)
- Gärtner, J.W., Kronenburg, A., Martin, T.: Efficient WENO library for OpenFOAM. *SoftwareX* **12**(100), 611 (2020)
- Gärtner, J.W., Kronenburg, A., Rees, A., et al.: Numerical and experimental analysis of flashing cryogenic nitrogen. *Int. J. Multiph. Flow* **130**(103), 360 (2020)
- Gärtner, J.W., Feng, Y., Kronenburg, A., et al.: Numerical investigation of spray collapse in GDI with OpenFOAM. *Fluids* **6**(3), 104 (2021)
- Guo, H., Nocivelli, L., Torelli, R., et al.: Towards understanding the development and characteristics of under-expanded flash boiling jets. *Int. J. Multiph. Flow* **129**(103), 315 (2020)
- Guo, H., Nocivelli, L., Torelli, R.: Numerical study on spray collapse process of ECN spray G injector under flash boiling conditions. *Fuel* **290**(2020), 119,961 (2021)
- Huang, J.X., Hug, S.N., McMullan, W.A.: Large eddy simulation of the variable density mixing layer. *Fluid Dyn. Res.* **53**(1), 015,507 (2021)
- Karplus HB (1958) The Velocity of Sound in a Liquid Containing Gas Bubbles
- Kraposhin M, Bovtrikova A, Strijhak S (2015) Adaptation of kurganov-tadmor numerical scheme for applying in combination with the piso method in numerical simulation of flows in a wide range of mach numbers. In: *Procedia Computer Science*, vol 66. Elsevier B.V., pp 43–52
- Kraposhin, M.V., Banholzer, M., Pfitzner, M., et al.: A hybrid pressure-based solver for nonideal single-phase fluid flows at all speeds. *Int. J. Numer. Meth. Fluids* **88**(2), 79–99 (2018)
- Lacey, J., Poursadegh, F., Brear, M.J., et al.: Generalizing the behavior of flash-boiling, plume interaction and spray collapse for multi-hole, direct injection. *Fuel* **200**, 345–356 (2017)

- Lamanna, G., Kamoun, H., Weigand, B., et al.: Towards a unified treatment of fully flashing sprays. *Int. J. Multiph. Flow* **58**, 168–184 (2014)
- Lee J, Madabhushi R, Fotache C, et al (2009) Flashing flow of superheated jet fuel. In: Proceedings of The Combustion Institute, pp. 3215–3222
- Loureiro, D.D., Reutzsch, J., Kronenburg, A., et al.: Primary breakup regimes for cryogenic flash atomization. *Int. J. Multiph. Flow* **132**(103), 405 (2020)
- Lyras, K., Dembele, S., Vyazmina, E., et al.: Numerical simulation of flash-boiling through sharp-edged orifices. *International Journal of Computational Methods and Experimental Measurements* **6**, 176–185 (2017)
- Manfletti, C., Kroupa, G.: Laser ignition of a cryogenic thruster using a miniaturised Nd:YAG laser. *Opt. Express* **21**(S6), A1126–A113 (2013)
- Mohapatra, C.K., Schmidt, D.P., Sforzo, B.A., et al.: Collaborative investigation of the internal flow and near-nozzle flow of an eight-hole gasoline injector (Engine Combustion Network Spray G). *Int. J. Engine Res.* **24**, 2297–2314 (2020)
- Neroorkar, K., Gopalakrishnan, S., Grover, R.O., Jr., et al.: Simulation of flash boiling in pressure swirl injectors. *Atom. Sprays* **21**, 179–188 (2011)
- Nicoud, F., Ducros, F.: Subgrid-scale stress modelling based on the square of the velocity. *Flow Turbul. Combust.* **62**, 183–200 (1999)
- Persad, A.H., Ward, C.A.: Expressions for the evaporation and condensation coefficients in the Hertz–Knudsen relation. *Chem. Rev.* **116**(14), 7727–7767 (2016)
- Poursadegh, F., Lacey, J.S., Brear, M.J., et al.: (2018) On the phase and structural variability of directly injected propane at spark ignition engine conditions. *Fuel* **222**, 294–306 (2017)
- Putnam, A.: Integratable form of droplet drag coefficient. *Ars J.* **31**(10), 1467–1468 (1961)
- Rees A, Araneo L, Salzman H, et al (2019) Investigation of velocity and droplet size distributions of flash boiling LN₂-jets with phase doppler anemometry. In: ILASS-Europe 2019, 29th Annual Conference on Liquid Atomization and Spray Systems
- Rees, A., Araneo, L., Salzman, H., et al.: Droplet velocity and diameter distributions in flash boiling liquid nitrogen jets by means of phase doppler diagnostics. *Exp. Fluids* **61**, 182 (2020)
- Saha, K., Som, S., Battistoni, M.: Investigation of homogeneous relaxation model parameters and their implications for gasoline injectors. *Atom. Sprays* **27**(4), 345–365 (2017)
- Schmidt, D., Gopalakrishnan, S., Jasak, H.: Multidimensional simulation of thermal non-equilibrium channel flow. *Int. J. Multiph. Flow* **36**, 284–292 (2010)
- Sher, E., Bar-Kohany, T., Rashkovan, A.: Flash-boiling atomization. *Prog. Energy Combust. Sci.* **34**(4), 417–439 (2008)
- Tominaga, Y., Stathopoulos, T.: Turbulent schmidt numbers for CFD analysis with various types of flow-field. *Atmos. Environ.* **41**(37), 8091–8099 (2007)
- UniCFD (2021) Hybrid central solvers. doi: <https://doi.org/10.5281/zenodo.3878441>
- Vieira, M.M., Simoes-Moriera, J.R.: Low-pressure flashing mechanisms in iso-octane liquid jets. *J. Fluid Mech.* **572**, 121–144 (2007)
- Witlox, H., Harper, M., Bowen, P., et al.: Flashing liquid jets and two-phase droplet dispersion: II. comparison and validation of droplet size and rainout formulations. *J. Hazard. Mater.* **142**(3), 797–809 (2007)
- Yeoh, G.H., Tu, J.: Computational techniques for multi-phase flows: basics and applications. Butterworth-Heinemann (2010)

Paper 4:

Title: A Novel ELSA Model for Flash Evaporation

Authors: Jan Wilhelm Gärtner
Institute for Combustion Technology (ITV),
University of Stuttgart, Stuttgart, Germany

Andreas Kronenburg
Institute for Combustion Technology (ITV),
University of Stuttgart, Stuttgart, Germany

Journal: International Journal of Multiphase Flow

Year: 2024

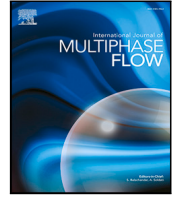
Author Contributions:

- Programming (100%)
- Data generation (100%)
- Scientific originality (50%)



Contents lists available at ScienceDirect

International Journal of Multiphase Flow

journal homepage: www.elsevier.com/locate/ijmulflow

A novel ELSA model for flash evaporation

Jan Wilhelm Gärtner, Andreas Kronenburg*

Institute for Combustion Technology, University of Stuttgart, Pfaffenwaldring 31, 70569 Stuttgart, Germany

ARTICLE INFO

Keywords:

Flashing
LES
Cryogenic liquids
Compressible two-phase flow

ABSTRACT

The development of novel upper-stage rocket engines with storable cryogenic liquids and laser ignition requires a detailed understanding of the processes prior to ignition. Due to the low atmospheric pressure at high altitudes or in space, the liquid is injected below its saturation conditions, causing bubble nucleation, growth, and spray break-up, referred to as flash evaporation. Given the multiscale nature of the phenomenon, modeling and simulating this intricate process pose challenges. Common strategies, like the Eulerian–Lagrangian method, encounter limitations in representing spray break-up dynamics and providing initial data, such as the droplet size and number distribution. On the other hand, Euler–Euler methods cannot resolve the interface for all length scales involved, and the information about the surface interface is lost. Therefore, this work introduces an extension of the Eulerian–Lagrangian spray atomization model (ELSA) for flashing sprays, used to regain the information about mean droplet size. The model incorporates terms for flashing break-up and droplet evaporation and is validated against a cryogenic liquid nitrogen test case, reflecting conditions pertinent to cryogenic fuel injection at high altitudes. Comparative analyses with standard ELSA and a second model from the literature highlight the significance of accounting for the flashing process in spray break-up and droplet formation dynamics. This work contributes to a refined understanding of the break-up process in flashing sprays, offering potential advancements in spray modeling for aerospace applications.

1. Introduction

The introduction of the REACH regulations (Regulation, Evaluation, Authorization and Restriction of Chemicals) by the European Union in 2006 identified hydrazine, the standard mono-propellant for orbital thrusters, as a substance of very high concern (Anon., 0000), and it is likely that not only the use of hydrazine itself but also the use of its derivatives will be restricted. Hence, a suitable alternative has to be found. One such alternative is the combustion of storable cryogenic liquids, which have the advantage that they also fulfill modern mission designs of multiple reignition and reuse. However, injection and ignition of the cryogenic fuel into near-vacuum conditions, present in space and high altitudes, poses several challenges. The cryogenic liquid is injected into conditions significantly below the fuel's saturation pressure, leading to bubble nucleation, growth, and succeeding spray break-up, causing large spray angles and small droplet sizes. This process is typically referred to as flash evaporation or flash boiling. The inherent multi-scale process, ranging from nanometers of the nucleating bubbles to micrometer bubbles and droplets, and the macro scale of the injector (Sher et al., 2008; Witlox et al., 2007; Rees et al., 2020), is a significant challenge for modeling and simulation. While direct numerical simulation (DNS) of the bubble growth and spray break-up of a small number of bubbles and droplets is possible (Loureiro

et al., 2021; Dietzel et al., 2019), macro-scale simulations of an injector become unfeasible. Another often applied approach is to model the continuous or carrier phase on an Eulerian grid and the dispersed phase as Lagrangian particles. However, for this approach, the carrier and dispersed phases are fixed and cannot represent the spray break-up when the continuous phase switches from liquid to vapor, and the Lagrangian particles always represent droplets instead of representing first bubbles and then droplets. Further, the size and velocity distribution of the dispersed phase must be provided as input for an Euler–Lagrange model. An alternative approach solves the full set of conservation equations of both phases, coupled with suitable mass, momentum, and energy exchange terms, on an Eulerian grid. This approach can be simplified by assuming a no-slip condition between the phases and solving for a pseudo mixture fluid. Then, an additional scalar transport equation, typically representing the mass or volume fraction, suffices to distinguish between the two phases. This approach is commonly referred to as the one-fluid model. In addition, models such as volume of fluid, level-set, or piecewise linear interface capturing (PLIC) can be chosen to resolve the phase interface (Dyadechko and Shashkov, 2005). However, for the investigated flashing case, it is not possible to resolve the interface for the large range of length scales on a macroscopic level

* Corresponding author.

E-mail address: andreas.kronenburg@itv.uni-stuttgart.de (A. Kronenburg).

with a reasonable computational effort. Hence, no interface is resolved in this work, and droplets or bubbles are modeled on a sub-grid scale, which is commonly applied to simulate flashing sprays (Schmidt et al., 2010; Guo et al., 2021; Lee et al., 2009; Lyras et al., 2019; Mohapatra et al., 2020; Saha et al., 2017; Neroorkar et al., 2011). Independent of the modeling choice, the mass transfer rates for nucleation, bubble growth, and droplet evaporation have to be modeled. Several models to describe single bubble growth or droplet evaporation exist in the literature. However, most require knowledge about the existing size distribution or phase interface area. A simple yet powerful and proven model is the homogeneous relaxation model (HRM) (Bilicki and Kestin, 1990), which does not require this information and can be directly applied to one-fluid simulation types. This model combines the deviation to equilibrium conditions with a relaxation time scale. A formulation for the relaxation time has been found by using empirical coefficients fitted to flashing water experiments (Downar-Zapolski et al., 1996). Despite being fitted to one fluid, the model has shown a wide range of applicability for various fluids and flashing conditions. In addition to the complex physics of flash evaporation, compressibility effects such as shocks have been observed for flashing sprays (Vieira and Simões-Moreira, 2007; Lamanna et al., 2014; Poursadegh et al., 2018). The evaporation of liquid within the injector causes the vapor–liquid mixture to exit with a higher than ambient pressure, leading to a shock system well known from underexpanded gaseous jets (Franquet et al., 2015). Hence, for a faithful representation of the spray dynamics, the numerical model must be able to capture the present transonic effects. Typical density-based solvers are not well suited for the all Mach-Number regime with compressible and nearly incompressible parts of the spray. Therefore, a pressure-based, two-phase solver has been developed in OpenFOAM. The capability to capture the shock system of flashing sprays was validated with flashing acetone experiments, in which the shock system could be visualized (Gärtner et al., 2020). Using the one-fluid method, however, has the drawback that the information about droplet sizes and phase interface area is lost, which is a crucial spray characteristic and essential for the succeeding ignition. Vallet et al. (2001) proposed to include the transport of an interface density scalar, comparable to the flame surface density for combustion simulations, for mechanical spray break-up of agricultural sprays to recover the lost information about the droplet size. This model approach is called the Eulerian–Lagrangian spray atomization model (ELSA) and relies entirely on the information of the Eulerian grid and avoids the problem of fixing the carrier and dispersed phase throughout the simulation. This model has been extended and validated with a theoretical DNS test case of a mechanical spray break-up by Lebas et al. (2009). Even though the model had been developed initially for primary atomization, some attempts have recently been made to extend the model to flashing sprays (Rachakonda et al., 2019; Lyras et al., 2019). The results seem acceptable, however, important differences in the dynamics of the spray breakup due to flashing were ignored and future models need to be developed to better respect the underlying physics of the breakup process.

In this work, we propose an extension of the existing ELSA framework for flashing sprays based on DNS results (Loureiro et al., 2021). First, the standard ELSA model without phase change is implemented and validated before additional terms representing the flashing break-up and droplet evaporation are added. The newly developed model is then applied to a cryogenic liquid nitrogen test case, where droplet sizes have been measured along the center line. This test case mimics the condition present for injection of cryogenic fuels at high altitudes and has been experimentally investigated at the DLR Lampoldshausen (Rees et al., 2020). The results are further compared to the standard ELSA model and a second model from the literature to investigate the importance of inclusion of the flashing process for spray breakup and droplet formation.

2. Numerical modeling

A compressible, pressure-based, two-phase solver with phase change has been developed in OpenFOAM to simulate sprays under flashing conditions. This solver treats the compressibility of each phase separately, allowing for regions of nearly incompressible liquid, liquid–vapor mixtures as well as regions of nearly pure vapor. The capability of the solver to predict the shock size and position for flashing sprays could be validated with flashing acetone experiments, for which unambiguous measurements of the shock front exist (Gärtner et al., 2020). In contrast to typical one fluid approaches, the solver uses separate energy transport equations for both phases. This separation of the two phases is required due to the significant temperature differences between the two phases at the same location (Gärtner et al., 2020). With this adaption, the governing equation system is given by

$$\frac{\partial \bar{\rho}_L \tilde{\alpha}}{\partial t} + \nabla \cdot (\bar{\rho}_L \tilde{\alpha} \tilde{\mathbf{u}}) + \nabla \cdot (\bar{\rho}_L \alpha'' \mathbf{u}'') = \bar{m}_L, \quad (1)$$

$$\frac{\partial \bar{\rho} \tilde{\mathbf{u}}}{\partial t} + \nabla \cdot (\bar{\rho} \tilde{\mathbf{u}} \tilde{\mathbf{u}}) = -\nabla \bar{p} + \bar{\rho} \mathbf{g} + \nabla \cdot \tilde{\boldsymbol{\tau}}, \quad (2)$$

$$\begin{aligned} \bar{\rho} \frac{D \tilde{h}_L}{Dt} + \bar{\rho} \frac{D \tilde{K}}{Dt} &= \left(\frac{\partial \bar{p}}{\partial t} + \nabla \cdot \left(\frac{k_{L, \text{Eff}}}{c_p} \nabla \tilde{h}_L \right) \right) \\ &+ \frac{\bar{p}}{\bar{\rho}_L \tilde{\alpha}_L} \bar{m}_L (h_{\text{SG}}(p) - \tilde{h}_L), \end{aligned} \quad (3)$$

$$\begin{aligned} \bar{\rho} \frac{D \tilde{h}_G}{Dt} + \bar{\rho} \frac{D \tilde{K}}{Dt} &= \left(\frac{\partial \bar{p}}{\partial t} + \nabla \cdot \left(\frac{k_{G, \text{Eff}}}{c_p} \nabla \tilde{h}_G \right) \right) \\ &+ \frac{\bar{p}}{\bar{\rho}_G \tilde{\alpha}_G} \bar{m}_L (\tilde{h}_G - h_{\text{SG}}(p)), \end{aligned} \quad (4)$$

where the liquid volume fraction α is defined as $\alpha = V_L/V$. The variables ρ and p without subscript are the mixture density and pressure with the overbars denoting Reynolds averages. We define the averaged mixture density $\bar{\rho}$ with

$$\bar{\rho} = \bar{\rho}_L \tilde{\alpha}_L + \bar{\rho}_G (1 - \tilde{\alpha}_L). \quad (5)$$

The averaged phase densities, $\bar{\rho}_L$ and $\bar{\rho}_G$, are obtained from the equation of state using the mean temperature and pressure. Further, \mathbf{u} , K , $\boldsymbol{\tau}_t$, h , k_{Eff} , \mathbf{g} represent the mixture velocity vector, kinetic energy, turbulent viscous stress tensor, enthalpy, effective thermal conductivity and gravity, respectively. The tildes and double prime superscripts denote Favre averages and their fluctuations. The subscripts “L” and “G” refer to the fluid properties of the respective phase, while properties without an index are volume-averaged quantities. The subscript “SG” denotes the saturation conditions of the vapor phase. Note that the equation system presented above is applicable for a RANS and LES framework.

The turbulent viscous stress, $\boldsymbol{\tau}_t$, includes the turbulent contributions of unresolved stresses in the momentum equation, which needs to be modeled according to the chosen turbulence model of RANS or LES. In the energy equation the unresolved turbulent contributions are modeled with the effective conductivity $k_{\text{Eff}} = k_t + k$, which is the sum of laminar and turbulent conductivities. Here, the turbulent conductivity is calculated with the turbulent Prandtl number, Pr_t ,

$$k_t = \rho \frac{\nu_t}{Pr_t}. \quad (6)$$

For the results presented in this work, the turbulent Prandtl number is set to 1.0.

To close the turbulent contributions of the volume fraction transport equation, $\nabla \cdot (\bar{\rho}_L \alpha'' \mathbf{u}'')$, the gradient diffusion assumption of Anez et al. (2019) is used,

$$-\nabla \cdot (\bar{\rho}_L \alpha'' \mathbf{u}'') = \bar{\rho}_L \nabla \cdot \left(\frac{\nu_t}{Sc_t} \nabla \tilde{\alpha} \right). \quad (7)$$

Here, ν_t is the turbulent viscosity and Sc_t the turbulent Schmidt number, which is set to $Sc_t = 0.5$ (Tominaga and Stathopoulos, 2007). A

detailed derivation of the equation system can be found in Gärtner et al. (2020).

The empirical homogeneous relaxation model (HRM) is chosen to model the mass transfer, \dot{m}_L . This model describes the change of mass fraction, χ , as being proportional to the difference to equilibrium conditions combined with a relaxation time, Θ , (Downar-Zapolski et al., 1996)

$$\frac{D\chi}{Dt} = -\chi \frac{h_L(p, T) - h_{SL}(p)}{h_{SG}(p) - h_{SL}(p)} \frac{1}{\Theta} = \frac{\dot{m}_L}{\rho}. \quad (8)$$

Here, χ is the mass fraction of liquid (Gärtner et al., 2020), h_L the enthalpy of the superheated liquid, h_{SG} and h_{SL} the saturation conditions at the current pressure p . The relaxation time is based on a constant factor Θ_0 , the void fraction, ϵ , and the normalized pressure difference, ψ ,

$$\Theta = \Theta_0 e^{\beta \psi^\lambda}, \quad (9)$$

$$\epsilon = \left(\frac{\rho_L - \rho}{\rho_L - \rho_v} \right), \quad (10)$$

$$\psi = \left(\frac{p_s(T) - p}{p_c - p_s(T)} \right), \quad (11)$$

with $p_s(T)$ denoting the saturation pressure and p_c the critical pressure of the fluid. The high-pressure fit coefficient for Θ_0 and the exponents β and λ of Downar-Zapolski et al. (1996) have shown in previous works a good agreement with the flashing behavior of cryogenic liquid nitrogen (Gärtner et al., 2020). Therefore, the high-pressure fit coefficients of $\Theta_0 = 3.84 \times 10^{-7}$, $\beta = -0.54$, and $\lambda = -1.76$ are selected for this work.

3. Standard ELSA model

The Eulerian–Lagrangian Spray Atomization (ELSA) model was originally developed to study atomization in high Weber and Reynolds number and highly variable density flows (Vallet et al., 2001). The main idea of the model is to represent the unresolved interface as a transported scalar, Σ , which represents the mean interfacial area per unit volume, similar to the transport of a flame surface density. The transport equation of the surface density equation is given with

$$\frac{\partial \Sigma}{\partial t} + \nabla \cdot (\Sigma \tilde{\mathbf{u}}) = S_\Sigma, \quad (12)$$

where S_Σ constitutes all source terms for the surface density due to primary spray break-up, droplet coalescence, secondary break-up, and phase change. Time averaging the equation results in

$$\frac{\partial \bar{\Sigma}}{\partial t} + \nabla \cdot (\bar{\Sigma} \tilde{\mathbf{u}}) + \nabla \cdot (\bar{\Sigma} \tilde{\mathbf{u}} - \bar{\Sigma} \tilde{\mathbf{u}}) = \bar{S}_\Sigma, \quad (13)$$

and an unclosed turbulent flux term appears. Following a similar analogy as for the volume fraction transport equation, the unclosed term is modeled with the gradient diffusion approach (Anez et al., 2019; Versteeg and Malalasekera, 2007; Vallet et al., 2001),

$$(\bar{\Sigma} \tilde{\mathbf{u}} - \bar{\Sigma} \tilde{\mathbf{u}}) = -\frac{v_t}{Sc_t} \nabla \bar{\Sigma}. \quad (14)$$

This model has been validated for the primary spray break-up of a Diesel spray by Lebas et al. (2009) by comparing the model to DNS results of Ménard et al. (2007). Further, Lebas et al. proposed a closed set of source terms for the primary and secondary spray break-up without phase change, leading to the following transport equation,

$$\frac{\partial \bar{\Sigma}}{\partial t} + \nabla \cdot (\bar{\Sigma} \tilde{\mathbf{u}}) = \nabla \cdot \left(\frac{v_t}{Sc_t} \nabla \bar{\Sigma} \right) + \Psi \left[\bar{S}_{\text{init}} + \bar{S}_{\text{turb}} \right] + (1 - \Psi) \left[\bar{S}_{\text{coll}} - \bar{S}_{\text{2ndBrk}} \right]. \quad (15)$$

Here, the source terms are split into a dense and dilute treatment. The dense part constitutes the region where a liquid core exists, and no droplets can be defined. In contrast, the dilute region denotes the spray behavior after the primary break-up, when droplets have already formed. The two modeling regimes are coupled by an indicator

function, Ψ , which blends between them based on the liquid volume fraction,

$$\Psi(\alpha) = \begin{cases} \alpha < 0.1; & 0 \\ 0.1 \geq \alpha \geq 0.5; & 2.5\alpha - 0.25 \\ \alpha > 0.5; & 1 \end{cases}$$

In the following, the description for the individual source terms are presented. For simplicity, the averaging operators are omitted and variables denote the averaged quantity as calculated and stored during the simulation.

3.1. Principal model design of the source terms

Except for the initialization term, all source terms follow the same principal design, in which the surface density is relaxed towards a so-called equilibrium value, Σ^{eq} , with a given relaxation time τ ,

$$S_\Sigma = \frac{C}{\tau} \Sigma \left(\frac{\Sigma^{\text{eq}} - \Sigma}{\Sigma^{\text{eq}}} \right). \quad (16)$$

Here, C is a modeling constant and is typically set to unity unless otherwise noted. The different source terms for the turbulent break-up, secondary break-up, or phase change then only differ in their relaxation time and equilibrium value. To derive the equilibrium surface density the modified Weber number definition is used,

$$We^* = \frac{E_{\text{kin}}}{E_{\text{surf}}} = \frac{\rho u^2 L}{12\sigma}, \quad (17)$$

with a characteristic density ρ , velocity u , length scale L and σ representing the surface tension. By setting the characteristic length scale to the Sauter mean diameter of the droplet D_{32} , which relates the mean droplet volume to the mean surface area, the Weber number can be related to the surface density (Lebas et al., 2009),

$$L = D_{32} = \frac{6\alpha}{\Sigma}. \quad (18)$$

Hence, the equilibrium surface density value can be obtained with

$$\Sigma^{\text{eq}} = \frac{\alpha \rho u^2}{2\sigma We^{\text{eq}}}, \quad (19)$$

where We^{eq} is the so-called equilibrium Weber number and is a model parameter.

3.2. Source terms for the dense region

To initialize the surface density, the liquid-gas mixture model of Beau et al. (2006) is used. It assumes that the first wrinkles in the jet surface or liquid blobs have the size of the turbulent length scale,

$$S_{\text{init}} = \frac{12\rho^2 v_t}{\rho_L \rho_G Sc_t l_t} (\nabla \chi_L \cdot \nabla \chi_L). \quad (20)$$

Here χ_L is the liquid mass fraction, and, based on the $k - \epsilon$ model, the large-scale turbulent length scale, l_t , is defined as

$$l_t = C_\mu^{0.75} \frac{k^{\frac{3}{2}}}{\epsilon}, \quad (21)$$

with k being the turbulent kinetic energy and ϵ being the turbulent dissipation rate. This source term can be seen as an initialization of surface density once liquid and gas mix directly at the injector exit, where the mass gradients are high. However, the gradients diminish shortly after the injector exit, and the term becomes negligible compared to the other source terms. Hence, it is only active directly after the injector exit, establishing a surface density value, as expected of an initialization term. For the dense, turbulent source term, the modified approach of Duret et al. (2013) is implemented in this work for the equilibrium surface density. This formulation uses an arithmetic mean

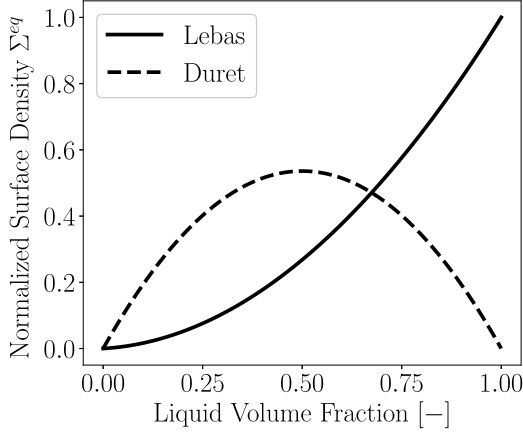


Fig. 1. $\Sigma_{\text{dense}}^{\text{eq}}$ for the model of Lebas et al. (2009) and Duret et al. (2013) normalized by the maximum value of the model of Lebas et al.

of the densities combined with an indicator function for maximum liquid vapor interface (Lebas et al., 2009),

$$\Sigma_{\text{dense}}^{\text{eq}} = 4 \frac{(\alpha(1-\alpha)(\rho_L + \rho_G)k}{2\sigma \text{We}_{\text{dense}}^{\text{eq}}}. \quad (22)$$

Eq. (22) satisfies the principal source term design as presented in Section 3.1 and following Duret et al. (2013), we set $\text{We}_{\text{dense}}^{\text{eq}}$ to unity. Eq. (22) differs from the original model by Lebas et al. (2009) with

$$\Sigma_{\text{dense}}^{\text{eq}} = \frac{\alpha(\alpha\rho_L + (1-\alpha)\rho_G)k}{\sigma \text{We}_{\text{dense}}^{\text{eq}}}. \quad (23)$$

The difference between the two models is a more faithful representation of the physical processes in the former, as the surface density value should reach a maximum for an equal mixture of liquid and gas, whereas it is zero in the extreme of pure liquid or gas. The difference between the two models is visualized in Fig. 1. For the relaxation time τ , the turbulent time scale is chosen in both models. Here the turbulent time scale is again based on the $k-\epsilon$ model and defined as (Lebas et al., 2009; Beau et al., 2006)

$$\tau_t = \frac{k}{\epsilon}. \quad (24)$$

3.3. Source terms for the dilute region

After the primary spray break-up and the formation of droplets, the change of the surface density is governed by the dilute source terms. Here, surface density can be created or destroyed through droplet collision or coalescence, S_{coll} , or surface density is generated through the secondary break-up, $S_{2\text{ndBrk}}$. The droplet collision or coalescence is based on particle collision theory and uses turbulent kinetic energy to derive a time scale. The equilibrium surface density is calculated by

$$\Sigma_{\text{coll}}^{\text{eq}} = \Sigma \left[\frac{6 + \text{We}}{6 + \text{We}_{\text{crit}}} \right] \quad (25)$$

with

$$\text{We} = \frac{4\alpha\rho^*k}{\sigma\Sigma}. \quad (26)$$

Here, the parameter We_{crit} is a model parameter separating the break-up and coalescence regime and set to 12 by default (Lebas et al., 2009). In Eq. (26), the Weber number definition is modified from the original model and uses a modified density definition,

$$\rho^* = 4.0 * (\rho_L - \rho)(\alpha - 0.5)^2 + \rho. \quad (27)$$

This is based on the idea that in the limit of $\lim_{\alpha \rightarrow 0}$, the Weber number is based on droplets, hence should use the liquid density. Whereas in

the transition region of the spray break-up, when $\alpha = 0.5$, the density of the mixture should be used. The time scale is modeled as a collision time based on the turbulence kinetic energy (Lebas et al., 2009),

$$\tau_{\text{coll}} = \frac{1}{\Sigma \sqrt{\frac{2}{3}k}}. \quad (28)$$

In addition to droplet collision/coalescence, the secondary break-up of droplets can occur in the dilute region. The equilibrium surface density, due to the break-up of droplets, is expressed by

$$\Sigma_{2\text{ndBrk}}^{\text{eq}} = \frac{6\alpha\rho_G u_{\text{rel}}^2}{\sigma \text{We}_{2\text{ndBrk}}^{\text{eq}}}. \quad (29)$$

By default the equilibrium Weber number, $\text{We}_{2\text{ndBrk}}^{\text{eq}}$, is set to 12 (Lebas et al., 2009). The relative velocity between the two phases, u_{rel} , is modeled by

$$u_{\text{rel}} = \frac{R}{\chi_L(1-\chi_L)}, \quad (30)$$

with R being based on the gradient approach (Lebas et al., 2009) and defined as

$$R = -\frac{v_t}{\text{Sc}_t} \nabla \chi_L. \quad (31)$$

In Eq. (30) χ_L is the liquid mass fraction. Note that this is very similar to the closure used for the volume fraction transport equation. The time scale $\tau_{2\text{ndBrk}}$ is defined by

$$\tau_{2\text{ndBrk}} = T \frac{D}{u_{\text{rel}} \sqrt{\frac{\rho_L}{\rho_G}}}. \quad (32)$$

The factor T comes from Pilch and Erdman (1987) (Eq. (6) therein) and is calibrated for spray break up initiation,

$$T = 1.9(\text{We}_{2\text{ndBrk}} - 12)^{-0.25} (1.0 + 2.2\text{Oh})^{1.6}. \quad (33)$$

The Ohnesorge, Oh , and the Weber number for secondary break-up are defined by

$$\text{Oh} = \frac{\mu_L}{\sqrt{\rho_L \sigma D_{32}}} \quad (34)$$

and

$$\text{We}_{2\text{ndBrk}} = \frac{\rho_G u_{\text{rel}}^2 D_{32}}{\sigma}, \quad (35)$$

respectively.

3.4. Validation of the standard ELSA model

The correct implementation of the presented ELSA model in our OpenFOAM two-phase solver for flashing flow is validated by comparison of 3D RANS with DNS results of Lebas et al. (2009). The results show that the model reproduces the DNS results within the given uncertainty. Therefore, the effects of the aerodynamic break-up can be faithfully represented, providing a validated code-basis to add the source terms accounting for the phase change and spray break-up of flashing sprays. More details on the validation of the ELSA model can be found in Appendix.

4. Extension of the ELSA model to flashing cases

In the literature, some authors have applied the standard ELSA model to flashing cases as is or with only one additional phase change term (Rachakonda et al., 2019; Lyras et al., 2019). However, this neglects the fundamental differences in the spray break-up of flashing sprays compared to the primary aerodynamic spray break-up. Whereas shear forces and turbulence are the dominating factors for an aerodynamic spray break-up, flashing sprays are characterized by nucleation, bubble growth, merging, and succeeding spray break-up. Hence, the

physical mechanism to drive the change of phase interface area is fundamentally different from an aerodynamic spray break-up. This affects all source terms in the dense model region. The generation of surface density due to the turbulent flow stretching and collision/coalescence, $\overline{S}_{\text{turb}}$, has been removed for the flashing case, as this term represents turbulent effects that are absent in the dense part of the flashing spray. Further, the source term design is based on an equilibrium value determined by characteristic turbulent scales (see Eq. 16). This value is, however, significantly lower than the surface density generated by bubble growth and would therefore lead here to a significant destruction of surface density. This is unphysical and motivates the removal of this source term.

The terms in the dilute region need to be expanded with an evaporation term, as droplet evaporation will be important and potentially contribute to changes in surface area of the order of the collision/coalescence and secondary droplet break-up source terms. Therefore, we propose a modified surface density transport equation,

$$\frac{\partial \Sigma}{\partial t} + \nabla \cdot (\Sigma \mathbf{u}) = \nabla \cdot \left(\frac{v_i}{Sc_i} \nabla \Sigma \right) + \Psi^* [S_{\text{init}} + S_{\text{evap,dense}}] + (1 - \Psi^*) [S_{\text{evap,dilute}} + S_{\text{coll}} + S_{\text{2ndBrk}}], \quad (36)$$

with $\Psi^*(\alpha)$ as a phase indicator function based on the volume fraction. The indicator function, Ψ^* , is modified from the expression given in Section 3 with the assumption that spray break-up has fully occurred for a volume fraction of the closest sphere packing, $V_G/V \approx 0.74 \Rightarrow \alpha = 0.26$. The blending to the dense treatment of bubble growth and coalescence for a liquid volume fraction larger than 0.5 shall be described by

$$\Psi^*(\alpha) = \begin{cases} \alpha < 0.26; & 0 \\ 0.26 \leq \alpha \leq 0.5; & \frac{\alpha}{0.24} - \frac{0.52}{0.48} \\ \alpha > 0.5; & 1 \end{cases}$$

The difference between the new indicator function to the standard ELSA model and a sketch of the different regimes is shown in Fig. 2.

4.1. Source terms for flashing sprays in the dense region

The initialization term of the standard ELSA model, Eq. (20), is built on the assumption that the first wrinkles of the size of the turbulent length scale generate the surface density. For flashing cases, however, the first interphase area is generated through nucleating bubbles, often already within the injector. These bubbles then start to grow until they merge and cause spray break-up and the generation of droplets (Loureiro et al., 2021). Hence, the surface density is generated through nucleating bubbles, which grow until the final bubble merging radius, R_f , is reached and the spray breaks up. Therefore, one can define a new initialization source term based on the minimum surface density of the bubbles generated and using Eq. (18) we obtain

$$\Sigma_{\text{min}} = \frac{3(1 - \alpha)}{R_f}. \quad (37)$$

Also note that the vapor volume fraction, $(1 - \alpha)$, is used. The initial source term then relaxes towards this minimum value with a relaxation time τ based on the bubble growth rate

$$S_{\text{init,ev}} = \frac{1}{\tau} (\Sigma_{\text{min}} - \Sigma), \quad (38)$$

with

$$\tau = \frac{R_f}{\frac{\partial R_f}{\partial t}}. \quad (39)$$

The bubble growth rate is modeled using the heat diffusion limit of Prosperetti (2017),

$$\frac{\partial R}{\partial t} = \frac{12}{\pi} \frac{\kappa \text{Ja}^2}{\rho_L c_p R}. \quad (40)$$

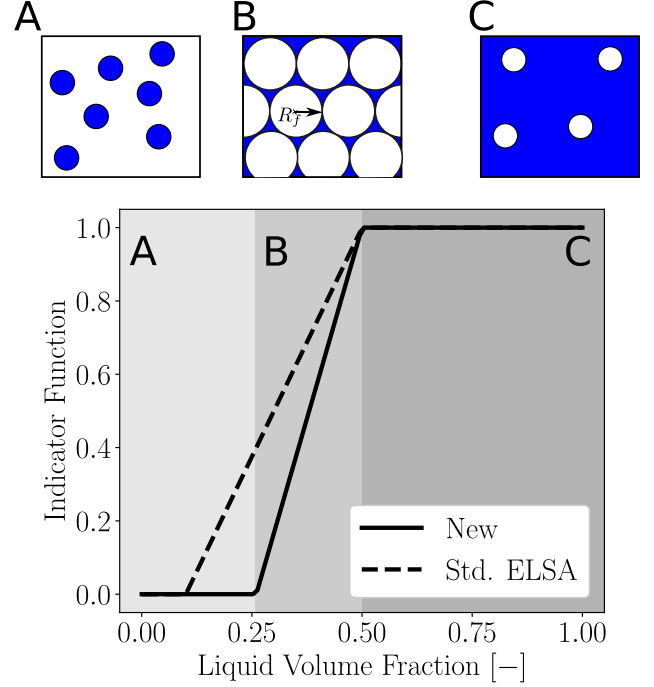


Fig. 2. Indicator function and comparison of dense spray turbulent source term modeling for surface density transport. The qualitative spray bubble/droplet morphology for each region of the liquid volume fraction is sketched above, blue is liquid and white represents vapor. The radius of the bubbles when they merge and the spray break-up occurs is marked with R_f . (For interpretation of the references to color in this figure legend, the reader is referred to the web version of this article.)

Here, the Jakob number, Ja , is defined as

$$Ja = \frac{\rho_L c_p (T_L - T_{\text{sat}}(p))}{\rho_G L_v}, \quad (41)$$

with L_v representing the latent heat. Note, that this term describes the surface density generation due to nucleation and bubble growth, but not due to the merging of the bubbles and the resulting spray break-up. The surface density generation due to spray break-up is described in the next paragraph.

In contrast to aerodynamic spray break-up, the surface density generation in the dense region should not be described by a turbulent time scale and turbulent kinetic energy. Instead, a formulation based on the spray break-up process seems more physical. Following the source term design of Lebas et al. (2009) an equilibrium surface density value has to be found, see Eq. (19). Here, the length scale is the droplet diameter D_{32} that results from the spray break-up just after the merging of the bubbles; But instead of using the turbulent kinetic energy, the velocity scale is the bubble growth rate, $\partial R/\partial t$, at the time of the spray break-up. As indicated above and verified by previous DNS studies (Loureiro et al., 2021; Dietzel et al., 2019), the dynamics of the bubbles prior to merging or more precisely, the growth rate at the time of merging, is one main parameter that determines the spray break-up process. The equilibrium surface density value is then obtained from

$$\Sigma_{\text{ev}}^{\text{eq}} = \frac{\rho_L \alpha R_f^2}{2 \text{We}_{\text{ev}}^{\text{eq}} \sigma}, \quad (42)$$

where $\text{We}_{\text{ev}}^{\text{eq}}$ is again a model parameter. Here, even though the bubble growth rate is used, the generated surface density represents the spray break-up and the generation of the droplets and not the bubbles (Loureiro et al., 2018, 2021). Loureiro et al. (2021) have studied the bubble growth and spray break-up behavior of flashing cryogenic oxygen and provided a theoretical estimate for the resulting droplet

diameter,

$$D_{\text{ref}} = \frac{8\sigma}{\rho_L \dot{R}_f^2}. \quad (43)$$

With $D_{32} = \frac{6\alpha}{\Sigma}$ we get

$$\Sigma = \frac{3\rho_L \alpha \dot{R}_f^2}{4\sigma}. \quad (44)$$

Combining Eq. (42) with (44) gives the equilibrium Weber number for flashing cryogenic flows as $We_{\text{ev}}^{\text{eq}} = 2/3$. Detailed DNS indicated, however, that a correction factor is needed and the resulting droplet diameter after spray break-up can be approximated by Loureiro et al. (2021),

$$D = 0.294 \sqrt{We_b} D_{\text{ref}}. \quad (45)$$

Hence, the corrected Weber number is

$$We_{\text{ev,corr}}^{\text{eq}} = 0.294 \sqrt{We_b} We_{\text{ev}}^{\text{eq}}, \quad (46)$$

and is implemented in the ELSA model using a corresponding pre-factor to the uncorrected equilibrium surface density,

$$\Sigma_{\text{ev,corr}}^{\text{eq}} = \frac{3.4}{\sqrt{We_b}} \Sigma_{\text{ev}}^{\text{eq}}. \quad (47)$$

The bubble Weber number, We_b , is here defined according to Loureiro et al. (2021) with,

$$We_b = \frac{2R_f \rho_L \dot{R}_f^2}{\sigma}. \quad (48)$$

The final source term for the surface density is then given by,

$$S_{\text{evap,dense}} = \frac{1.0}{\tau} \Sigma \left(\frac{\Sigma_{\text{ev,corr}}^{\text{eq}} - \Sigma}{\Sigma_{\text{ev,corr}}^{\text{eq}}} \right). \quad (49)$$

The time scale, τ , is the same as for the initialization term and given by Eq. (39).

4.2. Estimating the final bubble merging radius

It is evident that a suitable estimate of the final bubble merging radius, R_f , is essential to get valid results and for the model to have predictive capabilities. Starting from the critical radius of bubble nuclei, R_{crit} , the final bubble merging radius can be described as a multiple of R_{crit} ,

$$R_f^* = \frac{R_f}{R_{\text{crit}}}. \quad (50)$$

This normalized bubble radius, R_f^* , can be estimated as

$$R_f^* = \left(\frac{4}{3} \pi n_b R_{\text{crit}}^3 \left[\frac{1}{\eta} - 1 + \frac{\rho_G}{\rho_L} \right] \right)^{-1/3}. \quad (51)$$

The parameter n_b and η are the bubble number density and the vapor volume fraction at merging (Loureiro et al., 2021). Here, the densest packing of spheres with $\eta = 0.74$ is assumed, consistent to the assumption made for the indicator function Ψ^* . Note that this equation respects the decrease in bubble number density due to spatial expansion of the fluid volume during bubble growth. The main challenge is to determine the bubble number density n_b . Often, the homogeneous nucleation model from the classical nucleation theory (CNT), such as the one presented by Blander and Katz (1975) or Carey (2020), is selected in the literature to estimate the nucleation rate for flashing flows (Lamanna et al., 2014). However, these models predict zero nucleation for the conditions present in the flashing cryogenic LN2 case (see Table 1 and Fig. 3). This insufficiency of theoretical models, is a well-known phenomenon, despite the apparent flashing behavior of the spray (Liao and Lucas, 2017a). To reach realistic nucleation rates of the order of $1 \times 10^{15} \text{ m}^{-3} \text{ s}^{-1}$ for the investigated cases, previous studies modified the surface tension (Bossert et al., 2023). However, the

measured correction factors in the range of 1.0 to 1.25 (Bossert et al., 2023) would not suffice and significantly larger reduction by a factor of around 8 would be needed. In addition, changes in surface tension would still not change the nucleation rates very strong sensitivity on temperature. This is shown in Fig. 3 where the nucleation rate predicted by the CNT model for the cryogenic nitrogen is plotted. On the right, the nucleation rate, J , is normalized by its value at $T=90 \text{ K}$. It clearly shows, how already minor changes in the temperature lead to an extreme increase or decrease of J due to its exponential temperature dependence. Further, the superheat limit, when homogeneous nucleation occurs, is predicted at a liquid temperature of about 110 K, which is significantly higher than that of flashing nitrogen in the setup with $T = 90 \text{ K}$ that is investigated here.

The discrepancy between the theoretical model and the experimental observation indicates the importance of a different nucleation mechanism, namely heterogeneous nucleation (Gallo et al., 2021; Liao and Lucas, 2017a,b). To account for this behavior, some researchers have added a correction factor to the exponential term of the nucleation model (Liao and Lucas, 2017a; Valero and Parra, 2002). The obvious disadvantage is that the newly introduced parameter has to be matched to experiments and lacks any predictive capability. Independent of this correction factor, the homogeneous nucleation model exhibits an extremely strong sensitivity towards the relevant input parameters for the thermodynamic conditions typical for flash evaporation. Within a certain range, small pressure and temperature variations around the bubble trigger huge jumps in nucleation rates such that the homogeneous nucleation model effectively acts like an on/off switch (see also Fig. 3) and is unlikely to capture the physics of the onset of bubble nucleation and its variation with surrounding thermodynamic conditions, namely the temperature, correctly.

Two types of heterogeneous nucleation models can be distinguished: heterogeneous wall and heterogeneous bulk nucleation. The first type requires knowledge about the wall roughness or structure to determine the nucleation rate (Shin and Jones, 1993). Further, the hydrophilic properties of the wall affect the heterogeneous and bulk nucleation in the flow as well (Gallo et al., 2021). The heterogeneous bulk nucleation is typically modeled by adding a correction factor to the classical nucleation theory, as has been indicated above. The correction factor significantly alters the equation and can be of the order of 1×10^{-6} (Liao and Lucas, 2017a). Due to these complex, and often unknown, interactions we propose here to use the amount of dissolved gases as an estimation parameter (Martin, 2023; Kwak and Oh, 2004). Typically, working fluids or fuels in technical applications are not pure substances but contain potential nucleation sites, such as dissolved gases. This aspect is often not considered in numerical applications, and pure fluids are assumed despite all indications that impurities serve as nucleation kernels (Kwak and Oh, 2004; Martin, 2023). Due to the significant difference of $\Delta T \approx 20 \text{ K}$ to the superheat limit predicted by CNT for the investigated cryogenic nitrogen cases, we estimate that the majority of the nucleating bubbles are dissolved gas molecules (Kwak and Oh, 2004). Hence, the bubble number density is calculated with

$$n_b = \frac{3\alpha_d}{4\pi R_{\text{crit}}^3}, \quad (52)$$

where α_d represents the volume ratio of the dissolved gas in the fluid, which is here modeled as being in the form of bubbles with R_{crit} . The variable R_{crit} represents the critical radius, which describes the minimum stable vapor bubble size in a superheated liquid (Carey, 2020).

Combining Eqs. (52) and (51) gives then

$$R_f^* = \left(\alpha_d \left[\frac{1}{\eta} - 1 + \frac{\rho_G}{\rho_L} \right] \right)^{-1/3}, \quad (53)$$

which is independent of the critical radius. Due to the randomized distribution of the nucleating bubbles, however, an equidistant spacing of bubbles cannot be assumed. Hence, bubbles will coalesce before

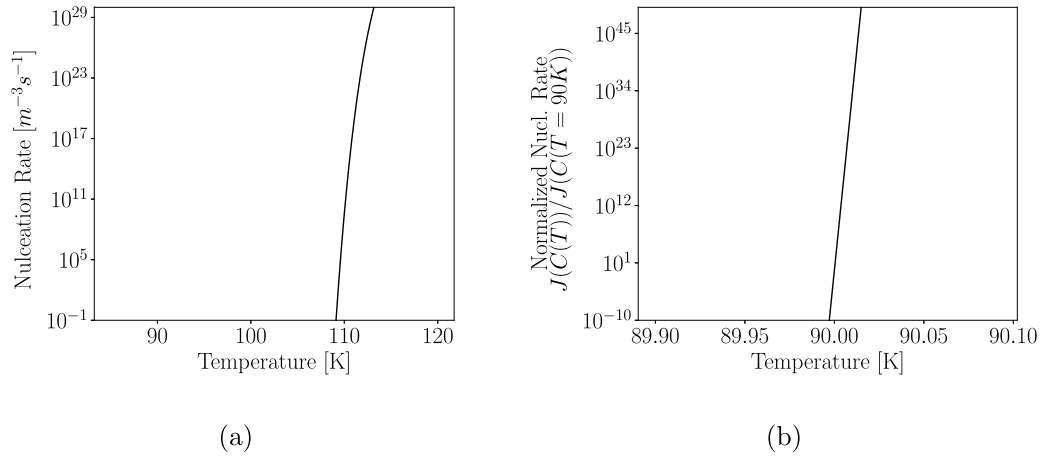


Fig. 3. (a) Nucleation rate predicted by CNT for cryogenic nitrogen. (b) Normalized homogeneous nucleation rate predicted by CNT.

the final spray break-up, which reduces the bubble number at merging (Loureiro et al., 2021). The mean distance between the bubbles can be estimated with probabilistic methods, e.g., of Bhattacharyya and Chakrabarti (2008), which states that the mean distance between the bubbles is about half to an equidistant spacing. However, as the bubble number density, n_b , is affecting the final bubble merging radius, R_f , with the cubed root $R_f \propto \sqrt[3]{1/n_b}$, a reduction of two is not significantly affecting the results. Therefore, as the number of bubbles at merging cannot be exactly determined and considering the uncertainties of the model, the simpler approach with an equidistant spacing of Eq. (53) is used.

In addition to R_f^* , the critical radius has to be determined to calculate the final bubble merging radius R_f , see Eq. (50). It is assumed that the liquid and vapor bubbles are in equilibrium at nucleation, hence the temperatures of the two phases are equal. However, the pressure inside the bubble differs from the liquid pressure due to the curvature of the bubble. This pressure difference is related through the Young–Laplace equation, which gives an expression for the critical radius,

$$R_{\text{crit}} = \frac{2\sigma}{p_{ve} - p}. \quad (54)$$

The pressure inside the bubble, p_{ve} , can be expressed by integrating and rearranging the Gibbs–Duhem equation, which leads to (Carey, 2020),

$$p_{ve} = \exp\left(\frac{p - p_{\text{sat}}(T_L)}{\rho_L R T_L}\right) p_{\text{sat}}(T_L). \quad (55)$$

4.3. Droplet evaporation in the dilute spray regime

Droplets within the dilute spray region have formed and continue to evaporate, which results in a decrease in the surface density. Several models for the approximation of the droplet evaporation are possible, from the Hertz–Knudsen relation to the model of Abramzon and Sirignano (1989). The Hertz–Knudsen model is an often used model for the evaporation of superheated droplets (Lyras et al., 2023; Dinh Le, 2022; Liao and Lucas, 2017a). While the unmodified model is based on statistical thermodynamics, several assumptions have to be made for an application in a CFD code (Persad and Ward, 2016). In particular, the empirical modeling coefficients have to be determined. These coefficients are case-dependent and require fitting before they can be applied (Marek and Straub, 2001; Dietzel, 2020). Further, the Hertz–Knudsen model provides a mass flux per unit area, hence requiring the surface interface area to result in the mass flux per volume required for the volume fraction transport equation, Eq. (1). Typically, this information is not available in a one-fluid context without resolving all droplets, which then requires further modeling (Devassy et al., 2019;

Lyras et al., 2019; Karathanassis et al., 2017). With the ELSA model, this information would be available and could be used in future work to derive a phase change model without assuming a droplet size and distribution. However, in this work, the HRM (cf. Eq. (8)) model used for the volume fraction transport is selected to avoid any inconsistencies between the two transport equations. For a correct prediction of D_{32} the liquid volume fraction must match the surface density. Therefore, the evaporation source term is based on the evaporation rate given by the HRM model. The change of surface density due to evaporating droplets can be described with,

$$\frac{\partial \Sigma}{\partial t} = \frac{4}{D \rho_L} \frac{\partial}{\partial t} (n_d m_d). \quad (56)$$

Here, n_d is the droplet number density and m_d is the mass of one droplet [kg]. The time derivative represents the mass change per volume, hence exactly the value the HRM model calculates. With this, the equation can be rewritten as,

$$\frac{\partial \Sigma}{\partial t} = \frac{\dot{m}_{\text{HRM}}'''}{\rho_L} \frac{4}{D}. \quad (57)$$

Replacing the diameter with the description of the Sauter mean diameter then gives,

$$\frac{\partial \Sigma}{\partial t} = \frac{\dot{m}_{\text{HRM}}'''}{\rho_L} \frac{2}{3\alpha} \Sigma, \quad (58)$$

with the triple prime superscript denoting a mass change per volume (not per droplet).

The modified surface density transport equation together with the proposed modifications of the source terms is called the flashing liquid atomization model (FLAM) to distinguish it from the standard ELSA model.

5. Cryogenic flashing liquid nitrogen test case

The new flashing model is applied to flashing, cryogenic, liquid nitrogen test cases, which mimic the conditions present when cryogenic liquids enter an upper-stage rocket engine in space, see Table 1. The test cases consist of a single-hole injector with an L/D ratio of 2.9 through which cryogenic nitrogen is injected into a low-pressure chamber (Rees et al., 2020). Droplet size measurements, obtained by phase Doppler anemometry (PDA) and shadowgraph images, allow a quantitative comparison of the results. However, only Case A provides a droplet size distribution along the center line. For the cases B and C, one single measurement along the center line is provided only (Rees, 2020). Fig. 4 shows a shadowgraph image of the flashing spray and the velocity magnitude of a 2D simulation. A sketch of the 2D simulation domain is given in Fig. 5. The cell size in the injector is set to 0.02 mm, and turbulence is modeled using the $k-\omega$ SST turbulence model. The boundary

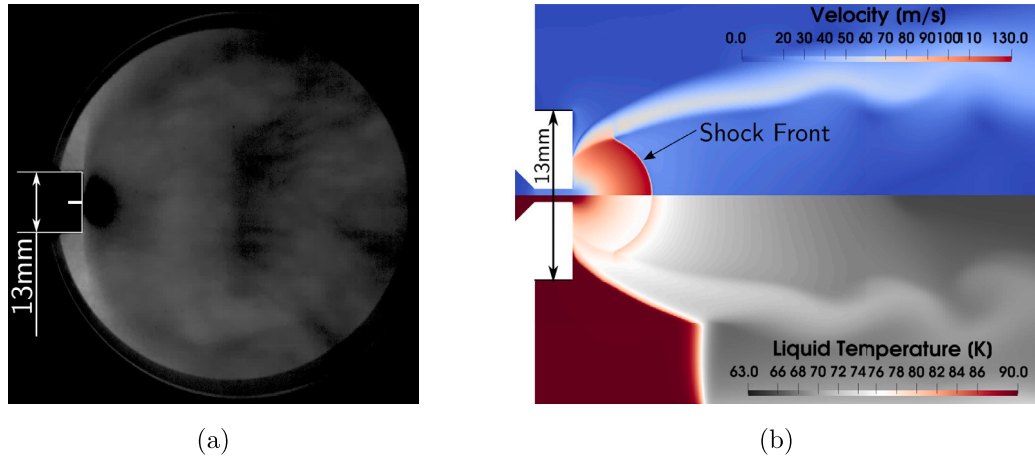


Fig. 4. (a) Shadowgraph image of a flashing LN2 case. (b) Velocity magnitude (top) and liquid temperature (bottom) obtained from the 2D RANS.

Table 1

Injection conditions of the experiment (Rees et al., 2020; Rees, 2020).

Parameter		Case A	Case B	Case C
Inj. temperature	K	89.7 ± 0.6	88	93
Inj. pressure	bar	4.4 ± 0.4	6 ± 6	6 ± 6
Chamber pressure	mbar	73 ± 27	80 ± 27	80 ± 27
Mass flow rate	g/s	10.6 ± 1.7	–	–
Inj. volume fraction	–	0.999	0.999	0.999
Injector diameter	mm	1.0	1.0	1.0
L/D	–	2.9	2.9	2.9
R_p	–	46.8	38	60
$p_{\text{sat}}(T_{\text{inj}})$	bar	3.51	3.03	3.03

Table 2

Boundary conditions of the simulation domain.

Boundary	Variable	Boundary condition
Inlet	p	Total pressure
	T	Fixed value
	U	Zero gradient
Outlet	p	Total pressure
	T	Zero gradient (outflow)
	U	Pressure based flux calculation
Wall	p	Zero gradient
	T	Zero gradient
	U	No slip

Table 3

Numerical schemes used for time and space discretization.

	Scheme
Time	Euler implicit
Volume fraction	van Leer (TVD)
Momentum	Upwind
Enthalpy	Upwind
Surface density	Second order limited linear (TVD)

conditions and employed numerical schemes are listed in Tables 2 and 3. Here, the first-order upwind scheme is used for this investigation to avoid any stability issues at the shock front. Standard TVD schemes of OpenFOAM, such as vanLeer, MUSCL, or linear upwind, lead to some instability at the shock front. This can be overcome by using a WENO scheme, which, however, has problems for 2D cases where the shock touches the centerline. The dependence on the discretization scheme has been assessed, but simulations with the second-order linear upwind scheme of OpenFOAM resulted in no significant difference in the surface density results and therefore, only results from the first-order upwind scheme are reported here due to its superior numerical stability.

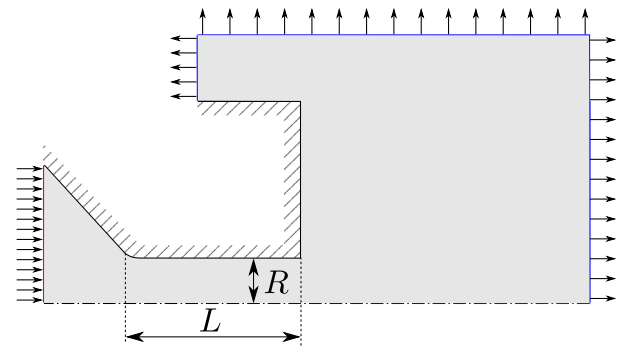


Fig. 5. Sketch of the 2D simulation domain.

5.1. ELSA settings

The new flashing liquid atomization (FLAM) model's main parameters are the final bubble merging radius and equilibrium Weber number, We_{ev}^{eq} . According to the DNS results of Loureiro et al. (2021), the Weber number is set to $We_{ev}^{eq} = 2/3$. The purity of the liquid nitrogen, used in the experiments, is given as $\alpha_{d, \text{std}} = 11.6$ ppm at standard conditions. This can be transformed into a volume fraction using

$$\alpha_d = \frac{p_{\text{std}} T}{p_{\text{sat}}(T_L) T_{\text{std}}} \alpha_{d, \text{std}}. \quad (59)$$

Inserting this into Eq. (53) with $\eta = 0.74$ as the densest packing of spheres gives a normalized final bubble merging radius of $R_f^* = 142$. All other model parameters are set to their default values.

5.2. Results

Case A is investigated first as it provides the most complete set of measurements and includes the evolution of the Sauter mean diameter along the centerline. Further, the new FLAM model is compared to other ELSA models. To estimate the uncertainties of the chosen model parameters, a sensitivity study of the two main parameters R_f^* and We_{ev}^{eq} is conducted. At last, cases A, B, and C are compared to the experimental results to investigate the effect of the superheat R_p on the droplet diameter and the newly developed surface density model.

5.2.1. Reference case A

The evolution of the Sauter mean diameters, D_{32} , of the simulation (black line) and as measured in the experiment (square symbols) are

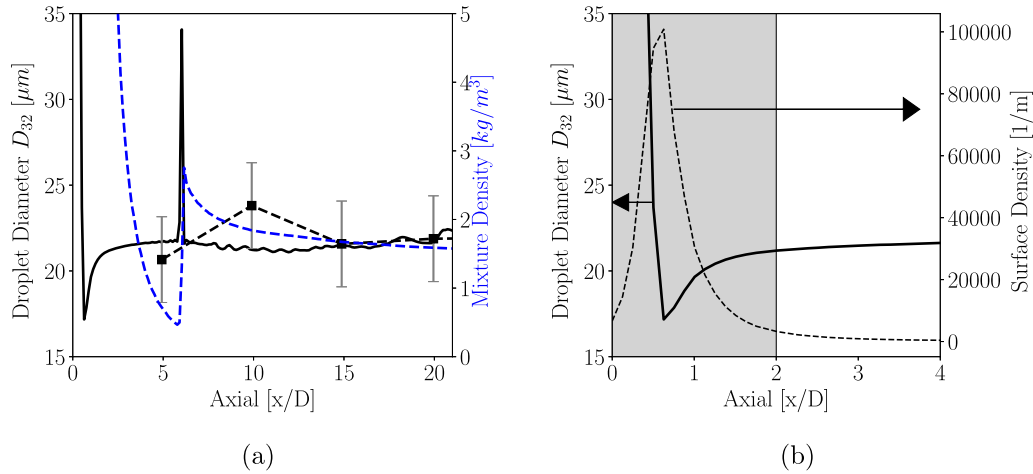


Fig. 6. (a) Mean Sauter diameter, D_{32} , with the model parameters $R_f^* = 140$, $We_{ev}^{eq} = 0.66$. The mixture density is plotted alongside on the right y-axis in blue. Subfigure (b) shows a zoomed in section of the D_{32} evolution, left y-axis, together with the surface density, right y-axis. The gray background marks the area in which the spray break-up occurs and the droplet population has not yet fully formed, hence Eq. (18) for the computation of the droplet diameter does not hold here.. (For interpretation of the references to color in this figure legend, the reader is referred to the web version of this article.)

plotted in Fig. 6. The agreement with experiments is very good but the evolution of D_{32} close to the nozzle warrants some further scrutiny. The evolution shows first a strong decrease, followed by a quick increase from which it stabilizes at a Sauter mean diameter of around $21 \mu\text{m}$. The jump of the droplet diameter at $x/D = 6$ is caused by the shock front, which will result in an accumulation of the surface density and liquid volume fraction. As OpenFOAM uses the corrected implicit–explicit MULES (Lin et al., 2018) method to transport the volume fraction, it differs slightly from the solution procedure of the conventional transport equation for the surface density, which causes slight numerical deviations of the shock front position. Hence, the increase of the surface density and liquid volume fraction over the shock front are not perfectly aligned, causing the observed peak. A detailed description and investigation of the numerical methods of OpenFOAM would go beyond the scope of this paper but can be found in the literature (Deshpande et al., 2013). After the shock and for $10 < x/D < 20$, the droplet diameter stays nearly constant due to the low volumetric mass change, \dot{m}''' , calculated by the HRM model, which is consistent with the experimental data in this region. To understand the behavior of the calculated droplet diameter close to the injector ($x/D < 2$), it is plotted alongside the surface density in Fig. 6(b). Here, the spray break-up close to the injector exit is visible in the sharp increase and subsequent decrease of the surface density. The growth phase of the surface density represents the growth of the vapor bubbles and the creation of surface density until the peak surface density is reached when bubbles merge and spray break-up occurs (Loureiro et al., 2021). Due to the merging of the bubbles and the formation of the smaller droplets, the surface density quickly drops. This evolution of the surface density follows the results observed in the DNS data of Loureiro et al. (2021). Therefore, the mean droplet diameter D_{32} should be interpreted with care for axial positions close to the injector with $x/D < 2$. The observed decrease of the diameter at $x/D = 1$ followed by an increase to $21 \mu\text{m}$ is not physical, but the result of applying Eq. (18) to a region where droplets have not formed yet. The region where the computation of the droplet diameter does not hold is marked in Fig. 6(b) by the gray background.

The importance of the novel ELSA flashing models can be shown by comparison to the standard ELSA implementations as presented in Section 3 and the model of Lyras et al. (2019). Fig. 7 shows the surface density and the resulting mean droplet diameter along the centerline for all three models. In contrast to the FLAM model, the standard ELSA model and the model of Lyras et al. do not show an increase in the surface density due to bubble merging and spray break-up. This can also be seen in the individual contributions of the source terms

plotted in Fig. 8 for the two models. Fig. 8 shows that the evaporation source term of the model of Lyras et al. only considers the decrease of surface density due to evaporation, but not the increase due to bubble growth and spray break-up. This leads to unphysically large droplet radii of about $10 \mu\text{m}$. Considering that the standard ELSA model relies on turbulent kinetic energy to produce surface density, it explains the absence of the surface density increase and – as for the model by Lyras et al. – leads to very large droplet sizes. It is thus apparent that inclusion of the right physics is vital for a correct prediction of droplet diameters in flashing sprays.

5.2.2. Parameter sensitivity study

To estimate the sensitivity of the results towards the model parameters, variations of R_f^* and We_{ev}^{eq} are investigated for Case A. They are the two quantities whose estimations can be associated with the largest uncertainties and have not been calibrated in existing ELSA studies of non-flashing flows. Fig. 9 shows the droplet diameter along the center line for a variation of R_f^* with a fixed Weber number. The results show that the final bubble merging radius changes the predicted droplet sizes but it does not change the relative variations with downstream position. With increasing R_f^* , the bubble growth rate of Eq. (40) decreases, leading to a reduced surface density, resulting in higher droplet diameters. A decreased R_f^* leads to an increased bubble growth rate and lower droplet diameters respectively (see Eq. (40)). Further, for moderate variations with $125 \leq R_f^* \leq 150$ the results are within the confidence interval of the measured experimental data. Hence, uncertainties in the determination of R_f^* using Eq. (51), such as the estimation of the bubble number density at merging as discussed above, do not lead to unrealistic results. Only larger variations in R_f^* will lead to larger differences in D_{32} , but note that changes in the final merging radius have a much larger effect on the bubble number and the assumption of much larger or much smaller bubble densities does not seem justified.

The second important model parameter for the FLAM model is the equilibrium Weber number for the evaporation term, We_{ev}^{eq} . From the DNS data, the parameter is estimated to be $We_{ev}^{eq} = 2/3$. However, unity is often assumed in the other surface density source terms for this kind of model parameter. Therefore, to quantify the effect of this parameter on the solution, the parameter is varied between $0.66 \leq We_{ev}^{eq} \leq 1.5$. Fig. 10 shows the droplet diameter for three equilibrium Weber numbers and a fixed final bubble merging radius of $R_f^* = 140$. It shows that a variation by a factor of 2 leads to an increase of about $4 \mu\text{m}$, which is within the range of the experimental deviations. Thus, a variation of the Weber number within reasonable bounds does not

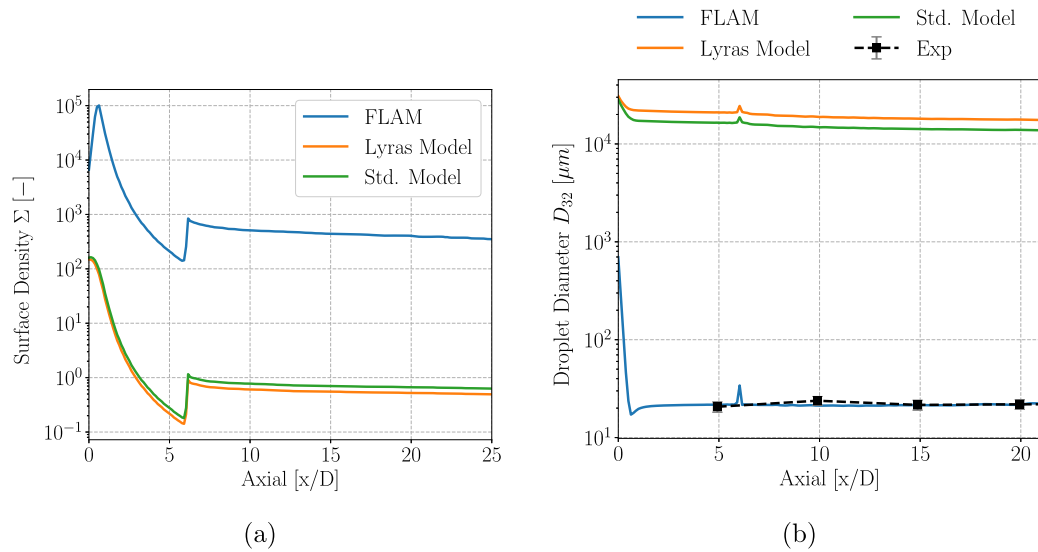


Fig. 7. (a) Surface density along the center line of the spray for the different ELSA models. (b) Resulting droplet diameter, D_{32} , for the three models. Note that both plots use a logarithmic y-axis to display the results.

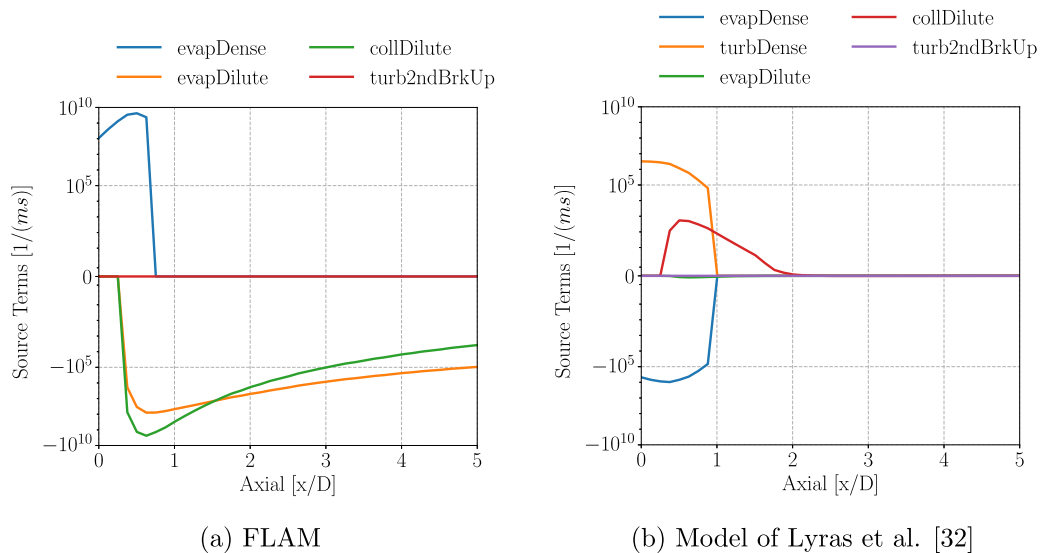


Fig. 8. Individual contributions of the source terms multiplied by their indicator function for the surface density model. Subfigure (a) shows the FLAM model while subfigure (b) shows terms from the model proposed by Lyras et al. (2019).

lead to unphysical or unrealistic results. Nevertheless, to be consistent with the DNS model assumptions, $We_{ev}^{eq} = 0.66$ is selected for all further simulations.

5.2.3. Investigation of the superheat R_p on droplet diameter

So far, the new model has been applied to a single test case, showing a good agreement with the experimental data. However, arguably any model can be fitted to one case. Thus the model's robustness needs to be determined by its applicability to other cases without any model modifications. Therefore, the developed FLAM model is now applied to cases B and C of Table 1. In addition, the effect of the superheat, R_p , on the droplet size can be studied. Note that only a single mean droplet diameter, D_{10} , measurement at the center line is available for cases B and C. However, the existence of only one measurement point may not be as limiting as it seems, as the results of Case A show a nearly constant droplet diameter along the centerline.

In all computations, the final bubble merging radius and the equilibrium Weber number are set to $R_f^* = 140$ and $We_{ev}^{eq} = 0.66$. For

the comparison between the simulations and the measurements, it is important to distinguish, however, between the mean droplet diameter, D_{10} , measured in the experiments and the Sauter mean diameter, D_{32} , that is obtained from the ELSA model. Measurements of D_{32} exist for case A only. The difference between the two mean droplet diameters, D_{10} and D_{32} , depends on the shape of the droplet size distribution and can be significant. Assuming a Weibull distribution, a shape factor of 2 results in a difference of 50%, i.e. $10\ \mu\text{m}$ for case A. A more narrow distribution with a shape factor of 5 results in less than 10% difference. Therefore a direct comparison between computed and measured values is difficult. However, the results presented in Fig. 11 show that the computations (squared filled symbols) capture the trends observed in the experiments (open circles) reasonably well. We may assume that also the absolute values can be captured as for case A, very good quantitative agreement between measured (open square symbol in the figure) and predicted D_{32} exists and has already been discussed in Section 5.2.1.

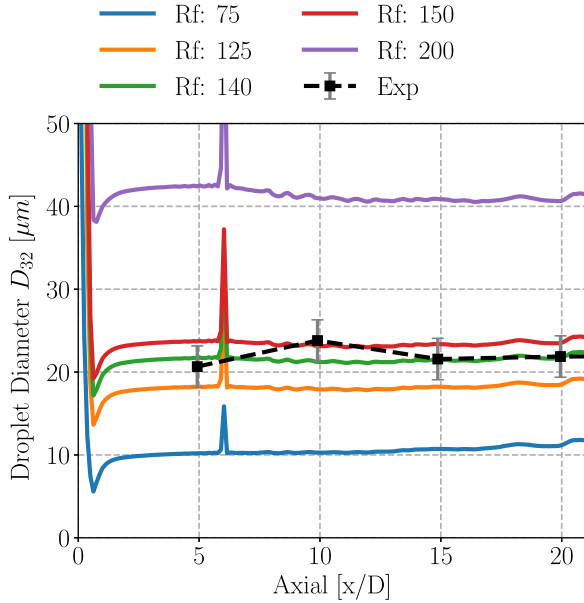


Fig. 9. Mean Sauter diameter, D_{32} , of the droplets for varying final bubble merging radius, R_f , and a fixed $We_{ev}^{eq} = 0.66$.

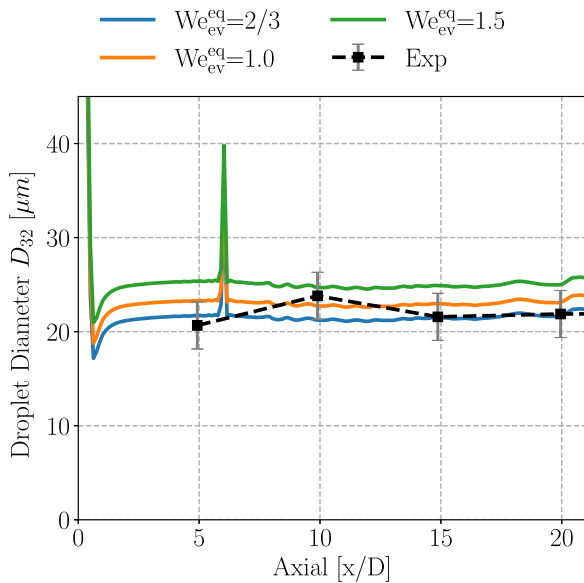


Fig. 10. Parameter study of the equilibrium Weber number, We_{ev}^{eq} with a fixed final bubble merging radius of $R_f^* = 140$.

The good agreement of the experimental data with the FLAM model also indicates that the assumption of heterogeneous nucleation, i.e. of a constant nucleation rate for all three cases based on the impurity of the liquid, is justified. A model based on homogeneous nucleation would predict significantly different nucleation rates for the different superheat ratios, this would lead to a very notable variation in R_f^* which would then lead to a much larger sensitivity of D_{10} on R_p as observed in the experiments.

We may conclude that the model presented here is applicable for flashing jets of cryogenic nitrogen. However, further investigation may be warranted to validate the model and its modeling constants for different injector geometries and fluids. It might also be beneficial to vary the purity of the working fluid to further strengthen the method of estimating R_f^* . This analysis must, however, be part of future work as corresponding experiments do not yet exist.

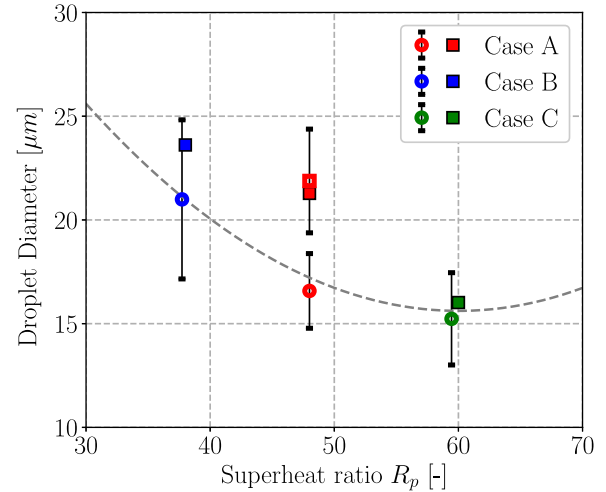


Fig. 11. Comparison of the droplet diameter for the three cases A, B, and C, plotted over the superheat ratio R_p . Square symbols denote Sauter mean diameters, D_{32} , whereas circles represent the mean diameter D_{10} . The gray dashed line represents a fit through the experimental data of D_{10} measurements.

6. Conclusion

A novel ELSA model for flashing sprays has been developed. At first, the standard ELSA model, developed for aerodynamic spray breakup, is presented. This model is then implemented into an existing compressible, two-phase solver in OpenFOAM, and its implementation is validated with a standard test case. The validated ELSA model is then extended to better represent the physical processes involved in flashing sprays. The generation of surface density in the spray's dense region is no longer based on the turbulent length and time scales but on the vapor bubble growth rates and their Weber number. In the dilute spray region, the model was extended to include the decrease of surface density due to evaporating droplets. A key parameter in this model is the bubble number density or alternatively the radius of the merging bubbles. It is found that standard models for the homogeneous nucleation cannot give a valid prediction of the bubble number density and, with it, the final bubble merging radius, R_f . Therefore, an alternative approach considering the amount of dissolved gases is used to estimate the bubble number density. The newly developed model is then applied first to a reference case of flashing cryogenic nitrogen where the axial distribution of the Sauter mean droplet diameter has been measured. A good agreement of the predicted droplet diameter of the model and the experimental data is observed. Further, the development of the surface density along the spray axis follows the trend of flashing spray breakup observed in DNS and provides a prediction of the spray breakup location. The results are then compared to the standard ELSA model and a second ELSA model of the literature. In both cases, these models fail to predict the significant increase of surface density due to the flashing spray break-up and, with it, cannot give a valid prediction of the mean droplet diameter. Therefore the results show, firstly, that the newly developed model can predict the surface generation of flashing cryogenic sprays, and secondly, the significance of basing the source term models on the physical processes driving the surface generation. The sensitivity of the results to the chosen model parameters is investigated in a parameter study of the two main parameters of the model. It is found, that the uncertainties in selecting the model's constants are in the range of the experimental uncertainty. Hence, the model is not overly sensitive towards the selection of the model parameter and the assumptions made to estimate the values are justified. At last the newly developed model is applied to two other cases of flashing cryogenic nitrogen with a varying superheat ratio, while keeping the model parameters constant. It is found that the model can predict the

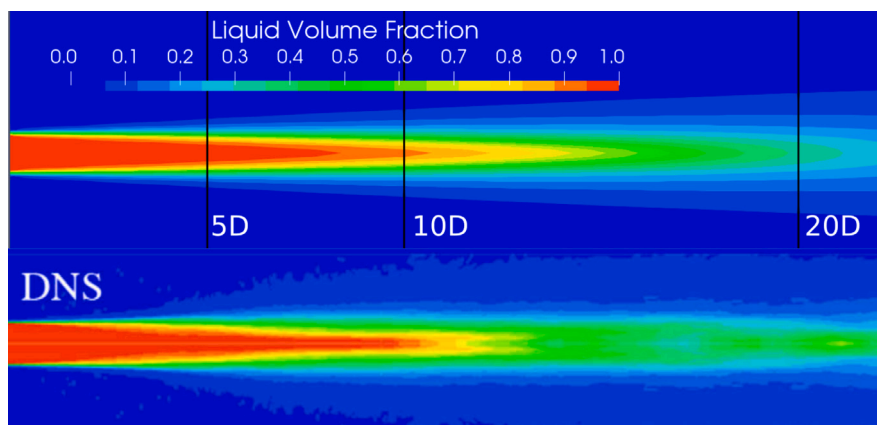


Fig. A.12. Liquid volume fraction distribution at the cut plane of the ELSA 3D RANS and DNS reference case.

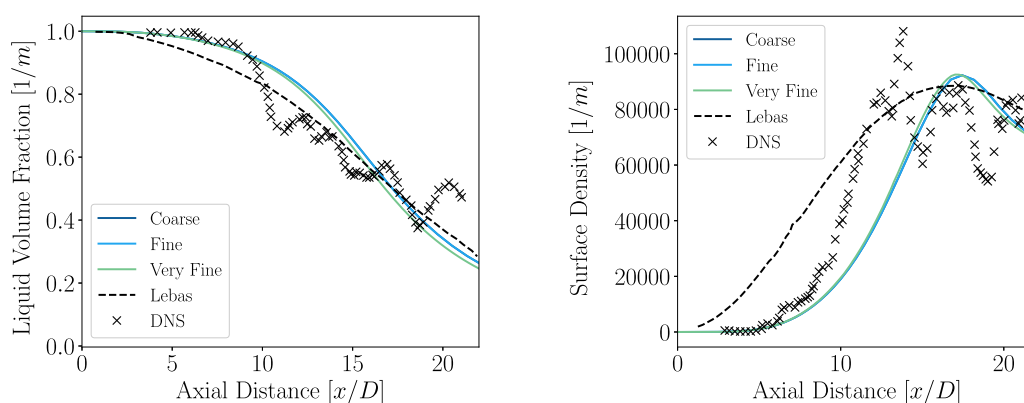


Fig. A.13. Axial profiles of the liquid volume fraction and surface density compared to the averaged DNS results and the reference solution.

decrease of the droplet diameter with increasing superheat ratio and that the predicted droplet sizes are in the range of the experimentally measured values. In addition, it supports the claim to use the dissolved gasses as prediction of the nucleation rate, in comparison to other nucleation models which would predict significant different bubble number densities for the three investigated cases. In conclusion, the model has shown its applicability for flashing cryogenic nitrogen cases for different superheat ratios. However, further test cases with different fluids, and flashing conditions would be beneficial to determine the model's capabilities and limitations. In addition, the model's application to high-fidelity simulations with 3D domains and LES modeling has to be tested and is part of future work.

CRediT authorship contribution statement

Jan Wilhelm Gärtner: Conceptualization, Data curation, Formal analysis, Investigation, Methodology, Software, Writing – original draft.
Andreas Kronenburg: Conceptualization, Formal analysis, Funding acquisition, Project administration, Resources, Writing – review & editing.

Declaration of competing interest

The authors declare that they have no known competing financial interests or personal relationships that could have appeared to influence the work reported in this paper.

Data availability

Data will be made available on request.

Acknowledgments

The authors thank the German Research Foundation (DFG) for financial support of the project within the collaborative research center SFB-TRR 75, Project number 84292822.

Appendix. Validation of standard ELSA model

To validate the implementation of the presented standard ELSA model, DNS results of Lebas et al. (2009) are compared to a 3D RANS test case. The test case consists of injecting a high-density liquid into a low-density atmosphere, mimicking the conditions of a Diesel injector. The chosen simulation domain of a cylinder with 2 mm diameter, 5 mm length recovers the computational domain of the reference entirely. To be consistent with the reference, the turbulence is modeled with the standard $k-\epsilon$ model. Further, the same cell size at the injector, of about 0.01 mm, over the injection diameter of $D_{inj} = 0.1$ mm is selected. To reduce the overall cell count, the cell size increases in the axial and radial directions. The effect of the chosen cell expansion is investigated by comparing three different meshes with 70 000, 144 000, and 337 000 cells. The coarse and fine mesh have the same cell number as the reference meshes. Except for the wall at the injector inlet, all other boundaries are modeled as free-stream exits. The pressure and molecular weight of the gas are chosen such that the density target of the gas is matched. Table A.4 lists the detailed boundary conditions and settings.

Fig. A.12 shows a planar cut of the coarse mesh's liquid volume fraction field compared to the average DNS results of Lebas et al. The comparison shows a good qualitative agreement of the spray, indicating that the chosen boundary conditions and the solver can reproduce the

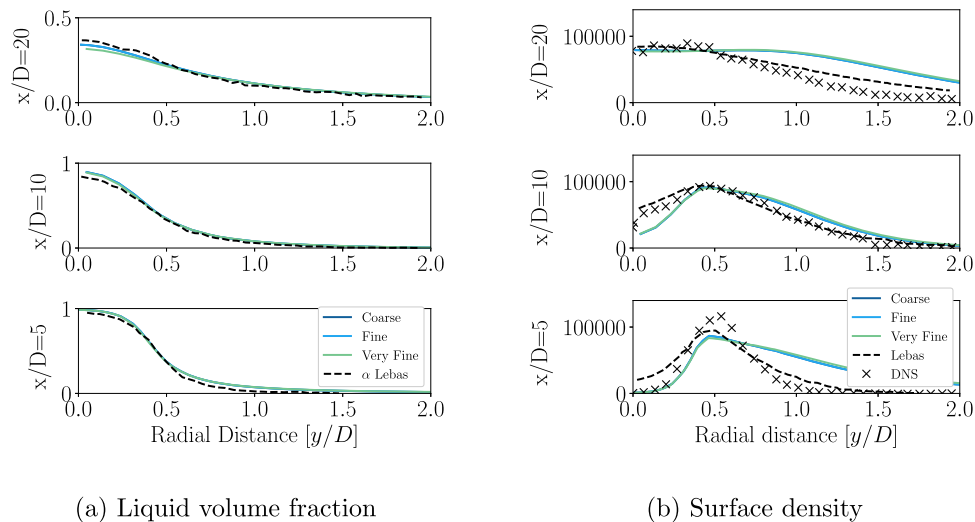


Fig. A.14. Radial profiles of the liquid volume fraction and surface density compared to the averaged DNS results and the reference solution.

Table A.4

Simulation settings for the mechanical spray break-up test case.

Turb. intensity 5%	Turb. length scale 10 μm	Velocity 100 m s^{-1}	Inj. diameter 100 μm	Pressure 1 $\times 10^5$ Pa
Surface tension 0.06 kg s^{-2}	Liquid density 696 kg m^{-3}	Gas density 50 kg m^{-3}	Liquid viscosity 1.2 $\times 10^{-3}$ $\text{kg m}^{-1} \text{s}^{-1}$	Gas viscosity 1.1 $\times 10^{-5}$ $\text{kg m}^{-1} \text{s}^{-1}$

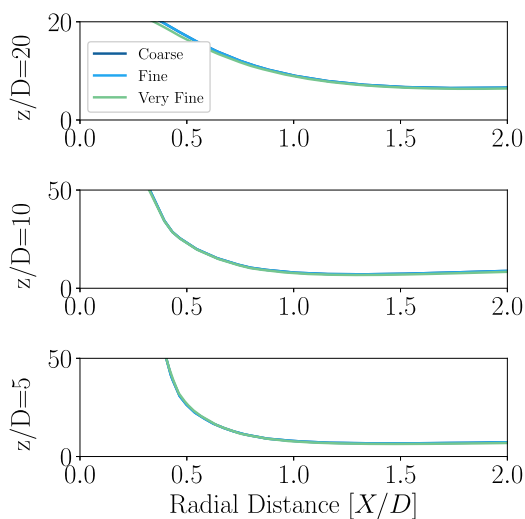


Fig. A.15. Sauter mean droplet diameter, D_{32} in μm for three axial positions.

results. To allow a quantitative comparison, the surface density and liquid volume fraction are plotted along the center line and three axial positions, see Figs. A.13 and A.14. The liquid volume fraction matches well with the DNS data and even better predicts the length of the liquid core than the reference RANS solution. Further, no difference between the three meshes can be observed. Hence the chosen cell expansion does not affect the results. The axial surface density below $x/D = 10$ gives a more faithful representation of the spray break-up than the RANS reference solution, as the liquid core is still intact up to this point, and no interphase surface is present at the axial line. However, after $x/D = 10$ the increase of the surface density due to the primary break-up is slightly delayed compared to the DNS results. The maximum generated surface density and the gradient of the increase can be varied with the chosen density ratio. A slightly increased gas density of 60 kg m^{-3} results in a better match with the DNS data. For

the three radial profiles at $x/D = 5$, $x/D = 10$, and $x/D = 20$, the liquid volume fraction matches again well with the reference solution. The surface density values are slightly overpredicted with increasing radial distance, yet the maximum peak and the peak position are matched. Within the simulation, the surface density and liquid volume fraction are consistent with each other and result in a physical representation of the droplet size, see Fig. A.15. In conclusion, these results show that the standard ELSA model is correctly implemented and can reproduce the results for non-flashing cases.

References

- Abramzon, B., Sirignano, W.A., 1989. Droplet vaporization model for spray combustion calculations. *Int. J. Heat Mass Transfer* 32 (9), 1605–1618. [http://dx.doi.org/10.1016/0017-9310\(89\)90043-4](http://dx.doi.org/10.1016/0017-9310(89)90043-4).
- Anez, J., Ahmed, A., Hecht, N., Duret, B., Reveillon, J., Demoulin, F., 2019. Eulerian-Lagrangian spray atomization model coupled with interface capturing method for diesel injectors. *Int. J. Multiph. Flow* 113, 325–342. <http://dx.doi.org/10.1016/j.ijmultiphaseflow.2018.10.009>.
- Anon., 0000. Substance information - ECHA. <https://echa.europa.eu/substance-information/-/substanceinfo/100.005.560>.
- Beau, P.A., Ménard, T., Lebas, R., Berlemont, A., Tanguy, S., Demoulin, F.X., 2006. Numerical jet atomization: Part II — Modeling information and comparison with DNS results. In: *Symposia, Parts A and B*, vol. 1, ASMEDC, pp. 555–563. <http://dx.doi.org/10.1115/FEDSM2006-98166>.
- Bhattacharyya, P., Chakrabarti, B.K., 2008. The mean distance to the n th neighbour in a uniform distribution of random points: An application of probability theory. *Eur. J. Phys.* 29 (3), 639–645. <http://dx.doi.org/10.1088/0143-0807/29/3/023>.
- Bilicki, Z., Kestin, J., 1990. Physical aspects of the relaxation model in two-phase flow. *Proc. R. Soc. Lond. Ser. A Math. Phys. Eng. Sci.* 428 (1875), 379–397. <http://dx.doi.org/10.1098/rspa.1990.0040>.
- Blander, M., Katz, J., 1975. Bubble nucleation in liquids. *AiChE J.* 21 (5), 833–848. <http://dx.doi.org/10.1002/aic.690210502>.
- Bossert, M., Trimaille, I., Cagnon, L., Chabaud, B., Gueneau, C., Spathis, P., Wolf, P.E., Rolley, E., 2023. Surface tension of cavitation bubbles. *Proc. Natl. Acad. Sci.* 120 (15), e2300499120. <http://dx.doi.org/10.1073/pnas.2300499120>.
- Carey, V.P., 2020. *Liquid-Vapor Phase-Change Phenomena*, third ed. Taylor and Francis, Boca Raton, ISBN: 978-1-4987-1661-1.
- Deshpande, S.S., Anumolu, L., Trujillo, M.F., 2013. Evaluating the performance of the two-phase flow solver interFoam. *Comput. Sci. Discov.* 5 (1), 014016. <http://dx.doi.org/10.1088/1749-4699/5/1/014016>.

- Devassy, B.M., Benkovi, D., Petranovic, Z., Edelbauer, W., Vujanovic, M., 2019. Numerical simulation of internal flashing in a GDI injector nozzle. In: ICLASS Europe 2019.
- Dietzel, D., 2020. Modeling and Simulation of Flash-Boiling of Cryogenic Liquids (Ph.D. thesis). University of Stuttgart, Stuttgart.
- Dietzel, D., Hitz, T., Munz, C.D., Kronenburg, A., 2019. Single vapour bubble growth under flash boiling conditions using a modified HLLC Riemann solver. *Int. J. Multiph. Flow* 116, 250–269. <http://dx.doi.org/10.1016/j.ijmultiphaseflow.2019.04.010>.
- Dinh Le, A., 2022. Study of thermodynamic effect on the mechanism of flashing flow under pressurized hot water by a Homogeneous model. *J. Fluids Eng.* 144 (1), 011206. <http://dx.doi.org/10.1115/1.4051972>.
- Downar-Zapolski, P., Bilicki, Z., Bolle, L., Franco, J., 1996. The non-equilibrium relaxation model for one-dimensional flashing liquid flow. *Int. J. Multiph. Flow* 22 (3), 473–483. [http://dx.doi.org/10.1016/0301-9322\(95\)00078-X](http://dx.doi.org/10.1016/0301-9322(95)00078-X).
- Duret, B., Reveillon, J., Menard, T., Demoulin, F., 2013. Improving primary atomization modeling through DNS of two-phase flows. *Int. J. Multiph. Flow* 55, 130–137. <http://dx.doi.org/10.1016/j.ijmultiphaseflow.2013.05.004>.
- Dyadechko, V., Shashkov, M., 2005. *Moment-of-Fluid Interface Reconstruction*. Los Alamos National Laboratory.
- Franquet, E., Perrier, V., Gibout, S., Bruel, P., 2015. Free underexpanded jets in a quiescent medium: A review. *Prog. Aerosp. Sci.* 77, 25–53. <http://dx.doi.org/10.1016/j.paerosci.2015.06.006>.
- Gallo, M., Magaletti, F., Casciola, C.M., 2021. Heterogeneous bubble nucleation dynamics. *J. Fluid Mech.* 906. <http://dx.doi.org/10.1017/jfm.2020.761>.
- Gärtner, J.W., Kronenburg, A., Rees, A., Sender, J., Oschwald, M., Lamanna, G., 2020. Numerical and experimental analysis of flashing cryogenic nitrogen. *Int. J. Multiph. Flow* 130. <http://dx.doi.org/10.1016/j.ijmultiphaseflow.2020.103360>.
- Guo, H., Nocivelli, L., Torelli, R., 2021. Numerical study on spray collapse process of ECN spray G injector under flash boiling conditions. *Fuel* 290, 119961. <http://dx.doi.org/10.1016/j.fuel.2020.119961>.
- Karathanassis, I., Koukouvinis, P., Gavaises, M., 2017. Comparative evaluation of phase-change mechanisms for the prediction of flashing flows. *Int. J. Multiph. Flow* 95, 257–270. <http://dx.doi.org/10.1016/j.ijmultiphaseflow.2017.06.006>.
- Kwak, H.-Y., Oh, S.-D., 2004. Gas–vapor bubble nucleation — A unified approach. *J. Colloid Interface Sci.* 278 (2), 436–446. <http://dx.doi.org/10.1016/j.jcis.2004.06.020>.
- Lamanna, G., Kamoun, H., Weigand, B., Steelant, J., 2014. Towards a unified treatment of fully flashing sprays. *Int. J. Multiph. Flow* 58, 168–184. <http://dx.doi.org/10.1016/j.ijmultiphaseflow.2013.08.010>.
- Lebas, R., Menard, T., Beau, P.A., Berlemont, A., Demoulin, F.X., 2009. Numerical simulation of primary break-up and atomization: DNS and modelling study. *Int. J. Multiph. Flow* 35 (3), 247–260. <http://dx.doi.org/10.1016/j.ijmultiphaseflow.2008.11.005>.
- Lee, J., Madabhushi, R., Fotache, C., Gopalakrishnan, S., Schmidt, D., 2009. Flashing flow of superheated jet fuel. *Prog. Combust. Inst.* 32 (2), 3215–3222. <http://dx.doi.org/10.1016/j.proci.2008.06.153>.
- Liao, Y., Lucas, D., 2017a. Computational modelling of flash boiling flows: A literature survey. *Int. J. Heat Mass Transfer* 111, 246–265. <http://dx.doi.org/10.1016/j.ijheatmasstransfer.2017.03.121>.
- Liao, Y., Lucas, D., 2017b. Possibilities and limitations of CFD simulation for flashing flow scenarios in nuclear applications. *Energies* 10 (1), 139. <http://dx.doi.org/10.3390/en10010139>.
- Lin, Z., Yang, W., Zhou, H., Xu, X., Sun, L., Zhang, Y., Tang, Y., 2018. Communication optimization for multiphase flow solver in the library of OpenFOAM. *Water* 10 (10), 7–9. <http://dx.doi.org/10.3390/w10101461>.
- Loureiro, D., Kronenburg, A., Reutzsch, J., Weigand, B., Vogiatzaki, K., 2021. Droplet size distributions in cryogenic flash atomization. *Int. J. Multiph. Flow* 142, 103705. <http://dx.doi.org/10.1016/j.ijmultiphaseflow.2021.103705>.
- Loureiro, D., Reutzsch, J., Dietzel, D., Kronenburg, A., Weigand, B., Vogiatzaki, K., 2018. DNS of multiple bubble growth and droplet formation in superheated liquids. In: *International Conference on Liquid Atomization and Spray Systems*. Chicago, pp. 1–8.
- Lyras, K.G., Dembele, S., Wen, J.X., 2019. Numerical simulation of flashing jets atomisation using a unified approach. *Int. J. Multiph. Flow* 113, 45–58. <http://dx.doi.org/10.1016/j.ijmultiphaseflow.2018.12.011>.
- Lyras, T., Karathanassis, I.K., Kyriazis, N., Koukouvinis, P., Gavaises, M., 2023. Numerical modelling of cryogenic flows under near-vacuum pressure conditions. In: White, M., El Samad, T., Karathanassis, I., Sayma, A., Pini, M., Guardone, A. (Eds.), *Proceedings of the 4th International Seminar on Non-Ideal Compressible Fluid Dynamics for Propulsion and Power*, vol. 29. Springer Nature Switzerland, Cham, pp. 114–124. http://dx.doi.org/10.1007/978-3-031-30936-6_12.
- Marek, R., Straub, J., 2001. Analysis of the evaporation coefficient and the condensation coefficient of water. *Int. J. Heat Mass Transfer* 44 (1), 39–53. [http://dx.doi.org/10.1016/S0017-9310\(00\)00086-7](http://dx.doi.org/10.1016/S0017-9310(00)00086-7).
- Martin, J., 2023. *The Gravity-Driven Flashing of Metastable Water in a Pool Heated from Below* (Doctoral thesis). University Ottignies-Louvain-la-Neuve, Belgium.
- Ménard, T., Tanguy, S., Berlemont, A., 2007. Coupling level set/VOF/ghost fluid methods: Validation and application to 3D simulation of the primary break-up of a liquid jet. *Int. J. Multiph. Flow* 33 (5), 510–524. <http://dx.doi.org/10.1016/j.ijmultiphaseflow.2006.11.001>.
- Mohapatra, C.K., Schmidt, D.P., Sforzo, B.A., Matusik, K.E., Yue, Z., Powell, C.F., Som, S., Mohan, B., Im, H.G., Badra, J., Bode, M., Pitsch, H., Papoulias, D., Neroorkar, K., Muzafferija, S., Marti-Aldaravi, P., Martínez, M., 2020. Collaborative investigation of the internal flow and near-nozzle flow of an eight-hole gasoline injector (engine combustion network spray G). *Int. J. Engine Res.* <http://dx.doi.org/10.1177/1468087420918449>.
- Neroorkar, K., Gopalakrishnan, S., Grover, R.O., Schmidt, D.P., 2011. Simulation of flash boiling in pressure swirl injectors. *Atomization Sprays* 21 (2), 179–188. <http://dx.doi.org/10.1615/AtomizSpr.2011003077>.
- Persad, A.H., Ward, C.A., 2016. Expressions for the evaporation and condensation coefficients in the Hertz–Knudsen relation. *Chem. Rev.* 116 (14), 7727–7767. <http://dx.doi.org/10.1021/acs.chemrev.5b00511>.
- Pilch, M., Erdman, C.A., 1987. Use of breakup time data and velocity history data to predict the maximum size of stable fragments for acceleration-induced breakup of a liquid drop. *Int. J. Multiph. Flow* 13 (6), 741–757. [http://dx.doi.org/10.1016/0301-9322\(87\)90063-2](http://dx.doi.org/10.1016/0301-9322(87)90063-2).
- Poursadegh, F., Lacey, J.S., Brear, M.J., Gordon, R.L., Petersen, P., Lakey, C., Butcher, B., Ryan, S., Kramer, U., 2018. On the phase and structural variability of directly injected propane at spark ignition engine conditions. *Fuel* 222, 294–306. <http://dx.doi.org/10.1016/j.fuel.2018.02.137>.
- Prosperetti, A., 2017. Vapor bubbles. *Annu. Rev. Fluid Mech.* 49 (1), 221–248. <http://dx.doi.org/10.1146/annurev-fluid-010816-060221>.
- Rachakonda, S.K., Paydarfar, A., Schmidt, D.P., 2019. Prediction of spray collapse in multi-hole gasoline direct-injection fuel injectors. *Int. J. Engine Res.* 20 (1), 18–33. <http://dx.doi.org/10.1177/1468087418819527>.
- Rees, A., 2020. *Experimental Investigation of Flash Boiling Cryogenic Nitrogen under High-Altitude Conditions* (Doctoral thesis). RWTH Aachen, Lampoldshausen.
- Rees, A., Araneo, L., Salzmann, H., Lamanna, G., Sender, J., Oschwald, C.M., 2020. Droplet velocity and diameter distributions in flash boiling liquid nitrogen jets by means of phase Doppler diagnostics. *Exp. Fluids* 61, 182. <http://dx.doi.org/10.1007/s00348-020-03020-7>.
- Saha, K., Som, S., Battistoni, M., 2017. Investigation of homogeneous relaxation model parameters and their implications for gasoline injectors. *Atomization Sprays* 27 (4), 345–365. <http://dx.doi.org/10.1615/AtomizSpr.2017016338>.
- Schmidt, D.P., Gopalakrishnan, S., Jasak, H., 2010. Multi-dimensional simulation of thermal non-equilibrium channel flow. *Int. J. Multiph. Flow* 36 (4), 284–292. <http://dx.doi.org/10.1016/j.ijmultiphaseflow.2009.11.012>.
- Sher, E., Bar-Kohany, T., Rashkovan, A., 2008. Flash-boiling atomization. *Prog. Energy Combust. Sci.* 34 (4), 417–439. <http://dx.doi.org/10.1016/j.pecs.2007.05.001>.
- Shin, T.S., Jones, O.C., 1993. Nucleation and flashing in nozzles-I. A distributed nucleation model. *Int. J. Multiph. Flow* 19 (6), 943–964. [http://dx.doi.org/10.1016/0301-9322\(93\)90071-2](http://dx.doi.org/10.1016/0301-9322(93)90071-2).
- Tominaga, Y., Stathopoulos, T., 2007. Turbulent Schmidt numbers for CFD analysis with various types of flowfield. *Atmos. Environ.* 41 (37), 8091–8099. <http://dx.doi.org/10.1016/j.atmosenv.2007.06.054>.
- Valero, E., Parra, I.E., 2002. The role of thermal disequilibrium in critical two-phase flow. *Int. J. Multiph. Flow* 28 (1), 21–50. [http://dx.doi.org/10.1016/S0301-9322\(01\)00064-7](http://dx.doi.org/10.1016/S0301-9322(01)00064-7).
- Vallet, A., Burluka, A.A., Borghi, R., 2001. Development of a Eulerian model for the Atomization of a liquid jet. *Atomization Sprays* 11 (6), 619–642. <http://dx.doi.org/10.1615/atomizspr.v11.i6.20>.
- Versteeg, H.K., Malalasekera, W., 2007. *An Introduction to Computational Fluid Dynamics: The Finite Volume Method*, second ed. Pearson Education Ltd, Harlow, England; New York, ISBN: 978-0-13-127498-3.
- Vieira, M.M., Simões-Moreira, J.R., 2007. Low-pressure flashing mechanisms in iso-octane liquid jets. *J. Fluid Mech.* 572, 121–144. <http://dx.doi.org/10.1017/S0022112006003430>.
- Witlox, H., Harper, M., Bowen, P., Cleary, V., 2007. Flashing liquid jets and two-phase droplet dispersion. II. Comparison and validation of droplet size and rainout formulations. *J. Hazard. Mater.* 142 (3), 797–809. <http://dx.doi.org/10.1016/j.jhazmat.2006.06.126>.

Chapter 6

Conclusions and Outlook

In this thesis, a novel, compressible, one-fluid, two-phase solver for flashing cryogenic liquids was developed and implemented into the open-source framework OpenFOAM. It was then successfully applied to different fluids and flashing conditions, investigating the flashing behavior inside the injector and the subsequent transonic effects and spray breakup. This final chapter summarizes the most important findings and results, further a final conclusion is given. In addition, an outlook for subsequent projects focusing on the technological and numerical aspects is presented.

6.1 Summary and Conclusions

The first objective of this work has been the development of suitable numerical tools to simulate flashing cryogenic jets in OpenFOAM. This has been addressed in Chapter 3 and Chapter 4 in which the modeling basis and the implementation in the existing numerical framework of OpenFOAM are elaborated. The chosen one-fluid approach allows the simulation of the complete flashing process from incompressible liquid to highly compressible vapor and droplet mixture after spray breakup without defining the continuous or dispersed phase. Further, a pressure-based solution algorithm is selected to derive an all-Mach-number solver suitable for the simulation of the incompressible as well as highly compressible transonic regions of the spray. The phase change rate is modeled with the robust and versatile homogeneous relaxation model of Downar-Zapolski et al. [34].

The application of the developed solver to flashing acetone cases demonstrated the applicability of the solver design for highly flashing flows with transonic effects by faithfully capturing the shock position and size. Following the successful validation of the solver, it was applied to flashing cryogenic liquid nitrogen cases in a 2D RANS

setup. Here, the good agreement of the mass flow rate through the injector served as a quantitative validation of the phase change model parameters, supporting the use of the model's default values. Further, the flow field investigation after the spray breakup showed a recirculation zone in the region of dark, nearly motionless, or even slightly upstream floating structures in the experimental shadowgraph images. However, the simplified 2D setup with RANS modeling required further investigation to estimate the numerical contribution to the observed phenomena. The solver was then applied to a single- and eight-hole injector with a 3D RANS setup to study the effect of shock interactions and their implications. Here, in the context of gasoline direct injection, the effect of spray collapse. The results of the single-hole injector, using *n*-hexane as a working fluid, were compared to a reference solution obtained with the commercial CFD software CONVERGE, demonstrating a good agreement between the two solvers. Therefore, verifying the applicability of the developed solver to three-dimensional setups. The effect of shock-to-shock interactions of neighboring injectors is studied with the eight-hole injector. Here, three cases with iso-octane and propane are investigated, focusing on the effect of spray collapse as a result of the shock interactions. It has been found that the superheat ratio R_p is an inadequate criterion for spray collapse and that a novel characteristic number D_n proposed by Lacey et al. [72], gives a reliable, though not necessary, criterion for spray collapse. Even though this investigation was carried out for non-cryogenic liquids, two conclusions can be drawn: first, that the developed solver can be successfully applied to 3D RANS setups, capturing the transonic effects faithfully, and second, that transonic effects arising with flashing flows in a multi-injector array, typical for rocket engines, may lead to vastly different spray behavior due to shock-to-shock interactions.

Following the 3D RANS investigation, a highly resolved LES study of the cryogenic liquid nitrogen case was conducted. A detailed comparison of the flow field inside the injector showed that the 2D RANS setup could capture the general characteristics of mass flow rate and bulk velocity. However, details such as the radial vapor distribution are affected by the resolved eddies of the LES and, therefore, can only be captured by the LES. However, the observed recirculation zone in the 2D RANS setup could not be observed in the 3D LES. A probable hypothesis is that the inverse energy cascade due to the missing vortex stretching effect in 2D simulations causes the pronounced recirculation. Nevertheless, smaller eddies and a region of low axial velocity are found in the same region, identifying it as a potential location for the future ignition of upper-stage rocket engines. In addition to the qualitative shadowgraph images, measured droplet velocities allowed a quantitative comparison of the simulated flow field and the

experimental data. The comparison revealed a good agreement of the velocities of the simulation and droplets in the slipstream and further downstream. However, closer to the shock front and the injector, a significant deviation of the measured droplet velocities and the one-fluid solution of the simulation appeared. This is attributed to two aspects: first favoring larger droplets in the experimental measurement and second the inertia of larger droplets violating the no-slip assumption of the one-fluid solver. This finding was corroborated by injecting one-way coupled passive particles with the measured droplet size distribution at the point of spray breakup, showing an excellent agreement with the measured droplet velocities. Therefore, while unable to capture the dynamics of larger droplets, the one-fluid solution provides the correct velocity field that governs their movement. This investigation concludes the second objective of this thesis, providing a thorough validation of the solver and an in-depth analysis of the flow and spray behavior.

At last, the final objective, considering the loss of surface interface information with the chosen solver design, was addressed. To recover the lost information, a novel ELSA model for flashing flows, called FLAM, grounded in physical principles of flashing flows, has been developed (cf. Section 3.3). In contrast to the standard ELSA model, it considers the vastly different physical processes driving the spray breakup and surface generation of flashing flows compared to a typical aerodynamic spray breakup. The novel model was then applied to the flashing cryogenic nitrogen cases, and a good agreement of the axial droplet size distribution to the experimental data was found. In addition, the model can predict the location of spray breakup and the surface density trend matches DNS results of the literature. A further comparison with the standard ELSA model and another model from the literature underscores the significance of accounting for the underlying physical mechanisms governing spray breakup. The inability of these alternative models to accurately replicate the behavior during spray breakup emphasizes the necessity of incorporating a robust understanding of the relevant physical processes. The model has then been applied to two other cases of flashing cryogenic nitrogen with different superheat ratios without modifying the model constants, demonstrating two points: first, the model parameters and the claim to base the nucleation rate on the amount of dissolved gases are supported. Secondly, it shows that the trend of decreasing droplet diameter with increasing superheat ratio is captured. Hence, the model shows general applicability to cryogenic flashing flows without re-fitting the model constants to every case.

In summary, the required numerical tools for simulation flashing cryogenic flows have been developed and verified for different fluids and conditions. Further, the present

work provides valuable insight into the spray behavior of fully flashing sprays, including the transonic effects and their potential interactions. Last but not least, a novel ELSA model for flashing flows has been developed and verified for flashing cryogenic nitrogen sprays.

6.2 Outlook

The presented solver, models, and their advantages and disadvantages in this thesis allow multiple future research projects, of which some will be listed in the following:

- **Simulation of combined injection of oxidizer and fuel**

In the presented thesis, the flashing behavior of a single fluid, e.g., nitrogen, acetone, *n*-hexane, etc., was investigated. However, considering rocket engines as the field of application of cryogenic flashing liquids, they typically consist of multiple coaxial injectors with at least two different fluids for the oxidizer and fuel, e.g., oxygen and hydrogen. Therefore, the solver needs to be adapted to handle multiple components and species. This can be achieved by coupling the multi-component thermodynamic model of OpenFOAM to the tabulated thermophysical property library developed in this work and adding an additional transport for the species mass fractions in each volume fraction. This would then allow us to study the mixing of the typically gaseous fuel with the evaporated oxygen, which is an important part of a successful subsequent ignition.

- **Application of the new ELSA model FLAM to 3D LES**

The new ELSA model for flashing flows presented in this work was applied to 2D RANS simulations. Therefore, two further aspects can be investigated: first, the application to 3D RANS, to verify its applicability to 3D cases, and second, the influence of the turbulence modeling on the model source terms. In particular, the influence of resolved to modeled turbulence can be investigated with 3D LES. Hereby, the focus is on the turbulent contribution to the source terms, which require the turbulent kinetic energy as an input. For RANS models, the turbulent kinetic energy is given by the turbulence model. However, for LES it is not sufficient to use the modeled turbulent kinetic energy, as with increasing resolution, hence decreasing modeled turbulence, the collision and coalescence of droplets or bubbles in the surface density model is not further resolved. Therefore, the model requires not the modeled turbulent kinetic energy but the total turbulent kinetic energy consisting of the modeled and resolved parts.

- **Development of a hybrid Euler-Lagrange solver to capture the dynamics of the larger droplets**

The 3D LES investigation of flashing cryogenic flow revealed that larger droplets do not follow the gas flow and thus violate the no-slip assumption of the one-fluid model. To capture the behavior of larger droplets faithfully, a hybrid Euler-Euler, Euler-Lagrange solver design could be used, where droplets are represented as Lagrangian particles after the spray breakup [10, 4]. This concept can then be coupled with the ELSA model to get the droplet diameter after spray breakup to initialize the Lagrangian particles. Further, with the knowledge of droplet diameter and surface area, the phase change model can be switched to more detailed models of evaporation [108].

- **Couple phase change model with ELSA**

The current ELSA model is only one-way coupled to the solver. Hence, the information of the surface density is not fed back to the solver for use in, e.g., the phase change model. Therefore, future work could use this information to create a two-way coupled solver, where the information of the surface density could be used after spray breakup in the phase change model. This would allow the use of a heat transfer or Hertz-Knudsen model without having to rely on empirical correlations for the surface area of the droplets.

Appendix A

Derivation of the Homogeneous Nucleation for Superheated Liquid and Subcooled Vapor

The derivation of the homogeneous nucleation rate, up to the point of the Gibbs free energy in Eq. (2.5), is valid for bubbles in a superheated liquid and droplets in a subcooled vapor. However, from then on, the derivation splits into a path for superheated liquid and one for subcooled vapor. The main difference is the description of the critical radius based on the Young-Laplace equation. In the case of superheated liquid, we know the liquid pressure p_l and have to compute the unknown vapor pressure, p_v , inside the bubble. Starting from the Gibbs-Duhem equation and integrating it assuming a constant temperature and using the ideal gas assumption gives the chemical potential for the liquid and vapor phase [23] with

$$\mu_l = \mu_{\text{sat}} + \frac{p_l - p_{\text{sat}}(T_l)}{\rho_l}, \quad (\text{A.1})$$

$$\mu_v = \mu_{\text{sat}} + (R_u/M)T_l \ln \left[\frac{p_v}{p_{\text{sat}}(T_l)} \right]. \quad (\text{A.2})$$

Assuming now that the vapor bubble is at equilibrium, the chemical potentials must be equal, $\mu_l = \mu_v$, which results then in Eq. (2.4) presented in Chapter 2,

$$p_v = p_{\text{sat}}(T_l) \exp \left(\frac{p_l - p_{\text{sat}}(T_l)}{\rho_l (R_u/M) T_l} \right). \quad (\text{A.3})$$

Inserting Eq. (2.4) in the Young-Laplace equation Eq. (2.3) leads then to

$$R_c = \frac{2\sigma}{p_{\text{sat}}(T_l) \exp\left(\frac{p_l - p_{\text{sat}}(T_l)}{\rho_l(R_u/M)T_l}\right) - p_l}. \quad (\text{A.4})$$

In the case of subcooled vapor and nucleation of droplets the same assumptions as for superheated liquid are made: the droplet is at equilibrium, hence $\mu_l = \mu_v$; the interface temperature is the vapor temperature, $T_l = T_v$. The chemical potential for the liquid and vapor phase is then

$$\mu_l = \mu_{\text{sat}} + \frac{p_l - p_{\text{sat}}(T_v)}{\rho_l}, \quad (\text{A.5})$$

$$\mu_v = \mu_{\text{sat}} + (R_u/M)T_v \ln \left[\frac{p_v}{p_{\text{sat}}(T_v)} \right]. \quad (\text{A.6})$$

Notably the properties in the gas phase are known and the liquid ones in the droplet unknown. Therefore, not the vapor pressure in the bubble, p_v , but the pressure inside the droplet, p_l , has to be calculated,

$$p_l = \rho_l(R_u/M)T_v \ln \left[\frac{p_v}{p_{\text{sat}}(T_v)} \right] + p_{\text{sat}}(T_v). \quad (\text{A.7})$$

The term in the natural logarithm could be misinterpreted as the superheat ratio R_p (cf. Eq. (2.1)). However, this is obviously not the case and using (A.7) to determine the nucleation rate of bubbles in superheated liquid is incorrect.

Appendix B

Derivation of the mixture velocity

The one-fluid method combines the governing equations of the two phases to create a set of equations describing the motion of the two-phase mixture. Hence, the solution of the one-fluid equation systems results in a mixture velocity u describing the motion of the mixture. However, for the advection of the volume or mass fraction the individual phase velocity u_k of phase k is required. Depending on the choice of averaging by the mass or volume fraction two descriptions of the mixture velocity exist.

In the following the derivation for the velocity based on the center of mass or center of volume is presented for two arbitrary phases p and q .

B.1 Velocity of Center of Mass

The velocity \vec{u}_m with the average density $\rho = \sum \alpha_k \rho_k$ is called the velocity of center of mass. The vector relations between the different phases and this velocity is shown in Figure B.1 for a two-phase system. The drift velocity is defined as,

$$\vec{u}_{dr,p} = \vec{u}_p - \sum_k (\chi_k \vec{u}_k) = \vec{u}_p - \vec{u}_m. \quad (\text{B.1})$$

with χ as the mass fraction defined by,

$$\chi_k = \frac{\alpha_k \rho_k}{\rho}. \quad (\text{B.2})$$

For a two phase system the drift velocity can also be expressed with,

$$\vec{u}_{dr,p} = (1 - \chi_p) \vec{u}_{qp}. \quad (\text{B.3})$$

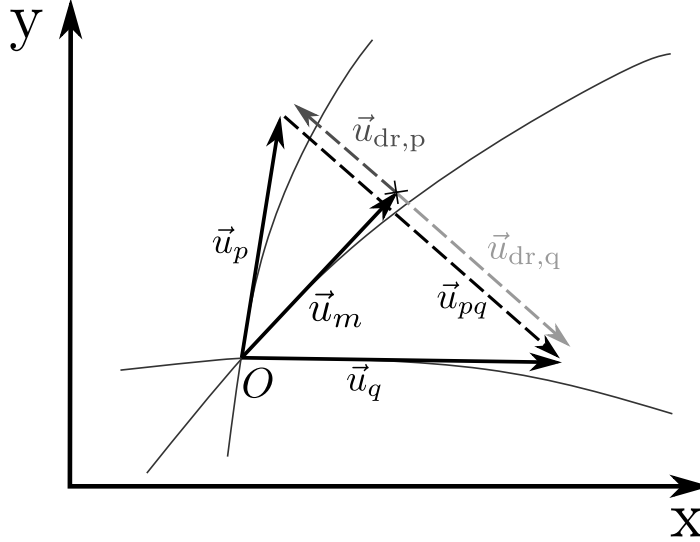


Figure B.1: Example of the velocity of center mass \vec{u}_m , the individual velocities \vec{u}_q, \vec{u}_p , the velocity drift $\vec{u}_{dr,q}$ and the relative velocity \vec{u}_{pq} , [29]

B.2 Velocity of Center of Volume

In the previous section the velocity of the phases is calculated with the individual density contributions. Additional to this description exists the velocity of center of volume. This velocity description for the phase mixture is based on the same averaging procedure used for intensive properties, averaging with the volume fraction. The mixture velocity is then,

$$\vec{u} = \sum \alpha_k \vec{u}_k. \quad (\text{B.4})$$

An example for a two phase system with the velocities is given in Figure B.2. From the Figure B.2 it is obvious, that $\vec{u}_q = \vec{u} + \vec{b} + \vec{u}_{dr,q}$. The vector \vec{b} can be expressed as:

$$\begin{aligned} \vec{b} &= \vec{u}_m - \vec{u} \\ &= \underbrace{\vec{u}_p - \vec{u}_{dr,p}}_{\vec{u}_m} - \underbrace{(\alpha_p \vec{u}_p + \alpha_q \vec{u}_q)}_{\vec{u}} \\ &= \vec{u}_p(1 - \alpha_p) - \alpha_q \vec{u}_q - \vec{u}_{dr,p} \\ &= \vec{u}_p(1 - \alpha_p) - \underbrace{\alpha_q(\vec{u}_q - \vec{u}_p)}_{-\alpha_q \vec{u}_q} - \vec{u}_{dr,p} \\ &= -\alpha_q \vec{u}_{qp} - \vec{u}_{dr,p}. \end{aligned} \quad (\text{B.5})$$

Inserting Eq. (B.5) in

$$\vec{v}_q = \vec{u} + \vec{b} + \vec{v}_{dr,q}$$

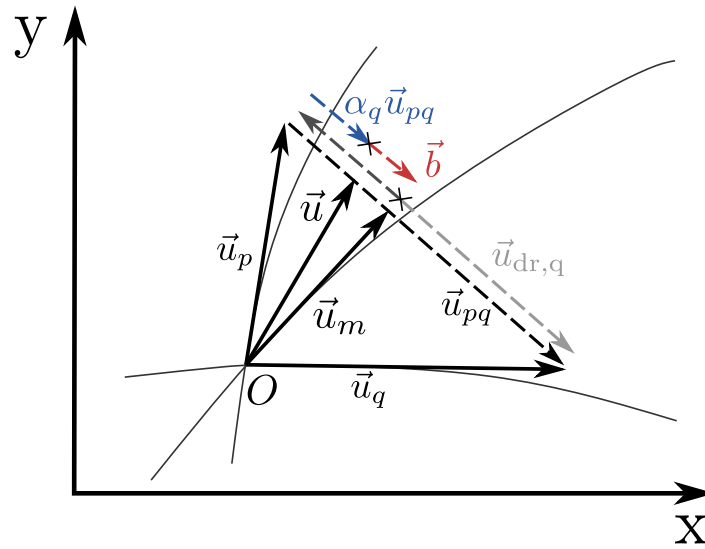


Figure B.2: Example of the velocity of center volume \vec{u} , the individual velocities \vec{v}_q, \vec{v}_p , the velocity drift $\vec{v}_{dr,q}$ and the relative velocity \vec{v}_{pq} [29]

leads to

$$\begin{aligned}
 \vec{v}_q &= \vec{u} - \alpha_q \vec{v}_{qp} - \vec{v}_{dr,p} + \vec{v}_{dr,q} \\
 &= \vec{u} - \alpha_q \vec{v}_{qp} + \vec{v}_{qp} \\
 &= \vec{u} + (1 - \alpha_q) \vec{v}_{qp}.
 \end{aligned}
 \tag{B.6}$$

Appendix C

Speed of Sound and Compressibility

Considering a control volume with a mixture of two or more species with the initial densities $\rho_A, \rho_B, \dots, \rho_n$ and the common initial pressure p . Now the pressure p is changed by the infinitesimal value δp . Assuming that the mass inside the control volume (CV) stays constant, the compressibility can be expressed by,

$$\frac{\partial \rho}{\partial p} = \frac{\partial \left(\frac{m}{V} \right)}{\partial p}. \quad (\text{C.1})$$

Applying the derivation chain rule and using that $\rho = m/V$, the equation can be written as

$$\frac{\partial \rho}{\partial p} = -\rho \frac{\partial V^*}{\partial p}, \quad (\text{C.2})$$

with V^* being the volume divided by the initial control volume $\frac{V}{V_{CV}}$. The compressibility can now be expressed by the volume change due to the infinitesimal pressure change,

$$\frac{\partial \rho}{\partial p} = -\rho \frac{\delta(V^*)}{\delta p}. \quad (\text{C.3})$$

The volume of the phase is calculated with

$$V_A = \frac{\rho_A \alpha_A V_{CV}}{\rho_A + \left(\frac{\partial \rho}{\partial p} \right)_A \delta p}, \quad (\text{C.4})$$

and the change of the volume is,

$$\delta V_A = V_A - \alpha V_{CV} \quad (\text{C.5})$$

$$= -\frac{\alpha_A \left(\frac{\partial \rho}{\partial p} \right)_A \delta p}{\rho_A + \underbrace{\left(\frac{\partial \rho}{\partial p} \right)_A \delta p}_{=0}} V_{CV}. \quad (\text{C.6})$$

Dividing the phase volume with the infinitesimal pressure δp gives then,

$$\frac{\delta V_A^*}{\delta p} = -\frac{\alpha_A \left(\frac{\partial \rho}{\partial p} \right)_A}{\rho_A + \underbrace{\left(\frac{\partial \rho}{\partial p} \right)_A \delta p}_{=0}} \quad (\text{C.7})$$

$$= -\frac{\alpha_A \left(\frac{\partial \rho}{\partial p} \right)_A}{\rho_A} \quad (\text{C.8})$$

Inserting Eq. (C.8) into Eq. (C.3) leads to,

$$\frac{\partial \rho}{\partial p} = \rho \left(\frac{\alpha_A}{\rho_A} \left(\frac{\partial \rho}{\partial p} \right)_A + \frac{\alpha_B}{\rho_B} \left(\frac{\partial \rho}{\partial p} \right)_B + \dots + \frac{\alpha_n}{\rho_n} \left(\frac{\partial \rho}{\partial p} \right)_n \right). \quad (\text{C.9})$$

As the mass is based on the volume fractions prior to the pressure change, the volume fraction values α are also from this point. In OpenFOAM the α -values are taken then from the previous time step and are thus known. The final description of the mixture compressibility for N species is then,

$$\frac{\partial \rho}{\partial p} = \sum_{i=1}^N (\rho_i \alpha_i) \sum_{i=1}^N \left(\frac{\alpha_i}{\rho_i} \left(\frac{\partial \rho}{\partial p} \right)_i \right). \quad (\text{C.10})$$

The speed of sound can be found by taking the square root of the inverse of Eq. (4.21). The formula to calculate the speed of sound for a mixture can also be found in Brennen [22, Chapter 9.3].

C.1 Difference to weighted average

In another work [85] the weighted average is used to calculate the mixture compressibility,

$$\psi = \left(\frac{\partial \rho}{\partial p} \right) = \alpha_A \psi_A + \alpha_B \psi_B + \dots + \alpha_n \psi_n. \quad (\text{C.11})$$

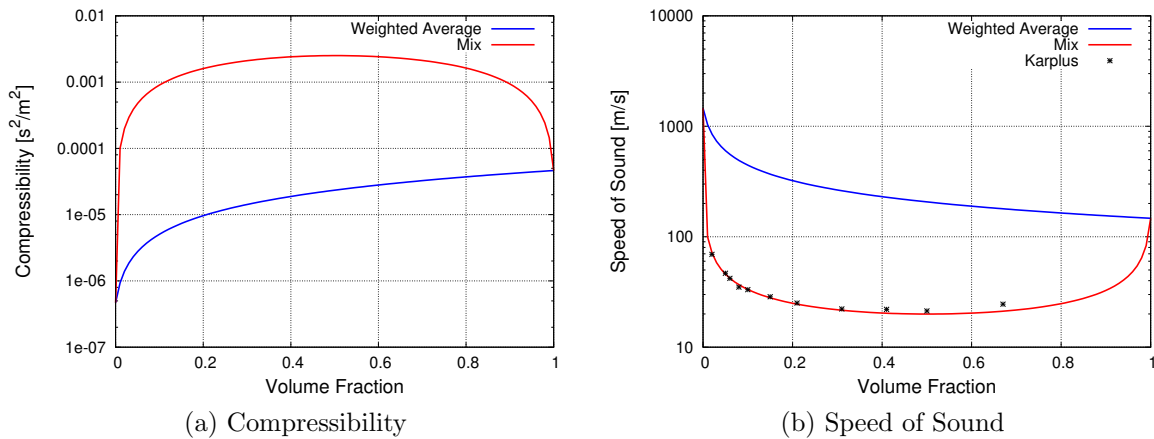


Figure C.1: Compressibility and speed of sound calculated with Eq. (4.21) for water and air compared to experimental data of Karplus [64].

However, this leads to a linear relationship which does not represent the 'U-Shaped' curve known from the speed of sound for a two phase mixture. For water and air at 1 bar pressure and 373 K the compressibility and speed of sound are plotted in Figure C.1 alongside the weighted average approach. For the speed of sound experimental results from [64] are plotted alongside. Figure C.1 shows clearly the large difference in the compressibility and speed of sound compared to a simple weighted average.

C.2 Compressibility and Phase Change

For the system of a liquid and its vapor, a pressure change will lead to a phase change as well. Therefore, instead of compressing the gas it condenses again to the liquid. However, this fact is not yet considered in the equation system. Further, for the case of superheated vapor an increase in pressure is only reducing the superheat but does not lead to condensation as for vapor bubbles in thermodynamic equilibrium.

Appendix D

Sub- and Transonic Treatment of the Pressure Equation in OpenFOAM

Although pressure based solvers are by design not the natural choice for transonic or supersonic flows, OpenFOAM provides a transonic option for most of their solvers. In the following the differences between the sub- and transonic treatment of the pressure equation is presented, using `rhoPimpleFoam` as a basis.

D.1 Pressure Equation

The Poisson equation for the pressure is derived by combining the mass with the momentum conservation equation. This is achieved by replacing the velocity flux in the discretized mass conservation with the discretized momentum equation,

$$\frac{\partial \rho}{\partial t} + \nabla \cdot \left(\rho \left[\frac{H(u)}{a_p} - \frac{\nabla p}{a_p} \right] \right) = 0. \quad (\text{D.1})$$

Here, the momentum equation is written in its discretized form using the H-operator notation of OpenFOAM.

D.1.1 H-operator of OpenFOAM

Any discretized and linearized partial differential equation system can be written in the matrix form $Ax = b$,

$$\underbrace{\begin{bmatrix} a_{11} & a_{12} & \dots & a_{1n} \\ a_{21} & a_{22} & \dots & a_{2n} \\ \vdots & \vdots & \ddots & \vdots \\ a_{n1} & a_{n2} & \dots & a_{nn} \end{bmatrix}}_A x = b \quad (\text{D.2})$$

with x as the solution vector and b as all sources and explicit terms. In the context of OpenFOAM the H-operator takes the off-diagonal (marked in red) and all source terms of the matrix systems and sums them up to provide an explicit term for each cell center. Hence, for the partially discretized momentum equation,

$$a_p u_p = S - \underbrace{\sum_n a_n u_n}_{H(u)} - \nabla p, \quad (\text{D.3})$$

the H-operator comprises of all terms except the pressure gradient. Here, the subscript p describes the cell values, thus the matrix diagonal, and n denotes the neighboring cells, hence the off-diagonal terms. However, as there is no difference between a source term and the pressure gradient in the matrix system $Ax = b$, the momentum equation is assembled without the pressure gradient. Only when the equation is solved, the pressure gradient is added.

D.2 Subsonic Solution

In OpenFOAM the pressure equation in `rhoPimpleFoam` for subsonic flow is described as,

$$\frac{\partial \rho}{\partial t} + \psi \left[\frac{\partial p}{\partial t} \right]_{\text{corr}} + \nabla \cdot \left(\rho \frac{H(u)}{a_p} \right) - \nabla \cdot \left(\frac{\rho}{a_p} \nabla p \right) \quad (\text{D.4})$$

The second term accounts for small changes in the density due to the pressure change over the current iteration cycle,

$$\psi \left[\frac{\partial p}{\partial t} \right]_{\text{corr}} = \psi \left[\frac{p^{k+1} - p^k}{\Delta t} - \frac{p^* - p^k}{\Delta t} \right] \quad (\text{D.5})$$

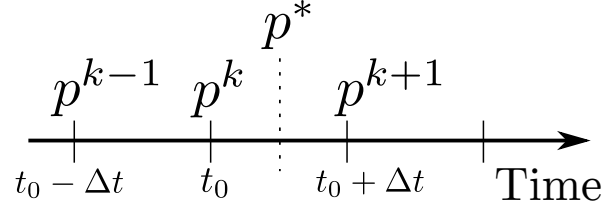


Figure D.1: Sketch of the superscript notation for the time values in OpenFOAM. The superscript k donates the already computed value of the previous time step, p^* is the currently stored value in the field, and $k + 1$ is the to compute value of the next time step. Typically values marked with $k + 1$ are computed implicitly, whereas k and $*$ denoted values are already known and computed explicitly.

where ψ represents the isentropic compressibility,

$$\psi = \left(\frac{\partial \rho}{\partial p} \right)_s. \quad (\text{D.6})$$

Here the superscripts denote different time values of the variable, with p^* as the current pressure value of the current PIMPLE/SIMPLE iteration and p^k as the value from the previously computed time step. Thus, p^k is the known pressure value and obtained with `oldTime()` in OpenFOAM, p^* is the pressure value currently stored and p^{k+1} the implicitly computed value of the next time step, see also Figure D.1.

D.3 Transonic Solution

With increasing Mach number the change of density with the velocity increases and can no longer be neglected,

$$-\text{Ma}^2 \frac{du}{u} = \frac{d\rho}{\rho}.$$

To include this effect into the pressure equation the density is modeled with a linear approach as,

$$\rho = \rho_0 + \psi p. \quad (\text{D.7})$$

The density in the divergence term is replaced in the pressure equation and reads for the example of `rhoPimpleFoam`,

$$\frac{\partial \rho}{\partial t} + \psi \left[\frac{\partial p}{\partial t} \right]_{\text{corr}} + \nabla \cdot \left(\rho \frac{H(u)}{a_p} - \psi p^k \frac{H(u)}{a_p} \right) + \nabla \cdot \left(\psi p^{k+1} \frac{H(u)}{a_p} \right) - \nabla \cdot \left(\frac{\rho}{a_p} \nabla p^{k+1} \right) \quad (\text{D.8})$$

The first and second term are the same as for the subsonic treatment. The third term

is added to increase the stability and only works for ideal gases correctly as only then,

$$\rho = \left(\frac{\partial \rho}{\partial p} \right)_s p = \frac{p}{RT} \quad (\text{D.9})$$

and $\rho_0 = 0$. The fourth term is the implicit divergence term and in the last Laplacian term the density cannot be replaced to avoid non-linear equation systems. It shall be noted that the change in density is still treated largely as an explicit source term,

$$\frac{\partial \rho}{\partial t} = \frac{\rho^* - \rho^k}{\Delta t} + \psi \left[\frac{p^{k+1} - p^k}{\Delta t} - \frac{p^* - p^k}{\Delta t} \right]. \quad (\text{D.10})$$

The change of the density due to temperature changes is solely included in the density derivation and is not considered implicitly. This is avoided in the developed `compressiblePhaseChangeFoam` solver of this thesis, where the density changes are treated fully implicitly as,

$$\frac{\partial \rho}{\partial t} = \frac{\partial \psi \rho}{\partial t} = \frac{(\psi p)^{k+1} - (\psi p)^k}{\Delta t}. \quad (\text{D.11})$$

Appendix E

Real Gas Treatment in the Energy Equation

The enthalpy transport equation for a single component is,

$$\frac{\partial \rho(h + K)}{\partial t} + \nabla \cdot (\rho \mathbf{u}(h + K)) = -\nabla \cdot \mathbf{q} + \frac{\partial p}{\partial t} + S_h, \quad (\text{E.1})$$

hereby the effects of viscosity and friction are neglected. To model the heat flux q , Fourier's law of heat conduction is used,

$$\mathbf{q} = -\kappa \nabla T, \quad (\text{E.2})$$

with κ as the heat conductivity. As it is solved for enthalpy and not temperature, it is useful to replace the temperature gradient with a term of the transported quantity, thus enthalpy.

To achieve this, the total derivative of the enthalpy can be used,

$$dh = \underbrace{\left(\frac{\partial h}{\partial T} \right)_p}_{c_p} dT + \left(\frac{\partial h}{\partial p} \right)_T dp. \quad (\text{E.3})$$

The first term of the equation is typically referred to as constant heat capacity c_p and is a fluid property. The second term is for an ideal gas zero, however for a real gas it has to be considered. To calculate this term the entropy definition,

$$dh = T ds + v dp, \quad (\text{E.4})$$

is used. Substituting the entropy with the total derivative with respect to pressure and

temperature in Eq. (E.4) gives then,

$$dh = T \left(\frac{\partial s}{\partial T} \right)_p dT + \left[T \left(\frac{\partial s}{\partial p} \right)_T + v \right] dp. \quad (\text{E.5})$$

From the Maxwell relations it is known that

$$\left(\frac{\partial s}{\partial p} \right)_T = - \left(\frac{\partial v}{\partial T} \right)_p, \quad (\text{E.6})$$

which then gives

$$dh = T \left(\frac{\partial s}{\partial T} \right)_p dT + \left[v - T \left(\frac{\partial v}{\partial T} \right)_p \right] dp. \quad (\text{E.7})$$

Comparing Eq. (E.7) to Eq. (E.3) shows, that the first term can again be expressed by $c_p dT$, thus the heat flux can be expressed with,

$$q = -\kappa \nabla T = -\kappa \left(\frac{1}{c_p} \nabla h + \frac{1}{c_p} \left[v - T \left(\frac{\partial v}{\partial T} \right)_p \right] \nabla p \right). \quad (\text{E.8})$$

It is now also easy to see that the second term is zero for an ideal gas.

For the case of cryogenic flashing jets the pressure is very low and the vapor phase is far from the critical point, hence the ideal gas assumptions are fulfilled and the heat flux can be approximated with $q = -\frac{\kappa}{c_p} dh$.

Appendix F

A compressible, Two-Phase Solver with Phase Change for OpenFOAM

In this chapter the novel compressible, two-phase solver `compressiblePhaseChangeFoam` is presented in detail. The scope of this chapter is to provide an in-depth view of the equation systems solved, the derivation of the equation system and the assumptions and choices made in the process. This chapter can be considered as an extension of the thesis for researchers interested in the solver. Further, the solver design is reviewed from a programming perspective.

F.1 Solver Outline

In Chapter 4 the *pressure-based* solution principle with OpenFOAM's PIMPLE method was outlined. The flow chart of the PIMPLE loop used for each time step is sketched in Figure F.1. This flow chart shows the main parts of the solver and in which order they are solved. In the following additional information about the individual parts, implementation details and further reasoning for the selected implementation method are given.

Here, a special notation is used. The volume flux stored at the cell faces is denoted with the Greek letter ϕ , consistent to the naming convention of OpenFOAM. The velocity stored in the cell center is denoted as the variable u . Capital Φ represents a general transported property.

F.1.1 Solving the the volume fraction transport in OpenFOAM

The volume fraction transport equation, Eq. (4.10), presented in Chapter 4 is solved in two parts in OpenFOAM. First only the convective part of the transport is solved

using the corrected multi-dimensional limiter for explicit solution (MULES), which uses an implicit solution with an additional explicit correction step to guarantee the boundedness of the volume fraction between 0 and 1 [80]. In the second part the diffusive transport arising from the turbulence modeling is solved.

The convective only transport of MULES solves following transport equation,

$$\frac{\partial \Phi}{\partial t} + \nabla \cdot (\phi \Phi) = S_u + S_p \Phi \quad (\text{F.1})$$

$$\frac{\Phi - \Phi^k}{\Delta t} + \int_A (\phi \Phi) \, dA = S_u + S_p \Phi \quad (\text{F.2})$$

$$\Rightarrow \Phi = \frac{\frac{\Phi^k}{\Delta t} - \int_A (\phi \Phi) \, dA + S_u}{\frac{1}{\Delta t} - S_p} \quad (\text{F.3})$$

The S_p and S_u terms represent source terms, with the OpenFOAM notation for linearizing a source term $\dot{S} = S_u + \Phi S_p$. The question arises now how to treat the source terms on the RHS. To guarantee diagonal dominance sinks should be treated implicitly and sources explicit. The divergence of the velocity is for cases of evaporating liquid positive and is therefore treated explicitly. For the compressibility terms a cell to cell evaluation is made. This leaves the source term of the evaporation \dot{m}_l . Assuming this source term is linearized as well with $\dot{m}_l = S_u + \alpha_l S_p$, and the assumption that S_p is negative, the equation can be rearranged in implicit and explicit treatment,

$$\begin{aligned} \frac{\partial \alpha_l}{\partial t} + \nabla \cdot (\alpha_l \phi) = & \alpha_l \left[\alpha_v \left(\frac{\psi_v}{\rho_v} - \frac{\psi_l}{\rho_l} \right) \frac{Dp}{Dt} + \alpha_v \left(\frac{p}{\rho_v} \frac{D\psi_v}{Dt} - \frac{p}{\rho_l} \frac{D\psi_l}{Dt} \right) + \nabla \cdot \phi \right] \\ & + \alpha_l \frac{S_p}{\rho_l} \left(1 + \alpha_l \left(\frac{\rho_l - \rho_v}{\rho_v} \right) \right) + \frac{S_u}{\rho_l} \left(1 + \alpha_l \left(\frac{\rho_l - \rho_v}{\rho_v} \right) \right) \end{aligned} \quad (\text{F.4})$$

The compressibility and temperature effects,

$$\alpha_l \left[\alpha_v \left(\frac{\psi_v}{\rho_v} - \frac{\psi_l}{\rho_l} \right) \frac{Dp}{Dt} + \alpha_v \left(\frac{p}{\rho_v} \frac{D\psi_v}{Dt} - \frac{p}{\rho_l} \frac{D\psi_l}{Dt} \right) \right]$$

are calculated in the pressure equation and named $\mathbf{dgd}t$. As $\mathbf{dgd}t$ can act as a sink or source term it is evaluated at each cell and either treated implicitly or an explicit formulation is found to enhance numerical stability.

Solving Diffusive Part: The MULES solver can only solve convective transport equations which requires to add an additional diffusion equation after having solved

the convective transport. This is done in OpenFOAM by solving the equation,

$$\left(\frac{\partial\alpha_l}{\partial t}\right)^{k+1} - \left(\frac{\partial\alpha_l}{\partial t}\right)^* - \left(\nabla \cdot \left(\frac{\nu_t}{Sc_t} \nabla \alpha_l\right)\right)^{k+1} = 0. \quad (\text{F.5})$$

Here, the superscript $k + 1$ indicates the implicit treatment and $*$ the explicit solution with the already computed value, see also Figure D.1.

$$\frac{\alpha_l^{k+1} - \alpha_l^k}{\Delta t} - \frac{\alpha_l^* - \alpha_l^k}{\Delta t} + \nabla \cdot \left(\frac{\nu_t}{Sc_t} \nabla \alpha_l^{k+1}\right). \quad (\text{F.6})$$

Here, α_l^* is the solution from the previous MULES iteration.

Determine volume and mass fluxes: After solving the volume fraction transport the volume fraction flux ϕ_α and the mass flux $(\rho\phi)$ are determined. The volume fraction flux is calculated in OpenFOAM with the `fvMatrix::flux()` function which returns the exact surface fluxes used in the matrix to solve the equation system. To calculate the mass flux, the volume fraction flux ϕ_α is used, instead of multiplying the general volume flux ϕ with the volume fraction,

$$\phi_\alpha = \alpha_l \phi \Rightarrow \text{fvc}::\text{flux}(\text{alphaEqn}), \quad (\text{F.7})$$

$$(\rho\phi)_f = \phi_\alpha \rho_{l,f} + (\phi - \phi_\alpha) \rho_{v,f}. \quad (\text{F.8})$$

The interpolated values of the densities, $\rho_{l,f}$ and $\rho_{v,f}$ are obtained with the same discretization scheme selected for the divergence operator of the momentum predictor.

F.1.2 Continuity equation to determine the mass error

After solving the volume fraction transport the mass continuity is solved. This, however, does not modify the density as typically found in the pressure equation, but it determines the current mass error, ϵ_ρ , due to non-converged solutions of momentum, energy and volume fraction transport,

$$\epsilon_\rho = \frac{\partial\rho}{\partial t} + \nabla \cdot (\rho\phi)_f. \quad (\text{F.9})$$

Once the PIMPLE algorithm comes to a converged solution for all governing equations, the mass continuity error vanishes. Nevertheless, before convergence is achieved the error can be used as a stabilizing source term in the momentum and energy equation. This resembles the bounded schemes of OpenFOAM.

F.1.3 Surface density transport equation

The modeling and derivation of the surface density transport is presented in detail in Sec. 3.3. As the surface density does not feed back information to the governing equations, of mass, momentum, and energy conservation, it is an optional model. Therefore, the complete ELSA model with the transport equation and all source terms are encapsulated in an own module which provides a simple `solve()` function to the user. The implementation of the different source terms is straight forward.

F.1.4 Momentum predictor step

In the momentum predictor step the momentum equation is assembled and potentially solved. As mentioned in the previous section the continuity error is added to stabilize the numerical procedure, leading to following equation

$$\frac{\partial \rho u}{\partial t} + \nabla \cdot ((\rho \phi)_f u) - (\epsilon_\rho u) - \nabla \cdot \boldsymbol{\tau} = -\nabla p + S. \quad (\text{F.10})$$

The solver can consider surface tension and gravity forces which would be included in the term S if activated. However, in the cases studied and for fully flashing flows these terms are typically switched off and not further discussed. Their implementation is straight forward and can be looked up in the published literature.

Implementation in OpenFOAM: The LHS of Eq. (F.10) is the part that is assembled for the subsequent pressure equation and is stored in the variable `UEqn`. Only if the momentum predictor switch is activated in OpenFOAM, the momentum equation will be solved to update the velocity and kinetic energy. However, to solve the momentum equation the pressure gradient is not computed directly but in a two step process illustrated in Listing F.1.

Listing F.1: Solving the momentum equation (simplified)

```

1 fvVectorMatrix UEqn (
2     fvm::ddt(rho, U) + fvm::div(rhoPhi, U)
3     + fvm::SuSp(-contErr, U)
4     + turbulence->divDevRhoReff(U)
5 );
6
7 if (pimple.momentumPredictor())
8     solve(
9         UEqn == fvc::reconstruct(fvc::snGrad(p))
10    );

```

First the surface normal gradient is calculated and then the pressure gradient in the cell center is recovered with the `fvc::reconstruct()` function. This process resembles a least-square fit and has been presented by Weller et al. [140] and enhances the stability slightly [5].

F.1.5 Energy conservation

After optionally solving the momentum equation the enthalpy transport for each phase is solved. Here, in the same manner as for the momentum equation, the mass error is used to create a more stable solution. Further, the source terms are treated slightly different for the vapor and the liquid phase. For the liquid phase the source term related to the liquid enthalpy is always positive (for evaporation), which leads to an explicit treatment. However, for the vapor phase it is negative which leads to an implicit treatment of the source term:

$$\begin{aligned} \frac{\partial \rho h_l}{\partial t} + \nabla \cdot (\rho \phi h_l) - (\epsilon_\rho h_l) + \frac{\partial \rho K}{\partial t} + \nabla \cdot (\rho \phi K) - (\epsilon_\rho K) \\ = \left(\frac{\partial p}{\partial t} - \nabla \cdot q \right) + \frac{\rho}{\rho_l \alpha_l} \dot{m}_l [h_{\text{SG}}(p) - h_l] \end{aligned} \quad (\text{F.11})$$

$$\begin{aligned} \frac{\partial \rho h_v}{\partial t} + \nabla \cdot (\rho \phi h_v) - (\epsilon_\rho h_v) + \frac{\partial \rho K}{\partial t} + \nabla \cdot (\rho \phi K) - (\epsilon_\rho K) \\ = \left(\frac{\partial p}{\partial t} - \nabla \cdot q \right) + \frac{\rho}{\rho_v \alpha_v} \dot{m}_l [h_v - h_{\text{SG}}(p)] \end{aligned} \quad (\text{F.12})$$

However, note that the saturation enthalpy of the gas is much higher than the liquid enthalpy, thus leading to a cool down of the liquid and an increase of the vapor temperature.

F.1.6 Pressure equation

In Eq. (4.26) the pressure equation is presented. However, this is not exactly what is solved. To solve the pressure equation in OpenFOAM it is split up in a compressibility contribution which are the first terms of Eq. (4.26), the phase change source term, and the incompressible solution. The last two terms are straight forward to implement, the first term, however, requires some special handling.

The compressibility contributions in the pressure equation can be solved in an explicit-corrected or an implicit way. Both versions are currently supported in the solver and the option for each solution procedure is selected through the `fvSolution` dictionary under the `PIMPLE` options, see Listing F.2.

Listing F.2: fvSolution - Selecting implicit/explicit method

```

1 PIMPLE
2 {
3     fullyImplicit      true;
4 };

```

Explicit-Corrected Pressure Equation

Assuming again the linear model $\rho = \rho_0 + \psi p$ for the phase densities, the compressibility term can be written as,

$$\frac{D\psi_l p}{Dt} = \frac{D\rho_l}{Dt}$$

$$\frac{\alpha_l D\psi_l p}{\rho_l Dt} + \frac{\alpha_v D\psi_v p}{\rho_v Dt} = \frac{\alpha_l D\rho_l}{\rho_l Dt} + \frac{\alpha_v D\rho_v}{\rho_v Dt},$$

which is then for one phase,

$$\begin{aligned} \frac{\alpha_l D\rho_l}{\rho_l Dt} &= \left(\frac{\partial\alpha_l \rho_l}{\partial t} + \nabla \cdot (\alpha_l \rho_l u) \right) \frac{1}{\rho_l} - \left(\frac{\partial\alpha_l}{\partial t} + \nabla \cdot (\alpha_l u) \right) \\ &= \left(\frac{\partial\alpha_l}{\partial t} + u \cdot \nabla \alpha_l + \alpha_l \nabla \cdot u + \frac{\alpha_l}{\rho_l} \frac{\partial\rho_l}{\partial t} + \frac{\alpha_l}{\rho_l} u \cdot \nabla \rho_l \right) \\ &\quad - \left(\frac{\partial\alpha_l}{\partial t} + u \cdot \nabla \alpha_l + \alpha_l \nabla \cdot u \right). \end{aligned} \quad (\text{F.13})$$

(Note, that the same could be achieved by taking the compressibility to zero and only using the temperature dependency of the total derivative)

Eq. (F.13) is then implemented for each of the two phases. As the description of Eq. (F.13) depends entirely on the change of the volume fraction, which has not seen the change of pressure yet, it needs to account for the missing implicit part. This is done with the function `fvMatrix::correction()` from the `fvMatrix.H` class. This function calculates the correction form of a matrix A by subtracting the matrix multiplied with its current field,

$$A\mathbf{x} = B$$

$$\rightarrow A_{\text{corrected}} = (A\mathbf{x} - A\mathbf{x}^*).$$

This correction term is split into a subsonic and transonic formulation.

Subsonic: For subsonic the formulation of the compressibility for one phase is then:

$$\left(\frac{\partial \alpha_l \rho_l}{\partial t} + \nabla \cdot (\alpha_l \rho_l \mathbf{u}) \right) \frac{1}{\rho_l} - \left(\frac{\partial \alpha_l}{\partial t} + \nabla \cdot (\alpha_l \mathbf{u}) \right) + \left(\frac{\alpha_l \psi_l}{\rho_l} \right) \left[\frac{\partial p}{\partial t} \right]_{\text{corr.}} \quad (\text{F.14})$$

Transonic: The transonic description uses for the correction term:

$$\left(\frac{\partial \alpha_l \rho_l}{\partial t} + \nabla \cdot (\alpha_l \rho_l \mathbf{u}) \right) \frac{1}{\rho_l} - \left(\frac{\partial \alpha_l}{\partial t} + \nabla \cdot (\alpha_l \mathbf{u}) \right) + \left(\frac{\alpha_l}{\rho_l} \right) \left[\frac{D(\psi_l p)}{Dt} \right]_{\text{corr.}} \quad (\text{F.15})$$

Implicit Pressure Equation

Instead of solving the compressibility explicitly and to correct then for the pressure change, the equation can also be solved entirely implicit. For this the material derivative is first rewritten, so that there are only divergence terms and no gradients,

$$\frac{D\psi p}{Dt} = \frac{\partial \psi p}{\partial t} + \nabla \cdot (\psi p \mathbf{u}) - \psi p \nabla \cdot \mathbf{u} \quad (\text{F.16})$$

This equation can then be solved entirely implicit where the velocity times the compressibility in the divergence term is calculated on the cell faces, thus:

```
1 phid1 = fvc::interpolate(psi1)*phi
```

However, as the compressibility of the liquid phase is small it is only available for the gas phase.

F.1.7 Update velocities

After solving the pressure equation the volume fluxes and the velocity stored in the cell center are updated. With the discretized momentum equation the velocity is,

$$\mathbf{u} = \frac{H(\mathbf{u})}{a_p} - \frac{1}{a_p} \nabla p. \quad (\text{F.17})$$

Typically the pressure gradient is calculated with the Gauss-Green theorem, however, here the flux of the pressure equation is used directly in combination with the reconstruction method described in Sec. F.1.4,

$$\mathbf{u} = \frac{H(\mathbf{u})}{a_p} + \frac{1}{a_p} \left[\frac{1}{a_p} \nabla p \times a_p \right]_{\text{flux \& reconstruct}}. \quad (\text{F.18})$$

Hence, the same gradients used to solve the pressure equation are selected for the reconstruction of the velocity. In the case of the volume flux the reconstruction can be omitted and the flux used directly.

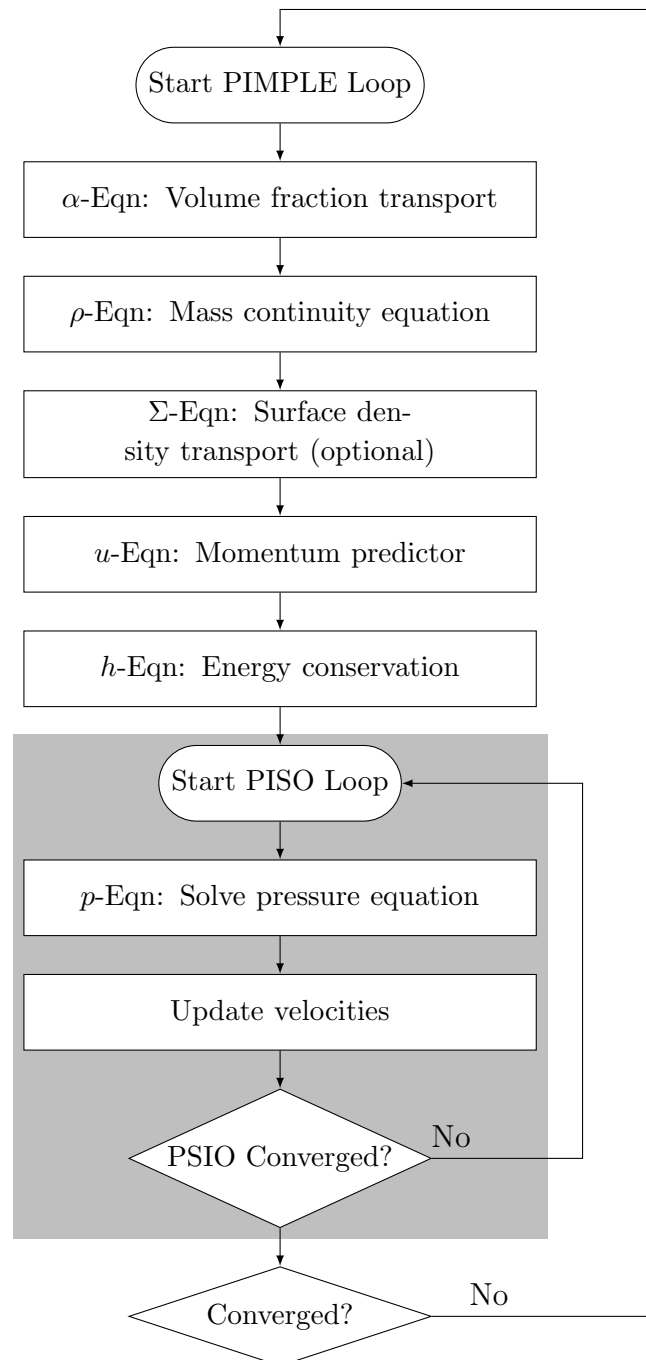


Figure F.1: Flow chart of the PIMPLE algorithm for the `compressiblePhaseChangeFoam` solver. The PISO part of the algorithm is marked with a light gray box.

F.2 Thermodynamic Modeling for Superheated and Saturation Conditions

Despite numerous thermodynamic models implemented in OpenFOAM, none can account for superheated and saturation conditions. Further, the direct calculation of superheated properties with an equation of state is prohibitively time consuming, as we will see in more detail below. Therefore, a novel thermodynamic library relying on thermodynamic tables is developed and implemented in this work to provide all required thermodynamic properties for the solver. In particular these are:

- Density of the vapor or liquid in superheated and subcooled conditions
- Enthalpy-temperature relation
- Compressibility of the liquid or vapor as the derivative of the density to pressure
- All saturation conditions such as saturation pressure, enthalpy, enthalpy, and temperature.

The advantage of this model is that the tabulated properties can be calculated with a high degree of accuracy, using sophisticated models, while the lookup of the values during the simulation can be done in constant time.

F.2.1 Interpolate intermediate values

To determine intermediate values between table entries two interpolation methods are implemented, first a linear and second a bicubic method. In the following the more accurate bicubic method is explained. However, handling of boundary values and outliers is the same for the linear and bicubic method.

The interpolation of an intermediate value of a property that depends on two variables, e.g., such as density on temperature and pressure, $\rho(p,T)$, can be generally described for a point p at the position x, y with,

$$p(x,y) = \sum_{i=0}^3 \sum_{j=0}^3 a_{ij} \bar{x}^i \bar{y}^j \quad (\text{F.19})$$

and

$$\bar{x} = \frac{x - f(0,0)}{f(1,0) - f(0,0)}, \quad (\text{F.20})$$

$$\bar{y} = \frac{y - f(0,1)}{f(1,1) - f(0,1)}. \quad (\text{F.21})$$

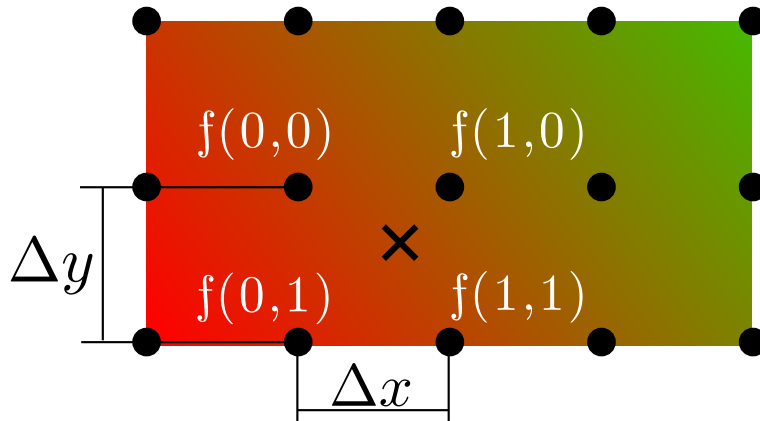


Figure F.2: Bicubic interpolation for points inside the table. Black dots mark table vertices and the cross is the point that is looked up.

Here $f(0,0)$, $f(0,1)$, $f(1,0)$, and $f(1,1)$ denote the tabulated points forming the cell around the interpolated point p , see Figure F.2 The coefficients a_{ij} are determined with,

$$\begin{bmatrix} a_{00} & a_{01} & a_{02} & a_{03} \\ a_{10} & a_{11} & a_{12} & a_{13} \\ a_{20} & a_{21} & a_{22} & a_{23} \\ a_{30} & a_{31} & a_{32} & a_{33} \end{bmatrix} = A * F * B$$

$$A = \begin{bmatrix} 1 & 0 & 0 & 0 \\ 0 & 0 & 1 & 0 \\ -3 & 3 & -2 & -1 \\ 2 & -2 & 1 & 1 \end{bmatrix}, B = \begin{bmatrix} 1 & 0 & -3 & 2 \\ 0 & 0 & 3 & -2 \\ 0 & 1 & -2 & 1 \\ 0 & 0 & -1 & 1 \end{bmatrix}$$

$$F = \begin{bmatrix} f(0,0) & f(0,1) & \Delta y f_y(0,0) & \Delta y f_y(0,1) \\ f(1,0) & f(1,1) & \Delta y f_y(1,0) & \Delta y f_y(1,1) \\ \Delta x f_x(0,0) & \Delta x f_x(0,1) & \Delta x \Delta y f_{xy}(0,0) & \Delta x \Delta y f_{xy}(0,1) \\ \Delta x f_x(1,0) & \Delta x f_x(1,1) & \Delta x \Delta y f_{xy}(1,0) & \Delta x \Delta y f_{xy}(1,1) \end{bmatrix}$$

Determining the partial differentials

The partial differentials as f_x , f_y and f_{xy} are determined either by central differencing or at the borders of the table by second order forward or backwards schemes to gain the same order of accuracy at the boundaries.

Interpolating the differential solution

When the partial derivative of a tabulated property $\frac{\partial f}{\partial x}$ is required the function $f_x(x,y)$ is evaluated at the position x and y . As the correct values for the differential are only

known at the table points, values in between have to be interpolated. For this bilinear interpolation is used. The motivation is, that otherwise the third derivative of the table function would be required and that a linear interpolation is sufficient if the differential of the EoS is needed.

F.2.2 Edge cases

Several different edge cases, points lying outside the table bounds are possible. In the following the handling of different scenarios is described.

Outside the table

If a point is outside the table, such that there can be a complete cell located in the axial direction the point is virtually moved to the table boundary by limiting the looked up value x or y to the table boundary.

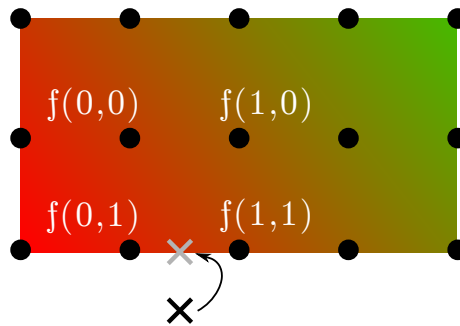


Figure F.3: Handling of interpolation for a point outside the table.

Outside a partially filled table

If the table is only partially filled, e.g. if some points do not give a physical valid solution the nearest neighbor is selected.

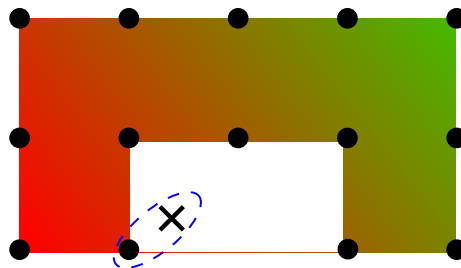


Figure F.4: Handling of interpolation for a point outside the table if the table is only partially filled.

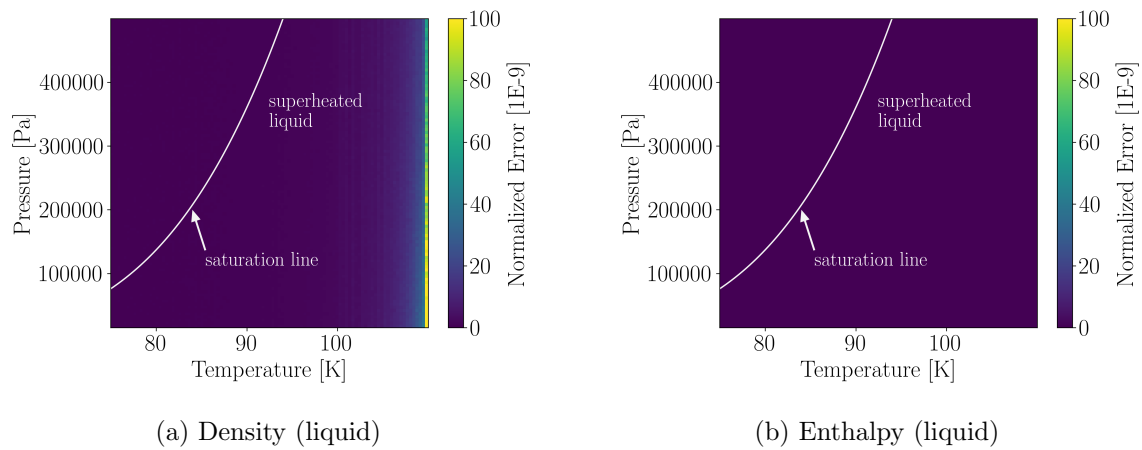


Figure F.5: Normalized error calculating the liquid density (a) and liquid enthalpy (b) of the tabulated properties compared to the exact CoolProp value.

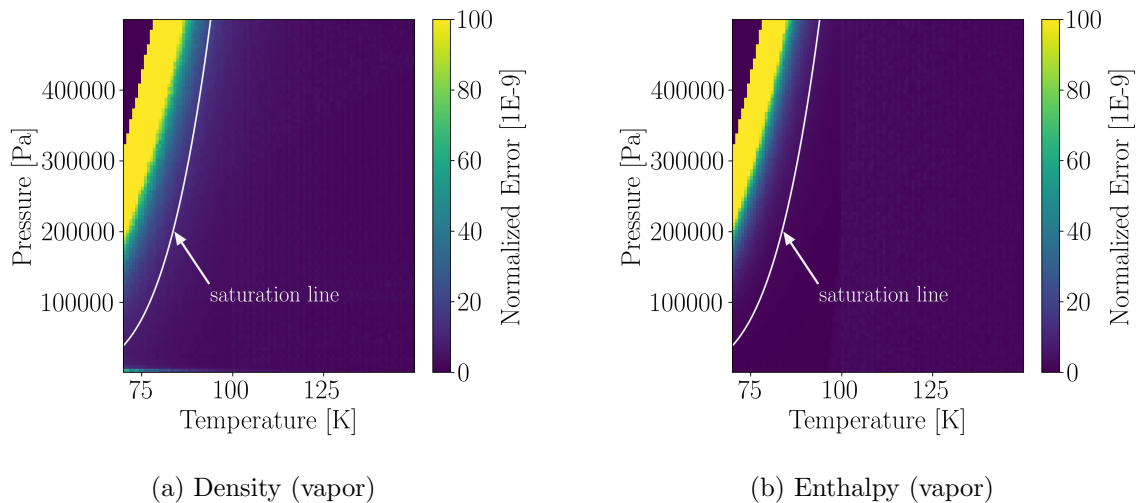


Figure F.6: Normalized error in calculating the vapor density (a) and vapor enthalpy (b) of the tabulated properties to the exact value calculated by CoolProp.

F.2.3 Accuracy of interpolated values

The accuracy of the interpolation is shown in Figure F.5 and F.6 which plot the normalized error of the density and enthalpy calculation for the liquid and vapor phase. In both cases the normalized error is in the valid region about 1×10^{-9} . Only close to the spinodal line for the subcooled vapor or superheated liquid the error increases. Which is however not caused by the tabulated method but by CoolProp no longer providing accurate or converged results close to the spinodal lines.

Appendix G

Data Storage

The solver developed within this work can be found on the University of Stuttgart GitHub server and on DaRUS (<https://doi.org/10.18419/darus-3886>) for permanent storage. The main solver is split in two git repositories. The first one *tabularThermo* adds a new thermodynamic library to OpenFOAM, required to read in the tabulated properties and to provide saturation conditions. The second repository, called *compressiblePhaseChangeFoam*, contains the main solver with the governing equations and all modeling aspects required to solve flashing flows. It shall be noted that the solver was and is undergoing permanent development, optimization, and extension of features. While the newest versions should reproduce the older results, there might be slight differences. Therefore it is advised to check out the version provided in the tables below. In addition, the log files stored with the cases on the ITV data server contain following header:

Listing G.1: Header printed during execution of *compressiblePhaseChangeFoam*

```
1 /*-----*\
2 |   compressiblePhaseChangeFoam |
3 |   Author:   Jan Gaertner (jan.gaertner@outlook.de) |
4 |   Build:    master v6.0-88-g50a5fa1 |
5 |   Using tabularThermo: master 3.0 |
6 \*-----*/
```

This header provides the exact git SHA value required to re-run the cases of the associated paper. In the provided example of Listing G.1 the code version is 'v6.0-88-g50a5fa1', translating to the git commit with the hash 50a5fa1, which is 66 commits after the version 6.0 tag. Further it states the version used for *tabularThermo*. However, this information is implicitly given through the main git sha commit, as the *tabularThermo* is included as a git submodule and the correct state of the library will

be checked out with the solver.

G.1 Paper 1

The LaTeX files of the paper, all required post-processing routines and a path the data storage for the OpenFOAM case files is provided in following git repository: https://github.tik.uni-stuttgart.de/ITV/2020_Gaertner_IJMF

LaTeX files:	https://github.tik.uni-stuttgart.de/ITV/2020_Gaertner_IJMF
Case Files:	2020_Gaertner_IJMF
Code version:	v4.1 v5.0 v5.1

G.2 Paper 2

The LaTeX files of the paper, all required post-processing routines and a path the data storage for the OpenFOAM case files is provided in following git repository: https://github.tik.uni-stuttgart.de/ITV/2020_Gaertner_Fluids

LaTeX files:	https://github.tik.uni-stuttgart.de/ITV/2021_Gaertner_Fluids
Cases Files:	2020_Gaertner_Fluids
Code version:	8cf160 5d8b442 7d27c98 a8cf160 8a9753d

G.3 Paper 3

The LaTeX files of the paper, all required post-processing routines and a path the data storage for the OpenFOAM case files is provided in following git repository: https://github.tik.uni-stuttgart.de/ITV/2023_Gaertner_FTC

LaTeX files:	https://github.tik.uni-stuttgart.de/ITV/2023_Gaertner_FTC
Cases Files:	2020_Gaertner_FTC
Code version:	a806d3f 5647b33 0ea0f29 50a5fa1

G.4 Paper 4

The LaTeX files of the paper, all required post-processing routines and a path the data storage for the OpenFOAM case files is provided in following git repository: https://github.tik.uni-stuttgart.de/ITV/2024_Gaertner_IJMF

LaTeX files:	https://github.tik.uni-stuttgart.de/ITV/2024_Gaertner_IJMF
Cases Files:	2024_Gaertner_IJMF
Code version:	b4731eb

Bibliography

- [1] B. Abramzon and W. A. Sirignano. “Droplet Vaporization Model for Spray Combustion Calculations”. In: *International Journal of Heat and Mass Transfer* 32.9 (1989), pp. 1605–1618. DOI: 10.1016/0017-9310(89)90043-4.
- [2] M. Adachi, V. G. McDonell, D. Tanaka, J. Senda, and H. Fujimoto. “Characterization of Fuel Vapor Concentration Inside a Flash Boiling Spray”. In: *SAE International*. 1997. DOI: 10.4271/970871.
- [3] A. A. Adedoyin, D. K. Walters, and S. Bhushan. “Investigation of Turbulence Model and Numerical Scheme Combinations for Practical Finite-Volume Large Eddy Simulations”. In: *Engineering Applications of Computational Fluid Mechanics* 9.1 (2015), pp. 324–342. DOI: 10.1080/19942060.2015.1028151.
- [4] A. A. Adeniyi, H. P. Morvan, and K. A. Simmons. “A Coupled Euler-Lagrange CFD Modelling of Droplets-to-Film”. In: *The Aeronautical Journal* 121.1246 (2017), pp. 1897–1918. DOI: 10.1017/aer.2017.107.
- [5] H. J. Aguerre, C. I. Pairetti, C. M. Venier, S. Márquez Damián, and N. M. Nigro. “An Oscillation-Free Flow Solver Based on Flux Reconstruction”. In: *Journal of Computational Physics* 365 (2018), pp. 135–148. DOI: 10.1016/j.jcp.2018.03.033.
- [6] Md. Alamgir and J. H. Lienhard. “Correlation of Pressure Undershoot During Hot-Water Depressurization”. In: *Journal of Heat Transfer* 103.1 (1981), pp. 52–55. DOI: 10.1115/1.3244429.
- [7] T. Alghamdi, S. T. Thoroddsen, and J. F. Hernández-Sánchez. “Ultra-High Speed Visualization of a Flash-Boiling Jet in a Low-Pressure Environment”. In: *International Journal of Multiphase Flow* 110 (2019), pp. 238–255. DOI: 10.1016/j.ijmultiphaseflow.2018.08.004.
- [8] J. Anez, A. Ahmed, N. Hecht, B. Duret, J. Reveillon, and F. Demoulin. “Eulerian–Lagrangian Spray Atomization Model Coupled with Interface Capturing

- Method for Diesel Injectors”. In: *International Journal of Multiphase Flow* 113 (2019), pp. 325–342. DOI: 10.1016/j.ijmultiphaseflow.2018.10.009.
- [9] C. Argyropoulos and N. Markatos. “Recent Advances on the Numerical Modelling of Turbulent Flows”. In: *Applied Mathematical Modelling* 39.2 (2015), pp. 693–732. DOI: 10.1016/j.apm.2014.07.001.
- [10] M. Arienti, L. Wang, M. Corn, X. Li, M. C. Soteriou, T. A. Shedd, and M. Herrmann. “Modeling Wall Film Formation and Breakup Using an Integrated Interface-Tracking/Discrete-Phase Approach”. In: *Journal of Engineering for Gas Turbines and Power* 133.3 (2011), p. 031501. DOI: 10.1115/1.4002019.
- [11] J. Barták. “A Study of the Rapid Depressurization of Hot Water and the Dynamics of Vapour Bubble Generation in Superheated Water”. In: *International Journal of Multiphase Flow* 16.5 (1990), pp. 789–798. DOI: 10.1016/0301-9322(90)90004-3.
- [12] R. Becker and W. Döring. “Kinetische Behandlung der Keimbildung in übersättigten Dämpfen”. In: *Annalen der Physik* 416.8 (1935), pp. 719–752. DOI: 10.1002/andp.19354160806.
- [13] I. H. Bell, J. Wronski, S. Quoilin, and V. Lemort. “Pure and Pseudo-pure Fluid Thermophysical Property Evaluation and the Open-Source Thermophysical Property Library CoolProp”. In: *Industrial & Engineering Chemistry Research* 53.6 (2014), pp. 2498–2508. DOI: 10.1021/ie4033999.
- [14] P. Bhattacharyya and B. K. Chakrabarti. “The Mean Distance to the N th Neighbour in a Uniform Distribution of Random Points: An Application of Probability Theory”. In: *European Journal of Physics* 29.3 (2008), pp. 639–645. DOI: 10.1088/0143-0807/29/3/023.
- [15] R. W. Bilger. “A Note on Favre Averaging in Variable Density Flows”. In: *Combustion Science and Technology* 11.5-6 (1975), pp. 215–217. DOI: 10.1080/00102207508946700.
- [16] Z. Bilicki and J. Kestin. “Physical Aspects of the Relaxation Model in Two-Phase Flow”. In: *Proceedings of the Royal Society A: Mathematical, Physical and Engineering Sciences* 428.1875 (1990), pp. 379–397. DOI: 10.1098/rspa.1990.0040.
- [17] M. Blander and J. Katz. “Bubble Nucleation in Liquids”. In: *AiChE Journal* 21.5 (1975), pp. 833–848. DOI: 10.1002/aic.690210502.

- [18] J. Blazek. *Computational Fluid Dynamics: Principles and Applications*. Third edition. Amsterdam: Butterworth-Heinemann, 2015. 447 pp.
- [19] M. Börner, J. C. Deeken, C. Manfretti, and M. Oswald. “Experimental Study of a Laser Ignited Thruster with a Porous Injector Head”. In: *International Journal of Energetic Materials and Chemical Propulsion* 17.4 (2018), pp. 263–286. DOI: 10.1615/IntJEnergeticMaterialsChemProp.2019027382.
- [20] M. Börner, C. Manfretti, G. Kroupa, and M. Oswald. “Laser Ignition of an Experimental Combustion Chamber with a Multi-Injector Configuration at Low Pressure Conditions”. In: *CEAS Space Journal* 9.3 (2017), pp. 299–311. DOI: 10.1007/s12567-017-0161-9.
- [21] M. Bossert, I. Trimaille, L. Cagnon, B. Chabaud, C. Gueneau, P. Spathis, P. E. Wolf, and E. Rolley. “Surface Tension of Cavitation Bubbles”. In: *Proceedings of the National Academy of Sciences* 120.15 (2023), e2300499120. DOI: 10.1073/pnas.2300499120.
- [22] C. E. Brennen. *Fundamentals of Multiphase Flow*. Cambridge [England] ; New York: Cambridge University Press, 2005. 345 pp.
- [23] V. P. Carey. *Liquid-Vapor Phase-Change Phenomena*. 3rd. Boca Raton: Taylor and Francis, 2020.
- [24] I. B. Celik, Z. N. Cehreli, and I. Yavuz. “Index of Resolution Quality for Large Eddy Simulations”. In: *Journal of Fluids Engineering, Transactions of the ASME* 127.5 (2005), pp. 949–958. DOI: 10.1115/1.1990201.
- [25] D. R. Chapman. “Computational Aerodynamics Development and Outlook”. In: *AIAA Journal* 17.12 (1979), pp. 1293–1313. DOI: 10.2514/3.61311.
- [26] W.-l. Cheng, H. Chen, L. Hu, and W.-w. Zhang. “Effect of Droplet Flash Evaporation on Vacuum Flash Evaporation Cooling: Modeling”. In: *International Journal of Heat and Mass Transfer* 84 (2015), pp. 149–157. DOI: 10.1016/j.ijheatmasstransfer.2014.12.078.
- [27] V. Cleary, P. Bowen, and H. Witlox. “Flashing Liquid Jets and Two-Phase Droplet Dispersion. I. Experiments for Derivation of Droplet Atomisation Correlations”. In: *Journal of Hazardous Materials* 142.3 (2007), pp. 786–796. DOI: 10.1016/j.jhazmat.2006.06.125.

- [28] “Guide: Guide for the Verification and Validation of Computational Fluid Dynamics Simulations (AIAA G-077-1998(2002))”. In: *Guide: Guide for the Verification and Validation of Computational Fluid Dynamics Simulations (AIAA G-077-1998(2002))*. Ed. by Computational Fluid Dynamics Committee. Washington, DC: American Institute of Aeronautics and Astronautics, Inc., 1998. DOI: 10.2514/4.472855.001.
- [29] S. M. Damian. “An Extended Mixture Model for the Simultaneous Treatment of Small-Scale and Large-Scale Interfaces”. Doctorial Thesis. Universidad nacional del Litoral, 2013. arXiv: DOI:10.1002/flid.1.
- [30] P. Deligiannis and J. Cleaver. “Determination of the Heterogeneous Nucleation Factor during a Transient Liquid Expansion”. In: *International Journal of Multiphase Flow* 18.2 (1992), pp. 273–278. DOI: 10.1016/0301-9322(92)90088-X.
- [31] B. M. Devassy, D. Benkovi, Z. Petranovic, W. Edelbauer, and M. Vujanovic. “Numerical Simulation of Internal Flashing in a GDI Injector Nozzle”. In: *ILASS Europe 2019*. 2019, pp. 2–4.
- [32] D. Dietzel, T. Hitz, C. D. Munz, and A. Kronenburg. “Single Vapour Bubble Growth under Flash Boiling Conditions Using a Modified HLLC Riemann Solver”. In: *International Journal of Multiphase Flow* 116 (2019), pp. 250–269. DOI: 10.1016/j.ijmultiphaseflow.2019.04.010.
- [33] A. Dinh Le. “Study of Thermodynamic Effect on the Mechanism of Flashing Flow Under Pressurized Hot Water by a Homogeneous Model”. In: *Journal of Fluids Engineering* 144.1 (2022), p. 011206. DOI: 10.1115/1.4051972.
- [34] P. Downar-Zapolski, Z. Bilicki, L. Bolle, and J. Franco. “The Non-Equilibrium Relaxation Model for One-Dimensional Flashing Liquid Flow”. In: *International Journal of Multiphase Flow* 22.3 (1996), pp. 473–483. DOI: 10.1016/0301-9322(95)00078-X.
- [35] F. Ducros, V. Ferrand, F. Nicoud, C. Weber, D. Darracq, C. Gacherieu, and T. Poinsot. “Large-Eddy Simulation of the Shock/Turbulence Interaction”. In: *Journal of Computational Physics* (1999). DOI: 10.1006/jcph.1999.6238.
- [36] B. Duret, J. Reveillon, T. Menard, and F. Demoulin. “Improving Primary Atomization Modeling through DNS of Two-Phase Flows”. In: *International Journal of Multiphase Flow* 55 (2013), pp. 130–137. DOI: 10.1016/j.ijmultiphaseflow.2013.05.004.

- [37] B. Düz, M. J. A. Borsboom, A. E. P. Veldman, P. R. Wellens, and R. H. M. Huijsmans. “Efficient and Accurate PLIC-VOF Techniques for Numerical Simulations of Free Surface Water Waves”. In: *Proceedings of the 9th International Conference on Computational Fluid Dynamics - ICCFD9*. 2016.
- [38] V. Dyadechko and M. Shashkov. “Moment-of-Fluid Interface Reconstruction”. In: *Los Alamos National Laboratory* (2005).
- [39] D. Edgington-Mitchell, D. R. Honnery, and J. Soria. “The Underexpanded Jet Mach Disk and Its Associated Shear Layer”. In: *Physics of Fluids* 26.9 (2014), p. 096101. DOI: 10.1063/1.4894741.
- [40] E. Elias, S. Levy, and P. Chambré. “A Mechanistic Non-Equilibrium Model for Two-Phase Critical Flow”. In: *International Journal of Multiphase Flow* 10.1 (1983), pp. 21–40. DOI: 10.1016/0301-9322(83)90058-7.
- [41] L. Farkas. “Keimbildungsgeschwindigkeit in Übersättigten Dämpfen”. In: *Zeitschrift für Physikalische Chemie* 125U.1 (1927), pp. 236–242. DOI: 10.1515/zpch-1927-12513.
- [42] E. Franquet, V. Perrier, S. Gibout, and P. Bruel. “Free Underexpanded Jets in a Quiescent Medium: A Review”. In: *Progress in Aerospace Sciences* 77 (2015), pp. 25–53. DOI: 10.1016/j.paerosci.2015.06.006.
- [43] Y. I. Frenkel. *Kinetic Theory of Liquids*. Dover, 1955.
- [44] M. Frey and G. Hagemann. “Restricted Shock Separation in Rocket Nozzles”. In: *Journal of Propulsion and Power* 16.3 (2000), pp. 478–484. DOI: 10.2514/2.5593.
- [45] C. Fureby. “ILES and LES of Complex Engineering Turbulent Flows”. In: *Journal of Fluids Engineering* 129.12 (2007), pp. 1514–1523. DOI: 10.1115/1.2801370.
- [46] M. Gallo, F. Magaletti, and C. M. Casciola. “Heterogeneous Bubble Nucleation Dynamics”. In: *Journal of Fluid Mechanics* 906 (2021), A20. DOI: 10.1017/jfm.2020.761.
- [47] W. Gao, J. Qi, J. Zhang, G. Chen, and D. Wu. “An Experimental Study on Explosive Boiling of Superheated Droplets in Vacuum Spray Flash Evaporation”. In: *International Journal of Heat and Mass Transfer* 144 (2019), p. 118552. DOI: 10.1016/j.ijheatmasstransfer.2019.118552.

- [48] J. W. Gärtner, Y. Feng, A. Kronenburg, and O. T. Stein. “Numerical Investigation of Spray Collapse in GDI with OpenFOAM”. In: *Fluids* 6.3 (2021), p. 104. DOI: 10.3390/fluids6030104.
- [49] J. W. Gärtner and A. Kronenburg. “A Novel ELSA Model for Flash Evaporation”. In: *International Journal of Multiphase Flow (submitted)* (2023 (submitted)).
- [50] J. W. Gärtner, A. Kronenburg, and T. Martin. “Efficient WENO Library for OpenFOAM”. In: *SoftwareX* 12 (2020), p. 100611. DOI: 10.1016/j.softx.2020.100611.
- [51] J. W. Gärtner, A. Kronenburg, A. Rees, and M. Oswald. “Investigating 3-D Effects on Flashing Cryogenic Jets with Highly Resolved LES”. In: *Flow, Turbulence and Combustion* (2023). DOI: 10.1007/s10494-023-00485-4.
- [52] J. W. Gärtner, A. Kronenburg, A. Rees, J. Sender, M. Oswald, and G. Lamanna. “Numerical and Experimental Analysis of Flashing Cryogenic Nitrogen”. In: *International Journal of Multiphase Flow* 130 (2020). DOI: 10.1016/j.ijmultiphaseflow.2020.103360.
- [53] M. Germano, U. Piomelli, P. Moin, and W. H. Cabot. “A Dynamic Subgrid-Scale Eddy Viscosity Model”. In: *Physics of Fluids A: Fluid Dynamics* 3.7 (1991), pp. 1760–1765. DOI: 10.1063/1.857955.
- [54] J. W. Gibbs. *The Scientific Papers of J. Willard Gibbs*. Dover Publ., 1961.
- [55] V. R. Gopala and B. G. Van Wachem. “Volume of Fluid Methods for Immiscible-Fluid and Free-Surface Flows”. In: *Chemical Engineering Journal* 141.1-3 (2008), pp. 204–221. DOI: 10.1016/j.cej.2007.12.035.
- [56] C. J. Greenshields and H. G. Weller. *Notes on Computational Fluid Dynamics: General Principles*. Reading, UK: CFD Direct Limited, 2022.
- [57] H. Guo, Y. Li, H. Xu, S. Shuai, and H. Zhang. “Interaction between Under-Expanded Flashing Jets: A Numerical Study”. In: *International Journal of Heat and Mass Transfer* 137 (2019), pp. 990–1000. DOI: 10.1016/j.ijheatmasstransfer.2019.04.010.
- [58] H. Guo, L. Nocivelli, and R. Torelli. “Numerical Study on Spray Collapse Process of ECN Spray G Injector under Flash Boiling Conditions”. In: *Fuel* 290 (December 2020 2021), p. 119961. DOI: 10.1016/j.fuel.2020.119961.

- [59] H. Guo, L. Nocivelli, R. Torelli, and S. Som. “Towards Understanding the Development and Characteristics of Under-Expanded Flash Boiling Jets”. In: *International Journal of Multiphase Flow* 129 (2020), p. 103315. DOI: 10.1016/j.ijmultiphaseflow.2020.103315.
- [60] H. Hertz. “Ueber Die Verdunstung Der Flüssigkeiten, Insbesondere Des Quecksilbers, Im Luftleeren Raume”. In: *Annalen der Physik und Chemie* 17 (1882).
- [61] S. Hickel, C. P. Egerer, and J. Larsson. “Subgrid-Scale Modeling for Implicit Large Eddy Simulation of Compressible Flows and Shock-Turbulence Interaction”. In: *Physics of Fluids* 26.10 (2014). DOI: 10.1063/1.4898641.
- [62] H. Jasak and H. G. Weller. *Interface Tracking Capabilities of the Inter-Gamma Differencing Scheme*. Imperial College of Science, Technology and Medicine, 1995.
- [63] I. Karathanassis, P. Koukouvinis, and M. Gavaises. “Comparative Evaluation of Phase-Change Mechanisms for the Prediction of Flashing Flows”. In: *International Journal of Multiphase Flow* 95 (2017), pp. 257–270. DOI: 10.1016/j.ijmultiphaseflow.2017.06.006.
- [64] H. B. Karplus. *The Velocity of Sound in a Liquid Containing Gas Bubbles*. United States, 1958.
- [65] Y. Kitamura, T. Takahashi, and H. Morimitsu. “Critical Superheat for Flashing of Superheated Liquid Jets”. In: *Industrial and Engineering Chemistry Fundamentals* 25.2 (1986), pp. 206–211. DOI: 10.1021/i100022a005.
- [66] M. Klein, J. Meyers, and B. J. Geurts. “Assessment of LES Quality Measures Using the Error Landscape Approach”. In: *Quality and Reliability of Large-Eddy Simulations*. Ed. by J. Meyers, B. J. Geurts, and P. Sagaut. Vol. 12. Dordrecht: Springer Netherlands, 2008, pp. 131–142. DOI: 10.1007/978-1-4020-8578-9_11.
- [67] M. Knudsen. *The Kinetic Theory of Gases*. 3rd ed. Vol. 64. Wiley, 1952.
- [68] N. I. Kolev. *Multiphase Flow Dynamics 4*. Berlin, Heidelberg: Springer Berlin Heidelberg, 2012. DOI: 10.1007/978-3-642-20749-5.
- [69] M. V. Kraposhin, M. Banholzer, M. Pfitzner, and I. K. Marchevsky. “A Hybrid Pressure-Based Solver for Nonideal Single-Phase Fluid Flows at All Speeds”. In: *International Journal for Numerical Methods in Fluids* 88.2 (2018). DOI: 10.1002/flid.4512.

- [70] T. Kurschat, H. Chaves, and G. E. Meier. “Complete Adiabatic Evaporation of Highly Superheated Liquid Jets”. In: *Journal of Fluid Mechanics* 236 (1992), pp. 43–59.
- [71] H.-Y. Kwak and S.-D. Oh. “Gas–Vapor Bubble Nucleation—a Unified Approach”. In: *Journal of Colloid and Interface Science* 278.2 (2004), pp. 436–446. DOI: 10.1016/j.jcis.2004.06.020.
- [72] J. Lacey, F. Poursadegh, M. J. Brear, R. Gordon, P. Petersen, C. Lakey, B. Butcher, and S. Ryan. “Generalizing the Behavior of Flash-Boiling, Plume Interaction and Spray Collapse for Multi-Hole, Direct Injection”. In: *Fuel* 200 (2017), pp. 345–356. DOI: 10.1016/j.fuel.2017.03.057.
- [73] G. Lamanna, H. Kamoun, B. Weigand, and J. Steelant. “Towards a Unified Treatment of Fully Flashing Sprays”. In: *International Journal of Multiphase Flow* 58 (2014), pp. 168–184. DOI: 10.1016/j.ijmultiphaseflow.2013.08.010.
- [74] R. Lebas, T. Menard, P. A. Beau, A. Berlemont, and F. X. Demoulin. “Numerical Simulation of Primary Break-up and Atomization: DNS and Modelling Study”. In: *International Journal of Multiphase Flow* 35.3 (2009), pp. 247–260. DOI: 10.1016/j.ijmultiphaseflow.2008.11.005.
- [75] H. S. Lee and H. Merte. “Spherical Vapor Bubble Growth in Uniformly Superheated Liquids”. In: *International Journal of Heat and Mass Transfer* 39.12 (1996), pp. 2427–2447. DOI: 10.1016/0017-9310(95)00342-8.
- [76] J. Lee, R. Madabhushi, C. Fotache, S. Gopalakrishnan, and D. Schmidt. “Flashing Flow of Superheated Jet Fuel”. In: *Proceedings of the Combustion Institute* 32 II.2 (2009), pp. 3215–3222. DOI: 10.1016/j.proci.2008.06.153.
- [77] S. Li, Y. Zhang, W. Qi, and B. Xu. “Quantitative Observation on Characteristics and Breakup of Single Superheated Droplet”. In: *Experimental Thermal and Fluid Science* 80 (2017), pp. 305–312. DOI: 10.1016/j.expthermflusci.2016.09.004.
- [78] Y. Liao and D. Lucas. “Computational Modelling of Flash Boiling Flows: A Literature Survey”. In: *International Journal of Heat and Mass Transfer* 111 (2017), pp. 246–265. DOI: 10.1016/j.ijheatmasstransfer.2017.03.121.
- [79] Y. Liao and D. Lucas. “Possibilities and Limitations of CFD Simulation for Flashing Flow Scenarios in Nuclear Applications”. In: *Energies* 10.1 (2017), p. 139. DOI: 10.3390/en10010139.

- [80] Z. Lin, W. Yang, H. Zhou, X. Xu, L. Sun, Y. Zhang, and Y. Tang. “Communication Optimization for Multiphase Flow Solver in the Library of OpenFOAM”. In: *Water (Switzerland)* 10.10 (2018), pp. 7–9. DOI: 10.3390/w10101461.
- [81] D. Loureiro, J. Reutzsch, D. Dietzel, A. Kronenburg, B. Weigand, and K. Vogiatzaki. “DNS of Multiple Bubble Growth and Droplet Formation in Superheated Liquids”. In: International Conference on Liquid Atomization and Spray Systems. Chicago, 2018, pp. 1–8.
- [82] D. D. Loureiro, J. Reutzsch, A. Kronenburg, B. Weigand, and K. Vogiatzaki. “Primary Breakup Regimes for Cryogenic Flash Atomization”. In: *International Journal of Multiphase Flow* 132 (2020), p. 103405. DOI: 10.1016/j.ijmultiphaseflow.2020.103405.
- [83] D. Loureiro, A. Kronenburg, J. Reutzsch, B. Weigand, and K. Vogiatzaki. “Droplet Size Distributions in Cryogenic Flash Atomization”. In: *International Journal of Multiphase Flow* 142 (2021), p. 103705. DOI: 10.1016/j.ijmultiphaseflow.2021.103705.
- [84] M. Luo, P. Zhu, U. Rana, H. Ma, Z. Yu, and O. J. Haidn. “Modeling Investigation of Liquid Oxygen Flashing Spray with CFD”. In: *Journal of Physics: Conference Series* 2235.1 (2022), p. 012061. DOI: 10.1088/1742-6596/2235/1/012061.
- [85] K. Lyras, S. Dembele, D. P. Schmidt, and J. X. Wen. “Numerical Simulation of Subcooled and Superheated Jets under Thermodynamic Non-Equilibrium”. In: *International Journal of Multiphase Flow* 102 (2018), pp. 16–28. DOI: 10.1016/j.ijmultiphaseflow.2018.01.014.
- [86] K. G. Lyras, S. Dembele, and J. X. Wen. “Numerical Simulation of Flashing Jets Atomisation Using a Unified Approach”. In: *International Journal of Multiphase Flow* 113 (2019), pp. 45–58. DOI: 10.1016/j.ijmultiphaseflow.2018.12.011.
- [87] T. Lyras, I. Karathanassis, N. Kyriazis, P. Koukouvinis, and M. Gavaises. “Modelling of Liquid Oxygen Nozzle Flows under Subcritical and Supercritical Pressure Conditions”. In: *International Journal of Heat and Mass Transfer* 177 (2021), p. 121559. DOI: 10.1016/j.ijheatmasstransfer.2021.121559.
- [88] T. Lyras, I. K. Karathanassis, N. Kyriazis, P. Koukouvinis, and M. Gavaises. “Numerical Modelling of Cryogenic Flows Under Near-Vacuum Pressure Conditions”. In: *Proceedings of the 4th International Seminar on Non-Ideal Compressible Fluid Dynamics for Propulsion and Power*. Ed. by M. White, T. El Samad, I. Karathanassis, A. Sayma, M. Pini, and A. Guardone. Vol. 29. Cham: Springer Nature Switzerland, 2023, pp. 114–124. DOI: 10.1007/978-3-031-30936-6_12.

- [89] C. Manfretti. “Laser Ignition of an Experimental Cryogenic Reaction and Control Thruster: Ignition Energies”. In: *Journal of Propulsion and Power* 30.4 (2014), pp. 952–961. DOI: 10.2514/1.B35115.
- [90] J. Martin. “The Gravity-Driven Flashing of Metastable Water in a Pool Heated from Below”. Doctoral Thesis. Belgium: University Ottignies-Louvain-la-Neuve, 2023.
- [91] T. Ménard, S. Tanguy, and A. Berlemont. “Coupling Level Set/VOF/Ghost Fluid Methods: Validation and Application to 3D Simulation of the Primary Break-up of a Liquid Jet”. In: *International Journal of Multiphase Flow* 33.5 (2007), pp. 510–524. DOI: 10.1016/j.ijmultiphaseflow.2006.11.001.
- [92] F. R. Menter. “Two-Equation Eddy-Viscosity Turbulence Models for Engineering Applications”. In: *AIAA Journal* 32.8 (1994), pp. 1598–1605. DOI: 10.2514/3.12149.
- [93] F. R. Menter. “Review of the Shear-Stress Transport Turbulence Model Experience from an Industrial Perspective”. In: *International Journal of Computational Fluid Dynamics* 23.4 (2009), pp. 305–316. DOI: 10.1080/10618560902773387.
- [94] O. Miyatake, Y. Koito, K. Tagawa, and Y. Maruta. “Transient Characteristics and Performance of a Novel Desalination System Based on Heat Storage and Spray Flashing”. In: *Desalination* 137.1 (2001), pp. 157–166. DOI: 10.1016/S0011-9164(01)00214-4.
- [95] C. K. Mohapatra, D. P. Schmidt, B. A. Sforzo, K. E. Matusik, Z. Yue, C. F. Powell, S. Som, B. Mohan, H. G. Im, J. Badra, M. Bode, H. Pitsch, D. Papoulias, K. Neroorkar, S. Muzaferija, P. Martí-Aldaraví, and M. Martínez. “Collaborative Investigation of the Internal Flow and Near-Nozzle Flow of an Eight-Hole Gasoline Injector (Engine Combustion Network Spray G)”. In: *International Journal of Engine Research* (2020). DOI: 10.1177/1468087420918449.
- [96] K. Neroorkar, S. Gopalakrishnan, R. O. Grover, and D. P. Schmidt. “Simulation of Flash Boiling in Pressure Swirl Injectors”. In: *Atomization and Sprays* 21.2 (2011), pp. 179–188. DOI: 10.1615/AtomizSpr.2011003077.
- [97] F. Nicoud and F. Ducros. “Subgrid-Scale Stress Modelling Based on the Square of the Velocity”. In: *Flow, Turbulence and Combustion* 62 (1999), pp. 183–200.
- [98] R. D. Oza and J. F. Sinnamon. “An Experimental and Analytical Study of Flash-Boiling Fuel Injection”. In: *SAE International* 92 (1983), pp. 948–962. DOI: 10.4271/830590.

- [99] A. H. Persad and C. A. Ward. “Expressions for the Evaporation and Condensation Coefficients in the Hertz-Knudsen Relation”. In: *Chemical Reviews* 116.14 (2016), pp. 7727–7767. DOI: 10.1021/acs.chemrev.5b00511.
- [100] M. Pilch and C. A. Erdman. “Use of Breakup Time Data and Velocity History Data to Predict the Maximum Size of Stable Fragments for Acceleration-Induced Breakup of a Liquid Drop”. In: *International Journal of Multiphase Flow* 13.6 (1987), pp. 741–757. DOI: 10.1016/0301-9322(87)90063-2.
- [101] M. S. Plesset and A. Prosperetti. “Bubble Dynamics and Cavitation”. In: *Annual Review of Fluid Mechanics* 9.1 (1977), pp. 145–185. DOI: 10.1146/annurev.fl.09.010177.001045.
- [102] M. S. Plesset and S. A. Zwick. “A Nonsteady Heat Diffusion Problem with Spherical Symmetry”. In: *Journal of Applied Physics* 23.1 (1952), pp. 95–98.
- [103] S. B. Pope. *Turbulent Flows*. 1. publ., 12. print. Cambridge: Cambridge Univ. Press, 2015. 771 pp.
- [104] F. Poursadegh, J. S. Lacey, M. J. Brear, R. L. Gordon, P. Petersen, C. Lakey, B. Butcher, S. Ryan, and U. Kramer. “On the Phase and Structural Variability of Directly Injected Propane at Spark Ignition Engine Conditions”. In: *Fuel* 222 (July 2017 2018), pp. 294–306. DOI: 10.1016/j.fuel.2018.02.137.
- [105] C. Price, A. Hamzehloo, P. Aleiferis, and D. Richardson. “An Approach to Modeling Flash-Boiling Fuel Sprays for Direct-Injection Spark-Ignition Engines”. In: *Atomization and Sprays* 26.12 (2016), pp. 1197–1239. DOI: 10.1615/AtomizSpr.2016015807.
- [106] A. Prosperetti. “Vapor Bubbles”. In: *Annual Review of Fluid Mechanics* 49.1 (2017), pp. 221–248. DOI: 10.1146/annurev-fluid-010816-060221.
- [107] S. K. Rachakonda, A. Paydarfar, and D. P. Schmidt. “Prediction of Spray Collapse in Multi-Hole Gasoline Direct-Injection Fuel Injectors”. In: *International Journal of Engine Research* 20.1 (2019), pp. 18–33. DOI: 10.1177/1468087418819527.
- [108] T. Ramcke, A. Lampmann, and M. Pfitzner. “Simulations of Injection of Liquid Oxygen/Gaseous Methane under Flashing Conditions”. In: *Journal of Propulsion and Power* 34.2 (2018), pp. 395–407. DOI: 10.2514/1.B36412.
- [109] J. Rayleigh. “On the Pressure Developed in a Liquid during the Collapse of a Spherical Cavity”. In: *The London, Edinburgh, and Dublin Philosophical Magazine and Journal of Science* 34.200 (1917), pp. 94–98. DOI: 10.1080/14786440808635681.

- [110] M. Razzaghi. “Droplet Size Estimation of Two-Phase Flashing Jets”. In: *Nuclear Engineering and Design* 114.1 (1989), pp. 115–124. DOI: 10.1016/0029-5493(89)90130-1.
- [111] A. Rees. “Experimental Investigation of Flash Boiling Cryogenic Nitrogen under High-Altitude Conditions”. Doctoral Thesis. Lampoldshausen: RWTH Aachen, 2020. 198 pp.
- [112] A. Rees, L. Araneo, H. Salzmänn, G. Lamanna, J. Sender, and M. Oswald. “Droplet Velocity and Diameter Distributions in Flash Boiling Liquid Nitrogen Jets by Means of Phase Doppler Diagnostics”. In: *Experiments in Fluids* 61 (2020), p. 182. DOI: 10.1007/s00348-020-03020-7.
- [113] A. Rees, H. Salzmänn, J. Sender, and M. Oswald. “About the Morphology of Flash Boiling Liquid Nitrogen Sprays”. In: *Atomization and Sprays* 30.10 (2020), pp. 713–740. DOI: 10.1615/AtomizSpr.2020035265.
- [114] R. C. Reid. “Superheated Liquids”. In: *American Scientist* 64.2 (1976), pp. 146–156.
- [115] J. R. Riznic and M. Ishii. “Bubble Number Density and Vapor Generation in Flashing Flow”. In: *International Journal of Heat and Mass Transfer* 32.10 (1989), pp. 1821–1833. DOI: 10.1016/0017-9310(89)90154-3.
- [116] U. S. Rohatgi and E. Reshotko. “Non-Equilibrium One-Dimensional Two-Phase Flow in Variable Area Channels”. In: *Proceedings of the Winter Annual Meeting*. Houston, Texas, 1975.
- [117] H. Rusche. “Computational Fluid Dynamics of Dispersed Two-Phase Flows at High Phase Fractions”. Doctoral Thesis. Imperial College London, 2003.
- [118] K. Saha, S. Som, and M. Battistoni. “Investigation of Homogeneous Relaxation Model Parameters and Their Implications for Gasoline Injectors”. In: *Atomization and Sprays* 27.4 (2017), pp. 345–365. DOI: 10.1615/AtomizSpr.2017016338.
- [119] R. Saurel, F. Petitpas, and R. Abgrall. “Modelling Phase Transition in Metastable Liquids: Application to Cavitating and Flashing Flows”. In: *Journal of Fluid Mechanics* 607 (2008), pp. 313–350. DOI: 10.1017/S0022112008002061.
- [120] D. P. Schmidt, S. Gopalakrishnan, and H. Jasak. “Multi-Dimensional Simulation of Thermal Non-Equilibrium Channel Flow”. In: *International Journal of Multiphase Flow* 36.4 (2010), pp. 284–292. DOI: 10.1016/j.ijmultiphaseflow.2009.11.012.

- [121] D. Schmidt, R. Maulik, and K. Lyras. “Machine Learning Accelerated Turbulence Modeling of Transient Flashing Jets”. In: *Physics of Fluids* 33.12 (2021), p. 127104. DOI: 10.1063/5.0072180.
- [122] S. Schütz, K. Kissling, M. Schilling, and C. Seyfert. “Numerical Simulation of Multiphase Flow Systems”. In: *Multiphase Flow Research*. Nova Science Publisher, 2009.
- [123] J. Senda, Y. Hijyo, and H. Fujimoto. “Modelling on Atomization and Vaporization Process in Flash Boiling Spray”. In: *JSAE Review* 15.4 (1994), pp. 291–296. DOI: 10.1016/0389-4304(94)90209-7.
- [124] E. Sher, T. Bar-Kohany, and A. Rashkovan. “Flash-Boiling Atomization”. In: *Progress in Energy and Combustion Science* 34.4 (2008), pp. 417–439. DOI: 10.1016/j.pecs.2007.05.001.
- [125] E. Sher and C. Elata. “Spray Formation from Pressure Cans by Flashing”. In: *Industrial & Engineering Chemistry Process Design and Development* 16.2 (1977), pp. 237–242. DOI: 10.1021/i260062a014.
- [126] T. S. Shin and O. C. Jones. “Nucleation and Flashing in Nozzles-1. A Distributed Nucleation Model”. In: *International Journal of Multiphase Flow* 19.6 (1993), pp. 943–964. DOI: 10.1016/0301-9322(93)90071-2.
- [127] P. A. Skovorodko. “About the Nature of the Recirculation Zone Behind a Mach Disk in an Underexpanded Jet”. In: 27th International Symposium on Rarefied Gas Dynamics. Pacific Grove, California, (USA), 2011, pp. 601–606. DOI: 10.1063/1.3562713.
- [128] V. P. Skripov. *Metastable liquids*. New York: J. Wiley, 1973. 272 pp.
- [129] J. Smagorinsky. “General Circulation Experiments with the Primitive Equations”. In: *Monthly Weather Review* 91.3 (1963), pp. 99–164. DOI: 10.1175/1520-0493(1963)091<0099:GCEWTP>2.3.CO;2.
- [130] S. Soller, N. Rackemann, A. Preuss, and G. Kroupa. “Application of Laser-Ignition Systems in Liquid Rocket Engines”. In: *Space Propulsion Conference*. 2016.
- [131] *Substance Information - ECHA*. URL: <https://echa.europa.eu/substance-information/-/substanceinfo/100.005.560> (visited on 04/14/2023).
- [132] R. C. Tolman. “The Effect of Droplet Size on Surface Tension”. In: *The Journal of Chemical Physics* 17.3 (1949), pp. 333–337. DOI: 10.1063/1.1747247.

- [133] G. Tryggvason, S. Thomas, J. Lu, and B. Aboulhasanzadeh. “Multiscale Issues in DNS of Multiphase Flows”. In: *Acta Mathematica Scientia* 30.2 (2010), pp. 551–562. DOI: 10.1016/S0252-9602(10)60062-8.
- [134] E. Valero and I. E. Parra. “The Role of Thermal Disequilibrium in Critical Two-Phase Flow”. In: *International Journal of Multiphase Flow* 28.1 (2002), pp. 21–50. DOI: 10.1016/S0301-9322(01)00064-7.
- [135] A. Vallet, A. A. Burluka, and R. Borghi. “Development of a Eulerian Model for the ”Atomization” of a Liquid Jet”. In: *Atomization and Sprays* 11.6 (2001), pp. 619–642. DOI: 10.1615/atomizspr.v11.i6.20.
- [136] E. R. Van Driest. “On Turbulent Flow Near a Wall”. In: *Journal of the Aeronautical Sciences* 23.11 (1956), pp. 1007–1011. DOI: 10.2514/8.3713.
- [137] H. K. Versteeg and W. Malalasekera. *An Introduction to Computational Fluid Dynamics: The Finite Volume Method*. 2nd ed. Harlow, England ; New York: Pearson Education Ltd, 2007. 503 pp.
- [138] M. M. Vieira and J. R. Simões-Moreira. “Low-Pressure Flashing Mechanisms in Iso-Octane Liquid Jets”. In: *Journal of Fluid Mechanics* 572 (2007), pp. 121–144. DOI: 10.1017/S0022112006003430.
- [139] M. Volmer and A. Weber. “Keimbildung in Übersättigten Gebilden”. In: *Zeitschrift für Physikalische Chemie* 119U.1 (1926), pp. 277–301. DOI: 10.1515/zpch-1926-11927.
- [140] H. Weller and A. Shahrokhi. “Curl-Free Pressure Gradients over Orography in a Solution of the Fully Compressible Euler Equations with Implicit Treatment of Acoustic and Gravity Waves”. In: *Monthly Weather Review* 142.12 (2014), pp. 4439–4457. DOI: 10.1175/MWR-D-14-00054.1.
- [141] H. Witlox, M. Harper, P. Bowen, and V. Cleary. “Flashing Liquid Jets and Two-Phase Droplet Dispersion. II. Comparison and Validation of Droplet Size and Rainout Formulations”. In: *Journal of Hazardous Materials* 142.3 (2007), pp. 797–809. DOI: 10.1016/j.jhazmat.2006.06.126.
- [142] G. H. Yeoh and J. Tu. *Computational Techniques for Multiphase Flows*. Second edition. Butterworth-Heinemann/ICChemE Series. Kidlington, Oxford, United Kingdom ; Cambridge, MA, United States : b Butterworth-Heinemann, an imprint of Elsevier, 2019. 629 pp.

- [143] Z. F. Zhou, G. Y. Lu, and B. Chen. “Numerical Study on the Spray and Thermal Characteristics of R404A Flashing Spray Using OpenFOAM”. In: *International Journal of Heat and Mass Transfer* 117 (2018), pp. 1312–1321. DOI: 10.1016/j.ijheatmasstransfer.2017.10.095.